STUDY ON
ION BEAM INTERACTIONS
WITH
CRYSTAL SURFACES

YOSHIKAZU FUJII

1993

DEPARTMENT OF ENGINEERING SCIENCE
KYOTO UNIVERSITY
KYOTO, JAPAN

ACKNOWLEDGMENTS

CONTENTS

Chapter 1

INTRODUCTION

This thesis is on the studies of ion beam interactions with crystal surfaces. The interactions, which include various phenomena such as charge-exchange, excitation and energy loss of fast ions, are experimentally investigated with the use of ion-surface scattering at glancing angle incidence of fast ions on clean single crystal surfaces under ultra high vacuum conditions.

Recently, various kinds of electronic elements are fabricated by ion-implantation and ion beam machining, material surfaces are modified by ion beam irradiation, and new materials are fabricated by ion beam deposition. All these new technologies are based on the characteristic behavior of fast ions at a solid surface. Thus understanding of the ion-surface interactions is indispensable not only for the physics of surface but also for the modern technologies where various ion beams are used.

The interactions of ions with solid surfaces have been one of the main subjects in research on ion-solid interactions[1-15]. Many experimental and theoretical studies have been performed on various phenomena such as the charge exchange process at solid surfaces[1-6], the anisotropic distribution of the orbital angular momenta of exited states of ions produced by ion-surface interactions[7-9] and the dynamical response of valence electrons to the fast ions traveling near surfaces[10-15]. However, it is often difficult to eliminate bulk effects in experimental studies of ion-surface interactions.

Recently, many studies[16-32] on the interactions of fast ions with the surfaces have been performed with the use of ion-surface
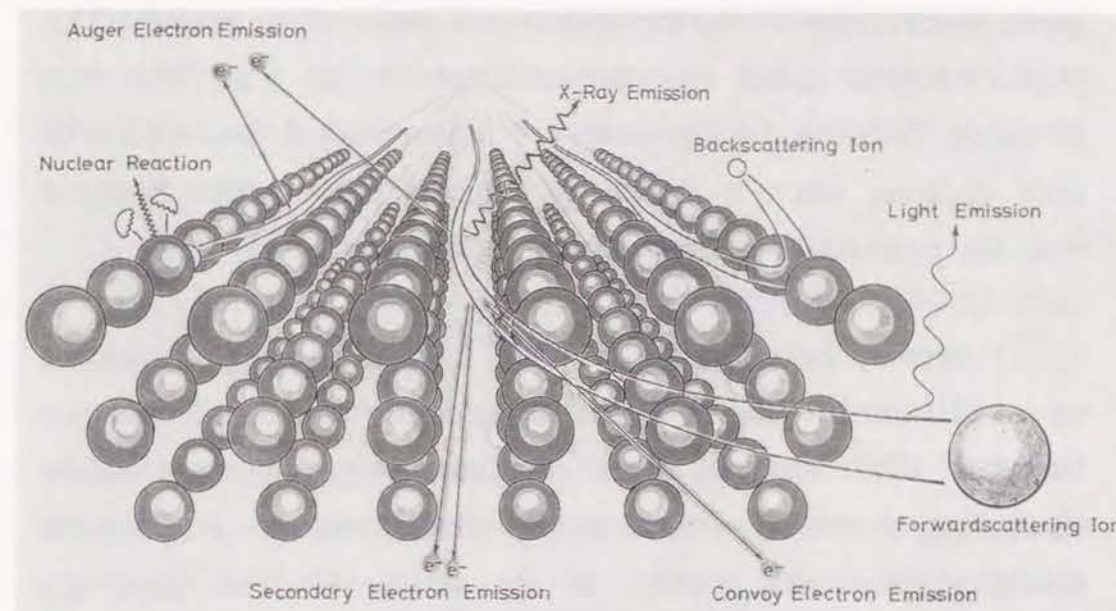
Figure 1.1: Schematic illustration of interactions at glancing angle incidence of fast ions on crystal surface

scattering at glancing angle incidence of fast ions on the surfaces as illustrated in Fig. 1.1. In relatively recent work, formation of coherent excited states of ions which lead to the alignment and polarization of emitted photons, has been studied at glancing angle incidence of fast ions on flat surfaces of single crystals[21]. In these and related studies on ion scattering at glancing angle incidence of fast ions on clean surface of single crystal, it is expected from the

concept of planar channelling of fast ions in crystal[33-35] that the ions do not penetrate into the target crystal but are subjected to specular scattering by the topmost atomic plane of the surface. This phenomenon is called specular reflection of fast ions. This is a favorable situation for the study of interaction of fast ions with solid surfaces, where a number of complex phenomena associated with the penetration of ions through solids can be avoided.

However, the scattering of ions at the glancing angle incidence on a surface of single crystal depends on the incident beam direction with respect to the surface atomic rows. Surface channeling occurs when the ions are incident towards a low index crystallographic axis parallel to the surface. In this case, the interaction between ion and surface is slightly complicated because subsurface atomic layers participate in the scattering of ions[36].

In the studies of this thesis the experimental technique of ion-surface scattering at glancing angle incidence of fast ions under ultra high vacuum conditions has been applied to study the inelastic ion-surface interactions. Processes of energy and charge transfer between fast ions and crystal surfaces are discussed. The inelastic interactions of the ions with the surface take place along a well-defined trajectory of ion at specular reflection, and thus the resulting energy and charge state of the ion are described by the position-dependent stopping powers and charge exchange probabilities as in the case of the planar channeling.[37-39]

The outline of this thesis is as follows:

Chapter 2 describes the experimental methods; preparation of target crystals, experimental setup for ion scattering, and measurement of the energy and charge-state distribution of the scattered ions.

In Chapter 3, the characteristic features of the glancing angle scattering of fast ions from single crystal surface are shown. When fast ions are incident on an atomically flat low-index surface of a crystal at a small glancing angle, the interaction of the ions with the surface is characterized by a series of correlated small angle scatterings with the atoms on the topmost atomic plane of the surface. Surface potentials with which the motions of the scattered ions can be described are introduced. Characteristic features of the angular distribution and energy spectrum of the scattered ions are shown.

In Chapter 4 and Chapter 5, energy losses of the scattered ions at glancing angle incidence on single crystal surfaces are discussed. In Chapter 4, position-dependent stopping powers of the crystal surfaces for MeV H and He ions are determined from the observed energy losses of the ions reflected from the surface. The results are explained by a sum of the stopping caused by collective excitation of surface valence electrons to the fast ion and that due to the single ion-electron collisions. In Chapter 5, energy loss of MeV He ions which have surface-channeled along atomic rows on

a clean (100) surface of SnTe is studied, and contribution of collective excitation of surface valence electrons to the stopping powers is extracted from the observed position–dependent stopping powers. This agrees well with the result of theories on the dynamical response of valence electrons to the fast moving ions.

In Chapter 6 and Chapter 7, charge–state distributions of the scattered ions at glancing angle incidence on single crystal surfaces are discussed. In Chapter 6, most of the features of the scattering–angle dependence of the charge–state distribution of the He ions which are reflected from the topmost atomic layer of the crystal are explained in terms of the position–dependent charge exchange probabilities which are calculated from Bohr and Bohr–Lindhard models. In Chapter 7, a stochastic model of charge exchange and energy loss of ions is developed, where inelastic interactions are assumed to depend on the distance of the ion from the surface. Position–dependent charge exchange probabilities of He ions near the surface are derived from the observed charge–state distributions and charge–state dependence of the energy losses of He ions.

Chapter 8 and Chapter 9 describe applications of the glancing angle scattering of fast ions from crystal surfaces. In Chapter 8, scattering phenomena of MeV light ion at crystal surface are calculated with the use of a computer simulation of the trajectory of the ion at glancing angle incidence on a crystal surface. It is found that the yield and angular distribution of scattered ions from the surface depend sensitively on the step density on the surface, and a new method to detect surface step density by measuring the ion yield at glancing angle incidence of MeV ions on the crystal surface is proposed. In Chapter 9, process of epitaxial growth of PbSe on SnTe (100) is studied with the use of glancing angle scattering of MeV He ions. Anomalous broadening of the angular distribution of scattered He ions from the surface of PbSe is observed at initial stage of the growth. This broadening is ascribed to the surface wrinkles caused by a square–net of misfit edge dislocations.

REFERENCES

1) B. A. Trubnikov and Yu. N. Yavlinskii, Zh. Eksp. Teor. Fiz. 25 (1967) 1089.

2) H. D. Hagstrum, in "Inelastic Ion–Surface Collisions", ed. N. H. Tolk, *et al.* (Academic Press, 1977) p.1.

3) M. Kitagawa and Y. H. Ohtsuki, Phys. Rev. B 13 (1976) 4682.

4) S. Datz, "Applied Atomic Collision Physics" (Academic press, Orlando, 1983) Vol. 4.

5) R. Haight, L. C. Feldman, T. M. Buck and W. M. Gibson, Phys. Rev. B 30 (1984) 734.

6) J. Burgdörfer, E. Kupfer and H. Gabriel, Phys. Rev. A 35 (1987) 4963.

7) H. J. Andrä, H. Winter, R. Fröhling, N. Kirchner, H. J. Plöhn, W. Wittmann, W. Graser and C. Varelas, Nucl. Instrum. Methods 170 (1980) 527.

8) R. Brako, D. M. Newns, N. H. Tolk, J. C. Tully and R. J. Morris, Phys. Lett. 114A (1986) 327.

9) H. Winter, Physica Scripta T6 (1983) 136.

10) R. M. Nieminen and C. H. Hodges, Phys. Rev. B 15 (1978) 2568.

11) F. Garcia–Moliner and F. Flores, "Introduction to the theory of solid surfaces", (Cambridge Univ. Press, 1979).

12) Y. H. Ohtsuki, Charged Beam Interaction with Solids, (Taylor & Francis Ltd., 1983).

13) G. Gumbs and M. L. Glasser, Phys. Rev. B 37 (1988) 1391.

14) M. Kitagawa, Nucl. Instrum. and Methods B 33 (1988) 409.

15) P. M. Echenique, F. Flores and R. H. Ritchie, in "Solid State Physics" vol. 43, ed. Seitz and Turnbull, (Academic Press, Inc. 1991) p.230.

16) A. D. Marwick, M. W. Thompson, B. Farmery and G. S. Harrison, Radiat. Eff. 10 (1971) 49, Radiat. Eff. 15 (1972) 195.

17) G. S. Harbinson, B. W. Farmery, H. J. Pabst and M. W. Thompson, Radiat. Eff. 27 (1975) 97.

18) R. Sizmann and C. Varelas, Nucl. Instrum. and Methods 132 (1976) 633.

19) V. S. Remizovich, M. I. Ryazanov and I. S. Tilinin, Sov. Phys. JETP 52 (1980) 225, Sov. Phys. Dokl. 25 (1980) 751.

20) N. Kuwata, K. Kimura and M. Mannami, Nucl. Instrum. and Methods B 1 (1984) 35.

21) H.Winter, Nucl. Instrum. and Methods B 2 (1984) 286.

22) E. S. Mashkova and V. A. Molchanov, "Medium–Energy Ion Reflection from Solids", (North–Holland, 1985).

23) C. Varelas, in "Structure and Dynamics of Surfaces I ", ed. W. Schommers and P. von Blanckenhagen (Springer–Verlag, 1987) p.111.

24) V. I. Shulga, Radiat. Eff. 100 (1986) 71.

25) H. Nienhaus, R. Zimny and H. Winter, Radiat. Eff. 109 (1989) 1, R. Zimny, H. Nienhaus and H. Winter, Radiat. Eff. 109 (1989) 9.

26) K. J. Snowdon, D. J. O'Connor and R. J. Macdonald, Appl. Phys. A 47 (1988) 83, Radiat. Eff. 109 (1989) 25, 33, Surf. Sci. 221 (1989) 465, K. J. Snowdon, D. J. O'Connor, M. Kato and R. J. Macdonald, Nucl. Instrum. and Methods B 48 (1990) 327.

27) H. Winter, Z. Phys. D 17 (1990) 109, Phys. Lett. 148A (1990) 258r, Nucl. Instrum. and Methods B 48 (1990) 382.

28) F. Stölzle and R. Pfandzelter, Phys. Lett. A 150 (1990) 315, Surf. Sci. 251/252 (1991) 383, Europhys. Lett. 20 (1992) 369.

29) H. Winter, R. Kirsch, J. C. Poizat and J. Remillieux, Phys. Rev. A 43 (1991) 1660.

30) A. Närmann, W. Heiland, R. Monreal, F. Flores and P. M. Echenique, Phys. Rev. B 44 (1991) 2003.

31) H. Winter, Europhys. Lett. 18 (1992) 20.

32) H. Winter and M. Sommer, Phys. Lett. 168A (1992) 409.

33) J. Lindhard, K. Dan. Vid. Selsk. Mat. Fys. Medd. 34, No.14 (1965).

34) D. V. Morgan, ed, "Channeling-Theory, Observation and Application, 1973", (John Wiley & Sons, New York).

35) D. S. Gemmell, Rev. Mod. Phys. 46 (1974) 129.

36) K. Morita, Radiat. Eff. 52 (1980) 235.

37) M. T. Robinson, Phys. Rev. 179 (1969) 327.

38) F. H. Eisen and M. T. Robinson, Phys. Rev. B 4 (1971) 1457.

39) M. T. Robinson, Phys. Rev. B 4 (1971) 1461.

Chapter 2

EXPERIMENTAL

ABSTRACT

In the present chapter, we describe the experimental methods; preparation of target crystals, experimental setup for ion scattering, and measurement of the energy and charge-state distribution of the scattered ions.

2.1. PREPERATION OF TARGETS

For the study of glancing angle scattering of fast ions from a single crystal surface, an atomically clean and low–index surface with less number of surface steps is required. Thus the cleavage surfaces of alkali halides and the epitaxial single crystals grown on the cleavage surfaces of alkali halide are used in the experiments. All the crystals used in the present experiments had NaCl type crystal structure and the ion scattering experiments were performed on the (100) surfaces. The cleaning of the cleavage surfaces and epitaxial growth had to be done under UHV conditions.

2.1.1. The (100) Surfaces of Alkali Halides

Alkali halide single crystal was cleaved along the {100} surfaces in air and the surface with less number of visible steps was chosen. The sizes of the crystals used were 30×30 mm^2 and the thicknesses were larger than 5 mm so that the deformation of the crystals introduced during the cleavage is as small as possible. It was then mounted in a precision 5–axis goniometer in a UHV scattering chamber and was heated to 250 $^{\circ}$C after the chamber was evacuated to the 10^{-10} Torr range. Alkali halides used in the experiments were NaCl, KCl and KBr.

2.1.2. The (100) Surfaces of SnTe

Single crystal of SnTe was prepared by epitaxial growth on the (100) surface of KCl. On the clean (100) surface of KCl which had been prepared by the procedure mentioned in 2.1.1., pure SnTe (purity 99.999 %) was evaporated from a tungsten helical filament,

while the vacuum chamber was kept below 2×10^{-9} Torr and the substrate KCl was kept at 250 $^{\circ}$C. In this case the SnTe film grew initially in the form of three–dimensional islands on the substrate KCl. When the thickness of SnTe was more than 100 nm, the islands were connected to form a uniform single crystal film. The SnTe crystal thus prepared had NaCl type crystal structure and was a well–oriented single crystal. The orientation relationship of the SnTe and KCl substrate was

$$(100)_{SnTe} \parallel (100)_{KCl}, \quad <001>_{SnTe} \parallel <001>_{KCl}.$$

The (100) surface of SnTe showed a clear 1×1 structure when examined with reflection high energy electron diffraction (RHEED). In order to keep the surface clean during the ion scattering experiment, and in order to avoid the contamination and radiation damage due to energetic ions, SnTe was evaporated intermittently on the SnTe(100) surface during the experiment.

The structure of the (100) surface of SnTe was studied by RBS/channeling of MeV He ions.[1] From the analysis of the yields of He ion backscattered from the surface, it was found that the SnTe(001) surface is "bulk-exposed", and that the one–dimensional thermal vibration amplitude of the surface atoms is 0.020 nm (Debye temperature 118 K) which is a little higher than that of the bulk atoms, 0.017 nm (Debye Temperature 138 K). It was also shown that the surface relaxation, if exists, is less than ± 5 % of the bulk interlayer spacing, and that surface rumpling which was

observed on the (100) surface of crystal with NaCl crystal structure does not exist on the (100) surface of SnTe.

2.1.3. The (100) Surfaces of Lead Chalcogenides

Lead chalcogenide crystals, PbS, PbSe and PbTe, were prepared by vacuum epitaxial growth on the (100) surface of SnTe which had been prepared by the procedure mentioned in 2.1.2. Pure lead chalcogenide was evaporated on the SnTe/KCl kept at 250 °C in the vacuum below 2×10^{-9} Torr. These grown crystals were good single crystals except for the misfit dislocations on the interfaces with substrate SnTe.[2-4] The orientation relationship of lead chalcogenides and SnTe were

$$(100)_{chal.} \| (100)_{SnTe}, \quad <001>_{chal.} \| <001>_{SnTe},$$

The (100) surfaces of the lead chalcogenides showed a clear 1 × 1 structure when examined with reflection high energy electron diffraction (RHEED).

2.2. MEASURMENT OF ION ENERGIES

2.2.1. Solid State Detectors

For the measurement of the energy of several 100's keV to a few MeV light ion, solid state detector (SSD) of ion-implantion passivated, bakeable type was used. Because the SSD has thin dead surface layer, the energy loss, E_L, in the dead layer has to be taken into account for the accurate energy determination. When the height of the output signal of the injected ion with energy, E_0, is C_0, the

energy E of an ion which gives rise to the signal height C in the detector is calibrated by the relation,

$$E = (E_0 - E_L) \cdot \frac{C}{C_0} + E_L . \tag{1}$$

Table 1 shows the energy losses within the dead layers of the SSD's used in the experiments. The losses were calculated from the thickness of the dead layer and the stopping powers with the use of the Ziegler's tables of stopping powers.[5]

Table 1

ION	ENERGY(keV)	ENERGY LOSS (keV)	
		MH−016−050−100 (EG&G ORTEC)	PD25−11−300AM (CANBERRA)
He⁺	400	74	17.5
	600	75	17.2
	900	70.5	15.7
	1200	65.5	14.2
	1500	60.5	13.0
	1800	56.5	12.0
H⁺	400	15.2	3.1
	600	12.4	2.7
	800	10.7	2.3
	1000	9.4	2.0
	1200	8.5	1.8
	1500	7.4	1.55
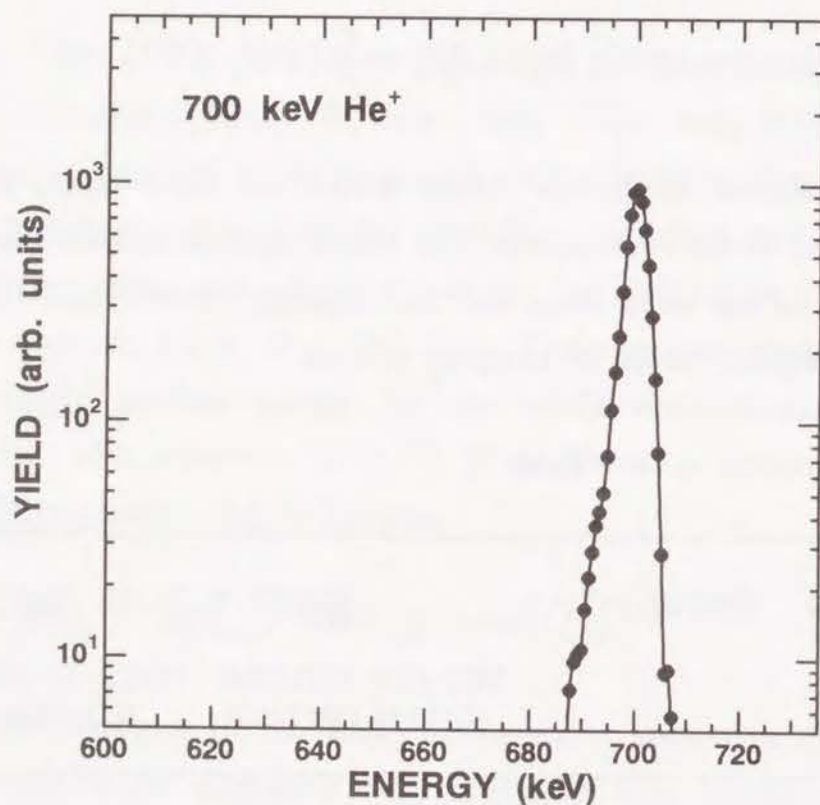
700 keV He⁺

Figure 2.1: Energy spectrum of 0.7 MeV He⁺ ions detected by SSD (PD25–11–300AM) fabriacated by Canberra. Ions were injected from the 4–MV Van de Graaff accelerator.

An example of the observed energy spectra of 700 keV He⁺ ions from the 4–MV Van de Graaff accelerator is shown in Fig. 2.1, where the SSD manufactured by Canberra (PD25–11–300AM) was used. It is important to know the full width at half maximum

(FWHM) of the energy spectrum as the energy resolution of the detector. The observed energy resolution of the used SSD's for various ions are shown in Table 2.

Table 2

ION	ENERGY(keV)	FWHM (keV)	
		MH–016–050–100 (EG&G ORTEC)	PD25–11–300AM (CANBERRA)
He⁺	700	14	9.5
	1000	15	10.5
	1500	16	11.5
H⁺	700	12	8
	1000	12.5	8
	1500	13	9

2.2.2. Cylindrical Radial Field Spectrometer

For the observation of the energy of several 10's keV N⁺ ions a cylindrical radial field spectrometer was constructed. A schematic drawing of the spectrometer is shown in Fig. 2.2, and the photograph of the inside of the spectrometer is shown in Fig. 2.3.
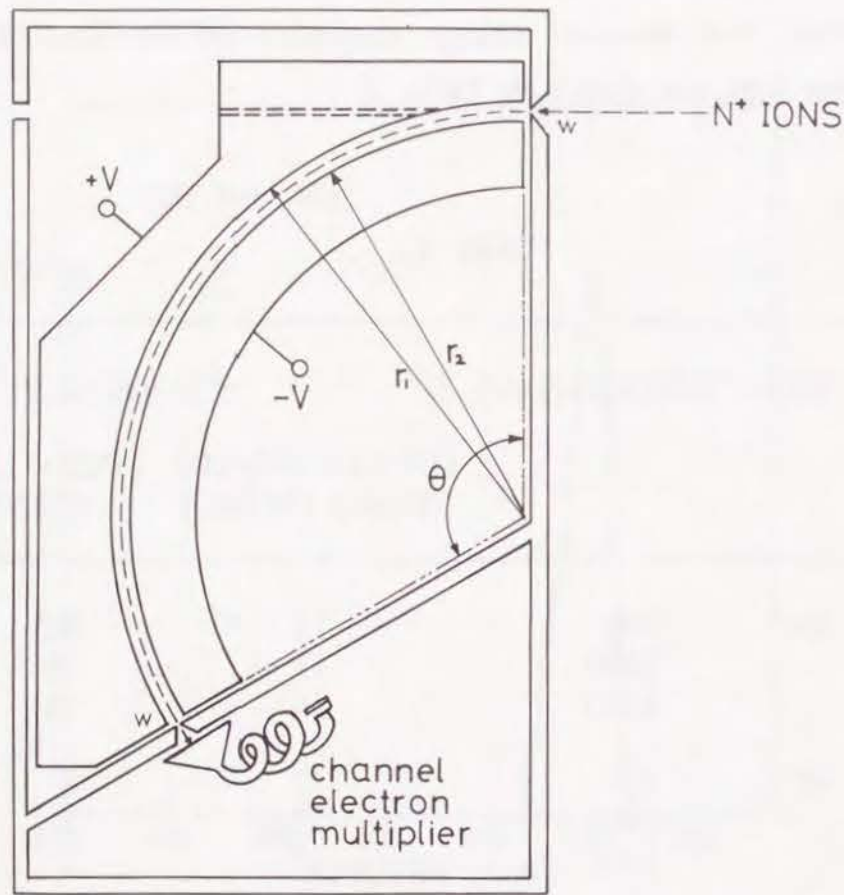
Figure 2.2: Schematic drawing of the cylindrical radial field spectrometer.

Potential V is applied to the coaxial cylindrical electrodes to define the radial field. When a sector angle θ is $\pi/\sqrt{2}$, the injected ions are focused on the field boundaries. The actual sector angle is only $119°$ in order to compensate for the fringing field effects.[6] The ions which have passed through the spectrometer system are detected by a channel electron multiplier.
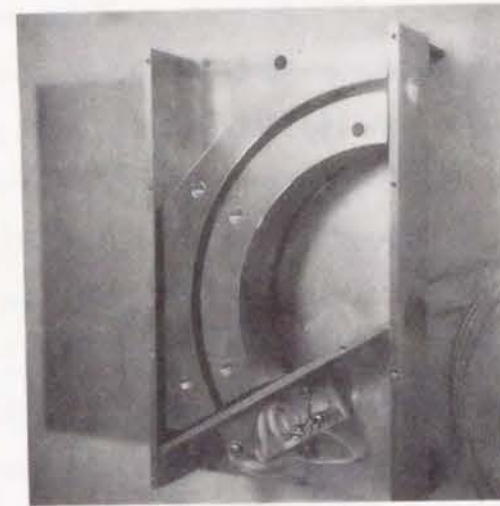
Figure 2.3: Photograph of the inside of the cylindrical radial field spectrometer.

The energy E of the detected ion is proportional to the potential V as,

$$E = \frac{V}{\ln (r_1 / r_2)} , \qquad (2)$$

where r_1 and r_2 are the radii of the outer and inner coaxial cylindrical electrodes, respectively. For the equal entrance and exit slit widths w, the energy resolution is given as,

$$\frac{\Delta E}{E} = \frac{2w}{r_1 + r_2} + \frac{4}{3}(\Delta \alpha)^2 , \qquad (3)$$
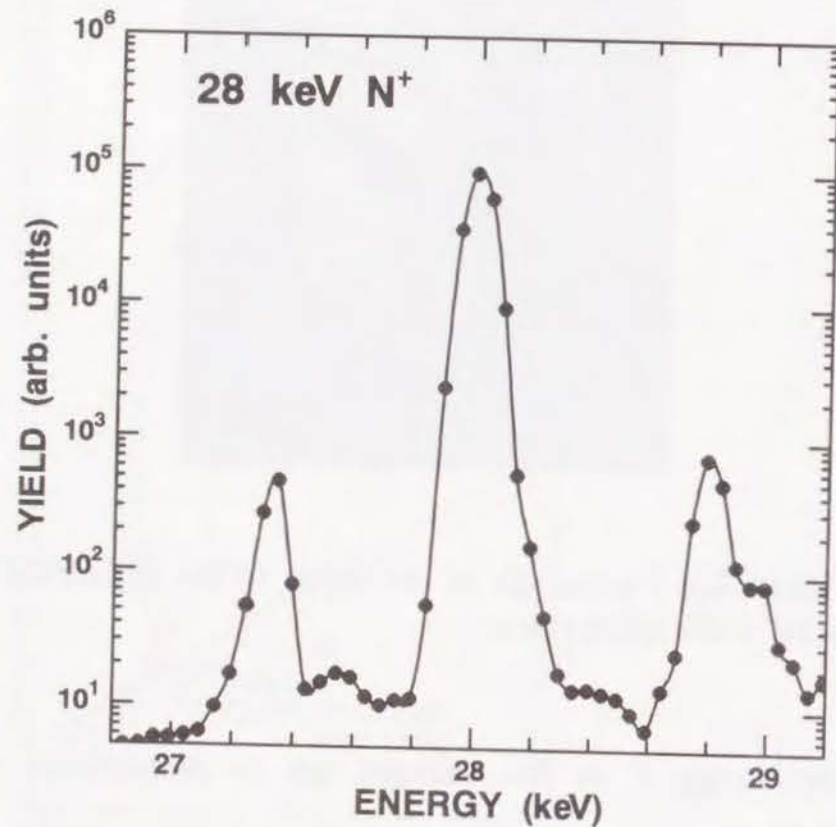
Figure 2.4: Energy spectrum of 28 keV N^+ ions analyzed by the cylindrical radial field spectrometer. The ions were injected from an RF ion source.

with no β aberration (in the perpendicular plane), where $\Delta\alpha$ is the angular aberration in the sector plane. The actual dimensions of the spectrometer were,

$$r_1 = 78 \text{ mm}, \quad r_2 = 82 \text{ mm}, \quad w = 0.2 \text{ mm}.$$

The acceptance angle of the analyzer was 2 mrad. In this case the energy resolution $\Delta E/E$ is 0.25 %. An example of the observed energy spectrum of 28 keV N^+ ions injected from an RF ion source is shown in Fig. 2.4. The FWHM of the energy spectrum is 0.1 keV and $\Delta E/E$ is 0.3 %, which agrees well with that expected from the design of the spectrometer. Although two sub–peaks which consist of the ions reflected from the electrodes are observed in the energy spectrum, there is no significant influence of the sub–peaks on the measurement of the energy spectra of ions because the heights of the sub–peaks are less than 1 % of the height of the main–peak.

2.2.3. Magnetic Spectrometer

For high–resolution measurement of the energy of several 100's keV ions, a magnetic spectrometer was constructed. A schematic drawing of the spectrometer is shown in Fig. 2.5. An aperture (slit 1) of diameter 0.06 mm as the entrance of the spectrometer was installed at 300 mm downstream from the target. The ions which have passed through the spectrometer system are energy analyzed and detected by an SSD. The velocity v of the detected ion is proportional to the magnetic field B as,

$$v = \frac{Bqsl}{md}, \tag{4}$$

where q and m are the charge and mass of the ion, respectively, and the dimensions of s, l and d are shown in Fig. 2.5.
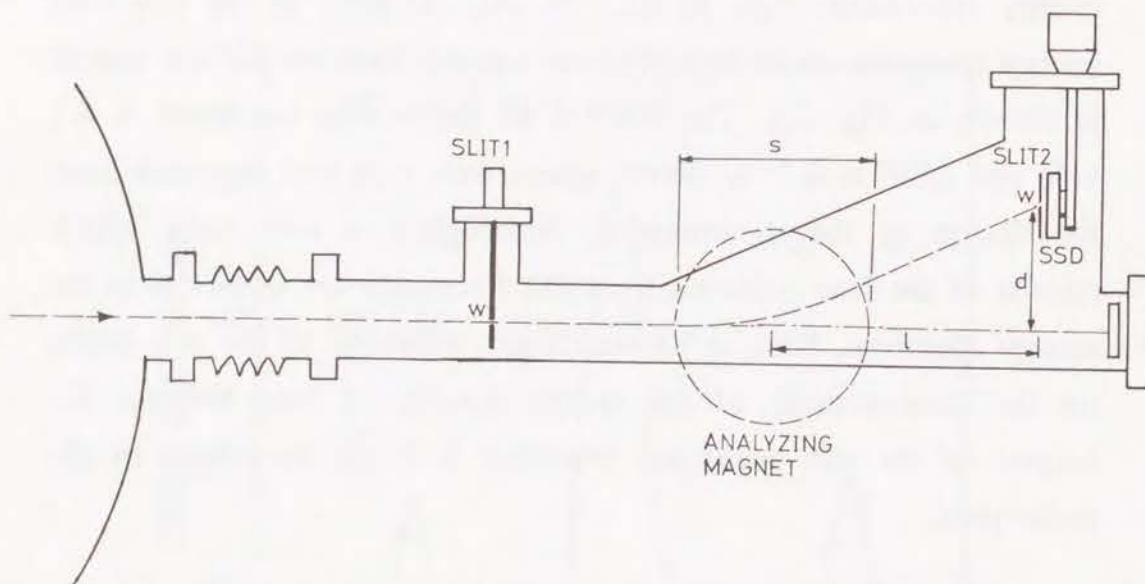
Figure 2.5: Schematic drawing of the magnetic spectrometer.

For equal entrance and exit slit widths w, the energy resolution of the spectrometer is

$$\frac{\Delta E}{E} = \frac{4w}{d} , \qquad (5)$$

where the angular aberrations are neglected. The actual dimensions of the spectrometer were,

d = 30 − 74 mm, w = 0.06 mm.

In this case the energy resolution $\Delta E/E$ is 0.8 − 0.32 %.
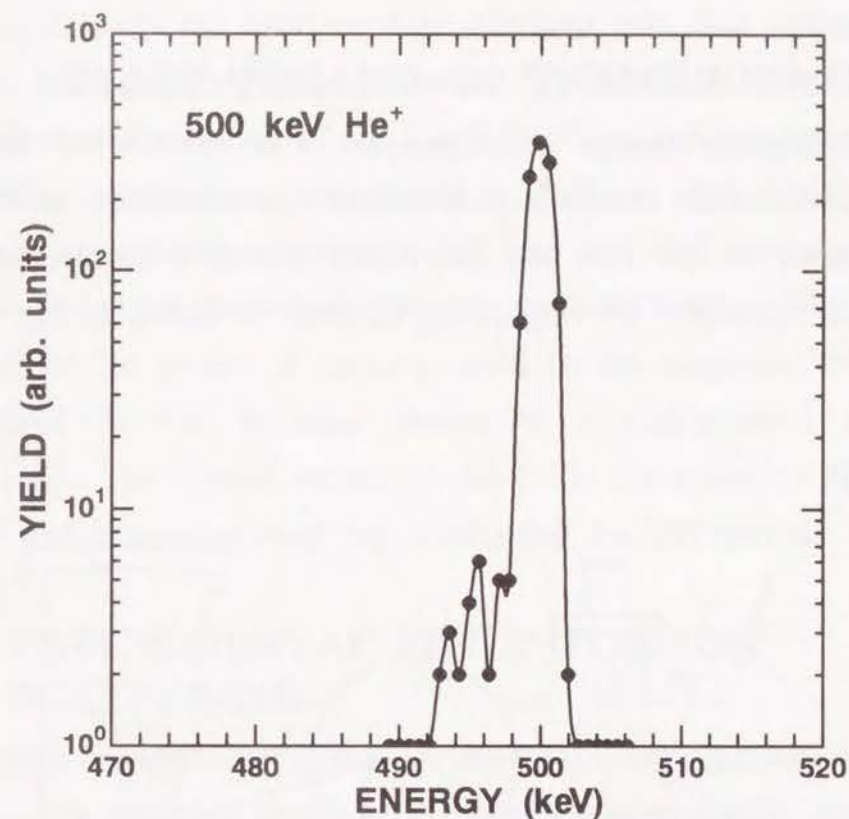
Figure 2.6: Energy spectrum of 500 keV He⁺ ions injected from the 4−MV Van de Graaff accelerator analyzed by the magnetic spectrometer.

An example of the observed energy spectra of 500 keV He⁺ ions injected from the 4−MV Van de Graaff accelerator is shown in Fig. 2.6. The FWHM of the energy spectrum is 2.5 keV and $\Delta E/E$ is 0.5 % when d is 30 mm. Because the incident He⁺ beam was collimated to 0.02×0.02 mm^2, the effective entrance slit width

was less than 0.02 mm, and thus the observed width of the energy peak was narrower than that estimated from the actual slit width.

2.3. MEASUREMENT OF CHARGE STATE

A magnetic charge state analyzer was constructed for the measurement of the charge state distribution of scattered ions, where the energies of the ions are distributed within a narrow energy region. A schematic drawing of the analyzer is shown in Fig. 2.7.
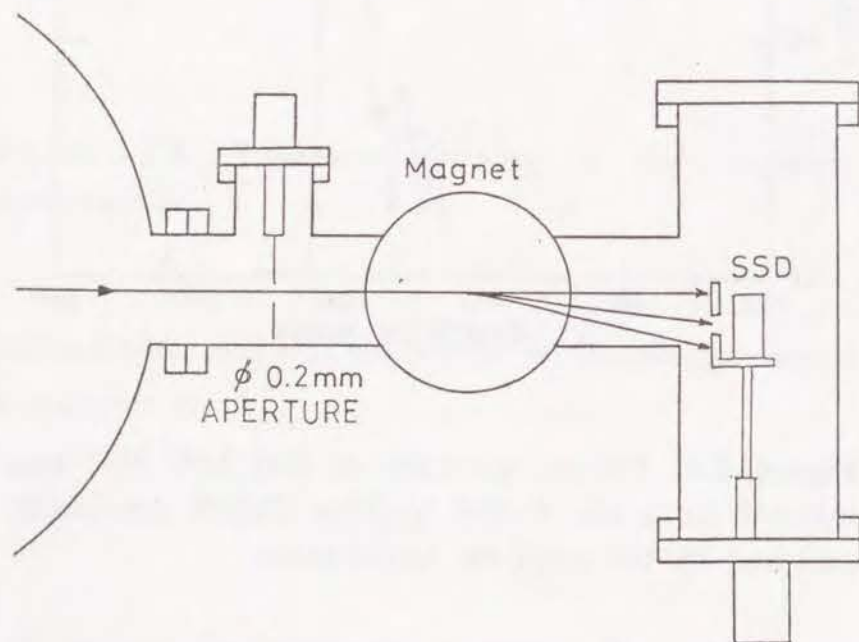
Figure 2.7: Schematic drawing of the magnetic analyzer for measuring the charge state distributions of ions.

An aperture of diameter 0.2 mm as the entrance of the analyzer was installed at 300 mm downstream from the target. The ions passing through the aperture were resolved into their charge states by the analyzing magnet and detected by an SSD. In order to avoid the effect of fluctuation of the intensity of the incident beam in the scattering experiment, the magnetic field of the analyzer was changed periodically so that the He^+ ions and He^{2+} ions (or neutral atoms and total particles) are detected alternately. The energy spectra of the groups of ions separated by the magnetic field were registered in two memory groups of a multichannel analyzer separately. The typical period of change in the magnetic field was 3 sec and a measurement was performed for 100 periods.

2.4. EXPERIMENTAL SETUP FOR ION SCATTERING

The experimental setup is shown in Fig. 2.8. A beam of momentum analyzed ions from the 4–MV Van de Graaff accelerator of Kyoto University was transported through a beam duct of about 10 m in length. A differential pumping system was installed between the accelerator and the UHV chamber in order to separate the UHV chamber vacuum in the 10^{-10} Torr range from the accelerator vacuum in the 10^{-6} Torr range. The beam was collimated by a series of slits (SLIT 1 and SLIT 2) to 0.03 mm × 0.03 mm and to the divergence angle less than 0.2 mrad on the target crystal mounted in a goniometer in the UHV chamber.

DIFFRENTIAL
PUMPING SYSTEM
~10⁻⁸ TORR

ION BEAM

SLIT 1

SLIT 2

UHV
SCATTERING
CHAMBER
~10⁻¹⁰TORR

FOIL

CRYSTAL

CRYOGENIC
PUMP

EVAPORATORS

CYLINDRICAL
ANALYSER

FLUORESCENT
SCREEN

APERTURE 1

ANALYZING
MAGNET

SLIT 3

SSD 1

SSD2
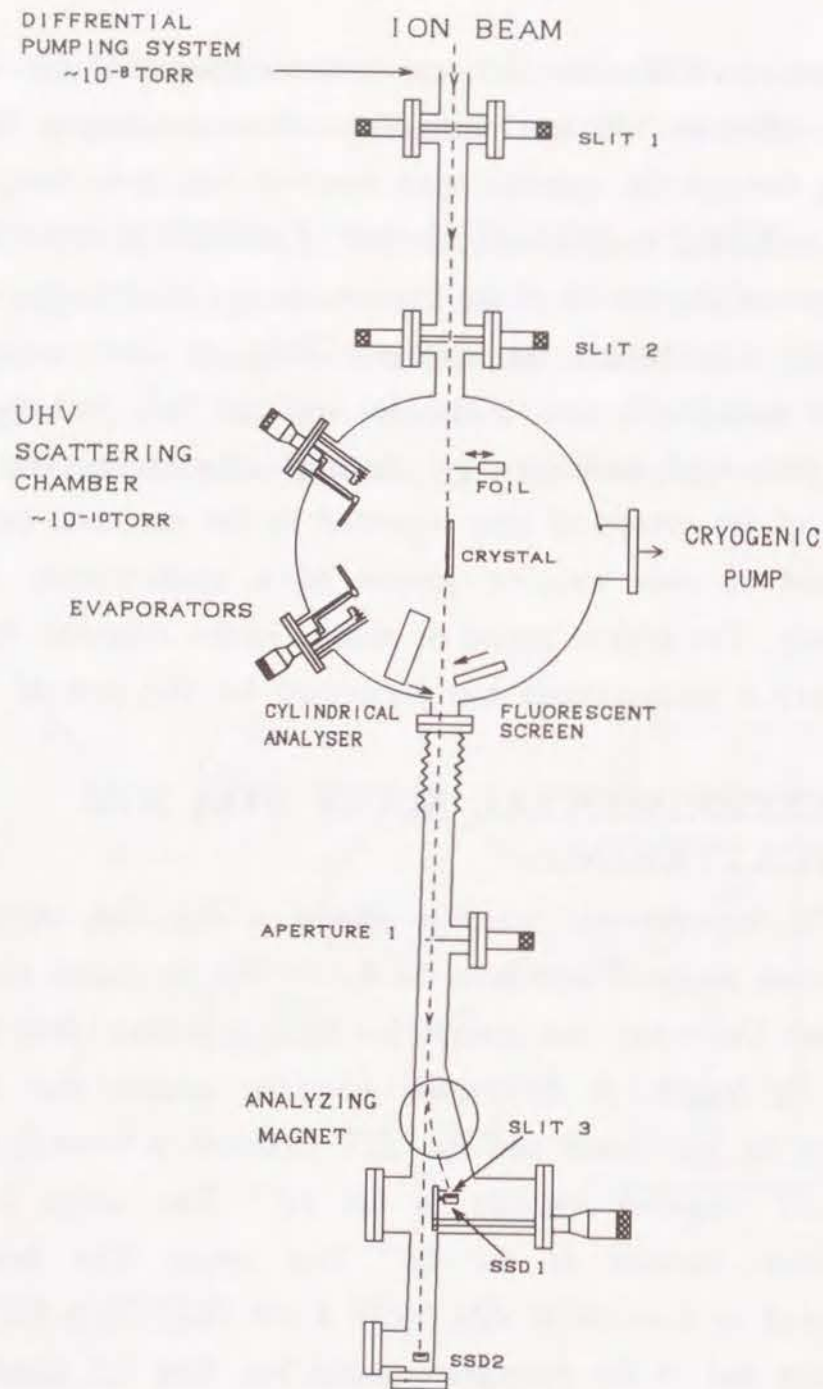
Figure 2.8: Schematic drawing of the experimental setup.

The scattered ions were chosen by a movable aperture (APERTURE 1) and they were analyzed by various measuring systems placed downstream from the aperture depending on the type of experiment. In Fig. 2.8, the magnetic spectrometer is shown. The base pressure of the UHV chamber was 3×10^{-10} Torr and the vacuum was maintained by a cryogenic pumping system. For degasing, the whole vacuum system was heated to 150 °C for 20 hours.

For the experiments with lower energy ions, the scattering chamber similar to the one shown in Fig. 2.8 was connected to the 30 kV ion separator and the cylindrical radial field spectrometer was installed downstream from the target for energy analysis.

Target crystal was mounted in a high–precision 5–axis goniometer in the UHV chamber. The goniometer was specially designed to have higher accuracy compared with the goniometer available commercially. Figure 2.9 shows the schematic drawing of the goniometer. It has two high precision rotation mechanisms. The target crystal mounted on a copperplate was heated with a sheathed heater embedded in the copper plate.

Orientation of the target crystal relative to the incident beam of ions was determined from the angular distribution of the scattered ions which could be observed on the fluorescence screen downstream the target. Change of the angular distribution of scattered He ions is shown in Fig. 2.10 at the incidence of 1.6 MeV He⁺ ions on the (100) surface of SnTe. Ions scattered along
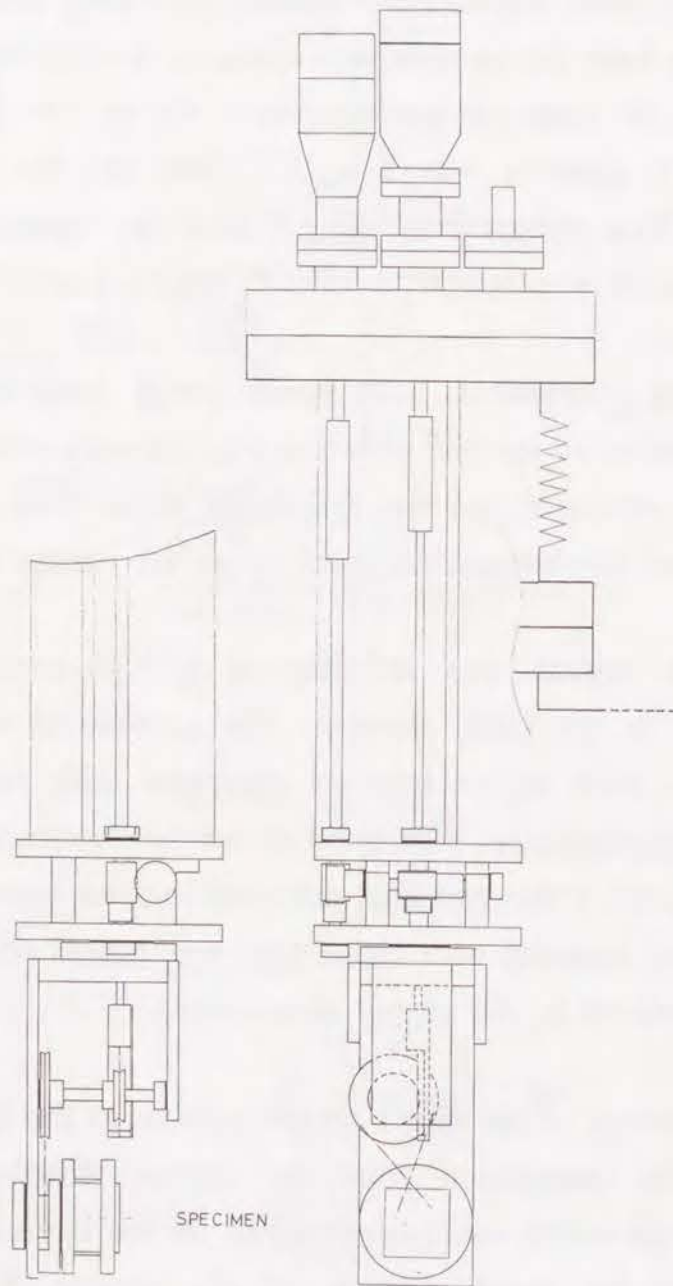
Figure 2.9: Schematic drawing of the goniometer.
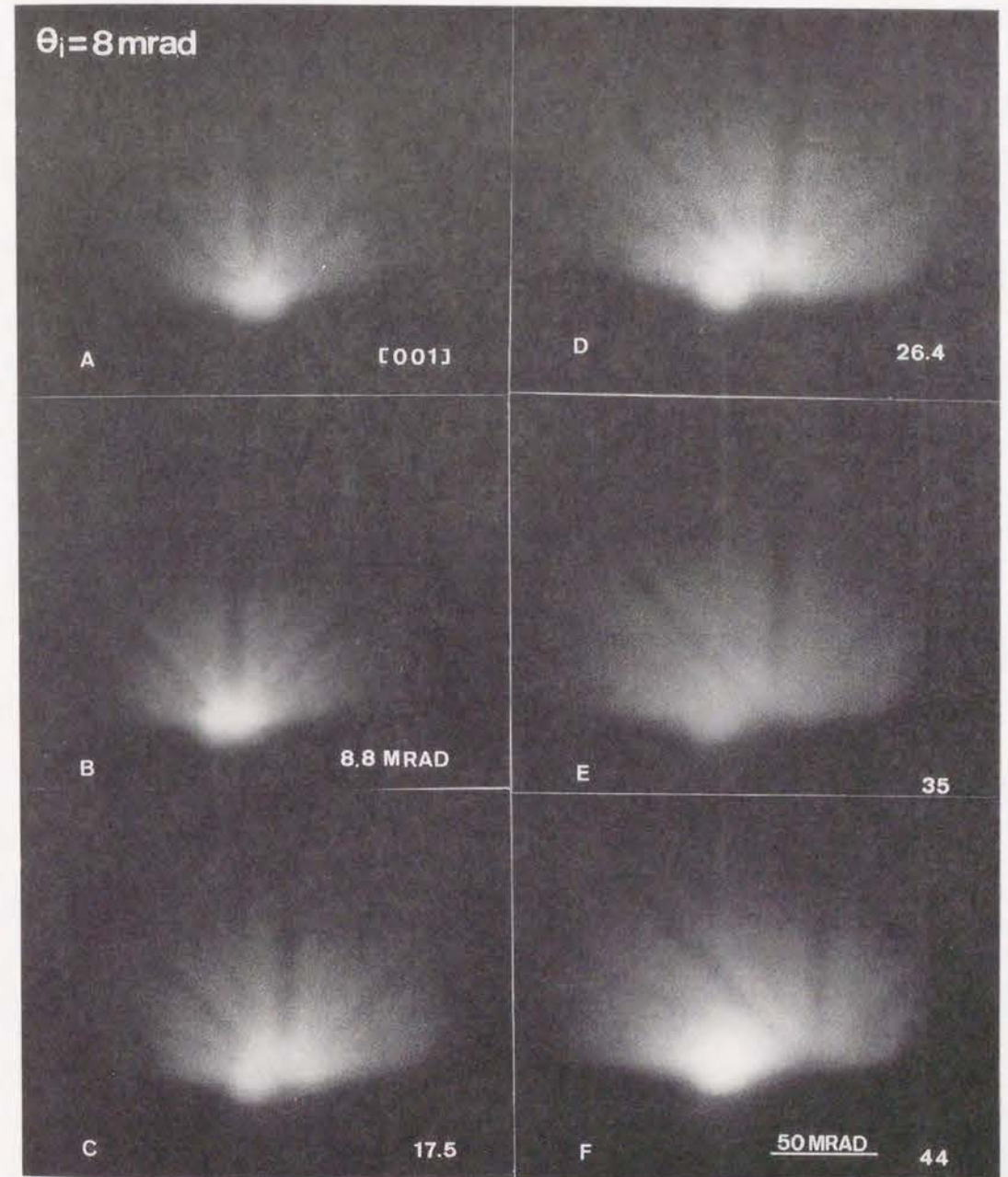
Figure 2.10: Distributions of scattered He ions at glancing angle incidence on (100) surface of SnTe for 1.6 MeV He ions incident near the [001] direction.

the directions parallel to the crystallographic planes are blocked and the characteristic pattern moves as the target is rotated around the [100] axis which is normal o the surface. Figure 2.10(a) shows the blocking pattern of He ions when the direction of the incident beam of ions is parallel to the (010) plane which is perpendicular to the surface, where the azimuthal angle of the incident beam is defined $\phi_i = 0$. The glancing angle θ_i of the incident beam of ions to the surface plane is defined by the angle of the beam relative to the surface plane.

REFERENCES

1) M. Suzuki, H. Kawauchi, K. Kimura and M. Mannami, Surf. Sci. 204 (1988) 223.

2) S. Sawada, K. Kimura and M. Mannami, Jpn J. Appl. Phys. 22 (1983) 1464.

3) Y. Fujii, S. Fujiwara, K. Kimura and M. Mannami, Radiat.Eff. 116 (1991) 111.

4) M. Tsuji, Y. Mizuno, Y. Susuki and M. Mannami, J. Cryst. Growth 108 (1991) 817.

5) J. F. Ziegler, The Stopping and Range of Ions in Matter, (Pergamon, New York, 1980) Vol.4.

6) H. Ehrhardt, L. Langhans, F. Linder and H. S. Taylor, Phys. Rev. 173 (1968) 222.
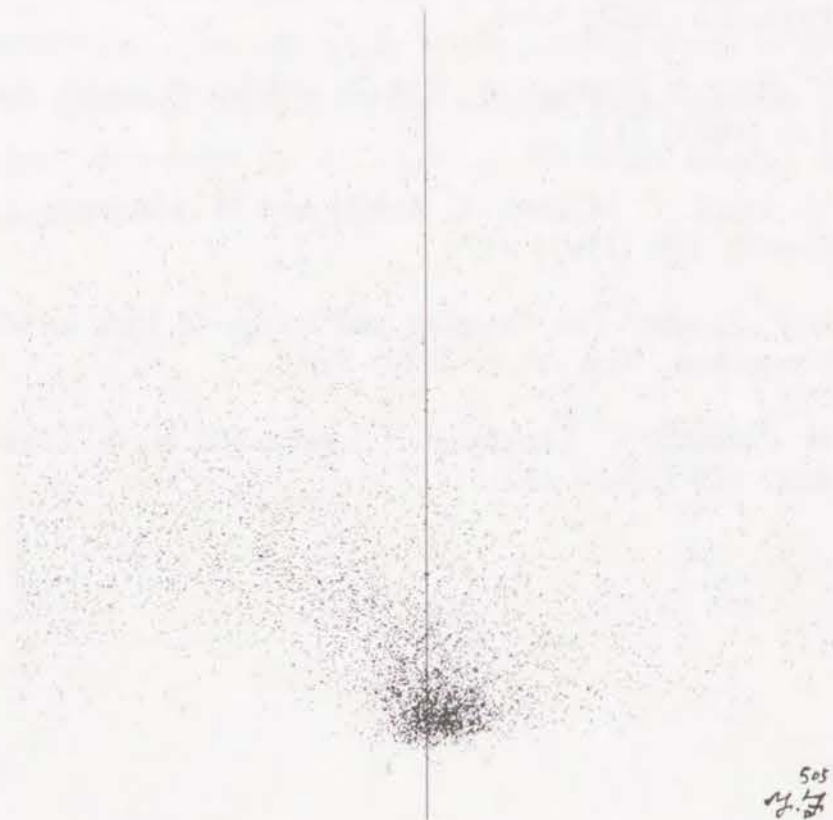
Chapter 3

GLANCING ANGLE SCATTERING
OF FAST IONS
FROM CRYSTAL SURFACE

ABSTRACT

When fast ions are incident at a small angle on an atomically flat low-index surface of a crystal, the ions are reflected from the surface. Interaction of the ions with the surface occurs along the trajectories which are determined by the glancing angle of the incident ions. In the present chapter, we show the characteristic features of the glancing angle scattering of fast ions from a single crystal surface.

3.1. SURFACE POTENTIALS AND TRAJECORIES OF IONS

3.1.1. Specular Reflection of Fast Ions

At glancing angle incidence of fast ions on an atomically flat low–index surface of a crystal, the ions interact only with atoms on the topmost atomic plane of the surface. The trajectories of the ions are characterized by a series of correlated small angle scatterings with the atoms on the surface as in the case of planar channeling of fast ions in crystal,[1-3] and the critical angle Φ_c for the scattering is equal to that for planar channeling. This phenomenon is called "specular reflection of fast ions". The ions are reflected at the angle for specular reflection, i.e., $\theta_o = \theta_i$ ($\theta_s = 2\theta_i$), as shown in Fig. 3.1, where the angle of incidence θ_i, the scattering angle θ_s and the exit angle θ_o are defined.

The motion of the specularly reflected ion is described approximately by the equation of motion of the ion in a continuum surface planar potential. In the coordinate system where the ion is in the xz–plane and the x–axis is perpendicular to the surface, the equation of motion of the ion becomes,

$$M\frac{d^2x}{dt^2} = -\frac{dV_p(x)}{dx} ,$$

$$M\frac{d^2z}{dt^2} = 0 ,$$

(1)
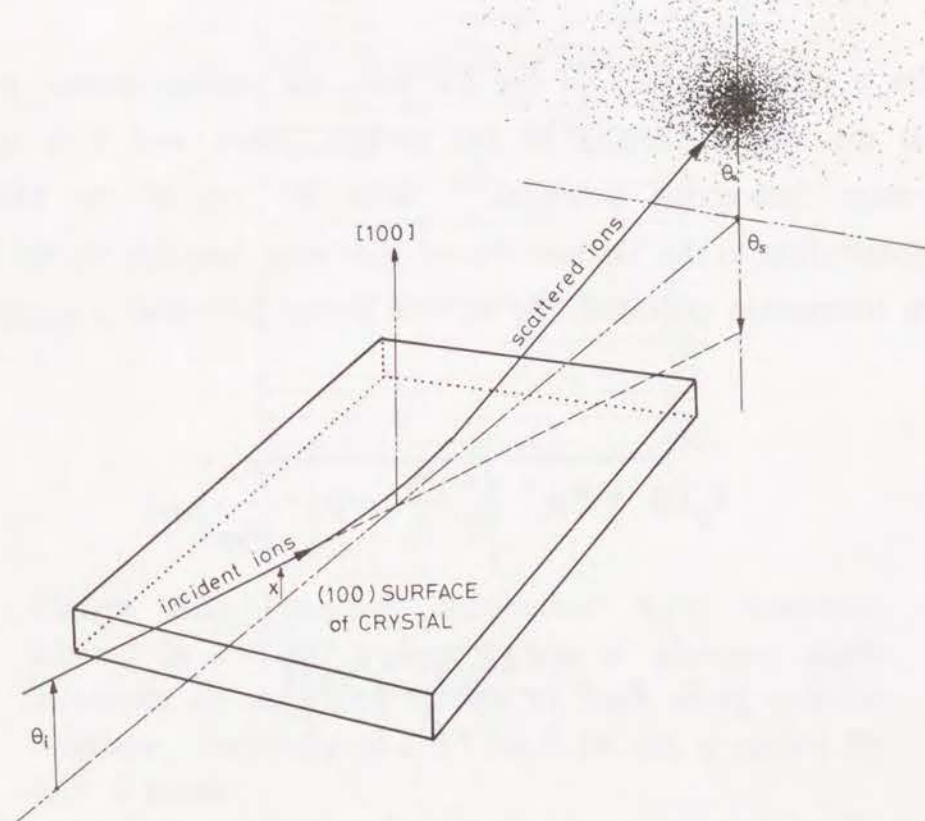
Figure 3.1: Schematic drawing of an ion trajectory and the angular distribution of specularly reflected ions at glancing angle incidence on a crystal surface. θ_i is the glancing angle of the incident ions, θ_s is the scattering angle, and θ_o is the exit angle. They are related by $\theta_s = \theta_o + \theta_i$.

where M is the mass of the ion and $V_p(x)$ is the continuum planar potential. In Eq. (1), change of kinetic energy of the ion on the motion is neglected. The continuum surface planar potential $V_p(x)$ is defined as

$$V_p(x) = n_p \int_0^\infty V\left(\sqrt{x^2 + R^2}\right) 2\pi R \, dR \,, \qquad (2)$$

where x is the distance of the ion from the surface atomic plane, n_p is the atomic density of the surface plane, and $V(r)$ is the ion–atom interaction potential.[1,2] With the use of the Molière approximation to the Thomas–Fermi screening function for the ion–atom interaction potential, the surface planar potential is expressed as

$$V_p(x) = E\psi_a^2 \sum_{i=1}^{3} \frac{\alpha_i}{\beta_i} \cdot \exp\left(-\frac{\beta_i x}{a_{TF}}\right) \,, \qquad (3)$$

$$\psi_a = \left(\frac{2\pi Z_1 Z_2 e^2 n_p a_{TF}}{E}\right)^{\frac{1}{2}} \,, \qquad (4)$$

where E is ion energy, ψ_a is the characteristic angle for planar channeling, Z_1 and Z_2 are the atomic numbers of ion and target atom respectively, e is the elementary charge, a_{TF} is the Thomas–Fermi screening distance, and α_i and β_i are the parameters in the Molière approximation to the Thomas–Fermi screening function.[1,2] The continuum surface planar potential of
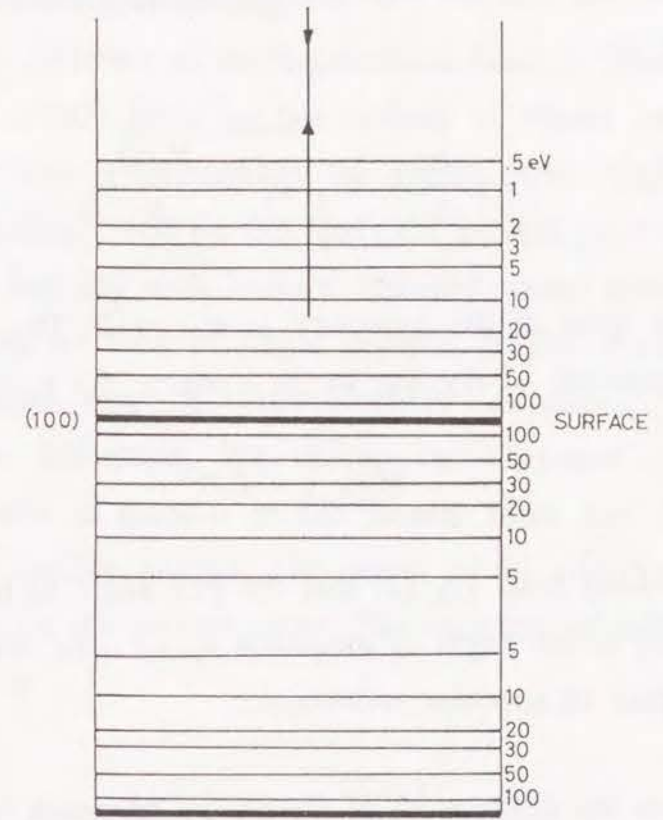
Figure 3.2: Potential distribution $V_p(x)$ (contours labeled in eV) for a fast He ion at glancing angle incidence on the (100) surface of SnTe along random direction. Trajectory of a 0.7 MeV He ion is shown for $\theta_i = 5$ mrad.

the (100) surface of SnTe for He ions is shown in Fig. 3.2, where Eqs. (3) was used in the calculation. The projected trajectory of a 0.7 MeV He ion incident at the glancing angle $\theta_i = 5$ mrad is also shown.

From Eq. (1), the trajectory of the specularly reflected ion is described as

$$\frac{dx}{dz} = \pm \sqrt{\theta_i^2 - \frac{V_p(x)}{E}} \, , \qquad (5)$$

where the apex of the trajectory is at $z = 0$. The distance of the closest approach of the ion to the surface, x_m, is given by

$$V_p(x_m) = E\,\theta_i^2 \, . \qquad (6)$$

It can be seen from Eq. (5) that the exit angle of the reflected ion θ_o is equal to the angle of incidence θ_i, i.e., the ion is reflected at the direction of specular reflection.

When the distance x_m of the closest approach of the ion to the surface is comparable to the Thomas–Fermi screening distance a_{TF}, the continuum surface planar potential cannot be applied to calculate the motion of the ion.[1,2] Thus, the critical angle Φ_c for the specular reflection of the ions is approximately given as

$$\Phi_c = \sqrt{\frac{V_p(a_{TF})}{E}} \, . \qquad (7)$$

For example, at 1 MeV He$^+$ on SnTe (100) surface, a_{TF} is $\sim$0.1 Å and Φ_c is $\sim$10 mrad.

3.1.2. Surface Channeling

When the direction of the incident ion beam is nearly parallel to low index atomic rows on the surface as shown in Fig. 3.3, motion of the ions is affected by the atomic rows. This is called "surface–channeling", and we can apply the general principles of the interaction of fast ion with orderly arranged atoms developed for axial channeling of ions in single crystals.[1,2] The motion of the surface–channeled ion is approximately described with the continuum row potentials. We choose the Cartesian coordinates where the z–axis is parallel to the atomic rows and the x–axis parallel to the surface normal. The origin of the coordinates is on a surface atom on the surface plane. The equation of motion of the ion is written as

$$M\frac{d^2x}{dt^2} = -\frac{\partial U(x,y)}{\partial x} \, ,$$
$$M\frac{d^2y}{dt^2} = -\frac{\partial U(x,y)}{\partial y} \, , \qquad (8)$$
$$M\frac{d^2z}{dt^2} = 0 \, ,$$

where M is the mass of the ion, and U(x,y) is the continuum potential for the ion. With the use of the continuum row potential $V_a(r)$ of an isolated atomic row, the potential U(x,y) is expressed as,
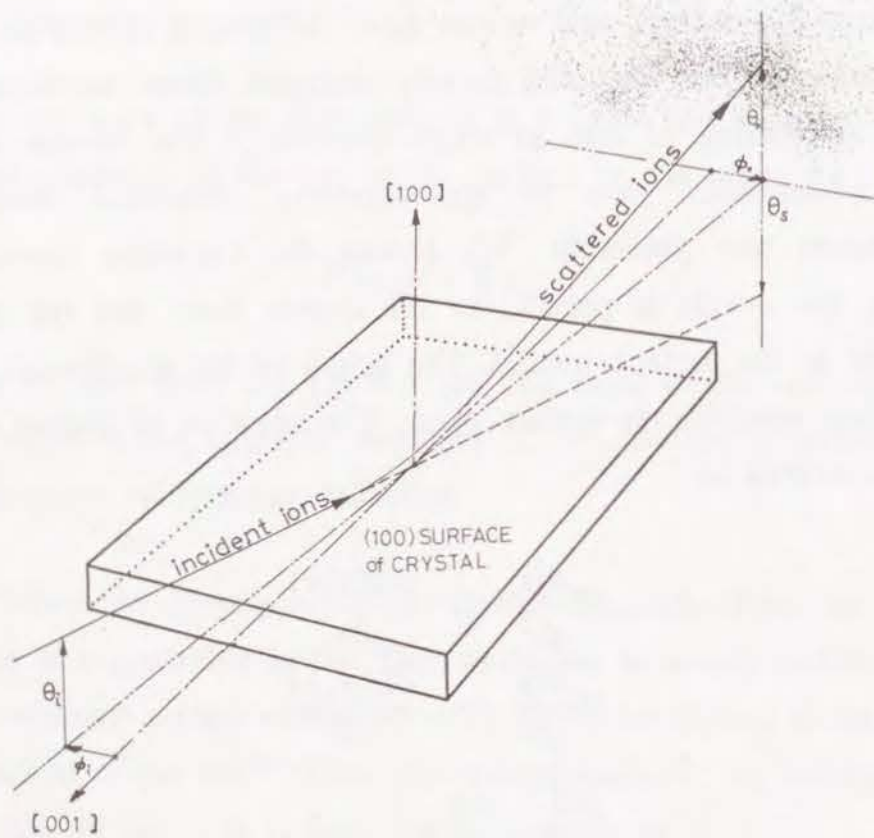
Figure 3.3: Schematic drawing of an ion trajectory and the angular distribution of surface-channeled ions at glancing angle incidence on a crystal surface. θ_i and ϕ_i are the glancing and azimuthal angles of the incident ions, respectively, and θ_s is the scattering angle. θ_o and ϕ_o are the exit glancing and azimuthal angles. They are related by the relations, $\theta_s = \theta_o + \theta_i$ and $\phi_s = \phi_o - \phi_i$.

$$U(x,y) = \sum_{n=-\infty}^{\infty} V_a\left(\sqrt{x^2 + \{y+nb\}^2}\right) , \qquad (9)$$

where b is the distance between the atomic rows on the surface. The continuum row potential $V_a(r)$ is defined as

$$V_a(r) = \frac{1}{d} \int_{-\infty}^{\infty} V\left(\sqrt{r^2 + z^2}\right) dz , \qquad (10)$$

where r is the distance from the row, d is the spacing between atoms in the row. With the use of the Molière approximation to the ion–atom interaction potential V, the continuum row potential $V_a(r)$ is expressed as

$$V_a(r) = E\psi_1^2 \sum_{i=1}^{3} \alpha_i \cdot K_0\left(\frac{\beta_i r}{a_{TF}}\right) , \qquad (11)$$

$$\psi_1 = \left(\frac{2Z_1Z_2e^2}{dE}\right)^{\frac{1}{2}} , \qquad (12)$$

where ψ_1 is the characteristic angle for axial channeling and K_0 is modified Bessel function. The potential distribution $U(x,y)$ for a fast He ion traveling along the [001] atomic row on the (100) surface of SnTe are shown in Fig. 3.4, where Eq. (11) was used in the calculation. An example of the projected trajectories of 0.7 MeV He ions incident at the glancing angle $\theta_i = 2.8$ mrad is shown.
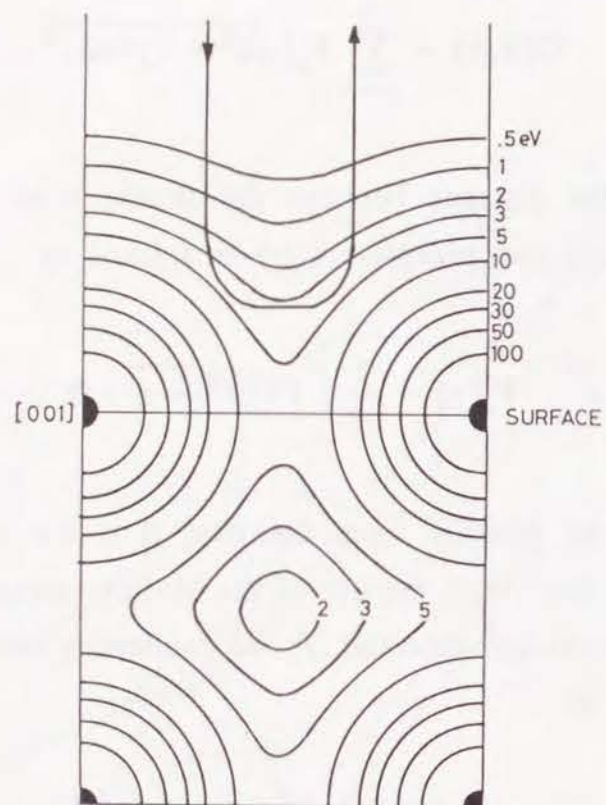
Figure 3.4: Potential distribution $U(x,y)$ (contours labeled in eV) for a fast He ion at glancing angle incidence of the (100) surface of SnTe along the [001] axis. An example of the trajectories of 0.7 MeV He ions is shown when $\theta_i = 2.8$ mrad.

When an ion is incident on the surface at the glancing angle θ_i and the azimuthal angle ϕ_i as shown in Fig. 3.3, from Eq. (8), the trajectory of the surface channeling ion is described as

$$\left(\frac{dx}{dz}\right)^2 + \left(\frac{dy}{dz}\right)^2 + \frac{U(x,y)}{E} = \theta_i^2 + \phi_i^2 \ . \qquad (13)$$

It is seen from Eq. (13) that the exit angle of the reflected ions measured from the direction of the atomic rows is equal to the angle of incident ions measured from the direction of the atomic rows as

$$\theta_o^2 + \phi_o^2 = \theta_i^2 + \phi_i^2 \ , \qquad (14)$$

where the exit glancing angle θ_o and the exit azimuthal angle ϕ_o are shown in Fig. 3.3. Thus the scattered ions are distributed along an arc when they are observed downstream the target crystal.

3.2. ANGULAR DISTRIBUTIONS

At glancing angle incidence of a beam of ions at random azimuthal angle, *i.e.*, at the "Specular Reflection", the ions are expected to be reflected at the direction of specular reflection, *i.e.*, $\theta_s = 2\theta_i$ ($\theta_o = \theta_i$). Figure 3.5 shows an example of the observed angular distribution of the reflected He ions at glancing angle incidence of 0.7 MeV He$^+$ ions on the (100) surface of SnTe with $\theta_i = 4.6$ mrad. The axes of θ_s and ϕ_s are shown in Fig. 3.5. The distribution of scattered ions along the θ_s-axis at $\phi_s = 0$ is shown in Fig. 3.6(a) and that along the ϕ_s-axis at $\theta_s = 2\theta_i$ is shown in Fig. 3.6(b). The angular distribution of the reflected ions has a maximum at the angle for specular reflection ($\theta_s = 2\theta_i$, $\phi_s = 0$). However, the observed distributions are broad, showing that the

Figure 3.5: Angular distribution of scattered He ions from the (100) surface of SnTe at the incidence of 0.7 MeV He⁺ with glancing angle 4.6 mrad. Specular reflection (incidence along random direction). Bright spots at bottom of patterns are the residual incident beam. θ_s- and ϕ_s-axes are shown.

actual crystal surface is not an ideal mirror for the incident ions. The broadening of the angular distribution is caused by collisions

of ions with thermally vibrating atoms (nuclear scattering), electrons (electronic scattering) and surface irregularities. In chapter 8, it will be shown from Monte Carlo simulation of the trajectories of specularly reflected ions from a crystal surface that most of the observed broadening is caused by the scattering events at surface steps.
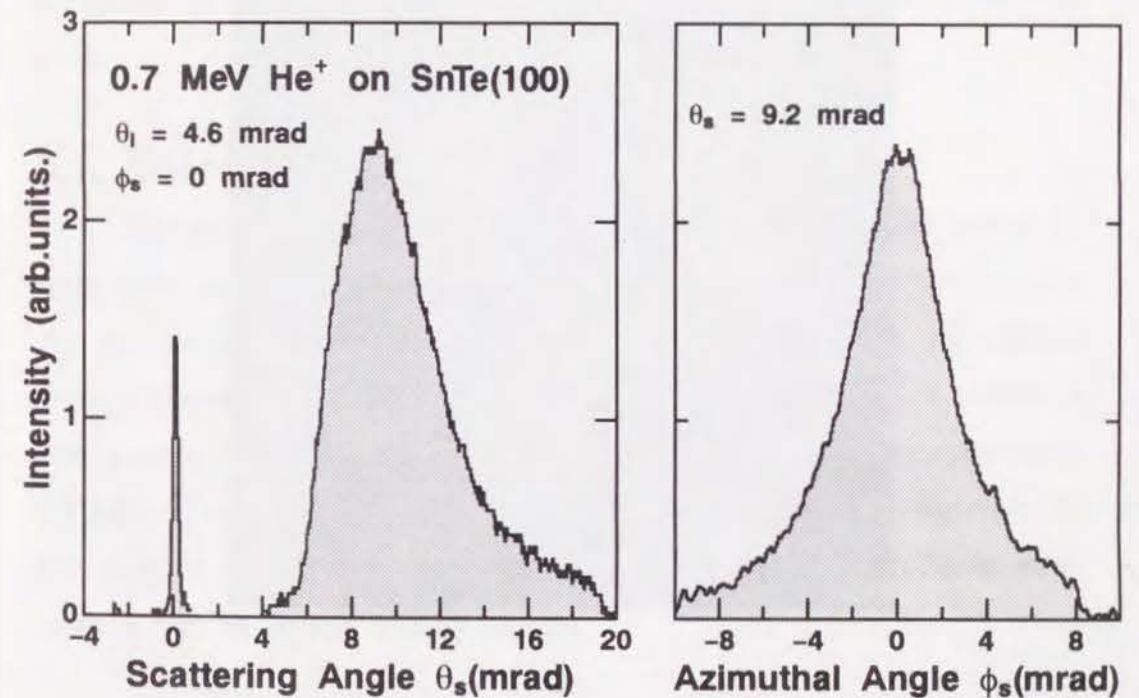
Figure 3.6: Angular distributions of specularly reflected He ions from the (100) surface of SnTe at the incidence of 0.7 MeV He⁺ with glancing angle 4.6 mrad. (a) The distribution along the θ_s-axis at $\phi_s = 0$. (b) The distribution along the ϕ_s-axis at $\theta_s = 2\theta_i$.
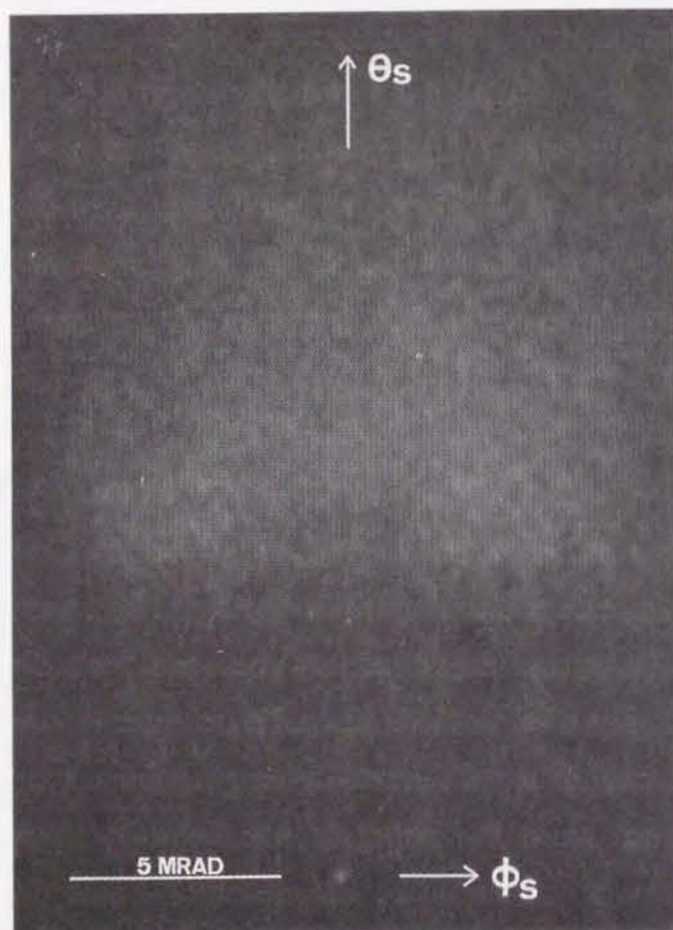
Figure 3.7: Angular distribution of scattered He ions from the (100) surface of SnTe at the incidence of 0.7 MeV He$^+$ with glancing angle 4.6 mrad. [011] surface channeling. Bright spots at bottom of patterns are the residual incident beam. θ_s– and ϕ_s–axes are shown.

At the incidence of ions nearly parallel to low index atomic rows on a crystal surface, *i.e.*, at the "surface–channeling", the ions are expected to be scattered on an arc when observed on a fluorescent screen downstream the crystal as shown in Eq. (14). Figure 3.7 shows the angular distribution of scattered He ions observed on the fluorescent screen at the [011] surface channeling of 0.7 MeV He$^+$ ions on the (100) surface of SnTe. A broad arc is observed, and the center of the arc is the projection of the direction of the atomic rows on the screen as expected from Eq. (14).

3.3. Energy Spectra

The specularly reflected ion interacts with the surface along its trajectory, and energy transfer between the ion and electrons occurs. As the result, even the specularly reflected ion loses its kinetic energy during its interaction with the surface. Figure 3.8 shows a few examples of the observed energy spectra of the ions specularly reflected from crystal surfaces. Although the spectrum depends on the surface conditions, all of the energy spectra show a sharp peak with a tail in lower energy region.

We will show in chapter 8 that the sharp peak in the energy spectrum corresponds to the ions which are reflected from the topmost atomic plane of the surface, and that the ions in the tail are reflected from inside the crystals. The incident ions cannot penetrate flat crystal surface at the angle of incidence smaller than the critical angle for specular reflection. However, actual crystal
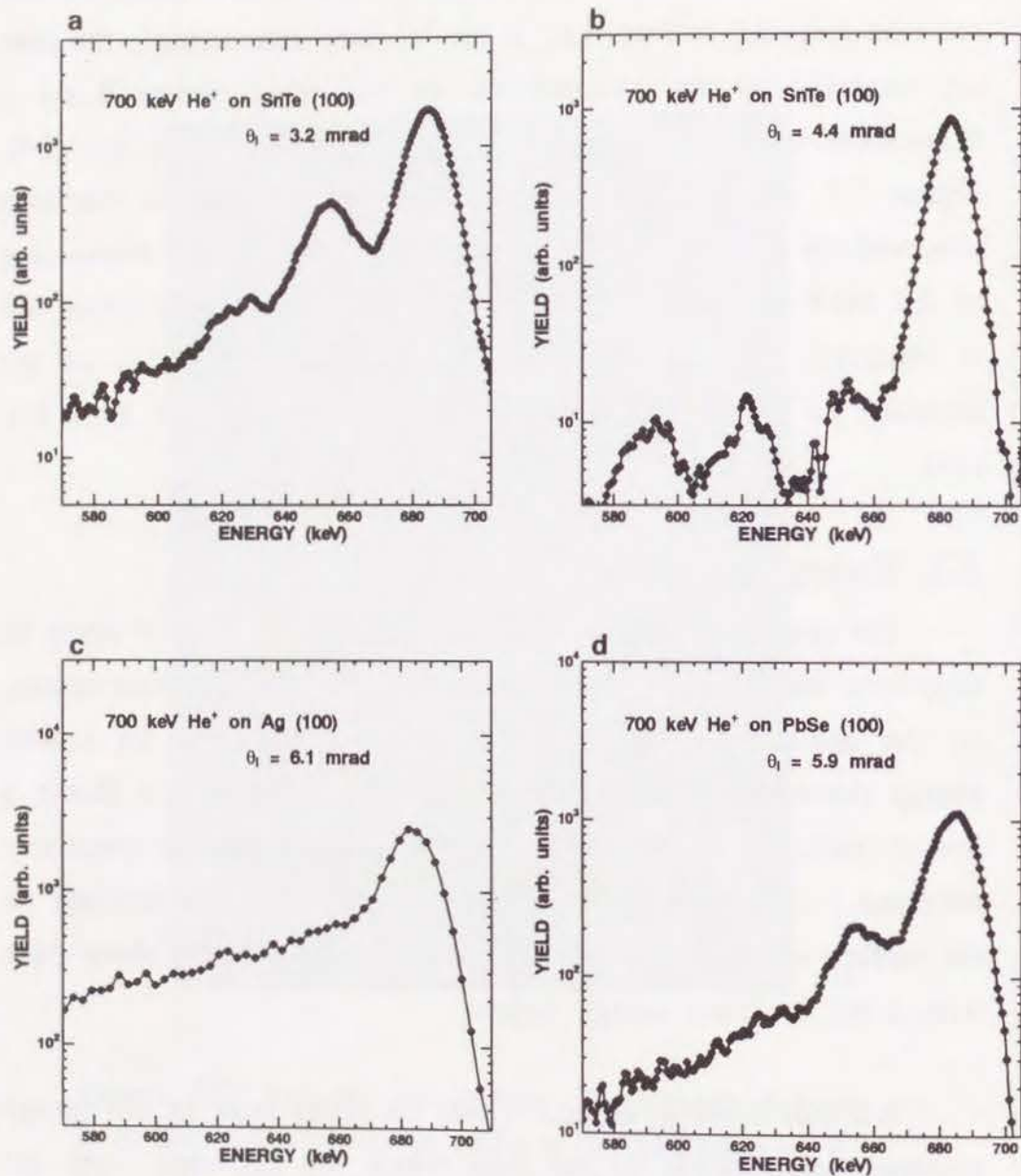
Figure 3.8
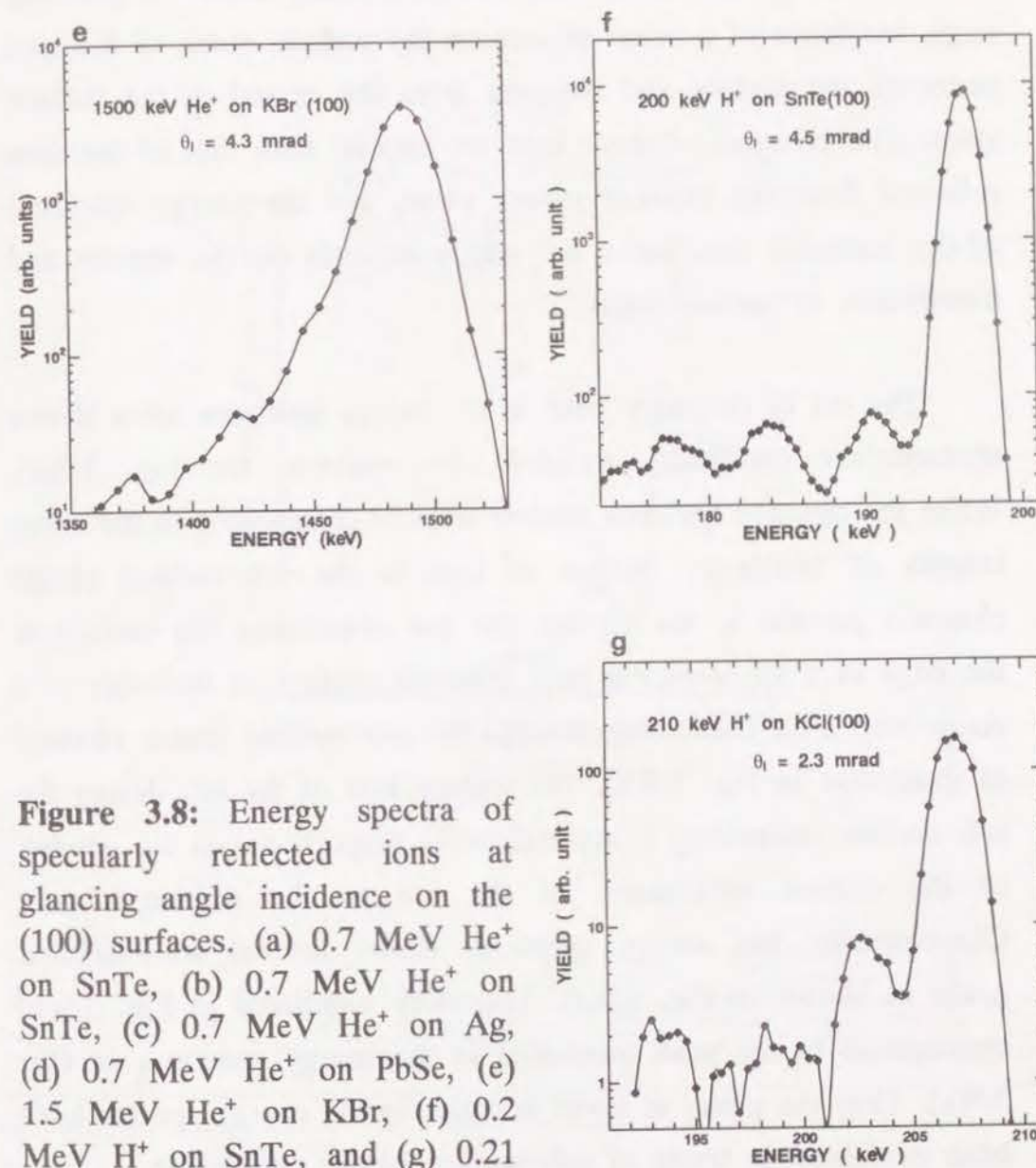
Figure 3.8: Energy spectra of specularly reflected ions at glancing angle incidence on the (100) surfaces. (a) 0.7 MeV He^+ on SnTe, (b) 0.7 MeV He^+ on SnTe, (c) 0.7 MeV He^+ on Ag, (d) 0.7 MeV He^+ on PbSe, (e) 1.5 MeV He^+ on KBr, (f) 0.2 MeV H^+ on SnTe, and (g) 0.21 MeV H^+ on KCl. The energy spectra of He ions were measured by SSD, and those of H^+ were measured by magnetic spectrometer.

surfaces are not atomically flat, and have many steps. At glancing angle incidence of a beam of ions on the surface, some of the ions penetrate the surface and reappear from the crystal at the surface steps. The energies of these ions are smaller than that of the ions reflected from the topmost atomic plane, and the energy spectrum of the scattered ions has a tail which depends on the density and distribution of surface steps.

The tail of the sharp peak in the energy spectrum often shows characteristic oscillatory structure, for instance, see Fig. 3.8(a). When the distance between surface steps is comparable to the wave lengths of oscillatory motion of ions in the sub-surface planar channels parallel to the surface, the ion penetrating the surface at the edge of a up-steps can exit from the surface at the edge of a down-step after channeling through the sub-surface planar channel as illustrated in Fig. 3.9(b). The energy loss of the ion during the sub-surface channeling is approximately proportional to the number of the closest approaches of the ion to the atomic planes. Consequently, the energy spectrum shows several well-defined peaks as shown in Fig. 3.9(a). Trajectory numbered in Fig. 3.9(b) corresponds to the peak numbered in the energy spectrum in Fig. 3.9(a). Thus the peaks at lower energies in the energy spectra have been explained in terms of sub-surface planar channeling.
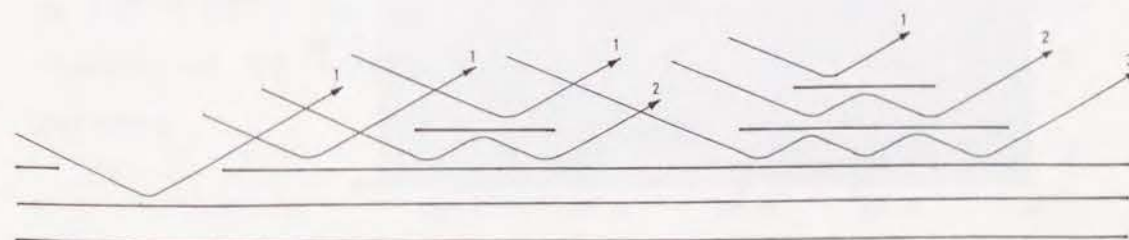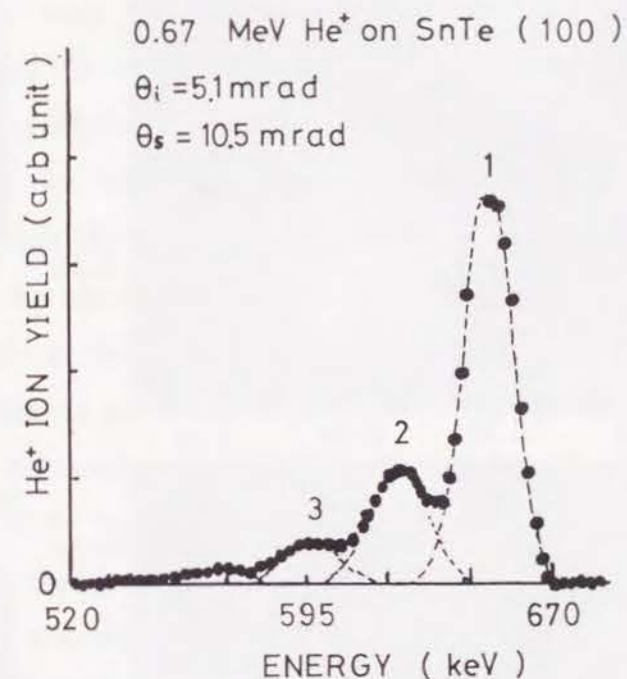
Figure 3.9: (a) Energy spectrum of specularly reflected He$^+$ ions from the (100) surface of SnTe at the incidence of 0.7 MeV He$^+$ ions with glancing angle 5.1 mrad. (b) Typical trajectories of the reflected ions.
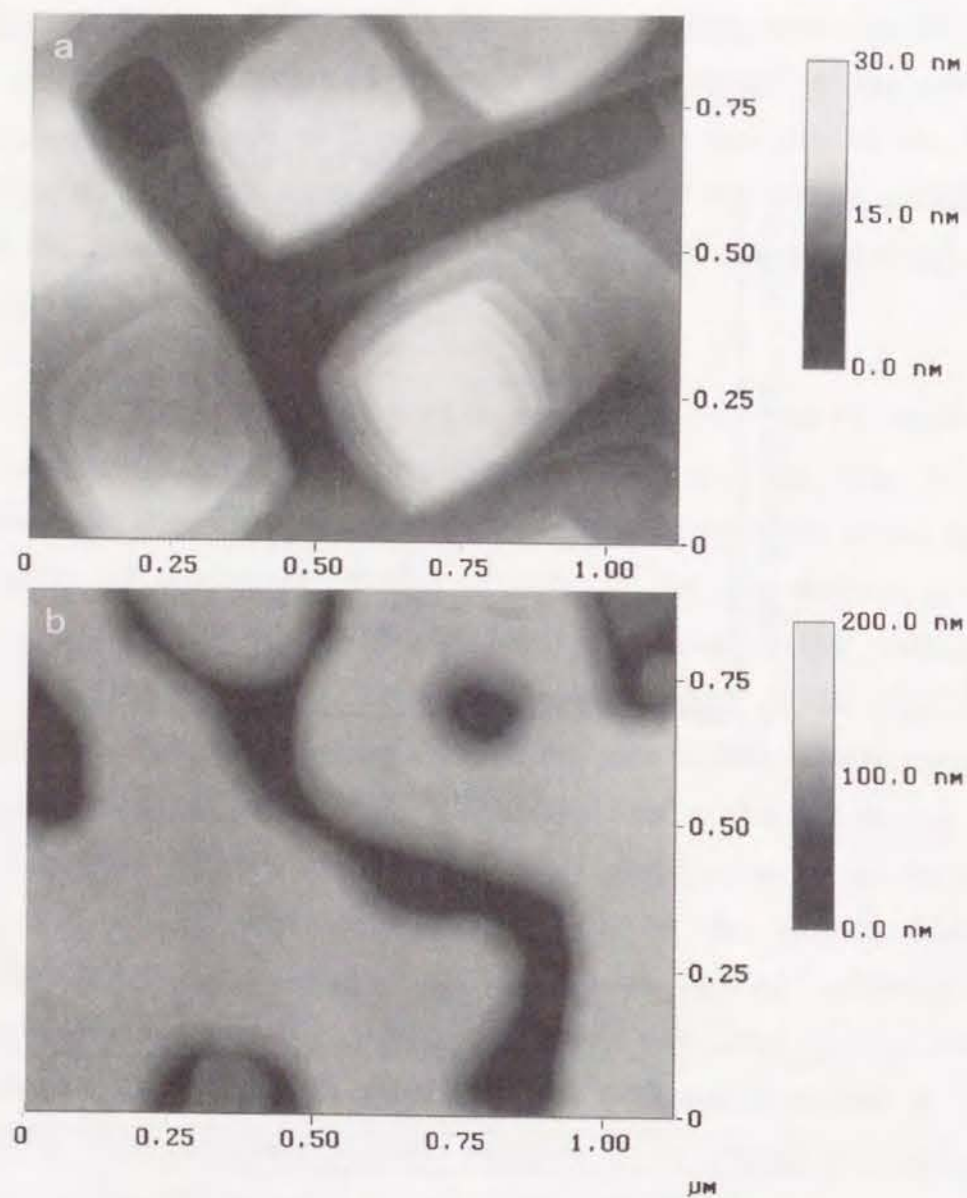
Figure 3.10: AFM images of the (100) surfaces of SnTe single crystals grown at 250 °C. (a) Surface of a crystal grown with the rate ∼2 nm/min. (b) Surface of a crystal grown with the rate ∼0.1 nm/min.

The oscillatory structure of the energy spectrum at its lower energy region depends on density and distribution of surface steps. This was confirmed by measuring the energy spectra with SnTe (100) surfaces with different step densities. We found by the observation with the use of an atomic force microscope (AFM) that the density and distribution of the surface steps depends on the growth rate of the SnTe crystal. In the AFM images of the (100) surfaces of epitaxially grown SnTe crystals, many small pyramidal hillocks with the mean distance between neighboring steps ∼50 nm were observed on the surface of SnTe crystal prepared at growth rate ∼2 nm/min as shown in Fig. 3.10(a). On the other hand, steps were hardly observed on the (100) surface when the growth rate of SnTe crystal was ∼0.1 nm/min as shown in Fig. 3.10(b). Figure 3.8(a) shows the energy spectrum of the He ions specularly reflected from the stepped surface of SnTe shown in Fig. 3.10(a), and Fig. 3.8(b) shows the energy spectrum of the He ions specularly reflected from the relatively flat surface of SnTe shown in Fig. 3.10(b). The oscillatory structure of the energy spectrum depends on the density and distribution of the surface steps as expected.

REFERENCES

1) J. Lindhard, Kgl. Danske Videnskab. Selskab. Mat. Fys. Medd. 34 No.14 (1965).

2) D. S. Gemmell, Rev. Mod. Phys. 46 (1974) 129.

3) D. V. Morgan, ed, "Channeling-Theory, Observation and Application, 1973", (John Wiley & Sons, New York).

Chapter 4

POSITION-DEPENDENT STOPPING POWERS OF THE (100) SURFACES OF NaCl-TYPE CRYSTALS FOR MeV LIGHT IONS

ABSTRACT

Energy losses of MeV H and He ions after interaction of clean surfaces of several NaCl-type crystals at glancing angle incidence are investigated. From the most probable energy losses of the ions reflected from the surface atomic plane, position-dependent stopping powers of the (100) surfaces of NaCl, KCl, KBr, SnTe, PbSe and PbTe for MeV H and He ions are determined. The results are explained by a sum of the stopping caused by the dynamic response of valence electrons to the fast ion in vacuum and that due to the single ion-electron collisions.

4.1. INTRODUCTION

At the incidence of fast ions on a flat low–index surface of a crystal with a small glancing angle θ_i, most of the ions are reflected at $\theta_s = 2\theta_i$, *i.e.*, at the angle of specular reflection. Interaction of the ions reflected from the topmost atomic plane of the surface is characterized by a series of small angle scatterings with the atoms of the surface as in the case of planar channeling.[1] The ions cannot penetrate the crystal surface when θ_i is less than the critical angle for specular reflection which is equal to that for planar channeling.

Actual crystal surfaces are not atomically flat. There are many steps and point defects. At glancing angle incidence of a beam of ions on the surface, some of the ions penetrate the surface and reappear from the crystal at the surface steps.[2,3] The energies of these ions are lower than that of ions reflected from the topmost atomic plane, and as the result, the energy spectrum of the scattered ions shows a characteristic structure, which depends on the density and distribution of the steps on the surface.

From the most probable energy losses of the ions reflected from the topmost atomic plane of the surface, we have derived the position–dependent stopping powers of the (100) surface of SnTe for MeV H and He ions, which are expressed as,[4]

$$S(x) = \frac{C}{\sqrt{E}} \exp\left(-\frac{\beta_3 x}{2 a_{TF}}\right), \qquad (1)$$

where E is the ion energy, x is the distance of the ion from the surface atomic plane, C is a constant depending on the ion species and the crystal surface, $\beta_i = 0.3$, and a_{TF} is the Thomas–Fermi screening distance.

The work presented here extends this research on the position dependent stopping power of SnTe for MeV light ions to the (100) surfaces of several other NaCl–type crystals, *i.e.*, NaCl, KCl, KBr, PbSe and PbTe. Comparison of the observed stopping powers with the theoretical stopping powers calculated from the dynamic response of valence electrons is made to clarify the origin of the stopping processes.

4.2. EXPERIMENTAL

A single crystal with clean surface, which was mounted in a precision goniometer in a UHV chamber (base pressure 2×10^{-10} Torr), was irradiated by a narrow parallel beam of MeV H^+ and He^+ ions from the 4 MV Van de Graaff accelerator of Kyoto University. The beam size was 0.04 mm $\times$ 0.04 mm and the divergence angle was less than 0.1 mrad. The angle of incidence θ_i of the beam to the crystal surface was less than 8 mrad, and the ions scattered at an angle θ_s in the plane of scattering, which contains the incident beam and the surface normal, were chosen by a movable aperture.[4]

Acceptance half angle of the aperture was 0.3 mrad. The ions chosen by the aperture were resolved into their charge states by a

magnetic analyzer and the energy spectra of the ions of each charge state were measured with a solid state detector.[5] The aperture and the detector could be rotated ±25 mrad around the direction of the incident beam. The energy resolution of the detector was 13 keV for 1 MeV He ions. Charge state fractions of the scattered ions were also measured by this setting. Fractions of the neutral ions in the scattered ions were less than 1 % for the present experimental conditions, and the energy loss of these ions was not studied.

The (100) surfaces of single crystals of NaCl, KCl, KBr, SnTe, PbSe and PbTe were used as the target: The surfaces of alkali halide crystals were prepared by cleavage in air parallel to the {100} planes, and the surfaces with less numbers of visible steps were chosen and heated to 250 °C under UHV conditions to prepare clean surfaces.[6] For PbSe and PbTe crystals, we first grew a single crystal of SnTe on the (100) surface of KCl and then grew PbSe or PbTe crystal on the SnTe surface by vacuum evaporation of pure materials. The epitaxial growth was carried out in a vacuum lower than 2×10^{-9} Torr. These grown crystals were good single crystals except for the misfit dislocations at the interfaces with substrate SnTe.[7-9]

4.3. EXPERIMENTAL RESULTS

Examples of the energy spectra of the reflected ions at glancing angle incidence of MeV H$^+$ and He$^+$ ions on the clean (100) surfaces are shown in Fig. 4.1, where the energy of the incident ions is shown by a vertical line. The spectrum depends
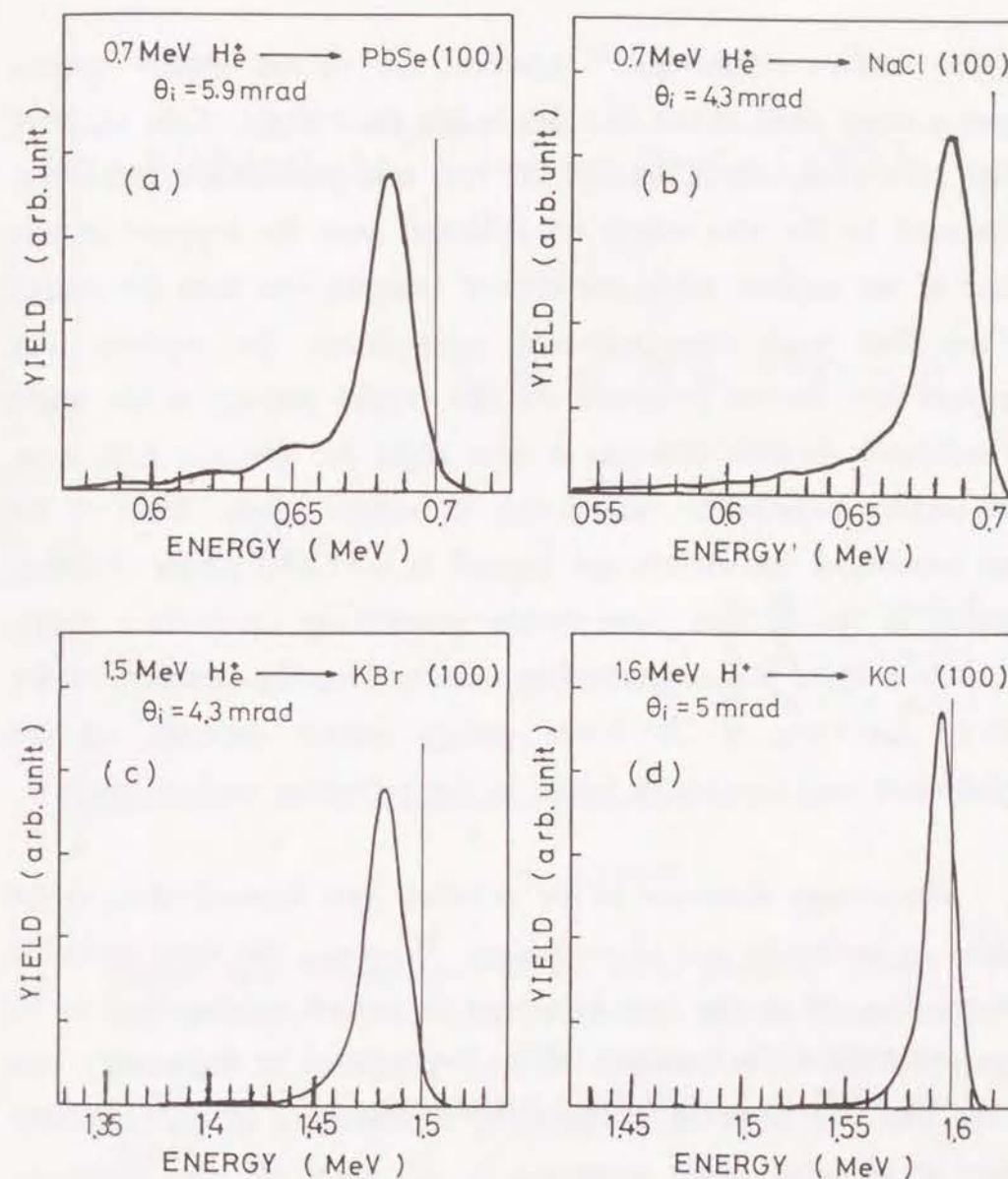
Figure 4.1: Examples of energy spectra of the ions scattered in the angle of specular reflection at glancing angle incidence of MeV ions.
(a) 0.7 MeV He$^+$ ions on the (100) surface of PbSe.
(b) 0.7 MeV He$^+$ ions on the (100) surface of NaCl.
(c) 1.5 MeV He$^+$ ions on the (100) surface of KBr. (d) 1.6 MeV H$^+$ ions on the (100) surface of KCl.

on the surface conditions,[2,8] however, all of the energy spectra show a sharp peak at the energies below the energy of the incident ions. The peak, which we call the first loss peak in the following, is formed by the ions which are reflected from the topmost atomic plane of the surface, while the ions of energies less than the energy at the first peak were reflected from inside the crystals. The incident ions cannot penetrate the flat crystal surface at the angle of incidence smaller than the critical angle for specular reflection. The surface penetration occurs only at surface steps. Most of the ions penetrated the surface are trapped in the (100) planar channels parallel to the surface plane before penetrating the surface again, *i.e.*, sub–surface planar channeling occurs. Thus the structure of the energy spectrum at its lower energy region depends on the distribution and density of steps on the reflecting surface plane.[2]

The energy spectrum of the reflected ions depends also on the angles of incidence and of scattering. However, the most probable energy loss ΔE at the first loss peak is almost independent of θ_i. Figure 4.2 shows an example of the dependence of the energy loss at the first loss peak on the angle θ_s of scattering in the scattering plane at glancing angle scattering of 0.7 MeV He ions from the (100) surface of PbSe. The most probable energy loss $\Delta E(\theta_i)$ of the ions scattered at the angle for specular reflection ($\theta_s = 2\theta_i$) is almost independent of the angle θ_i of incidence as shown in Fig. 4.3. However, there is a tendency that the loss $\Delta E(\theta_i)$ increases slightly with increasing θ_i for faster ions.
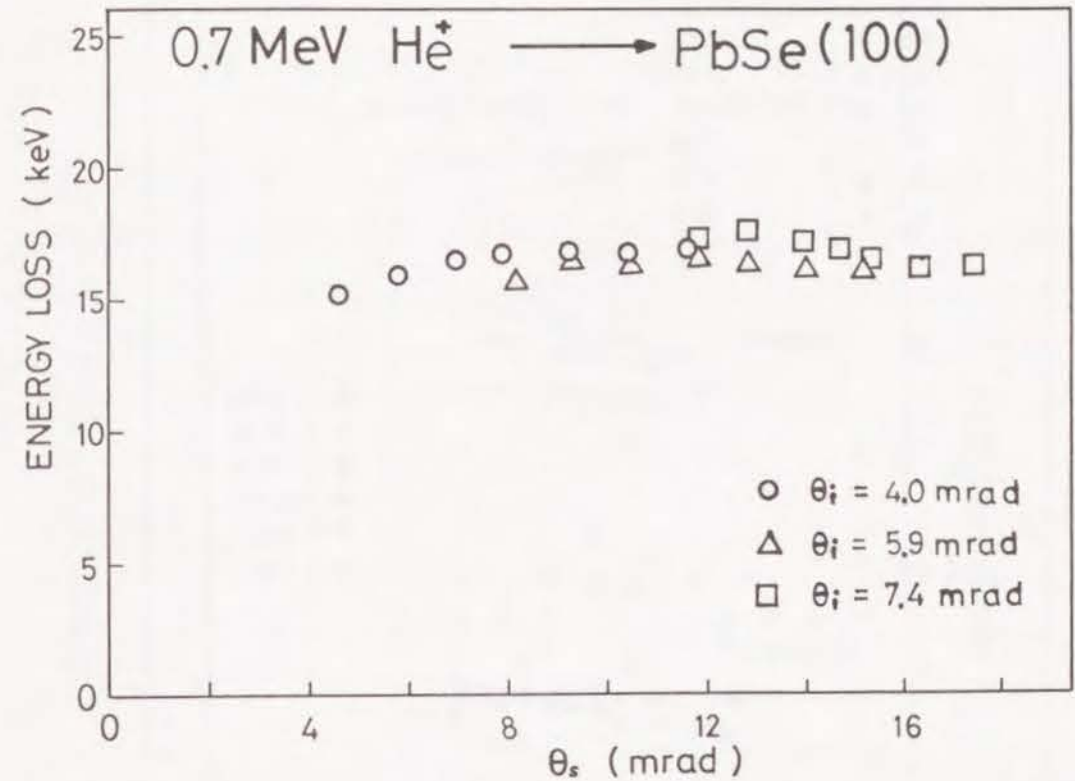
Figure 4.2: Dependence of the most probable energy loss of ions reflected from the surface atomic plane on the angle of scattering θ_s. The angles θ_i of incidences of 0.7 MeV He[+] ions on the (100) surface of PbSe are shown.

Summarizing the results of the measured most probable energy loss at the first loss peak, Fig. 4.4 shows the energy–dependence of the most probable energy losses of H^{+} and He^{+} ions specularly reflected from various target surfaces at angle of incidence $\theta_i = 5$ mrad. The loss depends both on the ion energy and target.
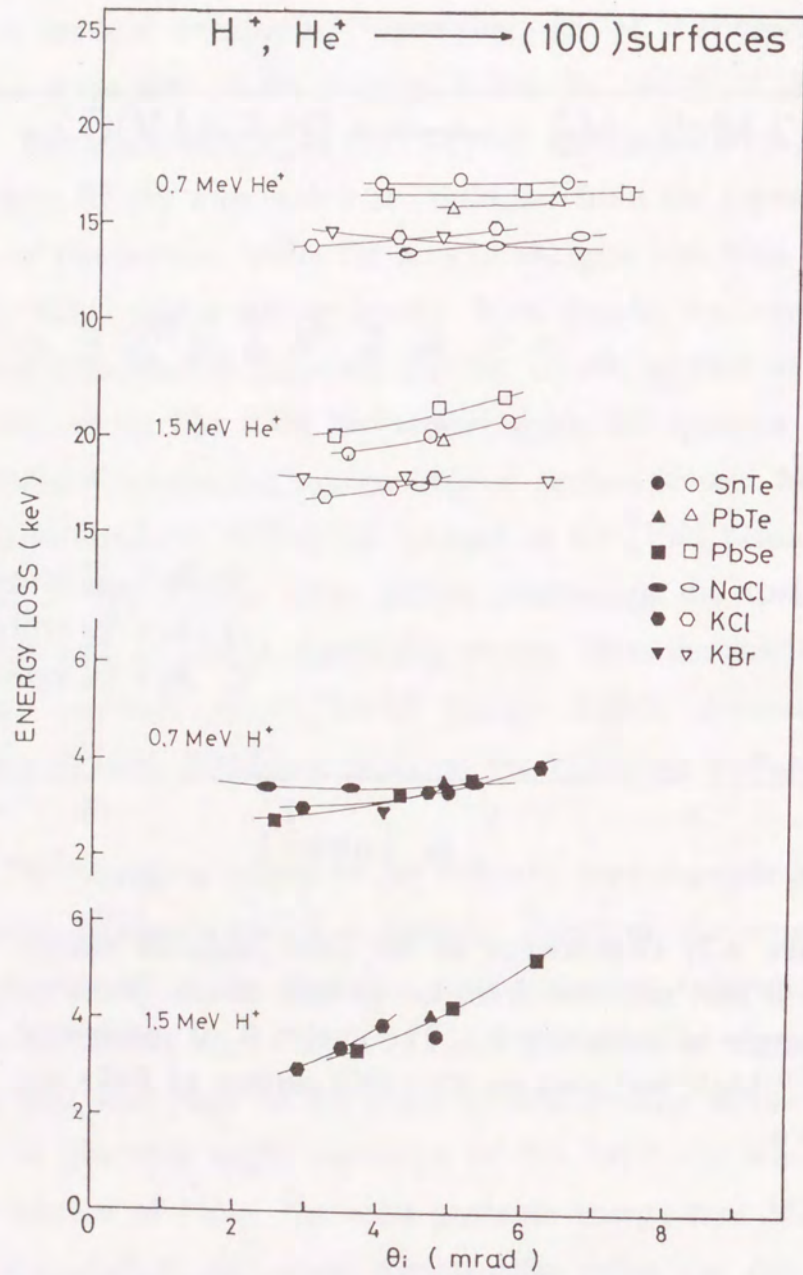
Figure 4.3: Dependences of the most probable energy loss $\Delta E(\theta_i)$ of specularly reflected ions on the angle θ_i of incidence of MeV ions.
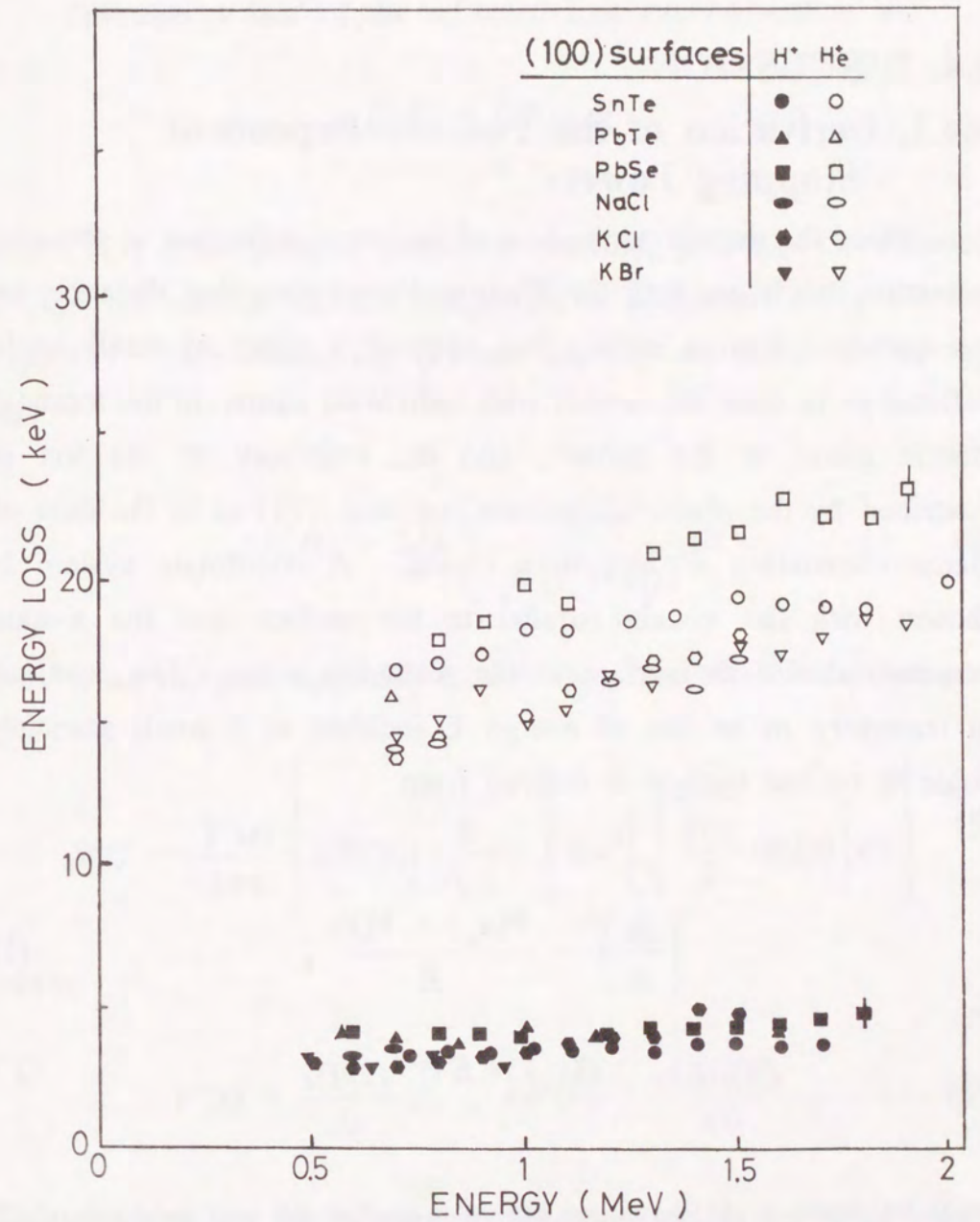
Figure 4.4: Energy–dependence of the most probable energy losses of H$^+$ and He$^+$ ions specularly reflected from various target surfaces at angle of incidence θ_i = 5 mrad.

4.4. DISCUSSION

4.4.1. Derivation of the Position–Dependent Stopping Powers

Since the impact parameters of ion–atom collisions at specular reflection are larger than the Thomas–Fermi screening distance, an ion scattered from a surface has suffered a series of small angle deflections in their encounters with individual atoms on the topmost atomic plane of the surface, and the trajectory of the ion is described by the planar continuum potential $V(x)$ as in the case of planar channeling of ions in a crystal. A coordinate system is chosen with the z-axis parallel to the surface and the x-axis perpendicular to the surface in the scattering plane. The equation of trajectory of an ion of energy E incident at a small glancing angle θ_i on the surface is derived from

$$\left(\frac{dx}{dz}\right)^2 = \frac{V(x_m) - V(x)}{E} , \qquad (2)$$

$$V(x_m) = E\,\theta_i^2 , \qquad (2')$$

where x_m is the closest approach distance of the ion to the surface atomic plane.

The energy loss of the reflected ions can be written as,

$$\Delta E(\theta_i) = \int_{traj.} S(x)\,dz , \qquad (3)$$

where $S(x)$ is the position–dependent stopping power at the distance x from the surface and the integration is performed along the ion trajectory. Substituting Eq. (2) into Eq. (3), we obtain the energy loss

$$\Delta E(\theta_i) = 2\sqrt{E} \int_{x_m}^{\infty} \frac{S(x)}{\sqrt{V(x_m) - V(x)}}\,dx . \qquad (4)$$

This is an integral equation of Abel type, and $S(x)$ is solved as,

$$S(x) = -\frac{V'(x)}{2\pi E}\left\{\Delta E(0)\sqrt{\frac{E}{V(x)}} + \int_0^{\frac{\pi}{2}} \Delta E'\left(\sqrt{\frac{V(x)}{E}}\,\sin(u)\right)du\right\} \qquad (5)$$

where,

$$V'(x) = \frac{dV(x)}{dx} , \qquad \Delta E'(\theta) = \frac{d\,\Delta E(\theta)}{d\theta} . \qquad (5')$$

Thus the position–dependent stopping power, $S(x)$, is obtained from the continuum surface planar potential $V(x)$ and the observed θ_i–dependence of the energy loss $\Delta E(\theta_i)$.

In the following, we use the Molière's approximation for Thomas–Fermi screening function, which gives the continuum planar potential V(x) as,

$$V(x) = 2\pi Z_1 Z_2 e^2 N_p a_{TF} \sum_{i=1}^{3} \frac{\alpha_i}{\beta_i} \cdot \exp\left(-\frac{\beta_i x}{a_{TF}}\right),$$ (6)

where Z_1 is the atomic number of the projectile ion, Z_2 is the averaged atomic number of target atoms, N_p is the atomic density on the topmost atomic plane, and $\{\alpha_i\} = \{0.1, 0.55, 0.35\}$ and $\{\beta_i\} = \{6.0, 1.2, 0.3\}$.

When $\Delta E(\theta_i)$ is independent of θ_i, i.e., $\Delta E(\theta_i) = \Delta E$, it is worth noting that Eq. (5) gives a position–dependent stopping power,

$$S(x) = -\frac{\Delta E}{\pi} \cdot \frac{d\sqrt{\frac{V(x)}{E}}}{dx}$$

$$= -\Delta E \cdot \frac{\psi_a}{\pi} \cdot \frac{d\sqrt{\sum_{i=1}^{3} \frac{\alpha_i}{\beta_i} \cdot \exp\left(-\frac{\beta_i x}{a_{TF}}\right)}}{dx},$$ (7)

We can obtain Eq. (1) when only the exponential term containing β_3 is retained in Eq. (7).

As it is seen from Fig. 4.3 that the experimental energy loss $\Delta E(\theta_i)$ cannot be observed at angle θ_i of incidence smaller than

about 2 mrad because of the experimental difficulties. Thus the experimental losses are extrapolated to $\theta_i = 0$ for the calculation of $S(x)$ with the use of Eq. (5). Three examples of the extrapolated $\Delta E(\theta_i)$ curves are shown in Fig. 4.5(a) at the scattering of 0.7 MeV He from the (100) surface of KCl. The position–dependent stopping powers calculated from the curves are almost equal except at the distances x larger than about 3.0 Å as shown in Fig. 4.5(b).
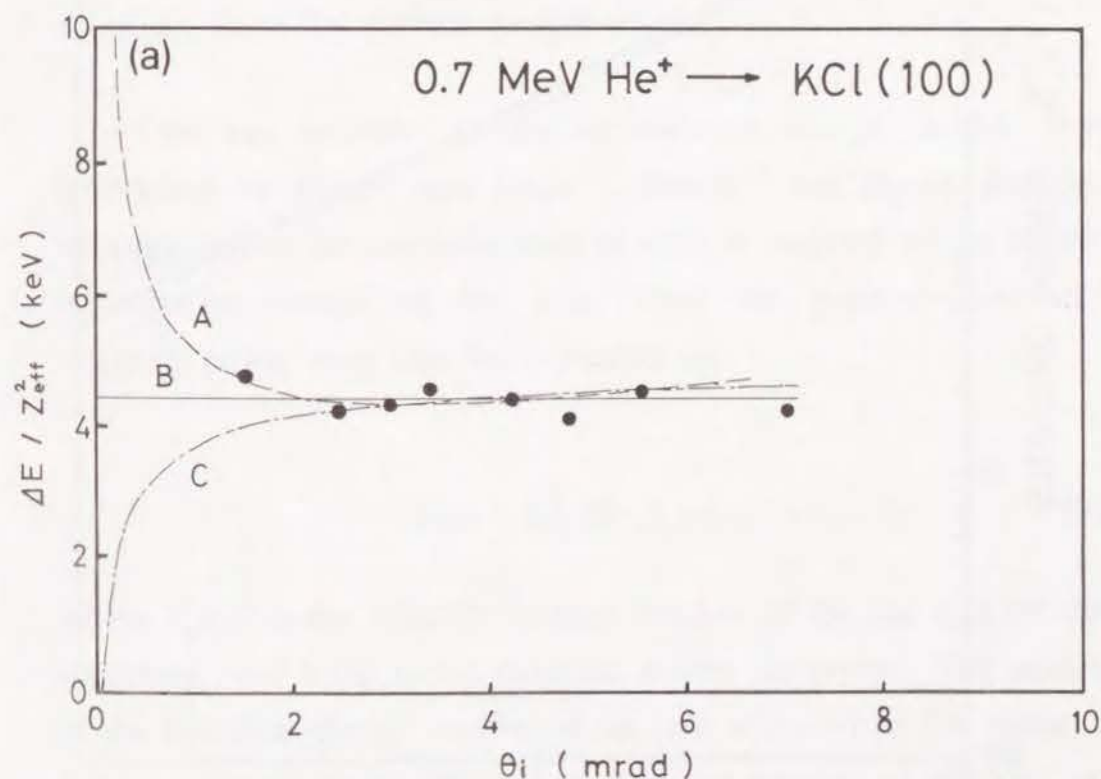
Figure 4.5(a): Three examples of the extrapolation of the experimental energy loss $\Delta E(\theta_i)/Z_{eff}^2$ to $\theta_i = 0$ at the incidence of 0.7 MeV He on the (100) surface of KCl.

STOPPING POWER $S_o(x)$ (eV/Å)

(b)   0.7 MeV He⁺ ⟶ KCl (100)

X (Å)
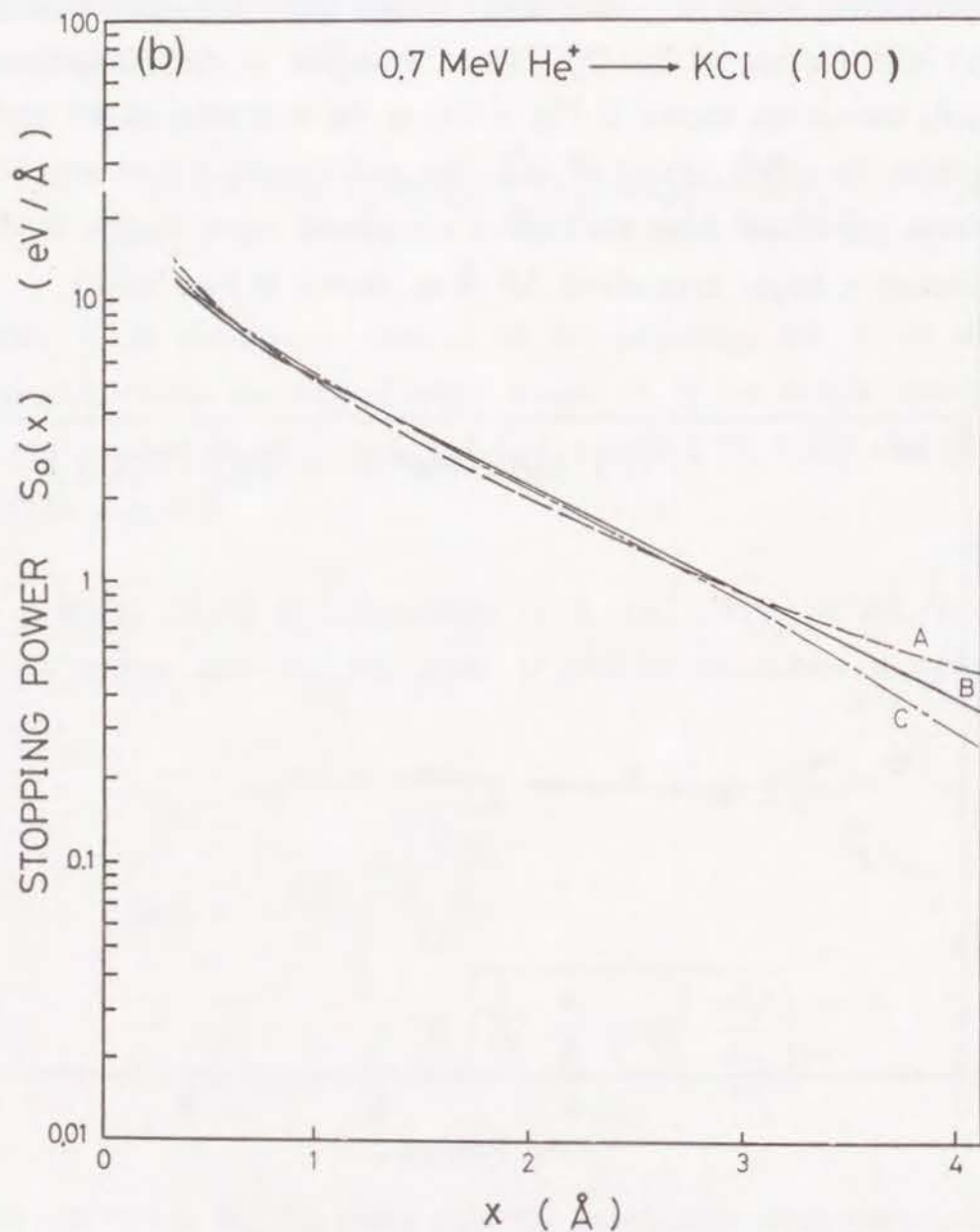
Figure 4.5(b): The position–dependent stopping powers $S_o(x)$ calculated from the extrapolated curves shown in (a).

This shows that the extrapolation procedure does not seriously affect the stopping power near the surface. On the other hand, the angle of incidence must be smaller than the critical angle θ_c for specular reflection, which is defined as

$$\theta_c^2 \sim \frac{V(a_{TF})}{E} \ .$$

Thus the stopping power can be determined only up to the distance about a_{TF} from the surface atomic plane.

One has recourse to the effective–ion–charge model, first introduced by Bohr[10] and Lamb[11]. Brandt[12] has shown that the stopping power for energetic ions in solid is proportional to square of effective–charge of the ions. Thus the position–dependent stopping power may also be expressed as,

$$S(x) = Z_{eff}^2(z) \cdot S_o(x) \ , \tag{8}$$

where $Z_{eff}(z)$ is the effective–charge number of the ion at z on the trajectory, and $S_o(x)$ is the stopping power for proton. The square of the effective–charge number of the ions scattered on the surfaces is approximated to the mean square charge number of the ions as,

$$Z_{eff}^2(z) = \sum_{q=1}^{Z_1} F_q(z) q^2 \ , \tag{9}$$
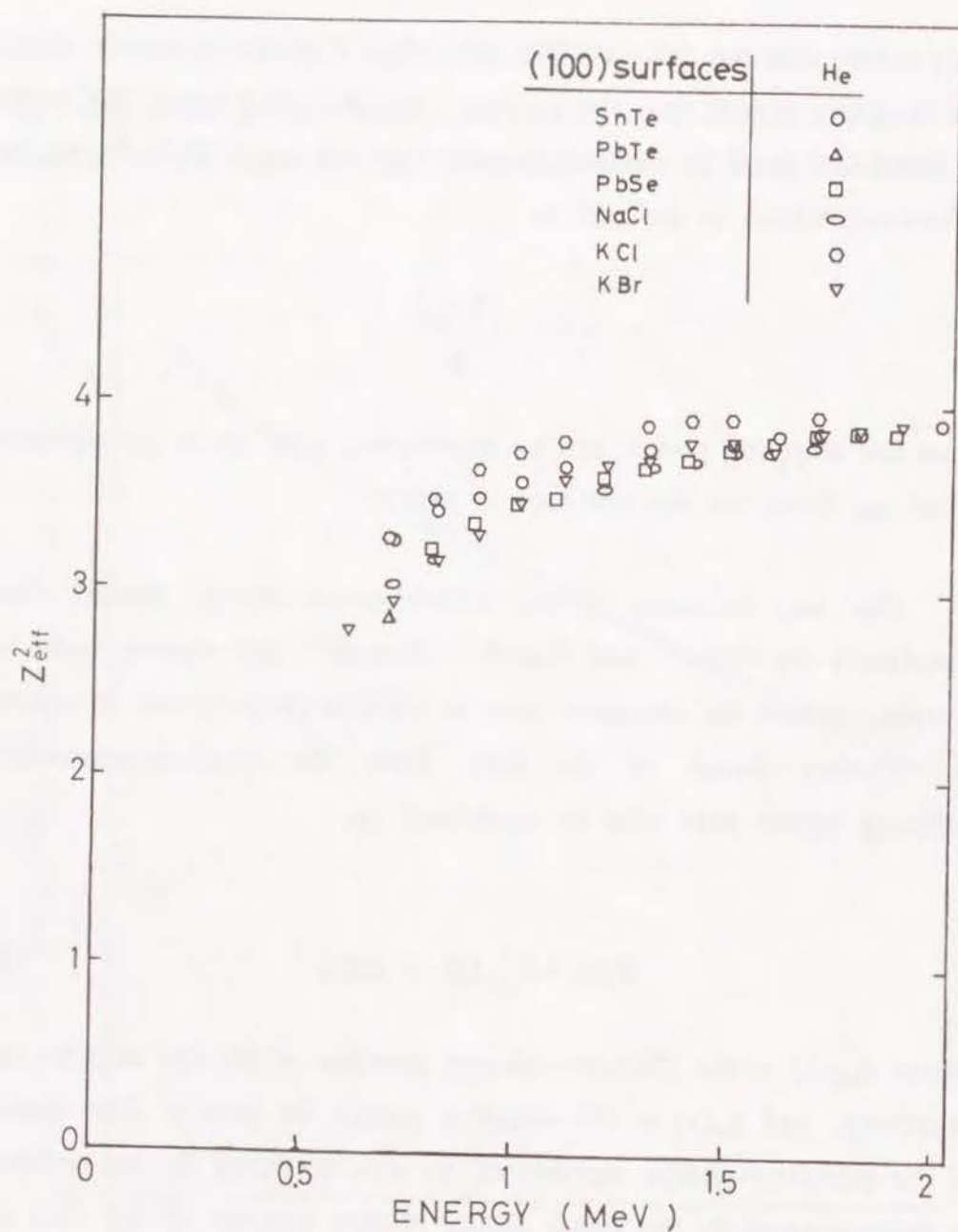
Figure 4.6: Energy dependence of the mean square charge Z_{eff}^2 of He ions reflected from various target surfaces.

where $F_q(z)$ is fraction of the ions with charge qe at z on the trajectory. Since the H^0 fraction in the scattered ions was less than 0.03 in the present experimental conditions, $Z_{eff}(z)$ at H^+ scattering was approximated to unity. At He scattering, on the other hand, the charge state of the He ions is no more constant along their trajectories near the surface. From our study on the charge exchange processes of MeV light ions at glancing angle incidence on a surface,[13] it has been shown that rapid change in the charge state of the ion occurs on its incoming trajectory to the surface and that the mean charge of the reflected ions is almost equal to that of the ions at their distances closer than 1.5 Å from the surface. Thus we approximated $F_q(z)$ in Eq. (9) by the observed fraction of the charge state $F_q(\infty)$, and obtained Z_{eff}^2 from Eq. (9). Figure 4.6 shows the observed energy dependences of Z_{eff}^2 of He ions specularly reflected from various crystal surfaces. They are almost on a curve independent of the target material.

With the use of the Z_{eff}^2, $S_o(x)$ was obtained from the observed energy losses. Several examples of the derived stopping powers, $S_o(x)$, for H and He ions are shown by thick solid lines in Fig. 4.7. These stopping powers $S_o(x)$ are approximated to exponentially decaying functions of x at the distances larger than 1 Å,[4] however, they deviate from the simple exponential decay at the distances closer than 0.5 Å from the surface. The deviation from the simple exponential decay becomes larger for faster ions, which is consistent with the fact that the observed loss $\Delta E(\theta_i)$ increases slightly with increasing θ_i for faster ions.
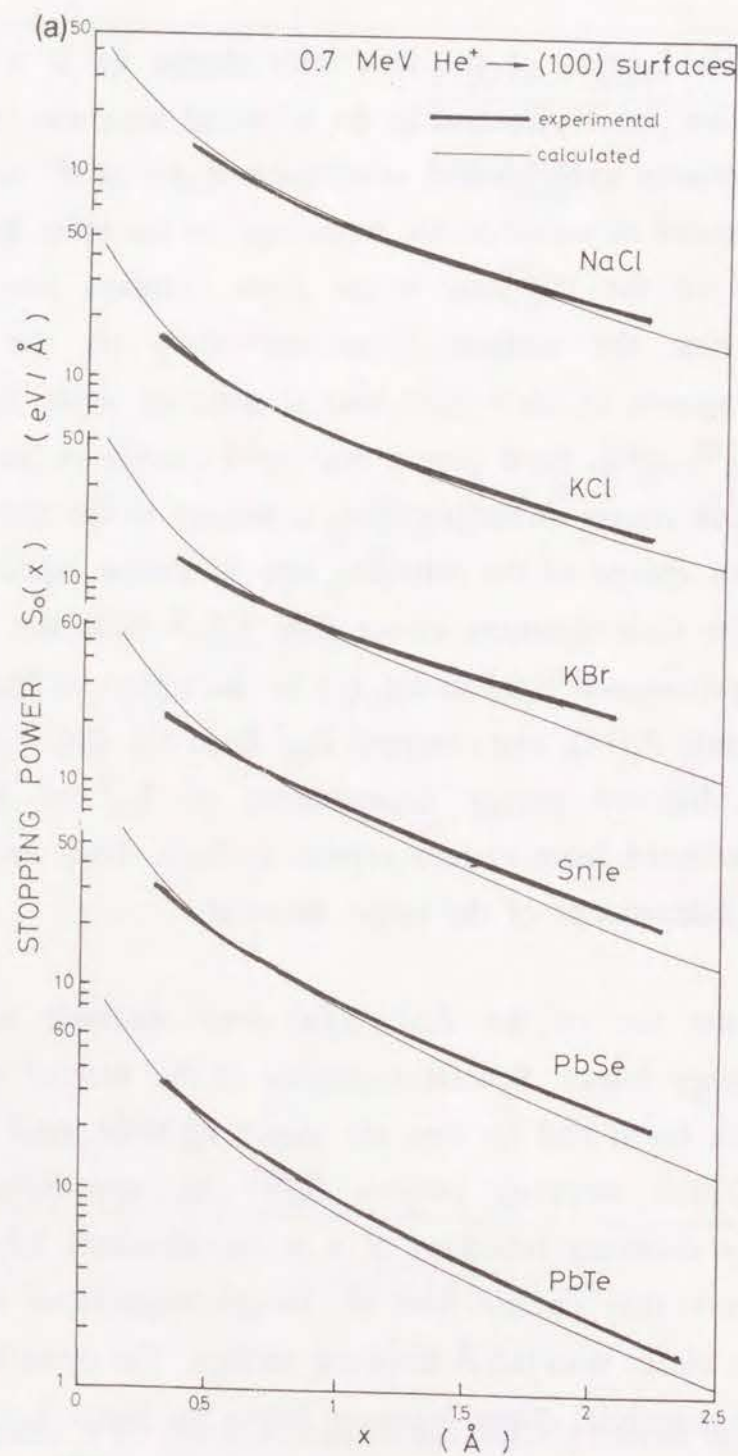
Figure 4.7: Position–dependent stopping powers.

Figure 4.7: Position–dependent stopping powers derived from the experimental energy losses are shown (a) for 0.7 MeV He ions, (b) for 1.5 MeV He ions. Calculated stopping powers $S_o(x)$, shown by thin solid lines, are compared with the experimental ones.

Figure 4.7(c): Position–dependent stopping powers derived from the experimental energy losses are shown for 0.7 MeV H$^+$ ions. Calculated stopping powers $S_o(x)$, shown by thin solid lines, are compared with the experimental ones.
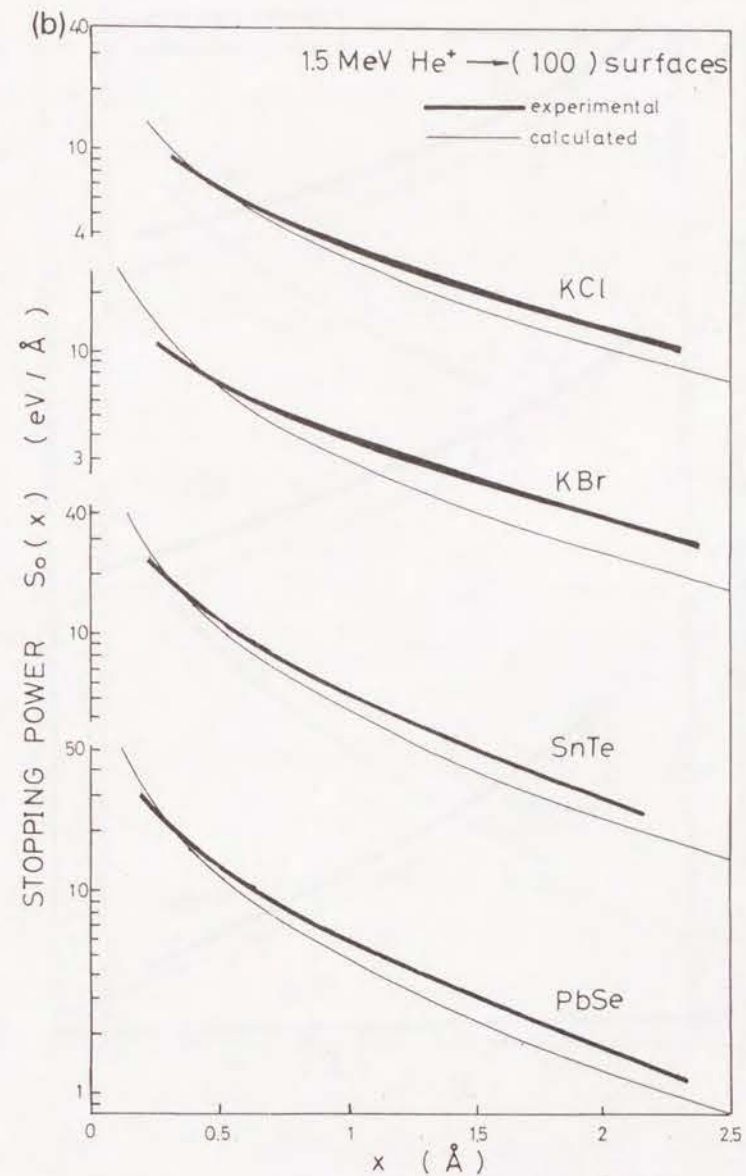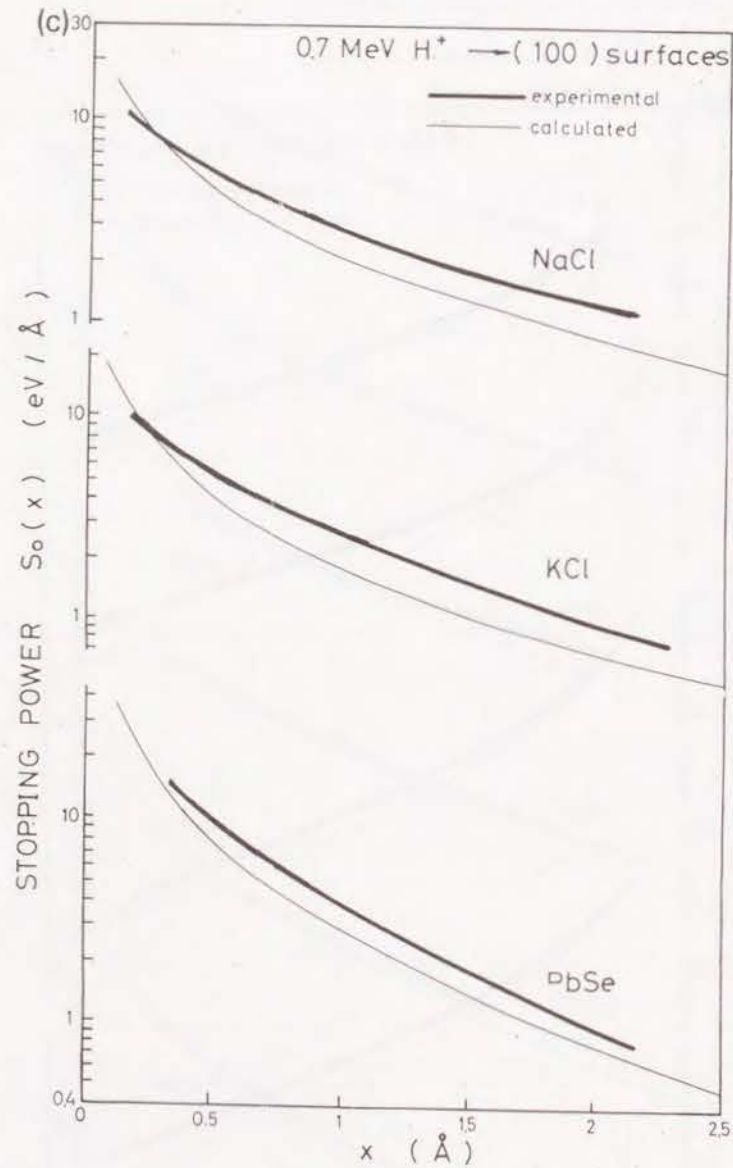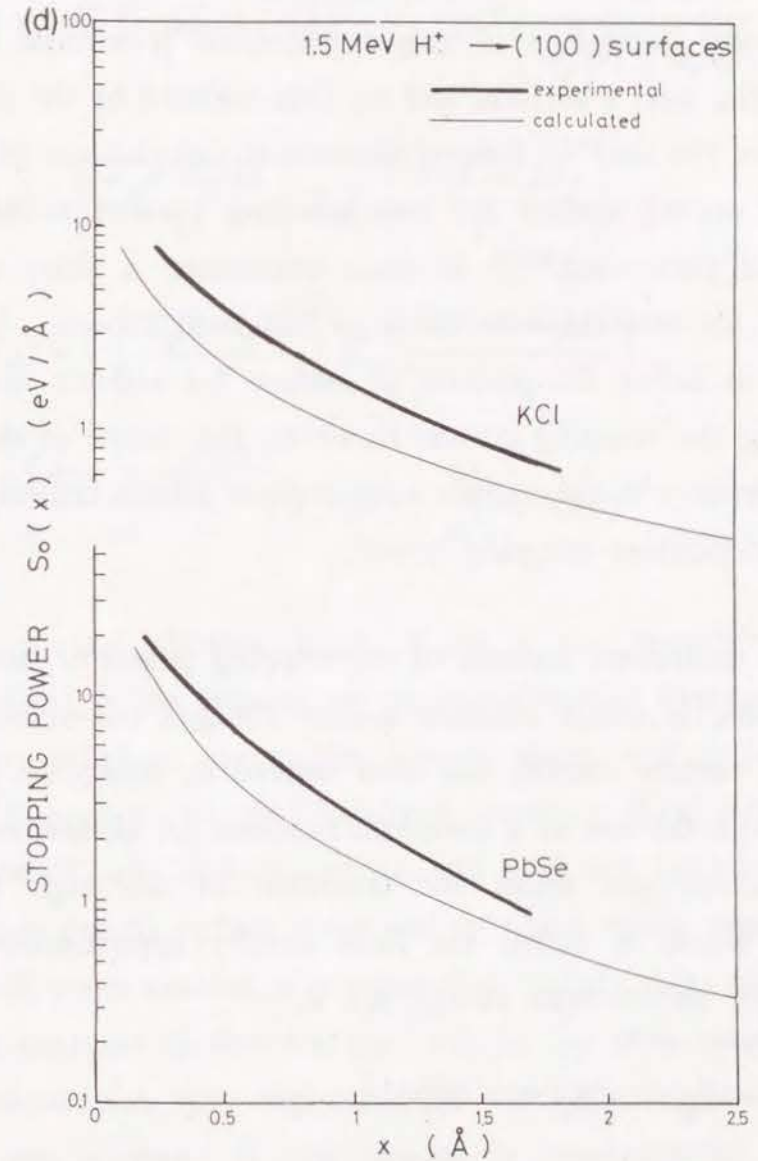

Figure 4.7(d): Position–dependent stopping powers derived from the experimental energy losses are shown for 1.5 MeV H$^+$ ions. Calculated stopping powers $S_o(x)$, shown by thin solid lines, are compared with the experimental ones.

4.4.2. Comparison with Theoretical Calculation

Density fluctuation of valence electrons is induced by a fast ion traveling near a surface, and the field induced by the fluctuation decelerates the ion.[14,15] Several theoretical calculations of stopping power of crystal surface for ions traveling parallel to the surface have been performed.[16-18] In their treatments, a sharp reflecting boundary for solid valence electrons has been chosen. Therefore, we have to define the position of surface for valence electrons in calculating the stopping power. However, the choice of the surface position relative to the surface atomic plane affects critically on the position-dependent stopping power.

The theoretical formula of the stopping power of such system of electrons, in which electron density changes one-dimensionally along the surface normal, has been derived by Kitagawa.[19] It was derived with the use of a dielectric function for an inhomogeneous many-electron gas under the condition of the high frequency response which is called the local density approximation. The formula for an ion with charge $Z_p e$ is,

$$S_c(x) = S_b(x) + S_s(x) + S_r(x) , \qquad (10)$$

$$S_b(x) = \left(\frac{Z_p e \, \omega_p(x)}{V} \right)^2 \cdot \ln\left(\frac{2V}{v_F(x)} \right) , \qquad (11)$$

$$S_{\binom{s}{r}}(x) = \int dX \, T_{\binom{s}{r}}(X,x) \frac{\partial \omega_p^2(X)}{2\partial X} \frac{x-X}{|x-X|} \mathrm{P}\left(\frac{1}{\omega_p^2(x) - \omega_p^2(X)} \right) , \quad (12)$$

$$T_s(X,x) = \left(\frac{Z_p e \, \omega_p(X)}{V} \right)^2 \mathrm{K}_0\left(\frac{2|x-X|\omega_p(X)}{V} \right)$$

$$T_r(X,x) = - \left(\frac{Z_p e \, \omega_p(x)}{V} \right)^2 \mathrm{K}_0\left(\frac{2|X-x|\omega_p(x)}{V} \right)$$

$$\omega_p(x) = \left(\frac{4\pi e^2 n_v(x)}{m} \right)^{1/2} , \quad v_F(x) = \frac{h}{m}\left(3\pi^2 n_v(x)\right)^{1/3} , \qquad (12')$$

where m is the electron mass, $\mathrm{K}_0(x)$ is the modified Bessel function, $n_v(x)$ is the density of valence electrons averaged along the plane parallel to the surface atomic plane, and $\omega_p(x)$ is the plasmon frequency of the localized mode. $S_b(x)$ shows the contribution of bulk excitation mode, and $S_s(x)$ and $S_r(x)$ are surface contributions due to surface mode and reflective mode, respectively. The cut-off wave number was equated to $\omega_p(x)/v_F(x)$ and $V \gg v_F(x)$ was assumed in deriving Eq. (11). In Eq. (12), dispersion of plasma frequencies was neglected and the infinite cut-off wave number was chosen. If we choose a semi-infinite uniform distribution of valence electrons in Eq. (10), the stopping power derived from Eq. (10) coincides with those derived from the other theories.[16-18]

In the stopping power $S_c(x)$ given by Eq.(10), the contribution of single electron–ion collision is not included. The contribution of the single collision to the stopping is calculated by the binary encounter approximation as,[20]

$$S_I(x) = \frac{2\pi Z_p^2 e^4}{mV^2} \sum_i n_i(x) \ln\left(\frac{2mV^2}{E_i}\right)$$

$$= \frac{1}{2}\left(\frac{Z_p e\,\omega(x)}{V}\right)^2 \cdot \ln\left(\frac{2mV^2}{\hbar\omega(x)}\right) , \qquad (13)$$

where $n_i(x)$ is the density of the i–th shell electrons averaged over surface plane and E_i is the binding energy of the i–th shell electrons. In deriving Eq. (13), use has been made of the relation,[21]

$$\sum_i n_i(x) \ln\left(\frac{2mV^2}{E_i}\right) = n(x) \ln\left(\frac{2mV^2}{E(x)}\right) ,$$

where $E(x)$ is the specific energy defined by,[21]

$$E(x) = \hbar\omega(x) = \hbar\left(\frac{4\pi e^2 n(x)}{m}\right)^{1/2} . \qquad (14)$$

The electron densities $n_v(x)$ and $n(x)$ have to be determined to calculate Eqs. (10) and (13). An approximate expression for the total electron density $n(x)$ was derived from the continuum surface planar potential, Eq. (6) with $Z_1 = 1$, using the Poisson equation as

$$n(x) = \frac{Z_2 N_p}{2a_{TF}} \cdot \sum_i^3 \alpha_i \beta_i \exp\left(-\frac{\beta_i x}{a_{TF}}\right) . \qquad (15)$$

For the approximate expression of valence electron density $n_v(x)$, the wave functions of isolated atoms calculated from the Hartree–Fock approximation were used.[22] Although the $n_v(x)$ thus calculated is too crude to describe the actual electron distribution at a solid surface, we had to content to use this expression of $n_v(x)$ since we have no other available expression.

An example of the calculated $S_c(x)$ and $S_I(x)$ of SnTe(100) for 1.5 MeV He ion is shown in Fig. 4.8. The theoretical stopping power $S_0(x)$ agree well with the experimental one: It is seen that the stopping due to the collective excitation dominates at distances larger than about 1 Å, while that due to single electron excitation does near the surface plane.

The calculated stopping powers $S_0(x)$ of various surfaces, which are shown by the thin solid lines, are compared with the experimental stopping powers in Fig. 4.7. The agreement of the calculated stopping powers with the experimental ones is good for
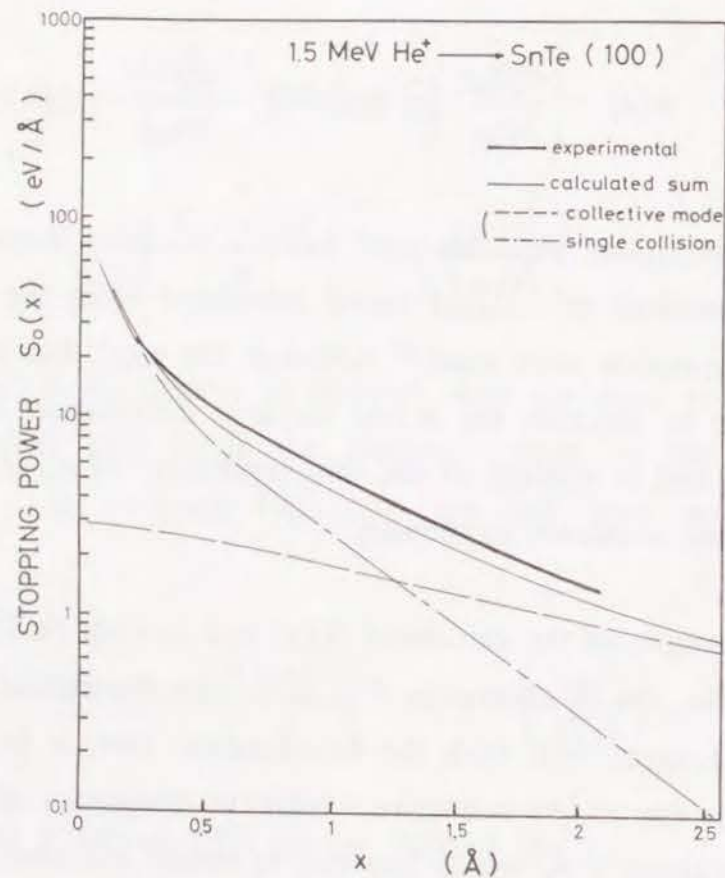
Figure 4.8: Position–dependent stopping powers derived from the experimental energy losses, $S_o(x)$ of the (100) surface of SnTe for 1.5 MeV He ions. Calculated stopping powers $S_I(x)$, and $S_c(x)$, and its sum S_o from Eqs (12) and (15) are compared with the experimental ones.

slower ions, while it becomes poorer for faster ions. The reason for this discrepancy is not clarified yet. Perhaps this discrepancy may be caused by several approximations made in deriving the experimental stopping powers and in the theory: (1) The continuum planar potential $V(x)$ used here was calculated from the Molière's approximation to Thomas–Fermi screening function. Ionic character of the constituent atoms of the present crystals has to be considered in the ion–atom collisions. (2) Elaborate theory of the stopping due to ion–atom single collision has to be used in the theoretical stopping power. (3) More realistic electron distribution near the surface has to be adopted in the numerical calculation of the theoretical stopping powers. These are difficult problems for us at the moment, and we have to wait for the further studies.

REFERENCES

1) G. S. Harbinson, B. W. Farmery, H. J. Pabst and M. W. Thompson, Radiat. Eff. 27 (1975) 97.

2) M. Mannami, Y. Fujii and K. Kimura, Surf. Sci. 204 (1988) 213.

3) Y. Fujii, K. Kimura, M. Hasegawa, M. Suzuki, Y. Susuki and M. Mannami, Nucl. Instrum. and Methods B 33 (1988) 405.

4) K. Kimura, M. Hasegawa and M. Mannami, Phys. Rev. 36 (1987) 7.

5) K. Kimura, Y. Fujii, M. Hasegawa, Y. Susuki and M. Mannami, Phys. Rev. B 38 (1988) 1052.

6) M. Prutton, "Surface Physics", Clarendon Press, 1983, p.9.

7) S. Sawada, K. Kimura and M. Mannami, Jpn J. Appl. Phys. 22 (1983) 1464.

8) Y. Fujii, S. Fujiwara, K. Kimura and M. Mannami, Radiat. Eff. 116 (1991) 111.

9) M. Tsuji, Y. Mizuno, Y. Susuki and M. Mannami, J. Cryst. Growth 108 (1991) 817.

10) N. Bohr, Phys. Rev. 58 (1940) 654; 59 (1941) 270.

11) W. E. Lamb, Phys. Rev. 58 (1940) 696.

12) W. Brandt, "Atomic Collisions in Solids", Vol. 1, p.261. (Plenum, New York), 1973.

13) Y. Fujii, S. Fujiwara, K. Kimura and M. Mannami, Nucl. Instrum. and Methods B 58 (1991) 18.

14) N. Takimoto, Phys. Rev. 146 (1966) 366.

15) L. Marton and L. B. Leder, Phys. Rev. 94 (1954) 203.

16) R. Núñez, P. M. Echenique and R. H. Ritchie, J. Phys. C 13 (1980) 4229.

17) Yu. A. Romanov and V. Ya. Aleshkin, Sov. Phys. Solid State 23 (1981) 147.

18) R. Kawai, N. Itoh and Y. H. Ohtsuki, Surf. Sci. 114 (1982) 137.

19) M. Kitagawa, Nucl. Instrum. and Methods B 33 (1988) 409.

20) J. J. Thompson, Phil. Mag. 23 (1912) 419.

21) J. Lindhard and M. Scharff, Kgl. Danske Videnskab. Selskab. Mat. Fys. Medd. 27 No.15 (1953).

22) H. Herman and S. Skillman, Atomic Structure Calculations, (Englewood Cliffs, N.J.Prentice–Hall, 1963).
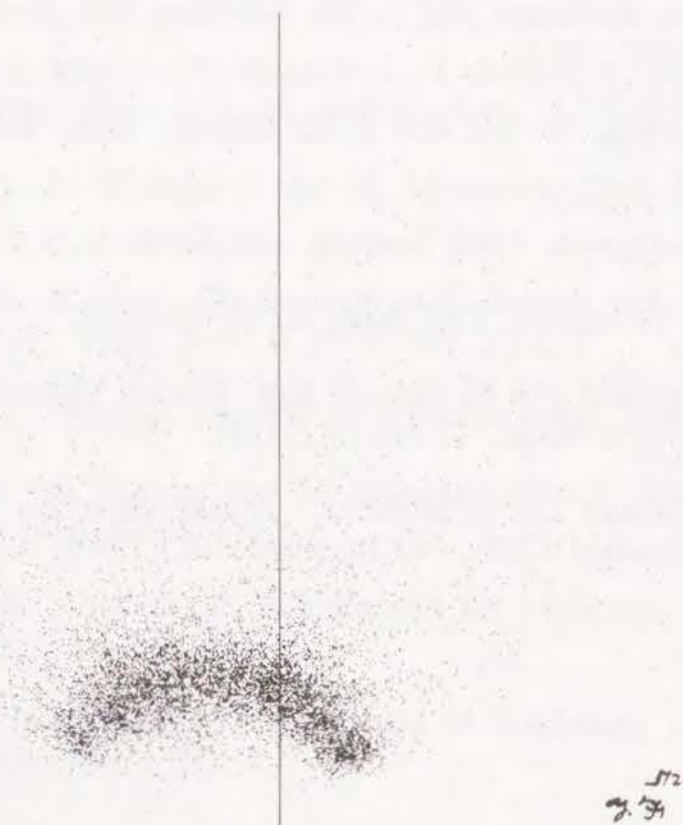
Chapter 5

ENERGY LOSS OF 0.7-MeV He IONS DUE TO THE DYNAMIC RESPONSE OF SURFACE ELECTRONS

ABSTRACT

Energy losses of 0.7-MeV He ions which have surface-channeled along atomic rows on a clean (100) surface of SnTe are studied. Energy spectrum of the surface-channeled ions shows a few peaks whose energies and heights depend on the angle of incidence of He ions, θ_i. From the θ_i dependence of the energy losses, position-dependent stopping powers of the (100) surface for the He ions are determined from the [001] and [011] surface-channeling. The contribution of collective excitation of surface valence electrons to the stopping powers is extracted from the obtained position-dependent stopping powers. This agrees well with the theories where the dynamical response of valence electrons to the fast moving ions is taken into account.

5.1. INTRODUCTION

Using glancing–angle scattering of MeV ions from a flat crystal surface, it has been shown that the ion loses kinetic energy even if it travels outside the solid.[1,2] The energy losses of the ions have been explained by a position–dependent stopping power of the (100) surface of SnTe for fast ions in vacuum. The stopping power has a form,[1]

$$S^{(100)}(x) = CE^{-1/2} \exp\left(-\frac{\beta_3 x}{2 a_{TF}}\right) , \qquad (1)$$

where x is the distance of the ion from the surface atomic plane, C is a constant depending on the ion species and target surface, E is the ion energy, β_3 is 0.3, and a_{TF} is the Thomas–Fermi screening distance. The stopping powers are explained in terms of the deceleration in the field induced by collective excitation of valence electrons to the charge of the fast moving ion near the surface, and of the collisions of the ion with electrons exuding out of the surface.

The trajectories of the specularly reflected ions can be obtained by applying the general principles of the interaction of fast ion with orderly arranged atoms developed for ion channeling in crystal.[3,4] Thus the losses of energy of the specularly reflected ions are obtained by integrating the position–dependent stopping power along ion trajectories.

In Chapter 4 we have proposed a new method to derive position–dependent stopping power of a surface for specularly reflected ions at glancing angle incidence on the surface. With this method, the position–dependent stopping power was derived experimentally only from the dependence of the energy loss ΔE of ions on the angle of incidence on the surface. In the present Chapter, we apply this method for the analysis of the energy losses of surface–channeled He ions at the (100) surface of SnTe. Then the position–dependent stopping powers of the (100) surface for 0.7–MeV He ions at the [001] and [011] surface–channeling are determined. Contribution of the collective excitation of surface valence electrons to the stopping powers is extracted from the obtained position–dependent stopping powers for surface–channeling ions, which can be compared with those derived from the theories.

5.2. EXPERIMENTAL

A single crystal of SnTe with a clean (100) surface was grown epitaxially by vacuum evaporation of SnTe (99.999 % purity) on the (100) surface of KCl mounted on a five–axis goniometer in a UHV scattering chamber. The (100) surface of the grown SnTe crystal was irradiated by a narrow beam of 0.7–MeV He$^+$ ions from the 4 MV Van de Graaff accelerator of Kyoto University. The beam was less than 0.04 mm in diameter and the beam divergence was less than 0.1 mrad at the target position. The SnTe crystals were grown with growth rates less than 0.5 nm/min at 250 °C. At these growth rates the densities of steps on the (100) surfaces were small, which was ascertained directly by the

observation with the use of an atomic force microscope as shown in Chapter 3.[5] Thus the fraction of He ions penetrating the surface at the steps was negligible. The base pressure of the UHV scattering chamber was 3×10^{-10} Torr. The vacuum of the chamber during the epitaxial growth was better than 2×10^{-9} Torr and was in the 10^{-10} Torr range during the ion scattering measurement.
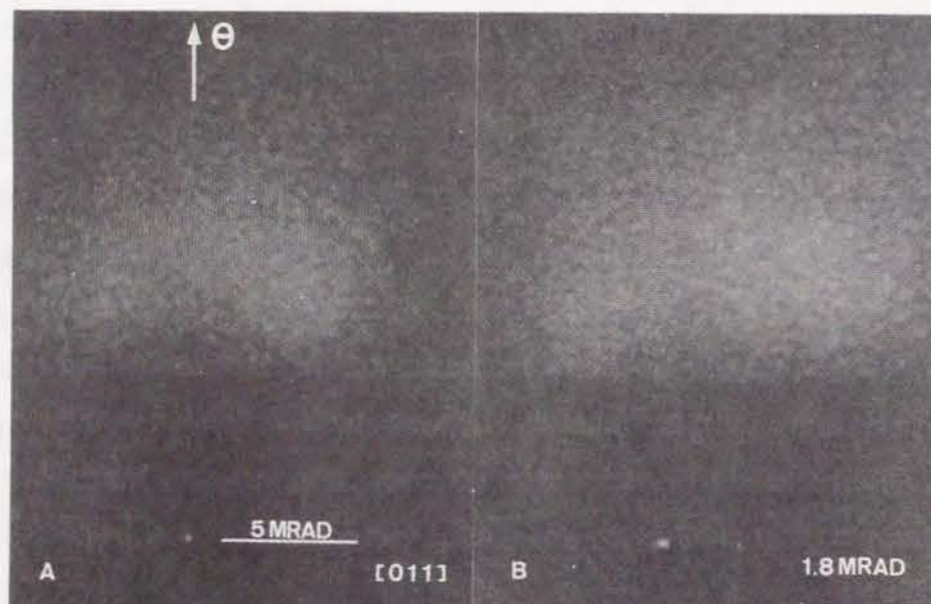
Figure 5.1: Angular distributions of scattered He ions at the [011] surface–channeling on the (100) surface of SnTe crystal at the incidence of 0.7 MeV He$^+$ ions. The glancing angle of the incident ions to the (100) surface was 4.8 mrad and the azimuthal angles in the figure were measured from the [011] axis parallel to the (100) surface of SnTe.
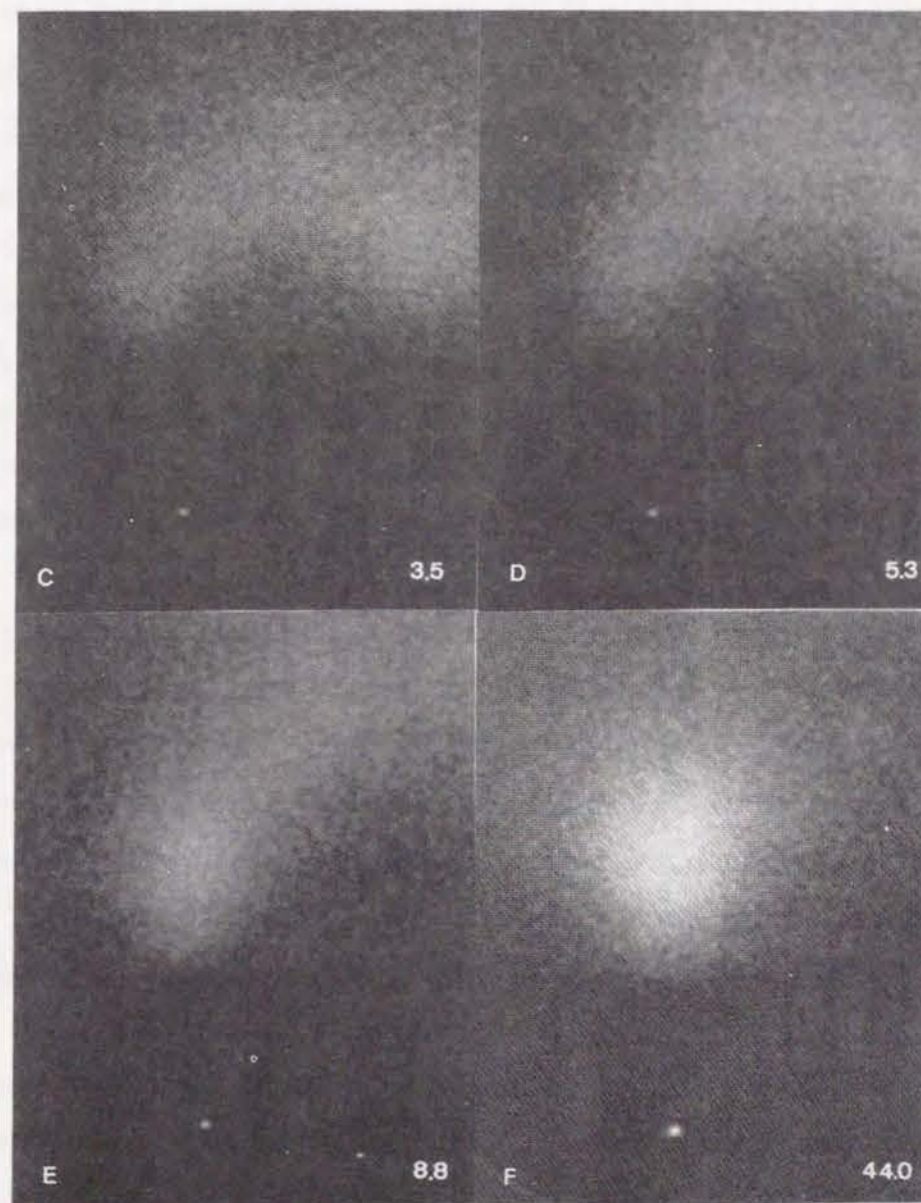
Figure 5.1: Angular distributions of scattered He ions at the [011] surface–channeling on the (100) surface. (f) Random incidence (along a high index axis).

Figure 5.1 shows the angular distribution of scattered He ions which are observed on a fluorescence screen downstream from the crystal when 0.7–MeV He$^+$ ions scatter at glancing angle incidence on the (100) surface of SnTe with various azimuthal angles, ϕ_i, of the incident beam relative to the [011] atomic rows. At the incidence of ions nearly parallel to low index atomic rows on a crystal surface, the ions are scattered on a broad arc as can be seen in Figs. 5.1(a)–5.1(e). The arc is formed by the ions scattered from the atomic rows, and thus the center of the arc is the projection of the direction of the atomic rows on the screen. The arc moves as the direction of the rows deviates from the incident beam direction.

An aperture was placed to select the ions scattered at the angle for specular reflection, *i.e.*, at the scattering angle θ twice the angle of incidence θ_i in the scattering plane. The acceptance angle of the aperture was 0.6 mrad. The ions passing through the aperture were energy–analyzed with a magnetic spectrometer. Energy resolution of the spectrometer was 8×10^{-3}. Fractions of He^{2+} and He$^+$ in the scattered ions at 0.7–MeV He$^+$ incidence are about 0.7 and 0.3 respectively, and He^0 fraction was less than 10^{-2}. The charge of He ion changes so frequently along its trajectory[6] that the energy spectrum of He$^+$ is almost equal to that of He^{2+}. Thus we studied the energy losses of scattered He^{2+} ions at the [001] and [011] surface–channeling.

5.3. RESULTS AND DISCUSSION

Figures 5.2 and 5.3 show the examples of the observed energy spectra of the [001] and [011] surface–channeled He^{2+} ions at the incidence of 0.7–MeV He$^+$ ions on the (100) surface of SnTe with azimuthal angle, $\phi_i=0$. Most of the spectra show a sharp peak at the energies about 15 keV smaller than that of the incident ions. The energy at the highest energy peak little depend on the angle of incidence as shown in Fig. 5.4. On the other hand, the energies at the lower energy peaks depend on the angle of incidence.
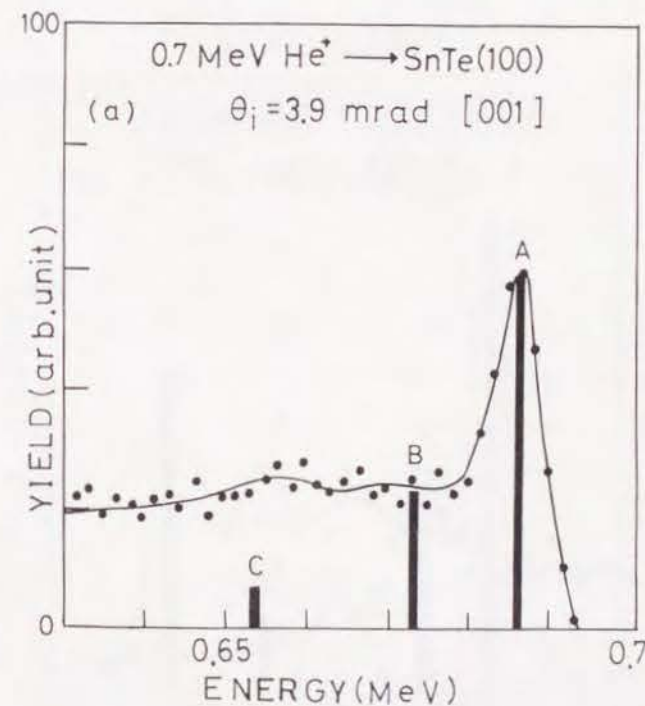
Figure 5.2: Energy spectra of the [001] surface–channeled He^{2+} ions at the incidence of 0.7 MeV He$^+$ ions on the (100) surface of SnTe. (a) θ_i = 3.9 mrad. The calculated yields at the peaks are shown by bars.
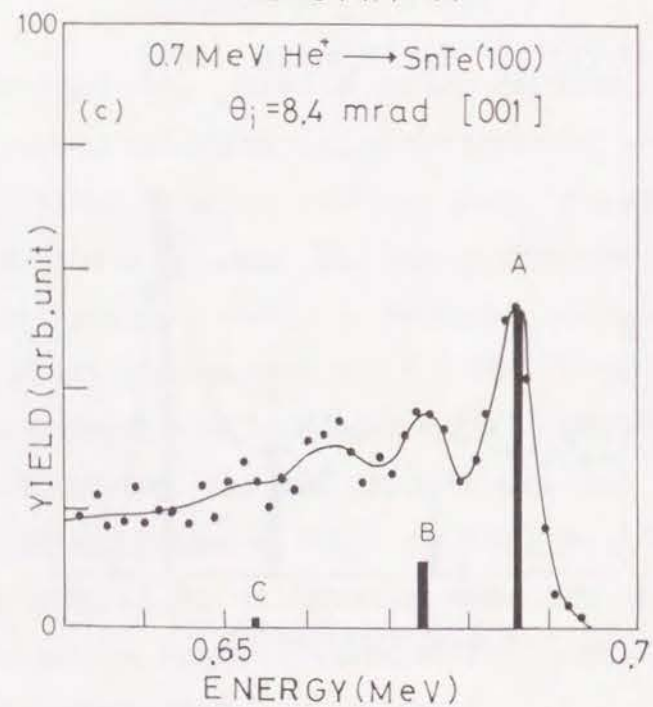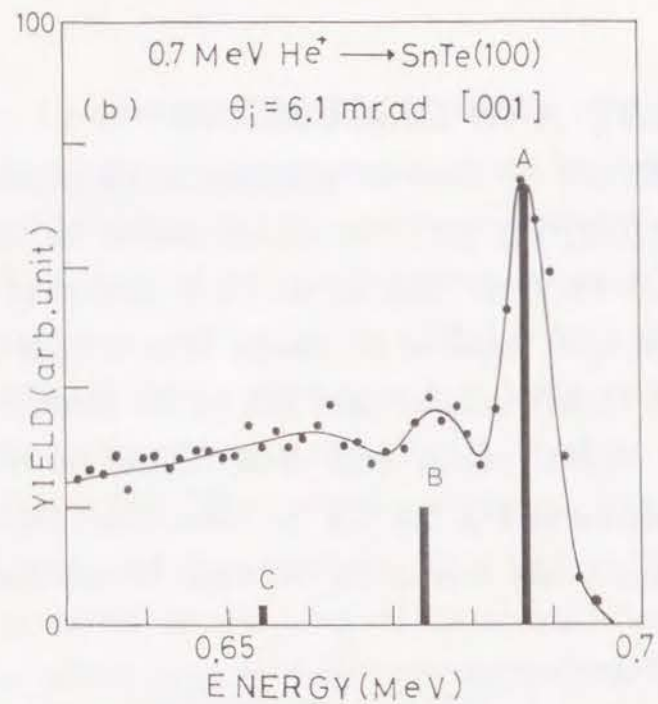
Figure 5.2: Energy spectra of the [001] surface–channeled He^{2+} ions at the incidence of 0.7 MeV He$^+$ ions on the (100) surface of SnTe. (b) θ_i = 6.1 mrad. (c) θ_i = 8.4 mrad.
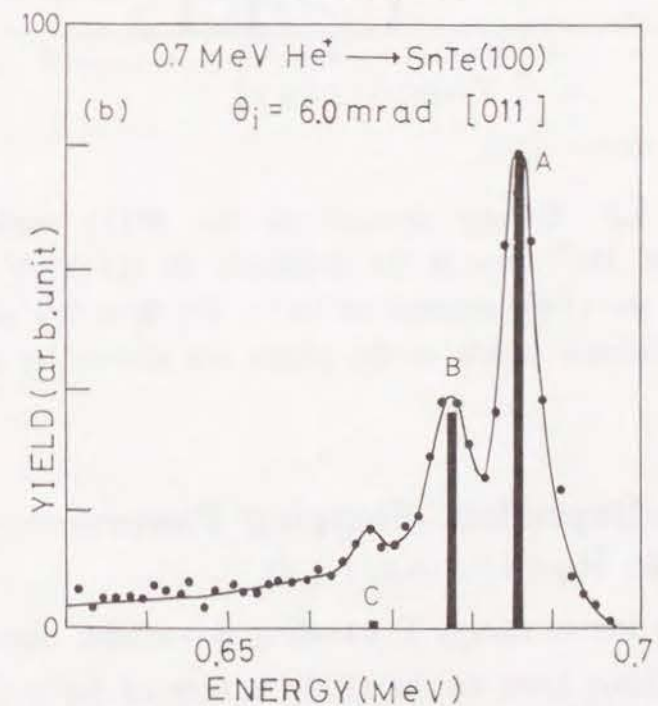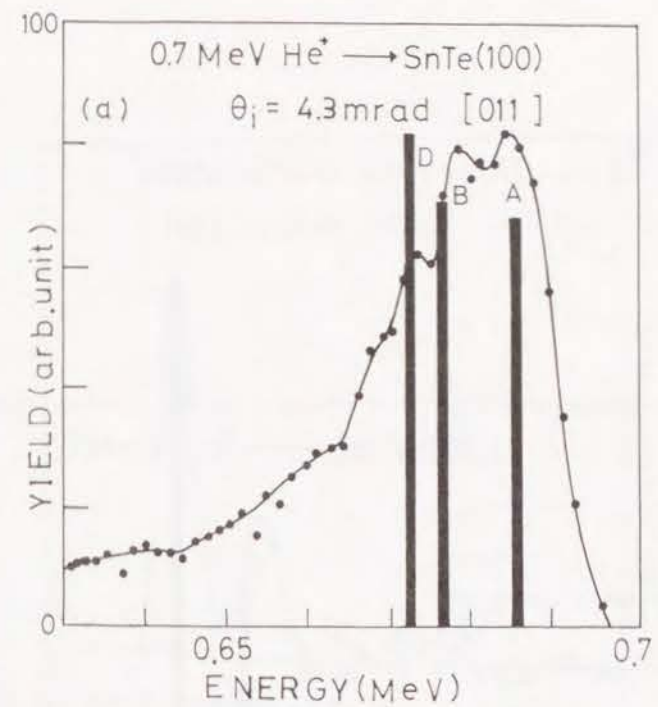
Figure 5.3: Energy spectra of the [011] surface–channeled He^{2+} ions at the incidence of 0.7 MeV He$^+$ ions on the (100) surface of SnTe. (a) θ_i = 4.3 mrad. (b) θ_i = 6.0 mrad.
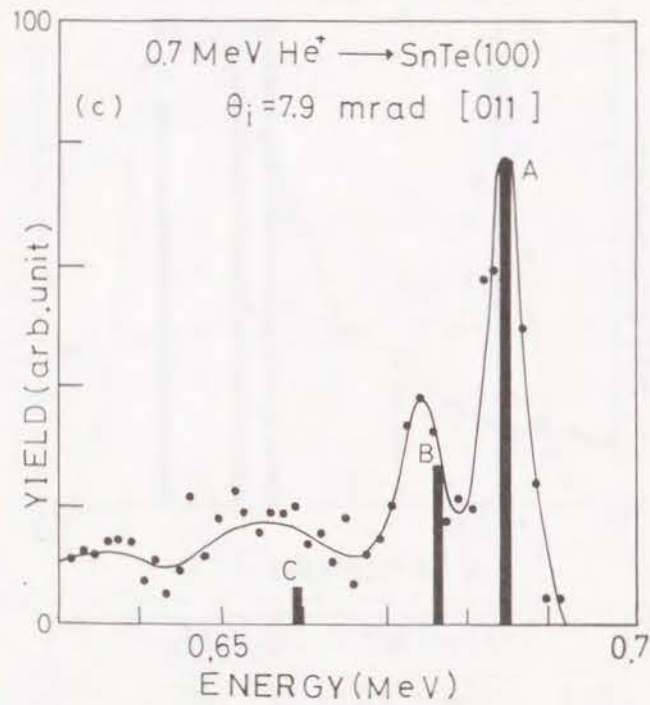
Figure 5.3: Energy spectra of the [011] surface–channeled He^{2+} ions at the incidence of 0.7 MeV He^+ ions on the (100) surface of SnTe. (c) θ_i = 7.9 mrad. The calculated yields at the peaks are shown by bars.

A. Position–Dependent Stopping Powers of Atomic Rows

For a fast ion of energy E traveling in vacuum nearly parallel to the [0kl] atomic rows on the (100) surface of SnTe crystal, we choose the Cartesian coordinates where the z–axis is parallel to the atomic rows and the x–axis parallel to the surface normal. The origin of the coordinates is on an atom on the surface.
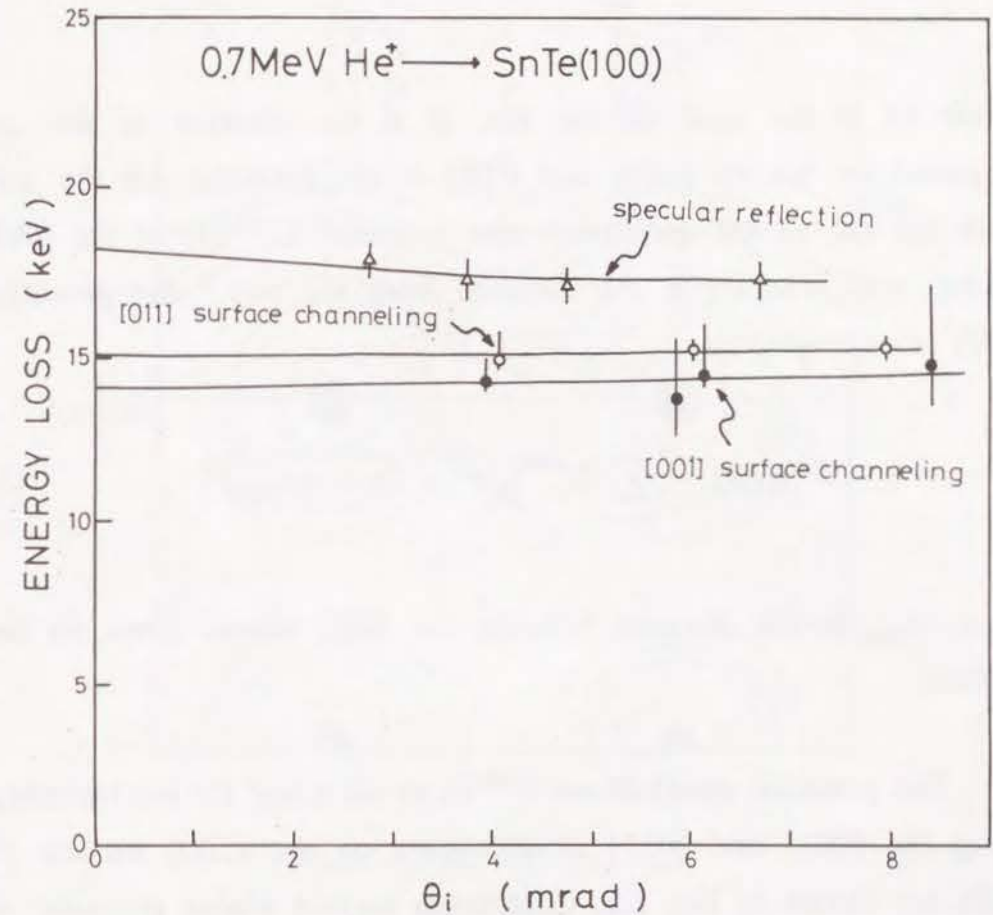
Figure 5.4: Dependence of the energy loss at the highest energy peak in the energy spectra of surface channeled He^{2+} on the angle of incidence. The energy losses at specular reflection from the (100) surface are shown for comparison.

Since the velocity of the ion parallel to the z–axis is approximately constant, the equation of motion of the ion projected on the xy plane is written as

$$M \frac{d^2 R}{dt^2} = - \nabla_{x,y} U(R) \; , \tag{2}$$

where M is the mass of the ion, R is the position of the ion projected on the xy–plane and $U(R)$ is the potential for the ion. With the use of the continuum row potential $U_a^{[0kl]}(r)$ of the [0kl] atomic row, where r is the distance from the row,[3] the potential $U(R)$ is expressed as

$$U^{[0kl]}(x,y) = \sum_{n=-\infty}^{\infty} U_a^{[0kl]}\left(\sqrt{x^2 + (y + na_{[0kl]})^2} \right) \; , \tag{3}$$

where $a_{[0kl]}$ is the distance between the [0kl] atomic rows on the surface.

The potential distributions $U^{[0kl]}(x,y)$ for a fast He ion traveling along the [001] and [011] atomic rows on the (100) surface of SnTe are shown in Fig. 5.5. Continuum surface planar potential of the (100) surface for He ions is also shown for comparison. The Molière approximation to Thomas–Fermi screening function was used in the calculation of the potentials.
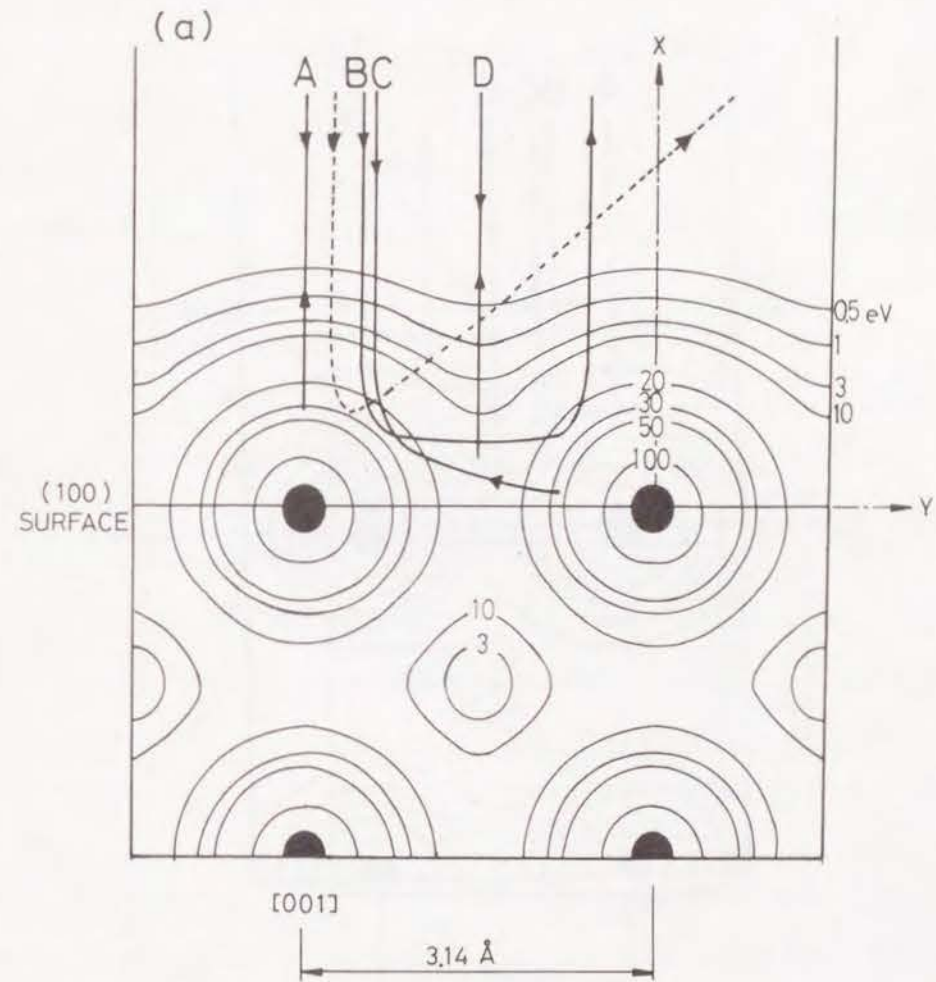
Figure 5.5(a): Potential distributions U(x,y) (contours labeled in eV) for a fast He ion at glancing angle incidence of the (100) surface of SnTe. Along the [001] axis. Possible trajectories of 0.7 MeV He ions which give rise to the specularly reflected ions at $\theta = 2\theta_i$ are shown.
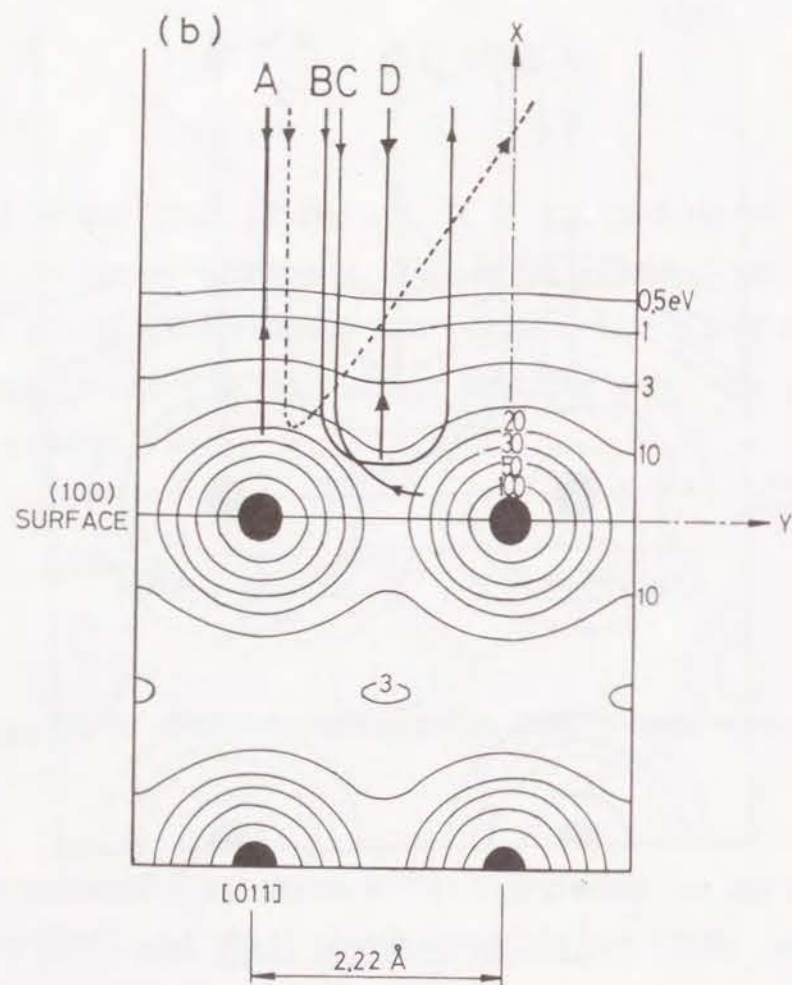
Figure 5.5(b): Potential distributions U(x,y) (contours labeled in eV) for a fast He ion at glancing angle incidence of the (100) surface of SnTe. Along the [011] axis. Possible trajectories of 0.7 MeV He ions which give rise to the specularly reflected ions at θ = 2θ$_i$ are shown.
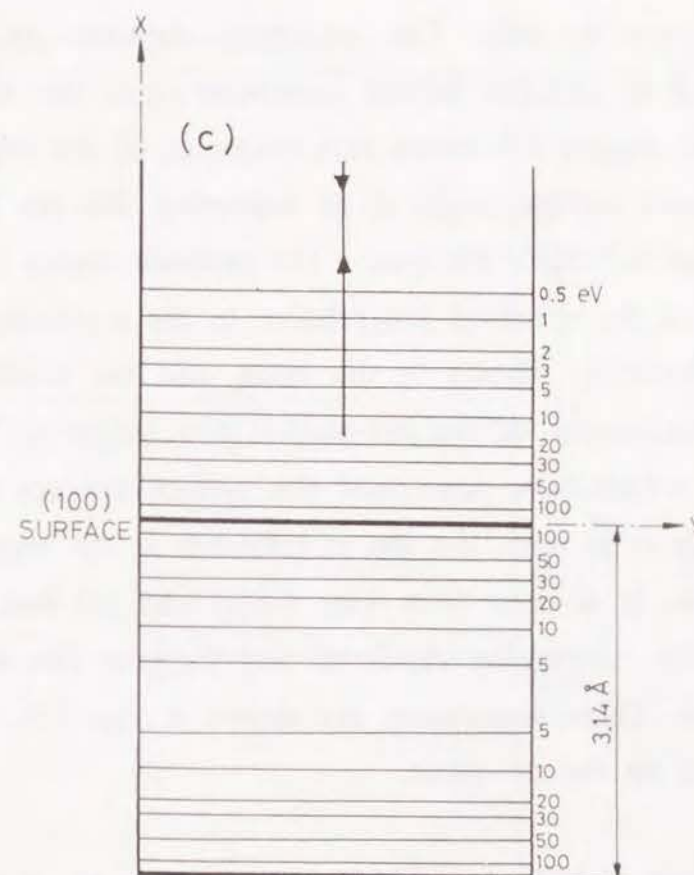
Figure 5.5(c): Potential distributions U(x,y) (contours labeled in eV) for a fast He ion at glancing angle incidence of the (100) surface of SnTe. Along the high index axis, the continuum surface planar potential of the (100) surface. Possible trajectories of 0.7 MeV He ions which give rise to the specularly reflected ions at θ = 2θ$_i$ are shown.

In order to explain the peaks in the energy spectra of the surface–channeled He ions such as those shown in Figs. 5.2 and 5.3, trajectories of He ions were calculated with the use of Eqs. (2) and (3), where the azimuthal angle of the incidence He$^+$ ions to the atomic row is zero. The trajectory depends on the angle of incidence θ_i and the impact parameter y of the ion–atomic row collision. Figure 5.6 shows two examples of the impact parameter dependence of the angle α of scattering for the [011] surface–channeled 0.7–MeV He ions. The ordinate shows the direction of motion of the scattered ion relative to the scattering plane, which is schematically shown in the inset, and the abscissa shows the impact parameter of the ion–atomic row collision. The angles for the ion which have penetrated the surface are not shown. When the angle α is zero, the ion is reflected at the angle for specular reflection. It is seen from Fig. 5.6(a) and (b) that four types of trajectories, shown by A, B, C and D, give rise to the specular reflection. These trajectories are shown in Fig. 5.5, where they are projected on the xy–plane.

Since the type A trajectory occurs at any angle θ_i of incidence, it is expected that the highest energy peaks in the energy spectra shown in Fig. 5.4 are formed by the ions with the type A trajectories. It is assumed that the trajectory of type A is governed only by an [0kl] atomic row on the scattering plane, since the trajectory is in the xz–plane containing the [0kl] atomic row. Thus the trajectory of the ion is described by the differential equation,
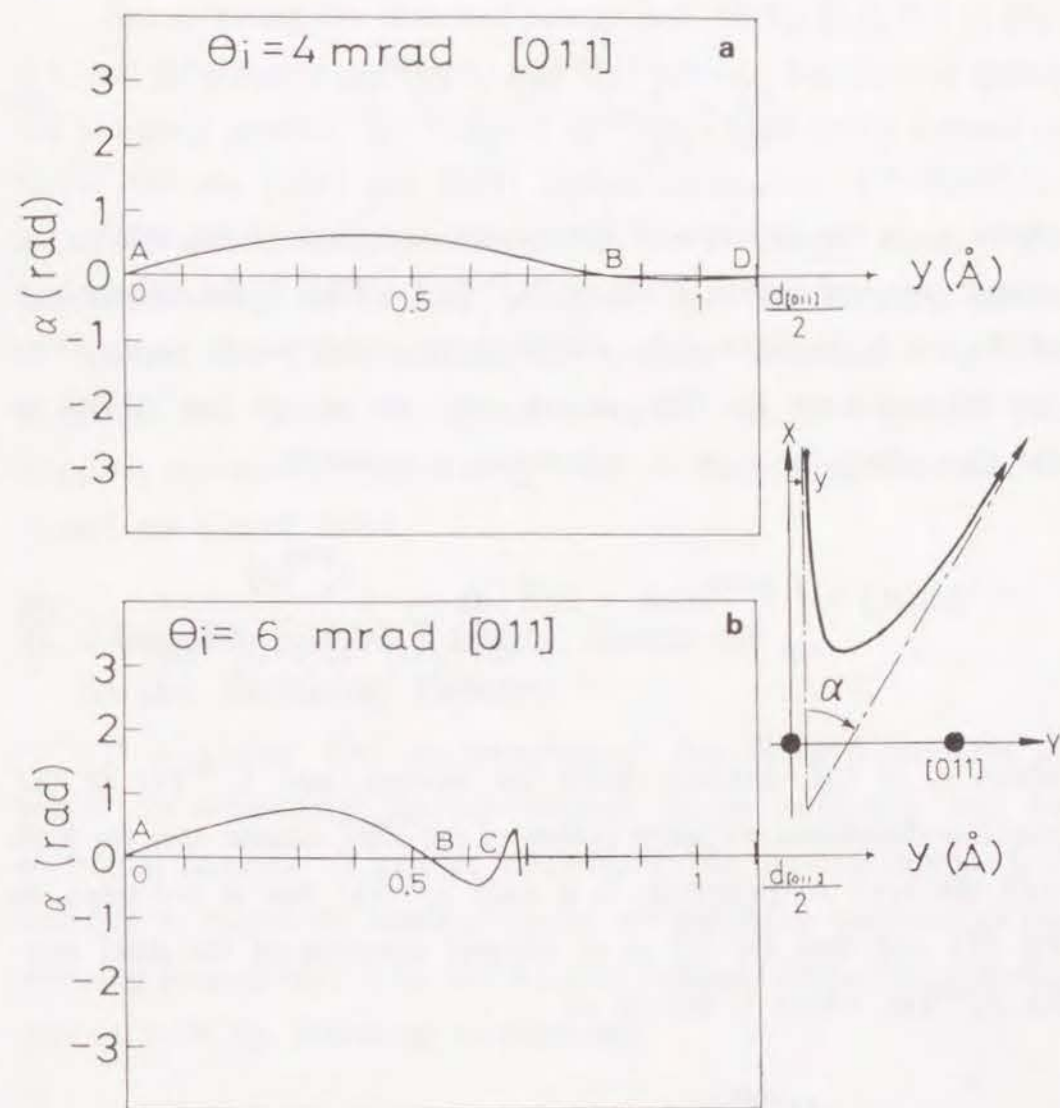
Figure 5.6: Examples of the dependence of the angle of scattering relative to the surface plane for the [011] surface–channeled 0.7 MeV He ions on the impact parameter y. The ordinate shows the angle of scattering projected on the scattering plane, (a) at the incidence θ_i = 4.0 mrad, and (b) at the incidence θ_i = 6.0 mrad.

$$\frac{dx}{dz} = \sqrt{\frac{U_a^{[0kl]}(x_c) - U_a^{[0kl]}(x)}{E}} \quad , \tag{4}$$

where x_c is the distance of the closest approach of the ion to the atomic row and is thus given by $U_a^{[0kl]}(x_c) = E\theta_i^2$. If the energy loss of the ion is determined by the stopping power which depends on the distance from the [0kl] atomic row, the energy loss $\Delta E(\theta_i)$ of the ions along the type A trajectories is given by

$$\Delta E(\theta_i) = \int_{traj.} S_a^{[0kl]}(x)\,dz = 2\sqrt{E} \int_{x_c}^{\infty} dx \frac{S_a^{[0kl]}(x)}{\sqrt{U_a^{[0kl]}(x_c) - U_a^{[0kl]}(x)}} \quad , \tag{5}$$

where x is the distance from the surface and $S_a^{[0kl]}(x)$ is the position-dependent stopping power of the [0kl] atomic row for ions with the type A trajectory. It is only $S_a^{[0kl]}(x)$ that is unknown in Eq. (5), and thus Eq. (5) is an integral equation of the Abel type for $S_a^{[0kl]}(x)$, which is solved as,

$$S_a^{[0kl]}(x) = -\frac{\dfrac{dU_a^{[0kl]}(x)}{dx}}{2\pi E}\left\{ \frac{\Delta E(0)}{\sqrt{\dfrac{U_a^{[0kl]}(x)}{E}}} + \int_0^{\frac{\pi}{2}} du\,\Delta E'\left(\sqrt{\dfrac{U_a^{[0kl]}(x)}{E}}\sin u\right)\right\} \tag{6}$$

where ' denotes the differentiation.

Extrapolating the observed energy loss $\Delta E(\theta_i)$ to $\theta_i = 0$ in Fig. 5.4, and substituting the $\Delta E(\theta_i)$ and $U_a^{[0kl]}(x)$ into Eq. (6), we obtain the stopping powers, $S_a^{[001]}(x)$ and $S_a^{[011]}(x)$ of the (100) surface of SnTe, for the [001] and [011] surface-channeling 0.7-MeV He ions. The same procedure was repeated for the energy losses at the incidence along the random orientation and the stopping power $S^{(100)}(x)$ of the (100) surface for specular reflection was also obtained. The results are shown by solid lines in Fig. 5.7. The stopping powers $S_a^{[001]}(x)$ and $S_a^{[011]}(x)$ are decreasing functions of x, and are almost equal.

B. Contribution of Valence Electrons to the Stopping Powers

It is known that the stopping of fast charged particles in matter is determined by ion-electron single collisions and by collective response of valence electrons to the moving charge. It is possible to derive the contribution of the collective response to the stopping powers only from the obtained position-dependent stopping powers with the following assumptions:

(1) The contribution of collective excitation to the position-dependent stopping power depends only on the distance from the surface. We defined it by $\gamma_c(x)$.

(2) Stopping power for surface-channeling ions depends both on x and y. This position-dependent stopping power $S^{[0kl]}(x,y)$ at the [0kl] surface-channeling is expressed by
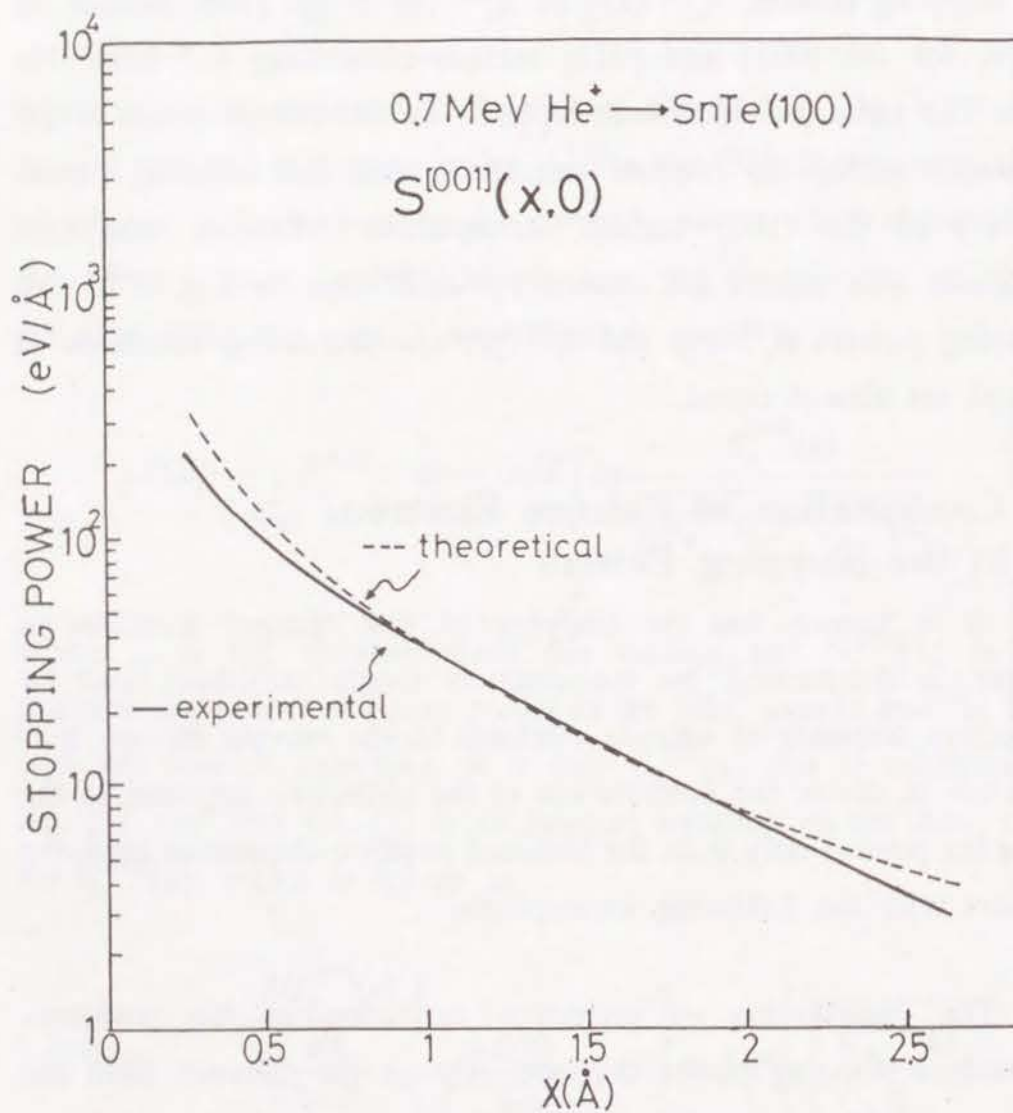
Figure 5.7(a): Position–dependent stopping powers $S_a^{[0kl]}(x,0)$ of the (100) surface for 0.7 MeV He ions. [001] atomic row.
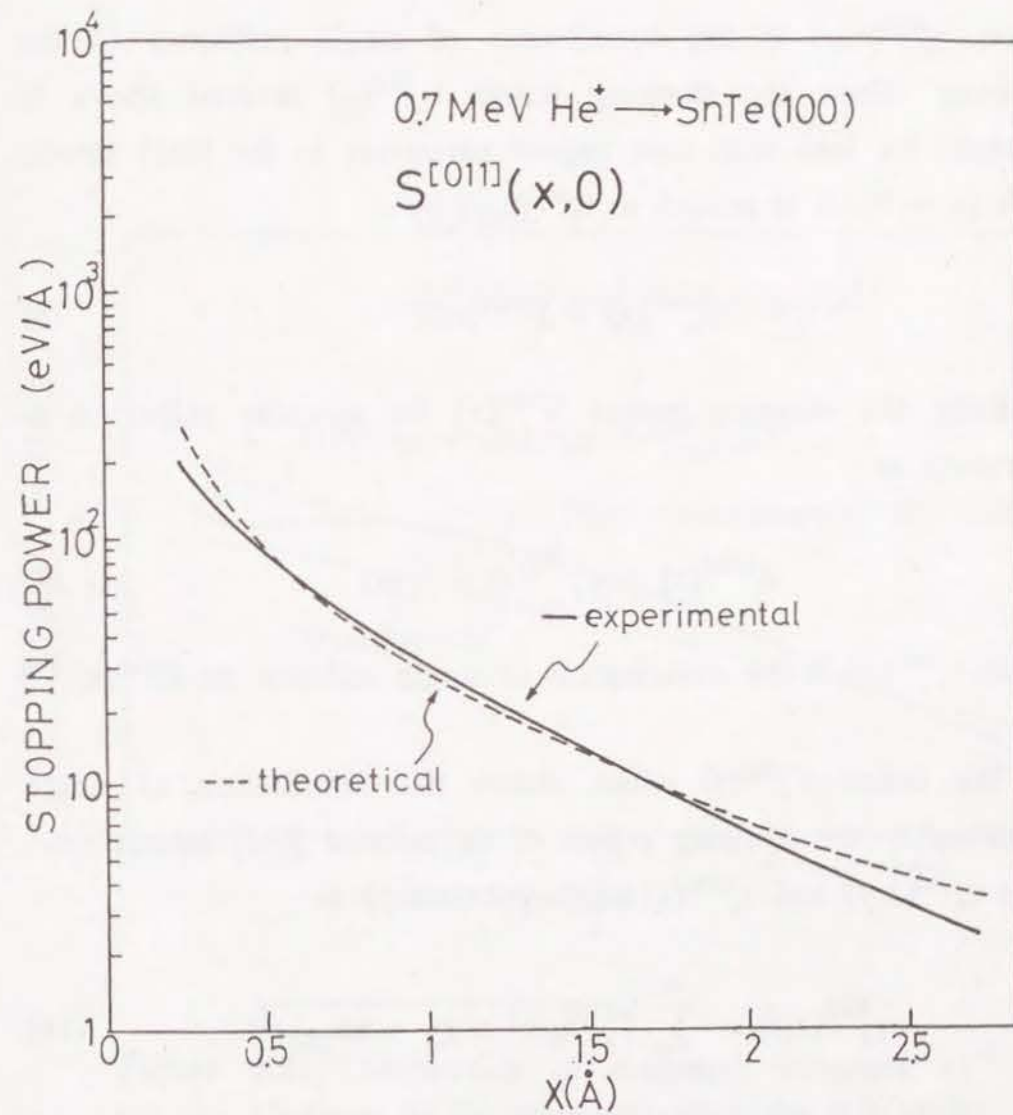
Figure 5.7(b): Position–dependent stopping powers $S_a^{[0kl]}(x,0)$ of the (100) surface for 0.7 MeV He ions. (b) [011] atomic row.

$$S^{[0kl]}(x,y) = \gamma_s^{[0kl]}(x,y) + \gamma_c(x) \quad , \qquad (7)$$

where $\gamma_s^{(0kl)}(x,y)$ is the contribution of single collisions to the stopping. Since the stopping power $S_a^{[0kl]}(x)$ derived above is obtained for ions with zero impact parameter to the [0kl] atomic rows $(y = 0)$, it is related to $S^{[0kl]}(x,y)$ by

$$S_a^{[0kl]}(x) = S^{[0kl]}(x,0) \quad . \qquad (8)$$

Similarly the stopping power $S^{(100)}(x)$ for specular reflection is expressed as

$$S^{(100)}(x) = \gamma_s^{(100)}(x) + \gamma_c(x) \quad , \qquad (9)$$

where $\gamma_s^{(100)}(x)$ is the contribution of single collision to $S^{(100)}(x)$.

(3) We define $\Gamma_s^{[0kl]}(r)$ which shows the contribution of single collisions to the stopping power of an isolated [0kl] atomic row. Thus $\gamma_s^{[0kl]}(x,y)$ and $\gamma_s^{(100)}(x)$ are approximated as

$$\gamma_s^{[0kl]}(x,y) = \sum_{n=-\infty}^{\infty} \Gamma_s^{[0kl]}\!\left(\sqrt{x^2 + (y + na_{[0kl]})^2}\right) \quad , \qquad (10)$$

$$\gamma_s^{(100)}(x) = \frac{1}{a_{[0kl]}} \int_{-\infty}^{\infty} dy\, \Gamma_s^{[0kl]}\!\left(\sqrt{x^2 + y^2}\right) \quad . \qquad (11)$$
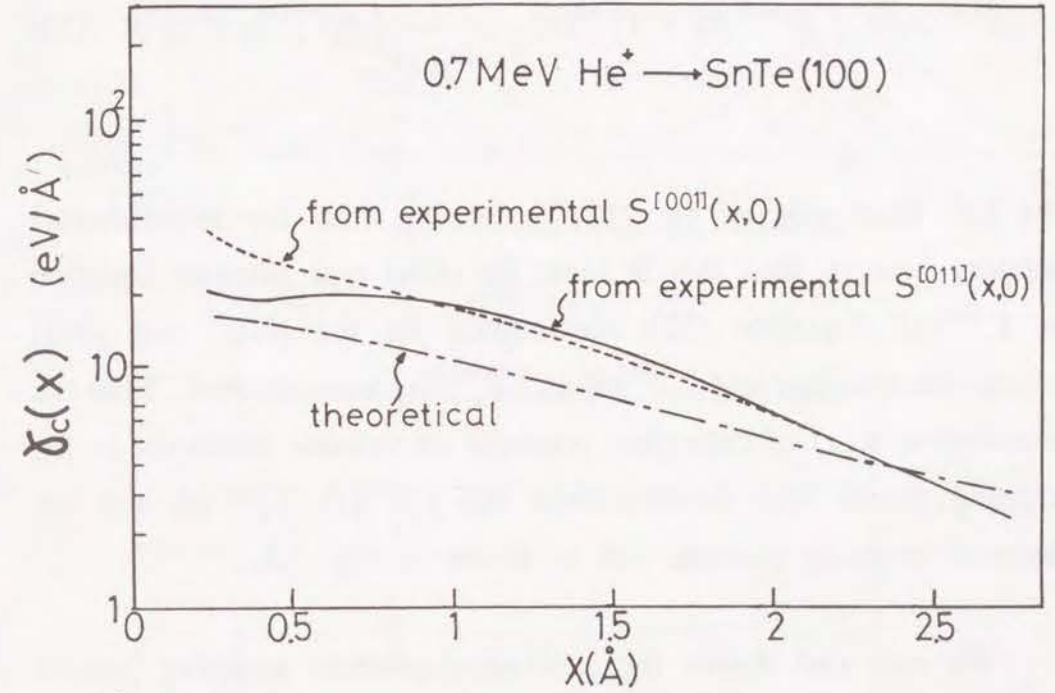
Figure 5.8: Contribution of collective response of valence electrons to the stopping power for 0.7 MeV He ion. Experimentally determined $\gamma_c(x)$ from the [001] and [011] surface–channeling are compared with the theoretical value $\gamma_c(x)$, where x is the distance from the (100) atomic plane.

Since type A trajectory is apart from the neighboring rows, we neglect their effects on $S_a^{[0kl]}(x)$ and retain only the term $n = 0$ in $\gamma_s^{[0kl]}(x,0)$ for $S_a^{[0kl]}(x)$. We then obtain an integral equation for $\Gamma_s^{[0kl]}(x)$ from Eqs. (7), (8), (9), (10) and (11);

$$S^{[0kl]}(x,0) - S^{(100)}(x) = \Gamma_s^{[0kl]}(x) - \frac{1}{a_{[0kl]}} \int_{-\infty}^{\infty} dy \Gamma_s^{[0kl]}\left(\sqrt{x^2+y^2}\right) \quad , (12)$$

The left hand side of eq. (12) is known from the experimental stopping powers, thus this is again the Abel type integral equation for $\Gamma_s^{[0kl]}(r)$. Equation (12) was solved for the [001] and [011] surface–channeling, and $\Gamma_s^{[001]}(r)$ and $\Gamma_s^{[011]}(r)$ were derived. Thus the contribution $\gamma_c(x)$ of collective response of valence electrons to the stopping power was derived from the $\Gamma_s^{[001]}(r)$, $\Gamma_s^{[011]}(r)$ and the observed stopping powers, and is shown in Fig. 5.8.

We can also derive the position–dependent stopping powers $S^{[001]}(x,y)$ and $S^{[011]}(x,y)$ from Eqs. (7) and (10) with the use of $\Gamma_s^{[001]}(r)$, $\Gamma_s^{[011]}(r)$ and $\gamma_c(x)$ obtained above. The results are shown by contours labeled in eV/Å in Fig. 5.9. Since the single ion–electron collisions dominate the stopping power near the surface at distances less than about 1.5 Å, the maxima of the stopping powers are on the atomic rows.
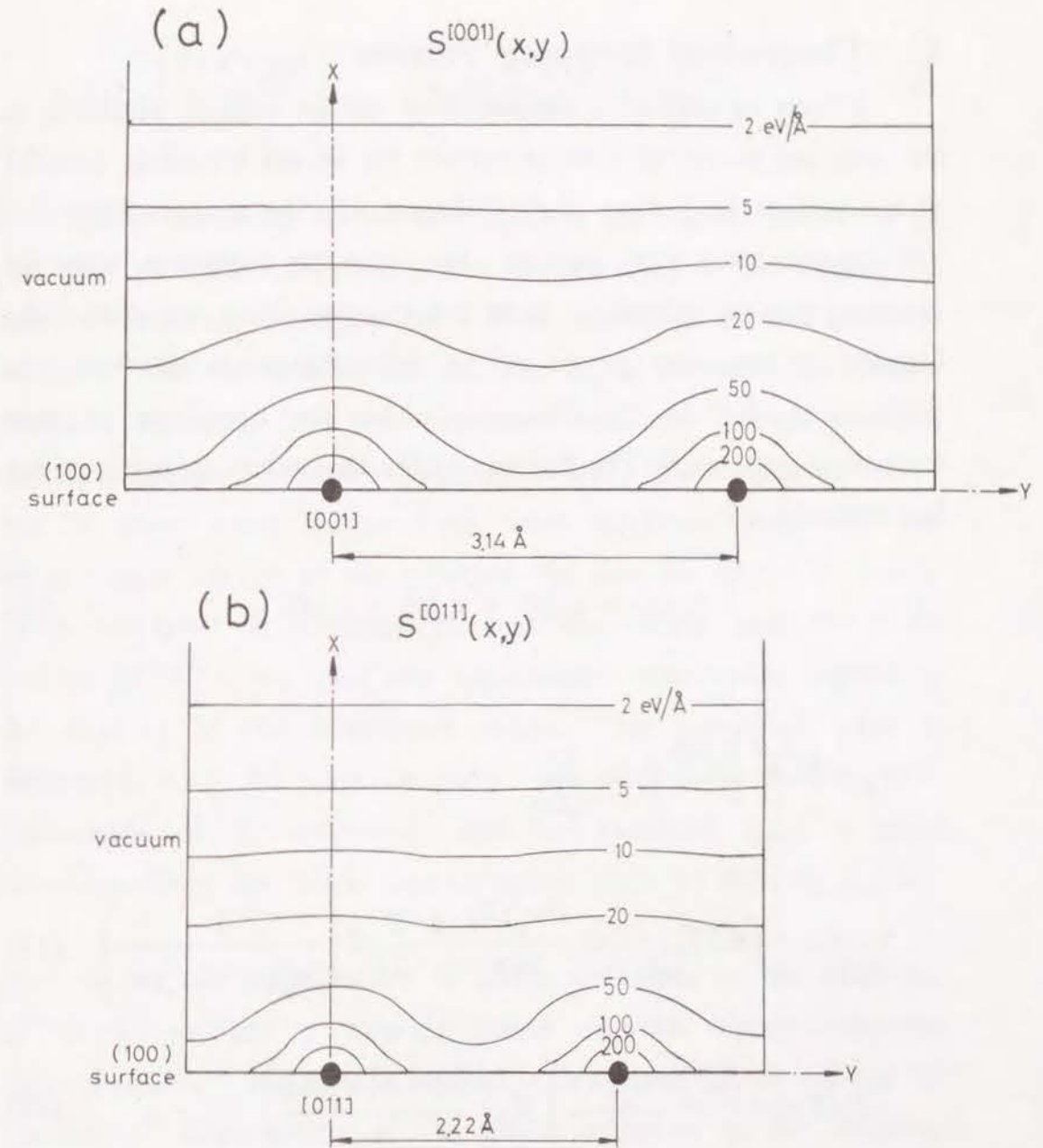
Figure 5.9: Position–dependent stopping powers $S^{[0kl]}(x,y)$ of the (100) surface of SnTe (a) at the [001] and (b) at the [011] surface–channeling for 0.7 MeV He ions. Atomic rows are shown by the full circles, and the stopping powers are shown by contours labeled in eV/Å.

C. Theoretical Stopping Powers

Effects of collective excitation of surface valence electrons to the stopping power of a metal surface for an ion travelling parallel to the surface have been studied theoretically by many authors.[7-11] The experimental $\gamma_c(x)$ derived above can be compared with the stopping powers calculated from the theories. Here we utilize the formula of stopping power of an inhomogeneous electron gas, which was derived by Kitagawa under the condition of high frequency response.[11] The formula of the theoretical stopping power is expressed as:

$$\gamma_c(x) = \gamma_b(x) + \gamma_d(x) + \gamma_r(x) \quad , \tag{13}$$

$$\gamma_b = \left(\frac{Z_p e\, \omega_p(x)}{v}\right)^2 \ln\frac{2v}{v_F(x)} \quad , \tag{14}$$

$$\gamma_{\binom{d}{r}}(x) = \int dX\, T_{\binom{d}{r}}(X,x)\, \frac{\partial \omega_p^2(X)}{2\partial X}\, \frac{x-X}{|x-X|}\, P\left(\frac{1}{\omega_p^2(x) - \omega_p^2(X)}\right) \quad , \tag{15}$$

$$T_d(X,x) = \left(\frac{Z_p e\, \omega_p(X)}{v}\right)^2 K_0\left(\frac{2|x-X|\omega_p(X)}{v}\right) \tag{16}$$

$$T_r(X,x) = -\left(\frac{Z_p e\, \omega_p(x)}{v}\right)^2 K_0\left(\frac{2|X-x|\omega_p(x)}{v}\right) \tag{17}$$

$$\omega_p(x) = \left(\frac{4\pi e^2 n_v(x)}{m}\right)^{1/2} , \quad v_F(x) = \frac{h}{m}\left(3\pi^2 n_v(x)\right)^{1/3} \quad , \tag{18}$$

here $Z_p e$ is the charge of the ion, $\omega_p(x)$ is the angular frequency of the bulk plasmon of the localized mode, $n_v(x)$ is the density of valence electrons averaged on the yz–plane, m is the mass of electron, v is the velocity of ion, and K_0 is the modified Bessel function. Equation (13) was calculated with the valence electron density calculated from the distributions of O–shell electrons of Te and Sn atoms using Hartree–Fock wave functions,[12] and with the mean square charge of the reflected He ions for $(Z_p e)^2$ ($= 3.3e^2$). Since we have no available electron distribution near the (100) surface of SnTe, we used this approximate distribution neglecting the binding of the constituent atoms. The calculated $\gamma_c(x)$ is compared with the experimentally extracted $\gamma_c(x)$ in Fig. 5.8. Agreement of the calculated and the extracted $\gamma_c(x)$ is good notwithstanding the crude approximation made in deriving $n_v(x)$.

As for the contribution of single collisions to the stopping, $\gamma_s^{[0kl]}(x,y)$, we use a formula based on the binary–encounter approximation,[13] which was derived with the use of the method by Lindhard.[14] Contribution of the single collisions to the stopping power is expressed;

$$\gamma_s^{[0kl]}(x,y) = \frac{1}{2}\left(\frac{Z_p e\, \omega^{[0kl]}(x,y)}{v}\right)^2 \cdot \ln\left(\frac{2mv^2}{\hbar\omega^{[0kl]}(x,y)}\right) \quad , \qquad (19)$$

where,

$$\omega^{[hkl]}(x,y) = \left(\frac{4\pi e^2 n^{[hkl]}(x,y)}{m}\right)^{1/2} , \qquad (20)$$

where $n^{[0kl]}(x,y)$ is the electron density averaged along the [0kl] axis. Electron density distribution $n^{[0kl]}(x,y)$ at the (100) surface was calculated with the use of Hartree–Fock wave functions. The calculated $\gamma_s^{[0kl]}(x,0)$ was added to the $\gamma_c(x)$ calculated above, and thus the theoretical stopping powers $S_a^{[0kl]}(x,0)$ for the [001] and [011] surface–channeling He ions were obtained. The results are shown by broken lines in Fig. 5.7, which agree well with the observed stopping powers shown by solid lines.

D. Energy Spectra of Surface–Channeled He Ions

In order to explain the peaks in the energy spectra of the surface–channeled He ions such as those shown in Figs. 5.2 and 5.3, trajectories of He ions were calculated and the stopping power $S^{[0kl]}(x,y)$ was integrated along the four types of trajectories as shown in Fig. 5.5. As we have expected, the type A trajectory has the least energy loss, which is approximately 15 keV smaller than the energy of the incident ion. Since the fraction of the ions of a trajectory type is inversely proportional to the gradient of the curve

at $\alpha = 0$ in Fig. 5.6, the relative heights of the peaks in an energy spectrum were determined as so. It is not shown in Fig. 5.6 but the curve crosses the line $\alpha = 0$ with larger gradients at several impact parameters larger than the parameter at the point C. The ions incident with such impact parameters have longer trajectories in the valleys or near the saddle points of the potential distribution, which result in larger energy losses.[15] Furthermore their fractions are smaller than those of type A, B, C and D trajectories. Thus they were neglected in the calculation of the spectra.

The calculated energy spectra are shown by bars in Figs. 5.2 and 5.3, where the yield of ions of type A trajectory is normalized to the least energy loss peak in the observed spectrum except for that in Fig. 5.3(a). It was not easy to fit the calculated spectra with those obtained experimentally at θ_i smaller than about 3 mrad, an example is shown in Fig. 5.3(a). Perhaps this may be caused by the experimental uncertainties in θ_i and the detection angle. However, the characteristic features of the observed energy spectra are well reproduced. This agreement shows that the derived position–dependent stopping powers $S^{[001]}(x,y)$ and $S^{[011]}(x,y)$ and thus the contribution $\gamma_c(x)$ of collective response of valence electrons to the stopping powers are reasonably accurate.

5.4. CONCLUSION

From the energy spectra of reflected He ions at the [001] and [011] surface–channeling of 0.7 MeV He$^+$ ions on the (100) surface of SnTe single crystal, the position–dependent stopping powers,

$S^{[001]}(x,y)$ and $S^{[011]}(x,y)$, of the (100) surface for the [001] and [011] surface–channeling 0.7–MeV He ions were determined. Peak structure of the energy spectra of the He ions reflected from the surface was fairly explained by the stopping powers. Contribution of collective response of valence electrons to the position–dependent stopping powers, $\gamma_c(x)$, was derived first time from the experimental position–dependent stopping powers. This agreed well with the theories where the dynamical response of valence electrons to the first moving ions is taken into account.

REFERENCES

1) K. Kimura, M. Hasegawa and M. Mannami, Phys. Rev. B36 (1987) 7.

2) Y. Fujii, K. Narumi, K. Kishine, K. Kimura and M. Mannami, Nucl. Instrum. and Methods B67 (1992) 82.

3) J. Lindhard, K. Danske Videnskab. Selsk. Mat. –Fys. Medd. 34 (1965) No. 14.

4) D. S. Gemmell, Rev. Mod. Phys. 46 (1974) 129.

5) K. Narumi, Y. Fujii, K. Kimura, M. Mannami and H. Hara, Surf. Sci.

6) Y. Fujii, S. Fujiwara, K. Kimura and M. Mannami, Nucl. Instrum. and Methods B58 (1991) 18.

7) A. A. Lucas, Phys. Rev. B20 (1970) 4990.

8) J. P. Muscat and D. M. Newns, Surface Sci. 64 (1977) 641.

9) R. Núñez, P. M. Echenique and R. H. Ritchie, J. Phys. C13 (1980) 4229.

10) R. Kawai, N. Itoh and Y. H. Ohtsuki, Surface Sci. 114 (1982) 137.

11) T. Kitagawa, Nucl. Instrum. and Methods B33 (1988) 409.

12) H. Herman and S. Skillman, Atomic Structure Calculations, N. J. Prentice–Hall, 1968.

13) J. J. Thompson, Phil. Mag. 23 (1912) 419.

14) J. Lindhard and M. Scharff, K. Danske Videnskab. Selsk. Mat.

-Fys. Medd. 27, No. 15 (1953).

15) W. Takeuchi and Y. Yamamura, Nucl. Instrum. and Methods B33 (1988) 425.

Chapter 6

CHARGE-STATE DISTRIBUTION OF MeV He IONS SPECULARLY REFLECTED FROM A SnTe(100) SURFACE

ABSTRACT

Charge state distributions of scattered ions were measured at glancing angles of incidence for MeV He ions incident on a clean (100) surface of a single crystal of SnTe under UHV conditions. Most of the features of the scattering-angle dependence of the charge state distribution of the He ions which are reflected from the topmost atomic layer of the crystal are explained in terms of the position-dependent charge exchange probabilities which are calculated from Bohr and Bohr-Lindhard models. The increase of the He^+ fraction of the ions scattered at angles smaller than the specular reflection angle is attributed to scattering at surface steps.

6.1. INTRODUCTION

For ion transmission through a thin single crystal along a planar channel, the energy loss of an ion is determined by the position–dependent stopping power.[1] We have shown in our previous studies that the charge state distribution of the channeled ions is also explained with the use of position–dependent electron–loss and –capture probabilities, *i.e.*, probabilities which depend on the position of ion relative to the atomic planes.[2,3] The probabilities were calculated with the use of the Bohr and Bohr–Lindhard models of electron capture and electron loss. On the other hand, a fast ion incidence at a glancing angle on an atomically flat crystal surface interacts only with atoms of the surface. Its trajectory is described approximately by the motion in a continuum planar potential due to the surface atoms as in the case of planar channeling of fast ions. The inelastic interaction of the ion with the surface takes place along a well–defined trajectory and thus the resulting excitation of the ion is expected to be described by the position–dependent excitation probability. In fact, we have shown in Chapter 4 that the energy losses of MeV He and H ions, which are specularly reflected from the (100) surfaces of NaCl–type crystal, are fairly well explained by position–dependent stopping powers.[4]

In our previous study of the charge state distribution of MeV He ions specularly reflected from a SnTe (100) surface, it was shown that the charge state distribution of the specularly reflected ions is determined by electron loss and the capture of valence electrons in the tail of the electron distribution at the crystal surface.[5] Although the charge state distributions of the specularly reflected ions were well explained with this model, the dependence of the charge state distribution on the angle of scattering could not be explained. Now we show that the charge state distributions of scattered MeV He ions incidence at glancing angles are explained in terms of position–dependent charge exchange probabilities and scattering at the surface steps.

6.2. EXPERIMENTAL PROCEDURE

A single crystal of SnTe(100) was prepared by epitaxial growth in situ by vacuum evaporation on a cleaved (100) surface of KCl which had been mounted on a high–precision goniometer in a scattering chamber whose base pressure was 3×10^{-10} Torr. A well defined 1×1 pattern from the (100) surface of SnTe was observed by RHEED. A beam of He ions from the 4 MV Van de Graaff accelerator of Kyoto University was collimated by apertures to 0.03 mm $\times$ 0.03 mm and to a divergence angle less than 0.1 mrad. For the beam incident at a glancing angle θ_i with respect to the (100) surface of SnTe, the ions scattered at an angle θ_s in a plane which contains the incident beam and the normal to the surface were chosen by a movable aperture. The acceptance angle of this aperture was 0.7 mrad for the scattered ions. The ions passing through the aperture were resolved into charge states by a magnetic analyzer and the energy spectrum of the ions of each charge state was measured by a solid state detector. The fraction of He^0 was less than 1 % for the present experimental conditions.[2]

The fractions of He$^+$ and He^{2+} ions in the beam were measured as follows. In order to avoid the effect of fluctuations in the incident beam intensity, the field of the magnetic analyzer was changed periodically so that the He$^+$ ions and He^{2+} ions reach the detector alternately. The energy spectra of He$^+$ and He^{2+} ions were registered in two memory groups of a multichannel analyzer separately. Experimental errors in the observed charge state fractions could be reduced considerably by this method.

6.3. EXPEIMENTAL RESULTS

When fast He ions are incident on a clean SnTe(100) surface at a small glancing angle, θ_i, the energy spectra of the scattered ions have an oscillatory structure.[4] We can identify the ions reflected from the surface atomic plane in this spectrum, since the ions form a peak in the energy spectrum.[7] In the following section, the fractions F_1 and F_2 of He$^+$ and He^{2+} ions in the beam, which were reflected from the surface atomic plane, are derived. Figures 6.1(a) and (b) show the dependences of the ratio F_1/F_2 on scattering-angle for incident 0.67 and 1.5 MeV He$^+$ ions, respectively. The arrow indicates the angles of specular reflection, $\theta_s = 2\theta_i$. The observed ratios of the specularly reflected ions are connected by chain lines. The observed ratios of the ions are connected by broken lines for $\theta_s < 2\theta_i$ and fine solid lines for $\theta_s > 2\theta_i$ to guide the eye. The ratio of the fractions of ions scattered at angles smaller than the angle of specular reflection $2\theta_i$ show complicated θ_s-dependence, while those at angles larger than $2\theta_i$ are almost independent of the angle of scattering θ_s.
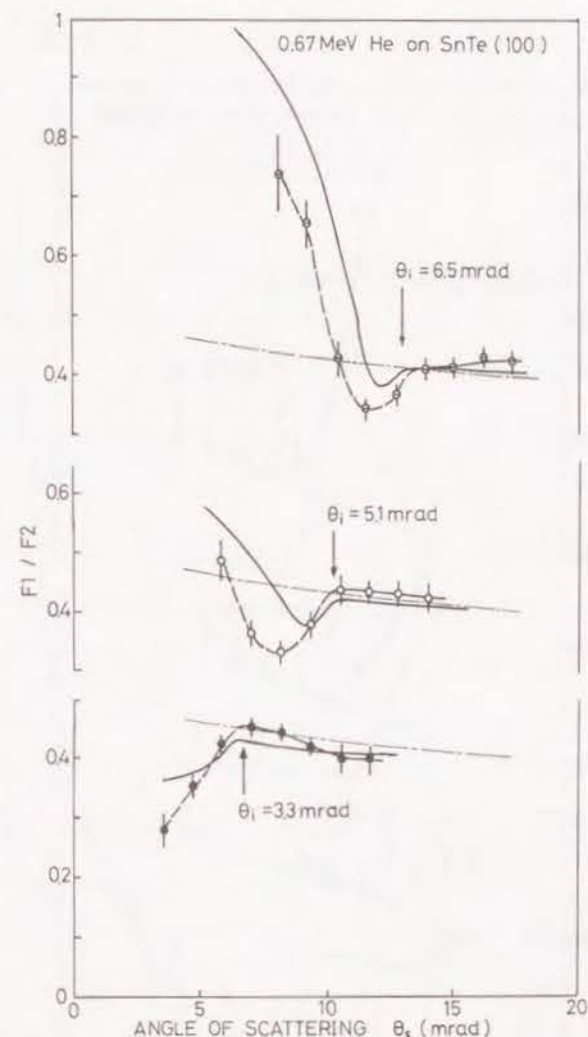
Figure 6.1(a): The ratio of the fraction of He$^+$ ions, F_1, to that of He^{2+} ions, F_2, for ions reflected from the (001) surface of SnTe as a function of the angle of scattering. The ratios for 0.67 MeV He$^+$ incident at glancing angles of 3.3 mrad (●), 5.1 mrad (○) and 6.5 mrad (○). The ratios F_1/F_2 calculated with the model are shown by solid curves.
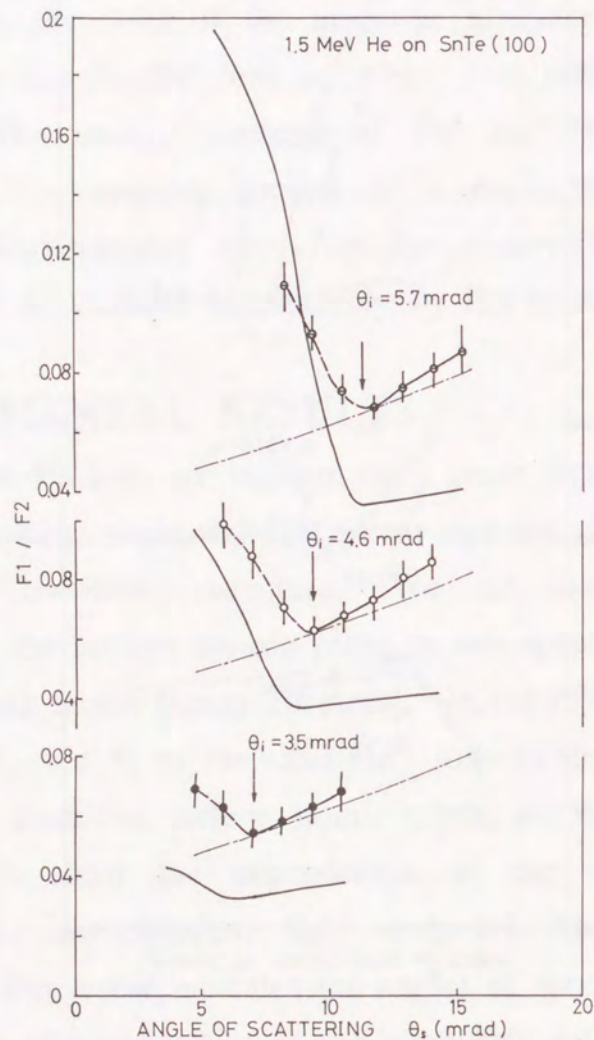
Figure 6.1(b): The ratio of the fraction of He$^+$ ions, F_1, to that of He^{2+} ions, F_2, for ions reflected from the (001) surface of SnTe as a function of the angle of scattering. The ratios for 1.5 MeV He$^+$ incident at glancing angles of 3.5 mrad (●), 4.6 mrad (○) and 5.7 mrad (○). The ratios F_1/F_2 calculated with the model are shown by solid curves.
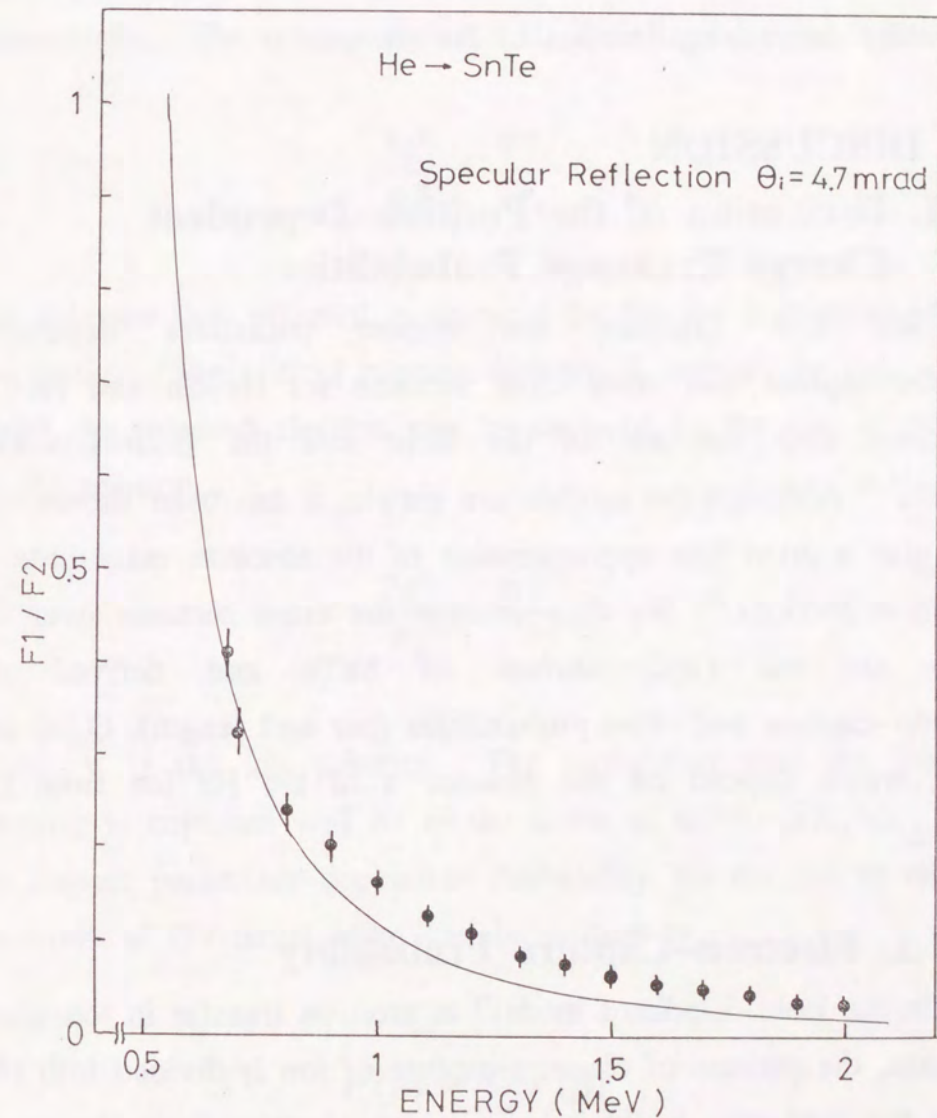
Figure 6.2: The observed energy dependence of the ratio F_1/F_2 for specularly reflected ions at an incidence glancing angle of 4.7 mrad. The calculated ratios are shown by a solid line.

Figure 6.2 shows the energy dependence of the ratio F_1/F_2 of the specularly reflected ions with an incident glancing angle of 4.7 mrad. The fraction of He$^+$ ions in the specularly reflected beam is a steadily decreasing function of He energy.

6.4. DISCUSSION

6.4.1. Derivation of the Position–Dependent Charge Exchange Probabilities

We first calculate the impact parameter dependent electron–capture and –loss cross sections for He–Sn and He–Te collisions with the use of the Bohr and the Bohr–Lindhard models.[8,9] Although the models are simple, it has been shown that they give a good first approximation of the absolute magnitude of the cross sections.[10] We then average the cross sections over the atoms on the (100) surface of SnTe and derived the electron–capture and –loss probabilities (per unit length), $Q_c(x)$ and $Q_l(x)$, which depend on the distance x of the He ion from the surface.[2,3]

6.4.1.1. Electron–Capture Probability

In the Bohr–Lindhard model[9] of electron transfer in ion–atom collision, the process of electron capture of ion is divided into two steps; the first step is the release of an electron from the target atom and the second step is the capture of the released electron by the ion. When a He^{2+} ion approaches to a target atom with an impact parameter ρ, each of the target electrons experiences the Coulomb force $2e^2/R^2$ due to the ion at distance R from it. The release of a target electron takes place when this force exceeds its binding force mv_t^2/r_t to the target nucleus, where m is the electron mass, v_t and r_t are orbital velocity and radius of the target electron, respectively. The release distance R_r is defined by the relation,

$$\frac{2e^2}{R_r^2} = \frac{mv_t^2}{r_t} .$$

The electron thus released is captured by the ion if its total energy is negative. The critical capture distance R_c around the ion, within which the released electron can be captured by the ion, is defined by the relation,

$$\frac{2e^2}{R_c} > \frac{mV^2}{2} ,$$

where V is the ion velocity. The probability that the released electron is captured will be of the order of $4/3(v_t/r_t)(R_c/V)$. Thus the impact parameter–dependent probability for the ion to capture electrons of the target atom can be written as,

$$P_c(\rho) = \sum_i P_i(\rho) , \qquad (1)$$

and

$$P_i(\rho) = \int_0^\infty dr_t \int_0^{2\pi} d\theta\, \Lambda(\rho) n_i(r_t) r_t \; , \tag{1'}$$

$$\Lambda(\rho) = \begin{cases} = \Theta(R_r - R) \, , & \text{for } R_r < R_c \, , \\[2ex] = \Theta(R_c - R) \cdot \left(\dfrac{4}{3}\right) \cdot \left(\dfrac{v_t}{r_t}\right) \cdot \left(\dfrac{R_c}{V}\right), & \text{for } R_r > R_c \, , \end{cases}$$

$$R(\rho) = \left(\rho^2 - 2\rho r_t \cos\theta + r_t^2\right)^{\frac{1}{2}} \, ,$$

where $P_i(\rho)$ is the contribution of the i-th shell target electrons, ρ is the impact parameter of He^{2+}-target atom collision, $n_i(r_t)$ is the projection of the density of electrons in the i-th shell of the target atom on the ρ-θ plane, and $\Theta(x)$ is a step function. $P_i(\rho)$ has a maximum at the crossing point $R_r = R_c$ for each respective shell electrons. This condition means that the orbital velocity of the electron which can be captured is almost the same as the ion velocity, i.e. so called velocity matching.

The dependence of the electron–capture probability per unit length for He^{2+} ion on the position x from the atomic plane of the surface is obtained from $P_c(\rho)$ as,

$$Q_c(x) = n_p \int_{-\infty}^{\infty} dy\, P_c\!\left(\sqrt{x^2 + y^2}\right) \, , \tag{2}$$

where n_p is the atomic density of the surface plane.

6.4.1.2. Electron–Loss Probability

The electron–loss probability of He^+ ions is estimated with the use of the Bohr model,[8] where the electron loss occurs by two processes; one is a collision of the ion with target electrons whose velocities are smaller than the ion velocity, and the other is a collision of the ion with target nucleus.

Firstly, the electron loss probability of He^+ ion by the collision with target electrons is calculated. In the rest frame of the ion, the ion is subjected to the bombardment of target electrons and the momenta of the target electrons are transferred to the electron of the He^+ ion. When the transferred energy exceeds the binding energy of the electron of the He^+ ion, the electron is released from the He^+. Thus the electron–loss probability, by the collision with the electrons of the target atom, can be written as a function of the impact parameter ρ of ion–atom collision

$$P_I^e(\rho) = \sum_i{}' \int_0^\infty dr_t \int_0^{2\pi} d\theta\, \Theta(b_I - R)\, n_i(r_t)\, r_t \, , \tag{3}$$

and,

$$b_I = 2a_B\left(\frac{v_B}{V}\right)^2 \left\{ \left(\frac{V}{v_I}\right)^2 - 1 \right\}^{\frac{1}{2}}$$

$$R(\rho) = \left(\rho^2 - 2\rho r_t \cos\theta + r_t^2\right)^{\frac{1}{2}} ,$$

where a_B and v_B are Bohr radius and Bohr velocity, respectively, v_I is orbital velocity of the electron in the ground state of hydrogen-like He^+, Σ' shows the sum over the shells in which the electron velocity is lower than projectile velocity, *i.e.*, only the electrons with orbital velocities lower than the ion velocity contribute to the electron-loss of He^+. Inner shell electrons contribute to the screening of target nucleus.

Secondly, the electron-loss probability of a He^+ ion by the collision with the screened target nucleus can be written as[8]

$$P_I^n(\rho) = \Theta(b_s - \rho) , \qquad (4)$$

$$b_s = \frac{a_B Z_t^{-\frac{1}{3}} v_B}{\sqrt{V v_I}} ,$$

where Z_t is the atomic number of the target atom.

The electron-loss probability of a He^+ ion is obtained by summing contributions of target electrons and of screened target nucleus and averaging the sum in the surface plane as,
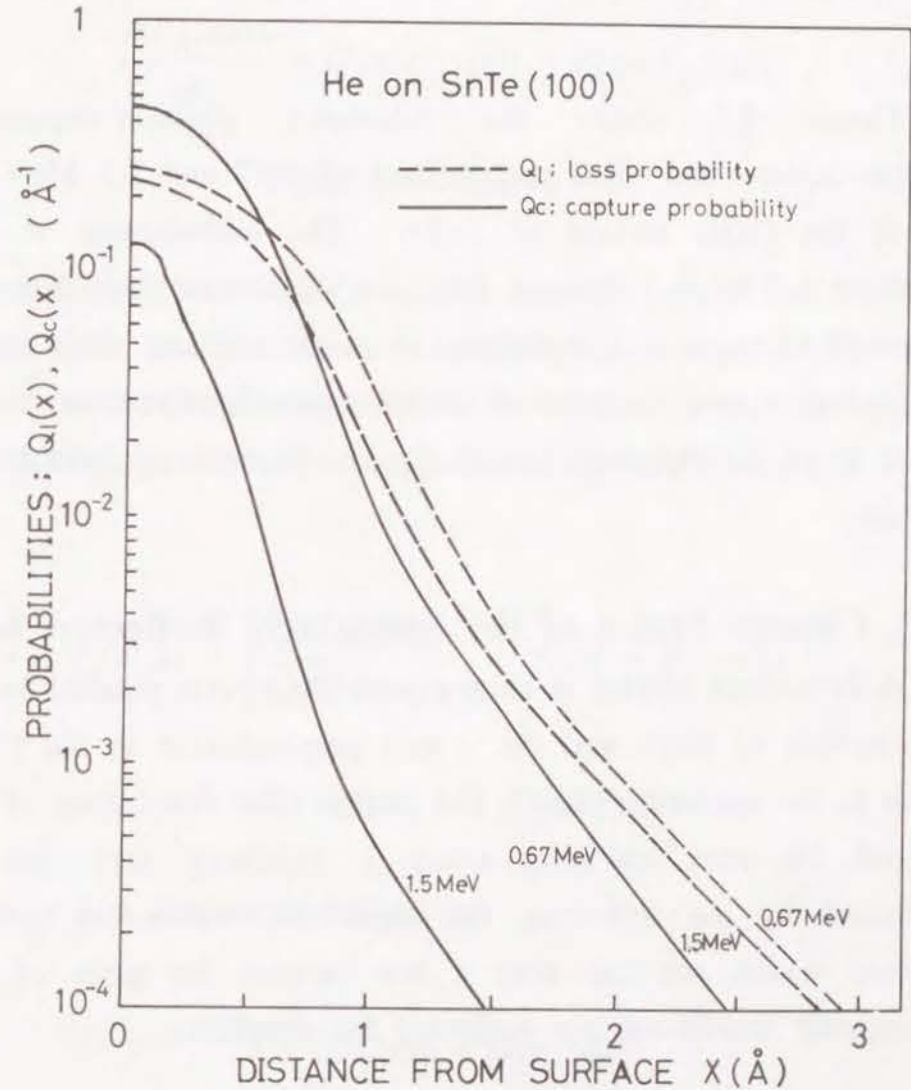
Figure 6.3: Position-dependent electron-capture and -loss probabilities, $Q_c(x)$ and $Q_l(x)$, for 0.67 and 1.5 MeV He ions at the (100) surface of SnTe.

$$Q_l(x) = n_p \int_{-\infty}^{\infty} dy \left\{ P_l^e \left(\sqrt{x^2 + y^2} \right) + P_l^n \left(\sqrt{x^2 + y^2} \right) \right\} \ . \qquad (5)$$

Figure 6.3 shows the calculated position–dependent electron–capture and –loss probabilities of 0.67 and 1.5 MeV He ions at the (100) surface of SnTe. The probabilities at one monolayer (3.14 Å) distance from the surface are less than one thousandth of those at 1 Å distance from the surface. This shows that the region near the point of closest approach of the ions to the surface plays an important role in the charge exchange process of the ions.

6.4.2. Charge States of the Specularly Reflected Ions

A coordinate system is chosen with the z–axis parallel to the (100) surface of SnTe and the x–axis perpendicular to the (100) surface in the scattering plane. The charge state distribution of the scattered He ions traveling along a trajectory x(z) can be determined by the following rate equations, where the neutral fractions, which are less than a few percent for most of our experimental conditions, are neglected for simplicity.

$$\frac{dF_1(x(z))}{dz} = Q_c(x) F_2(x(z)) - Q_l(x) F_1(x(z)) \ , \qquad (6)$$

$$\frac{dF_2(x(z))}{dz} = Q_l(x) F_1(x(z)) - Q_c(x) F_2(x(z)) \ , \qquad (6')$$

$$F_1(x(z)) + F_2(x(z)) = 1 \ , \qquad (7)$$

where $F_1(x(z))$ and $F_2(x(z))$ are the fractions of He^+ and He^{2+} ions in the beam at a distance x from the surface, respectively. Using $F_1(-\infty)$ as the initial condition for the fraction of He^+, the Eqs. (6) and (6') can be solved by integration along the trajectory (x = x(z)) as,

$$F_1(x(z)) = \int_0^s \frac{Q_c(x)}{Q_c(x) + Q_l(x)} e^{s'-s} ds' + F_1(-\infty) e^{-s} \ , \qquad (8)$$

$$F_2(x(z)) = 1 - F_1(x(z)) \ ,$$

where s is a parameter defined as

$$s = \int_{-\infty}^{z} \left(Q_c(x) + Q_l(x) \right) dz' \ . \qquad (9)$$

If the ion trajectory is a straight line parallel to the surface, *i.e.*, $x(z)$ is a constant x, the fractions F_1 and F_2 are equilibrated and become constants (F_1^{eq} and F_2^{eq} at $z \longrightarrow \infty$) which depend on the position x from the surface;

$$F_1^{eq}(x) = \frac{Q_c(x)}{Q_c(x) + Q_l(x)} \quad , \tag{10}$$

$$F_2^{eq}(x) = \frac{Q_l(x)}{Q_c(x) + Q_l(x)} \quad . \tag{10'}$$

Thus the ratio of the fractions at charge state equilibrium can be expressed by the charge exchange probabilities as,

$$\frac{F_1^{eq}(x)}{F_2^{eq}(x)} = \frac{Q_c(x)}{Q_l(x)} \quad . \tag{11}$$

Equation (11) was evaluated for 0.67 MeV and 1.5 MeV He⁺ ions at the (100) surface of SnTe crystal, and the results are shown by the chain curves in Fig. 6.4. The x–dependence of the ratio $F_1^{eq}(x)/F_2^{eq}(x)$ depends on ion energy. There is a tendency that the ratio is larger near the surface and becomes smaller at larger distances.
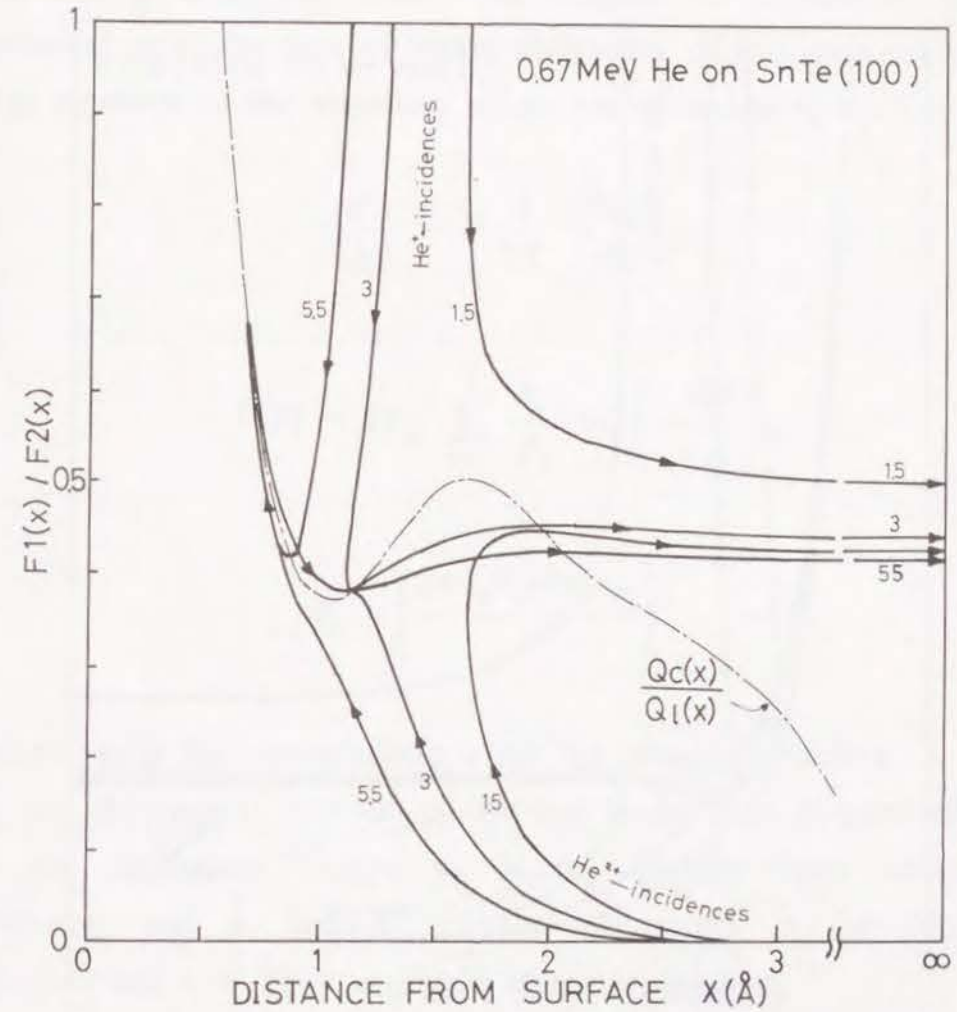
Figure 6.4(a): Change in the ratio $F_1(x)/F_2(x)$ of He ions for a few trajectories of specular reflection is shown as a function of the distance from the (100) surface of SnTe. The angle of incidence, θ_i^{in} mrad, of the He ions is indicated at the curve. The equilibrium ratio, $F_1^{eq}/F_2^{eq} = Q_c(x)/Q_l(x)$, is shown by a chain curve for comparison. Incident 0.67 MeV He⁺ and He²⁺ ions.
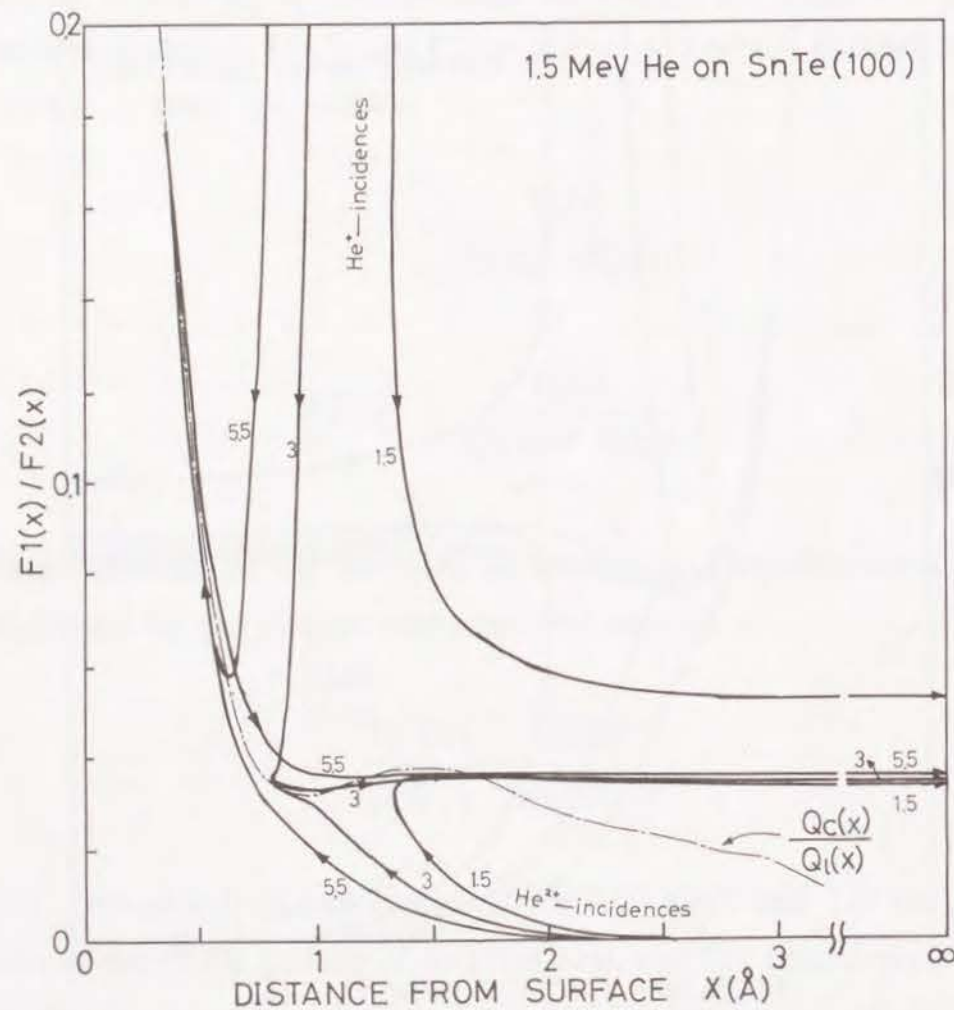
Figure 6.4(b): Change in the ratio $F_1(x)/F_2(x)$ of He ions for a few trajectories of specular reflection is shown as a function of the distance from the (100) surface of SnTe. The angle of incidence, θ_i^{in} mrad, of the He ions is indicated at the curve. The equilibrium ratio, $F_1^{eq}/F_2^{eq} = Q_c(x)/Q_1(x)$, is shown by a chain curve for comparison. Incident 1.5 MeV He$^+$ and He^{2+} ions.

For the potential describing glancing angle scattering of MeV He ions at a crystal surface, we adopted the continuum planar potential as in the case of planar channeling of ions in a crystal.[11] The equation of the trajectory of an ion of energy E is,

$$\frac{d^2x}{dz^2} = -\frac{1}{2E} \cdot \frac{dV(x)}{dx} , \tag{12}$$

$$V(x) = E\psi_a^2 \sum_{i=1}^{3} \frac{\alpha_i}{\beta_i} \cdot \exp\left(-\frac{\beta_i x}{a_{TF}}\right) , \tag{13}$$

$$\psi_a = \left(\frac{2\pi Z_1 Z_2 e^2 n_p a_{TF}}{E}\right)^{\frac{1}{2}} , \tag{14}$$

where ψ_a is the characteristic angle for planar channeling, Z_1 and Z_2 are the atomic numbers of ion and target atom respectively, e is the elementary charge, a_{TF} is the Thomas–Fermi screening distance, and α_i and β_i are the parameters in the Molière approximation to Thomas–Fermi screening function.[12]

The charge state fractions of He ions along trajectories of specular reflection, which start at $z = -\infty$ and $x = \infty$, were calculated and a few examples of the results are shown in Fig. 6.4, where the ratios of the fractions $F_1(x)/F_2(x)$ are plotted against the distance x of the ion from the surface. Angles of incidence of the He ions are indicated near the curves in mrad. For He$^+$ incident ($F_1(\infty) = 1$) and He^{2+} incident ($F_1(\infty) = 0$) with angles of

incidence $\theta_i > 3$ mrad, the ratios coincide with the chain curve at the closest approach of the ions to the surface. Negligible change in the ratios occurs on the receding trajectories at distances more than 2 Å from the surface. At glancing angles less than about 2.5 mrad, the ratios depend on the initial charge state and do not coincide with each other even at the closest approach. The following conclusions are drawn from the calculated ratios for incident MeV He ions with glancing angles larger than about 2.5 mrad:

(A) The charge state fractions of the reflected ions are independent of the charge of the incident ions.

(B) At the closest approach of the ions to the surface, charge exchange collisions are so frequent along the trajectories that local equilibrium of the charge states is attained. Since the trajectory is parallel to the surface at the closest approach and the parallel section of the trajectory is longer than the mean free path for charge exchange collisions, $1/(Q_c + Q_l)$, the fractions of ions are equilibriated at the closest approach.

(C) The charge state fractions of the specularly reflected ions are nearly equal to the charge state fractions of ions at one monolayer distant from the surface for the receding trajectories.
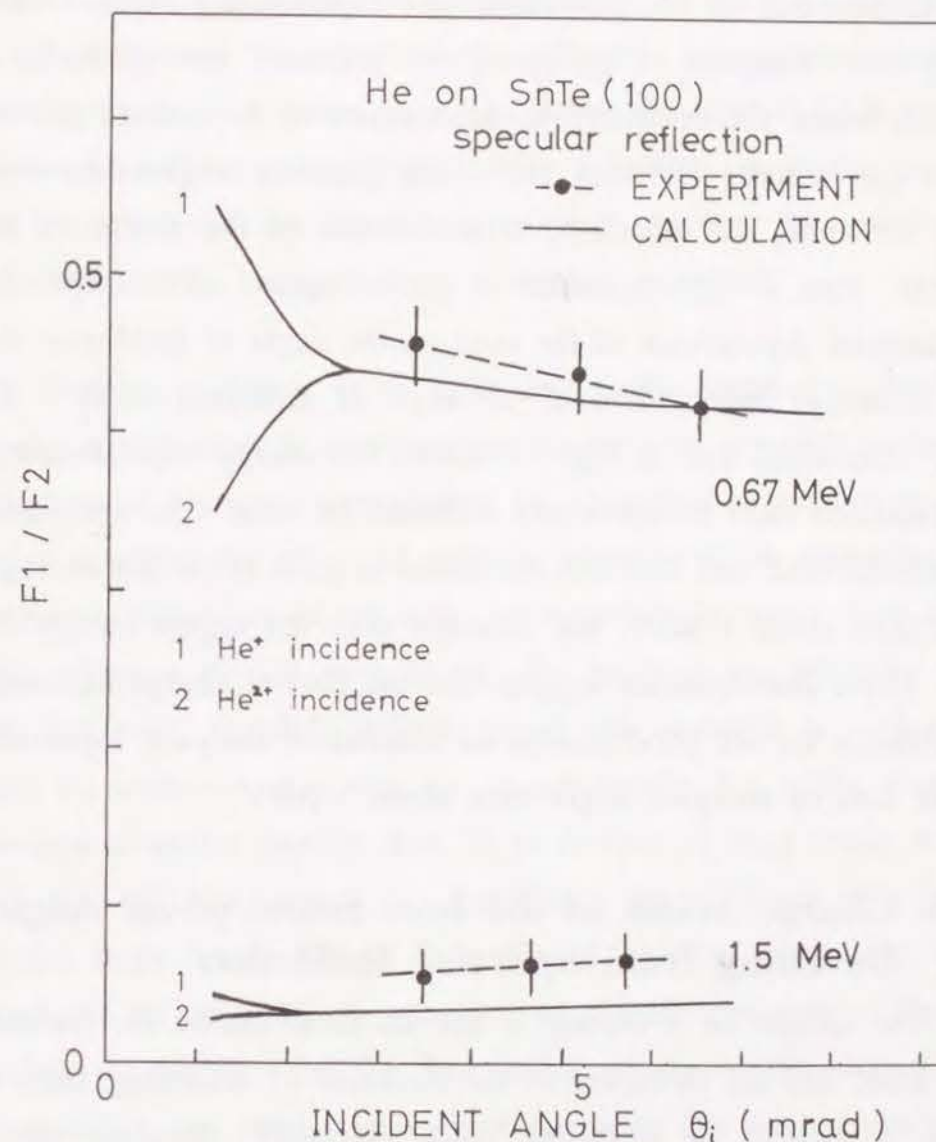
Figure 6.5: The ratios of the charge state fractions of specularly reflected He ions as a function of the incident glancing angle. The dashed curves connect the experimental ratios and the solid curves show the calculated ratios. At angles of incidence less than about 2.5 mrad, the ratios for He^+ and He^{2+} incident do not coincide and are labeled by 1 and 2, respectively.

Comparison of the calculated and experimental ratios of the charge state fractions of the specularly reflected ions is made in Fig. 6.5, where the calculated θ_i-dependence of the ratios F_1/F_2 are shown for incident He^+ and He^{2+}. At glancing angles less than about 2.5 mrad, the calculated ratio depends on the charge of the incident ions. The calculated ratios agree well with the experimental dependence of the ratio on the angle of incidence; the ratio is almost independent of the angle of incidence at $\theta_i > 2.5$ mrad. The solid line in Fig. 6.3 shows the energy dependence of the calculated ratio for specularly reflected He ions. The agreement of the calculated and experimental ratios is good at He ion energies lower than about 1 MeV, but becomes poor for higher energy He ions. These discrepancies suggest that the present charge exchange probabilities are not good enough for quantative analyses, especially for He ions of energies larger than about 1 MeV.

6.4.3. Charge States of the Ions Scattered at Angles Deviating from Specular Reflection

The surface of a crystal is not an ideal mirror for incident MeV ions, and the deviation of the direction of scattering from θ_s = $2\theta_i$ is caused by collisions with thermally vibrating atoms (nuclear scattering), electrons (electronic scattering) and surface irregularities. The angular deviations of an ion due to single scattering events by nuclear and electronic scatterings are small and take place frequently near the surface. Due to multiple small angle scatterings, an ion on a trajectory defined by the glancing angle θ_i is gradually scattered away from the trajectory and finally scattered

to the angle θ_s ($\neq 2\theta_i$). The final trajectory of the ion corresponds to the trajectory of a specularly reflected ion incident with a glancing angle θ_i' ($= \theta_s - \theta_i \neq \theta_i$). Since the ratio F_1/F_2 is almost independent of trajectory for specular reflection as shown in Fig. 6.5, the observed θ_s-dependence of F_1/F_2 at $\theta_s < 2\theta_i$ cannot be explained on the basis of these scattering processes.

We have shown from a Monte Carlo simulation that the angular distribution of scattered ions incident at glancing angles on a surface of a crystal is explained by scattering at surface steps.[13] Let us consider the effect of steps on glancing angle scattering. If the mean separation of the steps on a surface is larger than about a_o/θ_i, where a_o is the step height, the incident ion interacts with only one step. Possible trajectories of ions (incident at a glancing angle θ_i) scattered at a step are shown in Fig. 6.6. The ions are scattered at angles smaller than $2\theta_i$ at downward steps (cases A and B in Fig. 6.6), while they are scattered at angles larger than $2\theta_i$ at upward steps (cases C and D in Fig. 6.6). Ion trajectories were calculated by changing the position of closest approach of the ion relative to the step for the four cases shown in Fig. 6.6. Using these results the charge state fractions along the trajectories were calculated. The solid curves in Fig. 6.7 show the calculated results of the θ_s-dependencies of the ratios F_1/F_2 of the ions scattered at steps for MeV He^+ ions incident at a glancing angle of 5 mrad. The dashed curves show the ratios F_1/F_2 for the specularly reflected ions with incident angle $\theta_i = \theta_s / 2$. Except for case A, the ratios of the fractions F_1/F_2 are not much different from the dashed curves.
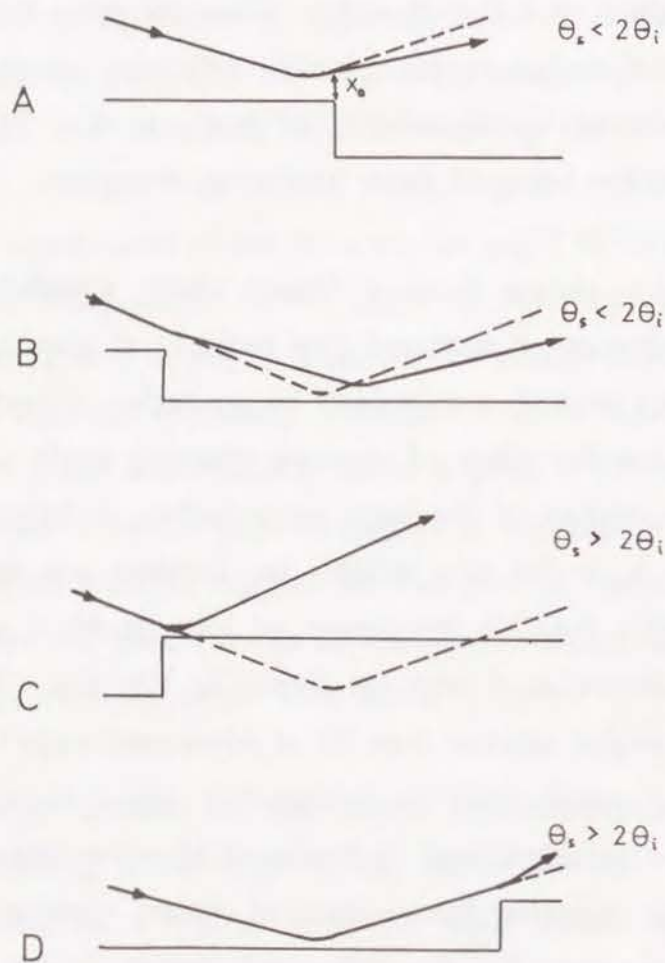
Figure 6.6: Possible trajectories of ions scattered at a surface step. A and B show the scattering at a downward step where the ions are scattered at angles smaller than those of specular reflection. C and D show the scattering at an upward step where the ions are scattered at angles larger than those of specular reflection. The dashed curves show specular reflection at a flat surface.
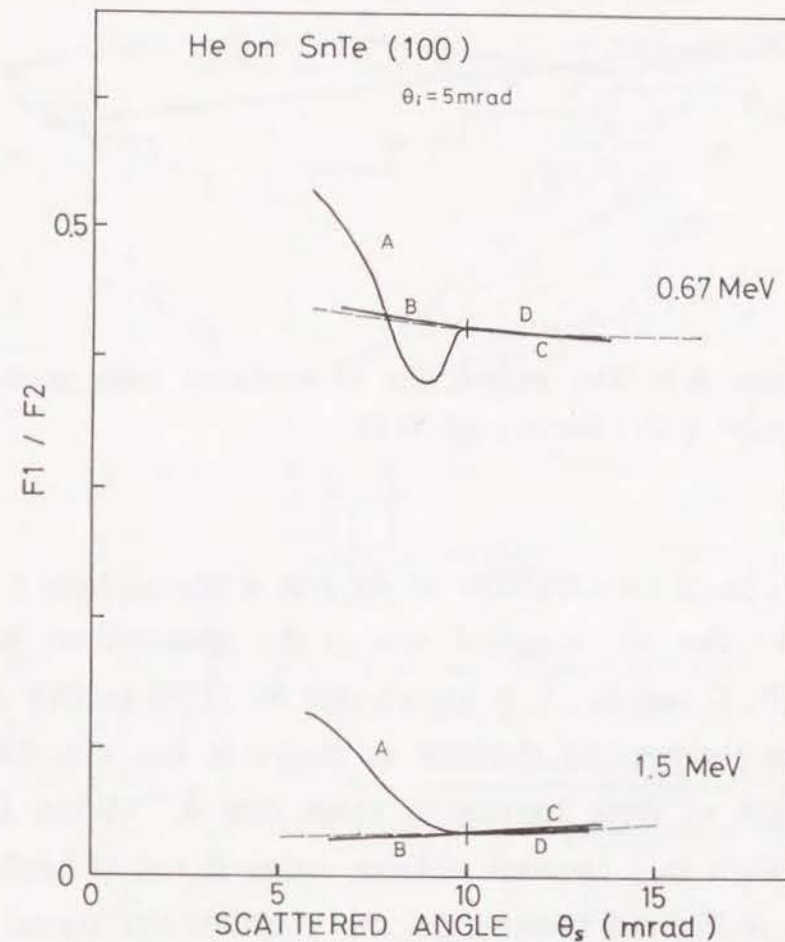
Figure 6.7: The calculated θ_s-dependencies of the ratios F_1/F_2 for 0.67 and 1.5 MeV He ions scattered at a step for an angle of incidence of $\theta_i = 5$ mrad. A, B, C and D show the ratios corresponding to the trajectories shown in Fig. 6.6. The dashed curves show the ratios of the charge state fractions of the specularly reflected ions for incident glancing angles of $\theta_s/2$.
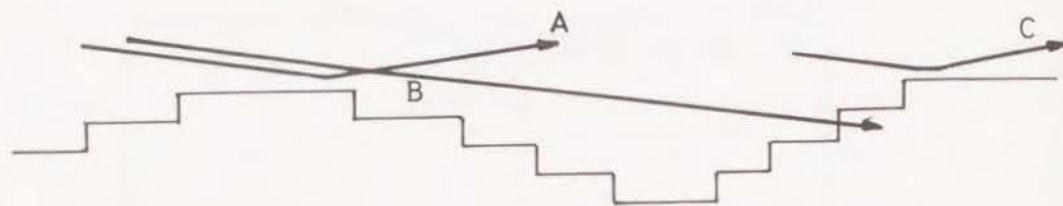
Figure 6.8: The trajectories of scattered ions at the terraced (001) surface of SnTe.

The charge state fractions of the ions scattered from a stepped surface are thus the weighted sum of the contributions from the cases A, B, C and D. It is known that the (100) surface of SnTe crystal has the terraced structure as shown in Fig. 6.8, where the mean length of these terraces is about 600 Å.[14] When ions are scattered from such terraced surfaces, cases B and D hardly occur as shown in Fig. 6.8 because the ions penetrate the crystal surface at the steps. Accordingly cases A and C are possible and the dependence of F_1/F_2 on angle of scattering must be that given by curves A and C in Fig. 6.7. The ratios F_1/F_2 calculated with this model are shown by solid lines in Fig. 6.1. Numerical agreement is again poor for 1.5 MeV He ions, however, these calculated ratios reproduce the observations for incident 0.67 MeV He ions.
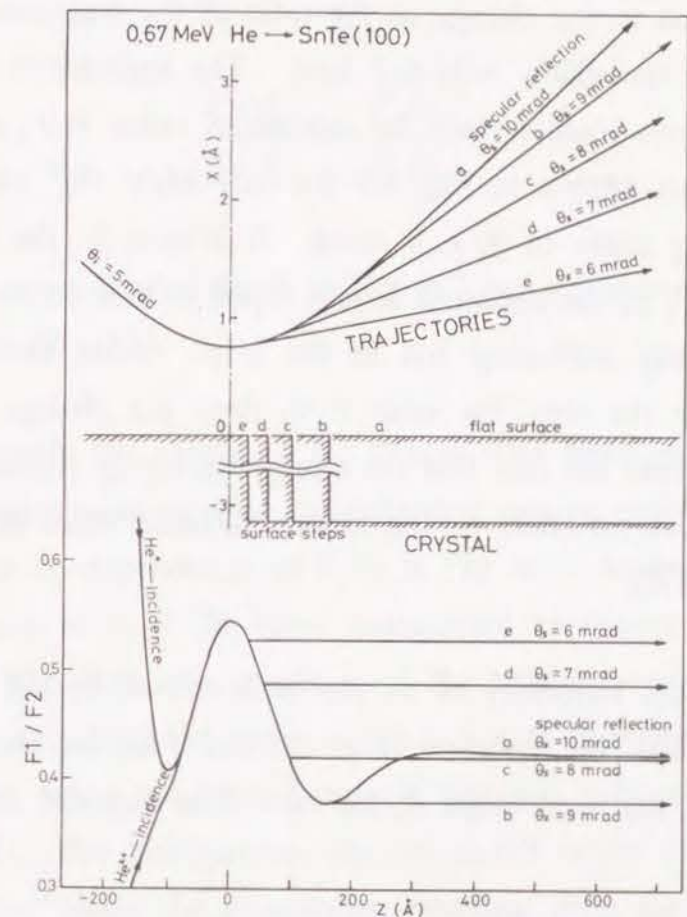
Figure 6.9: The trajectories (of type A in Fig. 6.6) of scattered ions at steps, and the changes in the ratios of the calculated charge state fractions of 0.67 MeV He ions on the trajectories. The trajectories are labeled by a to e. The closest approach of the ions to the surface are at z = 0. The angles θ_s of scattering are shown on the trajectories (the angle of incidence is 5 mrad).

6.4.4. Charge State Distributions of the Trajectories of He Ions at Specular Reflection

It is interesting to note that the curves labeled by A in Fig. 6.7 are related to the change in the ratio of the fractions along the trajectory of specularly reflected ions. The trajectories of ions at downward steps (case A) and the calculated ratios F_1/F_2 along these trajectories are shown in Fig. 6.9 for 0.67 MeV He$^+$ ions incident at a glancing angle of $\theta_i = 5$ mrad. It is seen in the figure that the ratio F_1/F_2 of the scattered ions is equal to that on the trajectory of a specularly reflecting ion at the step. After the ions have passed above the step, the ratio F_1/F_2 does not change. This is understood from the fact that the charge exchange probabilities are small and have no effect on the ion at distances more than the step height (3.14 Å).

When the trajectory of an ion is described by the continuum planar potential, the distance x_o of the ion from the surface at the step and the scattered angle θ_s for case A in Fig. 6.6 is related by

$$x_o = \frac{a_{TF}}{\beta_3} \cdot \ln\left(\frac{\alpha_3}{\beta_3} \cdot \frac{\psi_a^2}{\theta_s \cdot (2\theta_i - \theta_s)} \right), \tag{15}$$

where the first and second terms of the right hand side of Eq. (13) are neglected in the trajectory calculation, and the trajectory, after passing over the step, is assumed to be a straight line. This is a reasonable assumption because the errors of θ_s due to these approximations are less than 1 % for 0.67 MeV He ions incidence

with a glancing angle of 7 mrad. Charge exchange hardly occurs along the straight line trajectories, and the charge states of the ions at a x_o distance from the surface at the step are retained by the scattered ions;

$$\frac{F_1(\theta_s)}{F_2(\theta_s)} = \frac{F_1(x_o)}{F_2(x_o)} . \tag{16}$$

The solid curves labeled by A in Fig. 6.7 can be derived using this relation and Eq. (15).

Conversely the change in the charge state fractions of the ions along the trajectories of specular reflection can be derived from the experimental θ_s-dependence of F_1/F_2 in Fig. 6.1. Assuming that the ions scattered at $\theta_s < 2\theta_i$ have trajectories as shown in Fig. 6.9 (case A in Fig. 6.6), the height x_o of the trajectory of an ion at a step is obtained from the angle of scattering θ_s with the use of Eq. (15). These ratios are plotted against distance x from the surface in Fig. 6.10. For comparison, the calculated ratios of the charge state fractions along the trajectories receding from the surface are shown in Fig. 6.10. Agreement of the calculated and observed ratios for 1.5 MeV incident He is poor, however the features of the dependences of the observed ratios are similar to those of the calculated ratios. Good agreement was obtained for 0.67 MeV incident He.
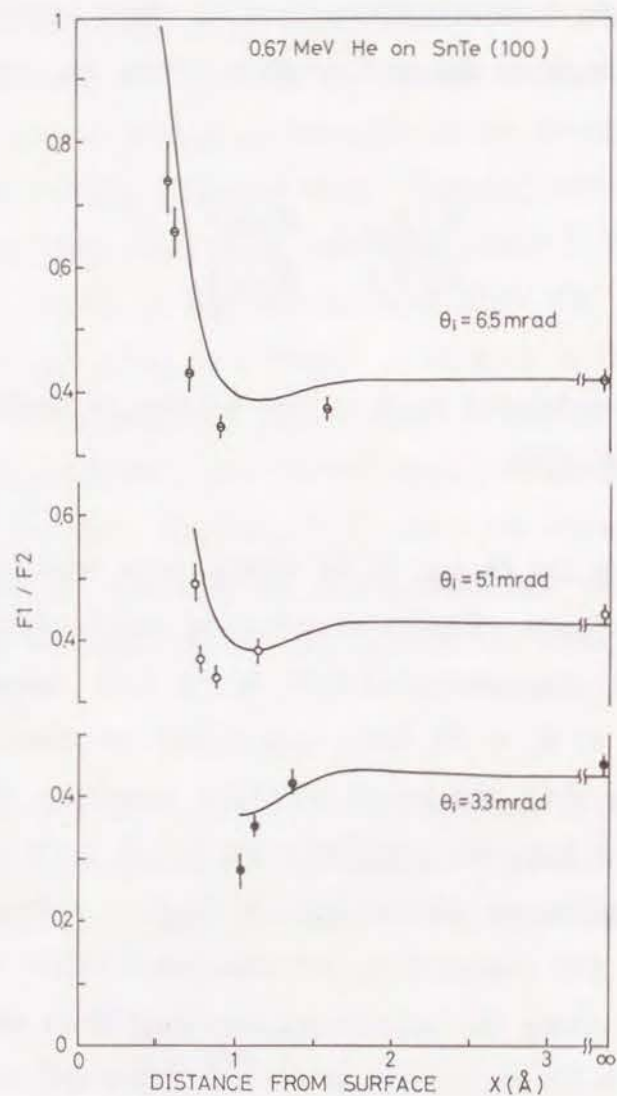
Figure 6.10(a): The change in the experimental ratio $F_1(x)/F_2(x)$ with the trajectory of specularly reflecting He ions. Solid lines show the ratios calculated from the theoretical position–dependent charge exchange probabilities, for 0.67 MeV He incident on the (100) surface of SnTe.
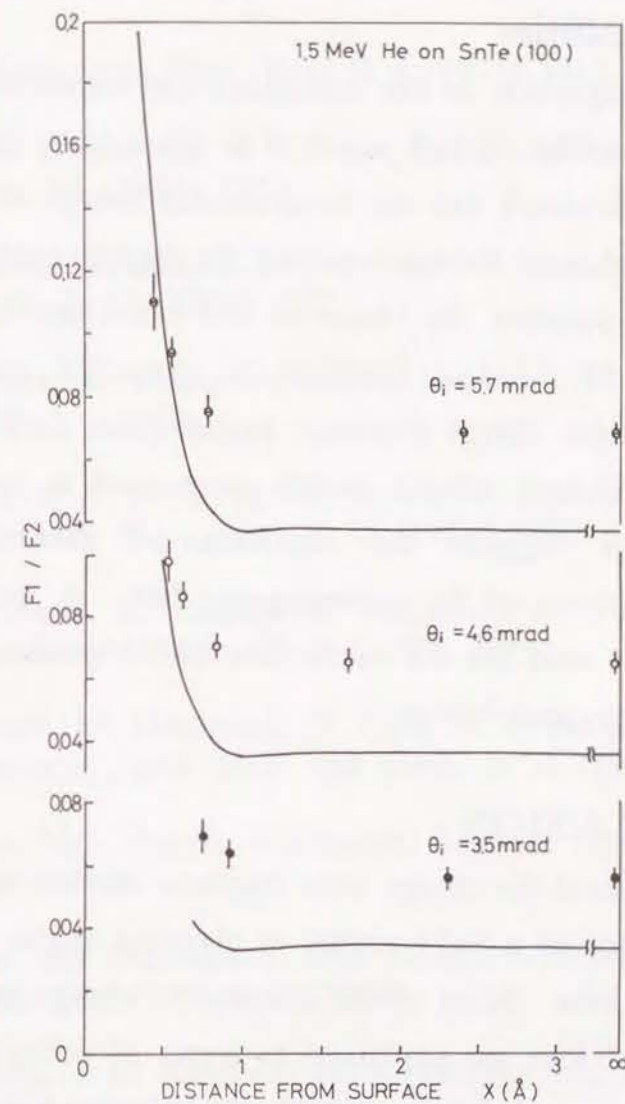
Figure 6.10(b): The change in the experimental ratio $F_1(x)/F_2(x)$ with the trajectory of specularly reflecting He ions. Solid lines show the ratios calculated from the theoretical position–dependent charge exchange probabilities, for 1.5 MeV He incident on the (100) surface of SnTe.

6.4.5. Position-Dependent Charge Exchange Probabilities

In the comparison of the calculated and experimental charge state fractions in Figs. 6.1, 2 and 5, it is shown that the agreement between the calculated and the experimental charge state fractions of reflected He^+ ions becomes poorer for higher energy He ions. A discrepancy between the observed and calculated fractions was also observed in the He^+ fractions of channeled ions,[2,3] where position-dependent charge exchange probabilities derived from the Bohr and the Bohr-Lindhard models were used as in the present analysis. This suggests the limitations of these models for quantitative analysis of the experimental data. A more elaborate theory must be used for the calculation of the position-dependent charge exchange probabilities.

6.5. CONCLUSION

We measured the charge state fractions of ions scattered from the (100) surface of a SnTe crystal at glancing angles of incidence for MeV He^+ ions. Most of the features of charge state fractions of the reflected ions are explained in terms of position-dependent charge exchange probabilities, which are calculated from the Bohr and the Bohr-Lindhard models. It is shown that surface steps can influence the observed charge state distribution of the scattered ions, especially for ions scattered at angles smaller than the angle of specular reflection.

REFERENCES

1) M. T. Robinson, Phys. Rev. B 4 (1971) 1461.

2) Y. Fujii, K. Sueoka, K. Kimura and M. Mannami, J. Phys. Soc. Jpn. 58 (1989) 2758.

3) Y. Fujii, K. Sueoka, K. Kimura and M. Mannami, Nucl. Instr. and Meth. B 48 (1990) 121.

4) K. Kimura, M. Hasegawa and M. Mannami, Phys. Rev. B 36 (1987) 7.

5) K. Kimura, Y. Fujii, M. Hasegawa, Y. Susuki and M. Mannami, Phys. Rev. B 38 (1988) 1052.

6) M. Mannami, K. Kimura, K. Nakanishi and A. Nishimura, Nucl. Instr. and Meth. B 13 (1986) 587.

7) K. Kimura, M. Hasegawa, Y. Fujii, M. Suzuki, Y. Susuki and M. Mannami, Nucl. Instr. and Meth. B 33 (1988) 358.

8) N. Bohr, Kgl. Danske Videnskab. Selskab. Mat. Fys. Medd. 18 No.8 (1948).

9) N. Bohr and J. Lindhard, Kgl. Danske Videnskab. Selskab. Mat. Fys. Medd. 28 No.7 (1954).

10) For instance, H. Knudsen, H. K. Haugen and P. Hvelplund, Phys. Rev. A 23 (1981) 597.

11) J. Lindhard, Kgl. Danske Videnskab. Selskab. Mat. Fys. Medd. 34 No.14 (1965).

12) D. S. Gemmell, Rev. Mod. Phys. 46 (1974) 129.

13) M. Mannami, Y. Fujii and K. Kimura, Surf. Sci. 204 (1989) 213.

14) Y. Fujii, K. Kimura, M. Hasegawa, M. Suzuki, Y. Susuki and M. Mannami, Nucl. Instr. and Meth. B 33 (1988) 405.

Chapter 7

INTERPLAY OF CHARGE EXCHANGE AND ENERGY LOSS OF MeV He IONS SPECULARLY REFLECTED FROM A CRYSTAL SURFACE

ABSTRACT

Charge state distributions and energy losses of MeV He ions scattered from a clean (100) surface of SnTe single crystal are studied at glancing angle incidence. A stochastic model of charge exchange and energy loss of ions is developed, where inelastic interactions depend on the distance of the ion from the surface. Observed charge state fractions and energy losses of the reflected He ions are explained with the model. Taking account of scattering of ions at surface steps, which gives rise to the deflection of ion trajectories, position–dependent charge exchange probabilities of He ions near the surface are derived from the observed charge state distributions and charge state dependence of the energy losses of scattered He ions.

7.1. INTRODUCTION

Fast ions incident on an atomically flat crystal surface interact only with atoms on the topmost atomic plane of the surface when the angle of incidence θ_i is small. Their trajectories are described approximately by the equation of motion of the ion in a continuum planar potential due to the surface atoms as in the case of planar channeling of fast ions.[1,2] Most of the ions are reflected at the angle for specular reflection, *i.e.*, at $\theta_s = 2\theta_i$, since the ions cannot penetrate the topmost atomic plane of the crystal surface when θ_i is less than the critical angle for specular reflection.[3]

The inelastic interaction of the ions with the surface takes place along a well–defined trajectory at specular reflection and thus the resulting interaction of the ion is described by the position–dependent interaction probabilities as in the case of the planar channeling.[1,2,4] In fact, we have shown in Chapter 4 that the energy losses of MeV He and H ions, which are specularly reflected from the (100) surfaces of several crystals, are explained by position–dependent stopping powers.[5,6] We have also shown in Chapter 6 that the charge state distribution of the specularly reflected MeV He ions is explained with the use of position–dependent electron–loss and –capture probabilities.[7] It was shown in the Chapter that the ions scattered at surface steps are deflected at the angles deviated from the angle for specular reflection and that the charge state of the ion does not change after the deflection at the step.

Actual crystal surfaces are not atomically flat, and have many steps and point defects. At glancing angle incidence of a beam of ions on the surface, some of the ions penetrate the surface and reappear from the crystal at the surface steps.[8,9] The energies of these ions are smaller than that of ions reflected from the topmost atomic plane, and, as the result, the energy spectrum of the scattered ions shows a characteristic structure, which depends on the density and distribution of the steps on the surface. The energy spectra of He ions scattered from a SnTe crystal surface have a few well–defined peaks, and the peaks at lower energies have been explained in terms of sub–surface planar channeling.[3,8] Thus we can identify the ions reflected from the topmost atomic plane of the surface from their energies since the specularly reflected ions have the least energy loss.[3,8,9]

For MeV He ions reflected from the topmost atomic plane of the crystal surface, we observed that the energy loss of the specularly reflected He^{2+} ions is about 10 % as large as that of He^+ ions at glancing angle incidence of He^+ ions on the (100) surface of SnTe.[5] For the ions transmitted through matter, similar differences of energy losses of ions of different charge states have been observed when the charge state equilibrium of the ions is not attained in the matter: Using thin gas target, Allison *et al.* determined fixed–charge stopping powers for each charge state of H and He ions.[10-12] In channeling conditions, where charge exchange is greatly reduced, it is possible to observe the ions transmitting target without charge exchange.[13-15] Datz *et al.* have

observed energy losses which depend on the charge state of the foil transmitted heavy ions after planar channeling in Au single crystals.[13] At transmission through very thin solid foils, where it is possible to realize charge state non-equilibrium of the transmitted ions,[16-23] Cowern et al. have measured the charge state dependence of energy losses of ions passing through carbon foils, and derived fixed-charge stopping powers and the energy losses accompanied by electron-transfer with the use of a stochastic model.[17-20]

In the present Chapter, we measure the charge state and energy distributions of scattered He ions at glancing angle incidence of MeV He ions on the clean (100) surfaces of SnTe. With the use of the stochastic model of the charge exchange and the energy loss of fast ions in inhomogeneous media, we analysed our experimental results of the charge state and energy distributions. Position-dependent charge exchange probabilities of He ions near the surface are derived from the observed distributions.

7.2. EXPERIMENTAL PROCEDURE

Experimental apparatus was the same as that in Chapter 6. So only a brief description is given here. The scattered ions from a (100) surface of SnTe were resolved into their charge states by a magnetic analyzer and the energy spectra of the ions of each charge state were measured with a solid state detector. The energy resolution of the solid state detector was 13 keV for 1 MeV He ions.

7.3. EXPERIMENTAL RESULTS

Energy spectra and charge state fractions of the scattered ions at glancing angle incidence of 0.67 MeV $\sim$ 1.5 MeV He$^+$ ions on the (100) surface of SnTe were measured. Examples of the energy spectra of the scattered He$^+$ and He^{2+} ions at glancing angle incidence of 0.7 MeV He$^+$ ions on the clean SnTe(100) surface are shown in Fig. 7.1, where the energy of the incident ions is shown by a vertical line. The energy spectra of scattered He ions have a few well-defined peaks. The highest energy peak is due to the He ions specularly reflected from the topmost atomic plane of the surface, while the lower energy peaks are due to the ions channeled along the (100) planar channels parallel to the surface.[3,6,7] Although the incident ions cannot penetrate atomically flat crystal surface at the angle of incidence smaller than the critical angle for specular reflection, surface penetration occurs at surface steps.[3,7,8] Thus the oscillatory structure of the energy spectrum depends on the distribution and density of steps on the reflecting surface plane.[3,8]

In the following, we study only the energy loss of the ions reflected from the topmost atomic plane. Since we could not observed the skewness of the highest energy peak, the peak energy was determined by fitting the peak profile to a Gaussian distribution. The error in the determined peak energy is less than 1 %, thus the accuracy of the determined mean energy loss is of the order of 0.1 keV. The observed mean energy loss does not depend on the angle of incidence θ_i, but depends on the scattering angle θ_s and the charge state of the scattered ions.
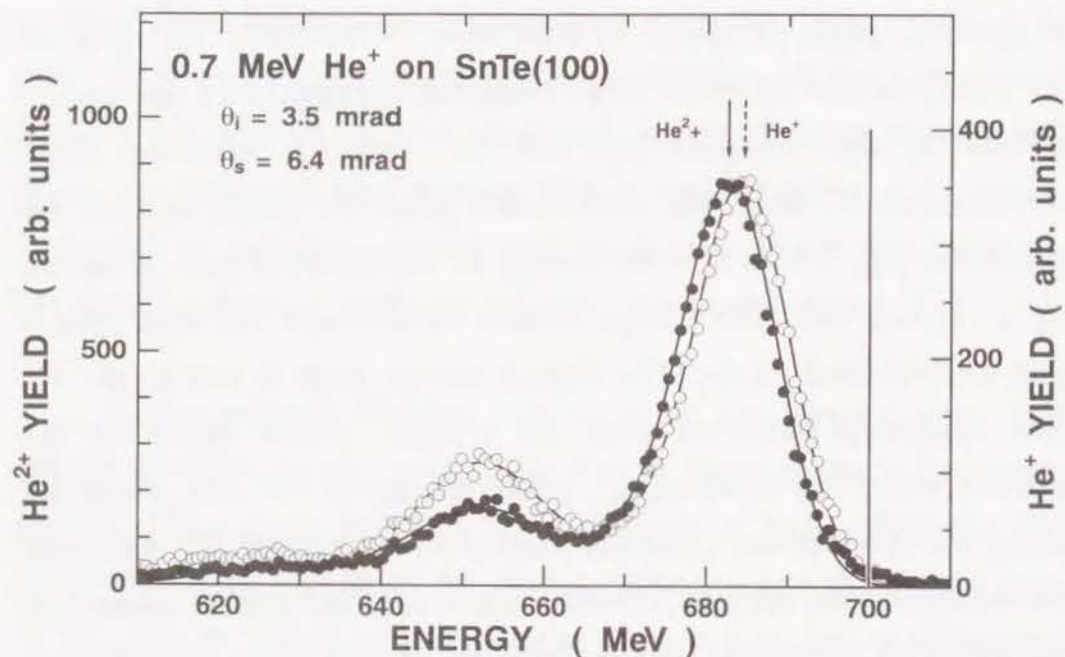
Figure 7.1: Energy spectra of scattered He$^+$ and He^{2+} ions at glancing angle incidence of 0.7 MeV He$^+$ ions on the clean SnTe(100) surface.

Figures 7.2(a) and (b) show θ_s–dependence of the energy losses of He ions reflected from the topmost atomic plane at glancing angle incidence of 0.67 MeV and 1.5 MeV He ions respectively. The energy losses $\Delta E_1(\theta_i;\theta_s)$ of the scattered He$^+$ ions and $\Delta E_2(\theta_i;\theta_s)$ of the scattered He^{2+} ions are shown by open and filled circles respectively. They are connected by lines for the guide of eyes. The angles of incidence are shown in the figures, and the angles for
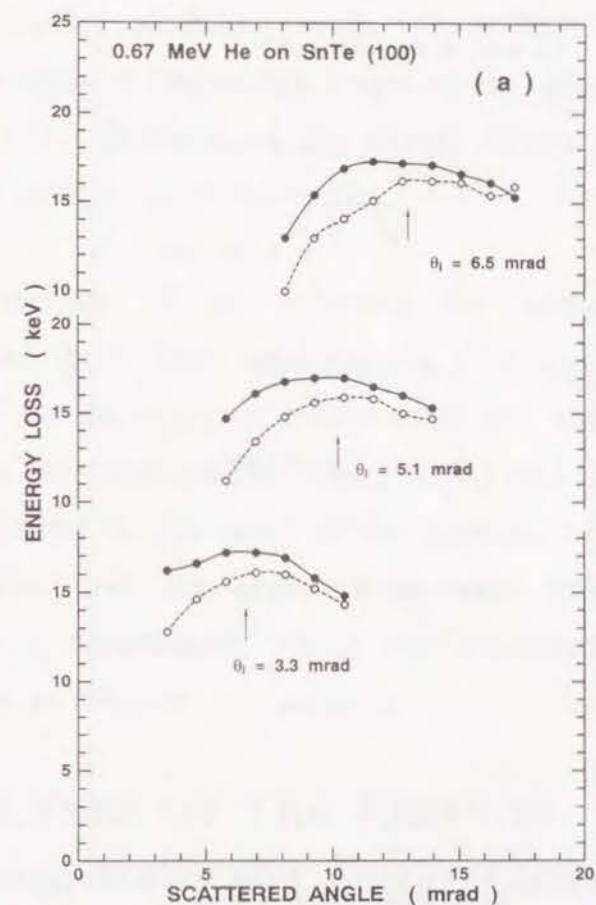
Figure 7.2(a): The energy losses, $\Delta E_1(\theta_i;\theta_s)$ (○) and $\Delta E_2(\theta_i;\theta_s)$ (●), of He$^+$ and He^{2+} ions, for the ions reflected from the (100) surface of SnTe vs. the angle of scattering, for 0.67 MeV He$^+$ incident at glancing angles 3.3 mrad, 5.1 mrad and 6.5 mrad. The arrows indicate the angles for specular reflection.
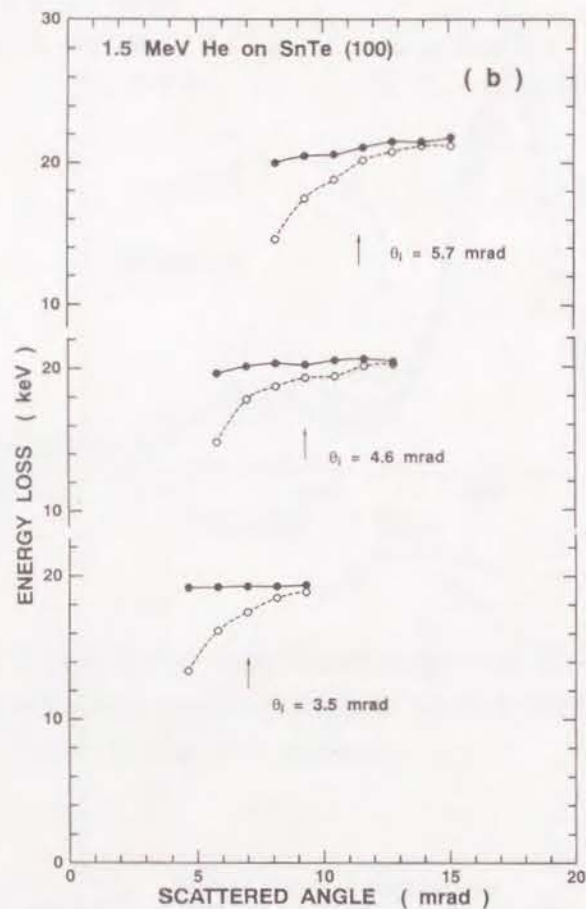
Figure 7.2(b): The energy losses, $\Delta E_1(\theta_i;\theta_s)$ (○) and $\Delta E_2(\theta_i;\theta_s)$ (●), of He$^+$ and He^{2+} ions, for the ions reflected from the (100) surface of SnTe vs. the angle of scattering, for 1.5 MeV He$^+$ incident at glancing angles 3.5 mrad, 4.6 mrad and 5.7 mrad. The arrows indicate the angles for specular reflection.

specular reflection $\theta_s = 2\theta_i$ are indicated by arrows. The losses of He^{2+} ions are larger than those of He$^+$ ions, and the difference of the losses is larger at smaller scattering angles. There is a tendency in the θ_s-dependence of the energy loss that the energy loss is smaller at smaller scattering angles ($\theta_s < 2\theta_i$). This tendency is more conspicuous in the energy losses of He$^+$ ions than in those of He^{2+} ions. The difference of the energy losses of He$^+$ and He^{2+} increases at smaller scattered angles.

The fractions of the reflected He$^+$ and He^{2+} ions were measured and have been analyzed in Chapter 6. The fractions depend both on the angle of incidence θ_i and scattering angle θ_s. The ratios of the observed fractions $F_1(\theta_i;\theta_s)$ and $F_2(\theta_i;\theta_s)$ have been shown in Chapter 6. The ratios of the fractions of ions scattered at angles smaller than the angle of specular reflection $2\theta_i$ show complicated θ_s-dependence, which was attributed to scattering at surface steps in Chapter 6.

7.4. ANALYSES OF THE RESULTS

7.4.1. Charge States and Energy Losses of Specularly Reflected Ions

Charge state and energy of the ions at specular reflection at a crystal surface change along their trajectories. In order to describe the change of states of the specularly reflected ion along its trajectory, we define the Cartesian coordinate system, where the x–axis is parallel to the surface normal and the scattering is in the xz–plane. The origin of the coordinates is on the topmost atomic

plane of the surface. For the ions at glancing angle incidence on the surface, we now define the probability distribution $f_i(z,E)$ for the ions with charge $+ie$ and energy E on a trajectory $z(x)$. The probability distribution $f_i(z,E)$ satisfies the following relation,

$$f_i(z+\delta z,E) = Q_{ii}(z)\delta z \cdot \int_0^\infty d(\delta E)\big(f_i(z,E+\delta E)\cdot\omega_i(z;\delta E)\delta z\big) \tag{1}$$

$$+ \sum_{j \neq i} Q_{ji}(z)\delta z \cdot \int_0^\infty d(\delta E)\big(f_j(z,E+U_{ji}+\delta E)\cdot\omega_j(z;\delta E)\delta z\big) \ ,$$

where,

$$Q_{ii}(z)\delta z = 1 - \sum_{j \neq i} Q_{ij}(z)\delta z \ , \tag{2}$$

where $\omega_j(z(x);\delta E)$ is the probability (per unit path length) of energy loss δE of He^{j+} ions at the distance x from the surface, $Q_{ij}(z(x))$ is the probability (per unit path length) of change of ionic charge from $+ie$ to $+je$ at the distance x from the surface on the trajectory $z(x)$, and U_{ji} is the mean energy loss of an ion due to electron transfer from ionic charge $+je$ to $+ie$. Dependence of $\omega_j(z;\delta E)$ and $Q_{ij}(z)$ on ion energy E is neglected, since the energies of the ions we are interested in here are nearly equal to that of incident ions. Expanding $f_i(z+\delta z,E)$, $f_i(z,E+\delta E)$ and $f_j(z,E+U_{ji}+\delta E)$ in Eq. (1) into Taylor series at (z,E) and neglecting the terms containing $(\delta z)^n$ and $(\delta E)^n$ $(n > 1)$, we obtain a set of partial differential equations for the evolution of $f_i(z,E)$'s;

$$\frac{\partial f_i(z,E)}{\partial z} = S_i(z(x)) \cdot \frac{\partial f_i(z,E)}{\partial E}$$

$$+ \sum_{j \neq i}\left\{Q_{ji}(z)\left(f_j(z,E)+U_{ji}\cdot\frac{\partial f_j(z,E)}{\partial E}\right) - Q_{ij}(z)f_i(z,E)\right\} \ , \tag{3}$$

where $S_i(z(x))$ is the position–dependent stopping power for the ion with charge $+ie$ at distance x from the surface, and is related to $\omega_i(z(x);\delta E)$ as,

$$S_i(z(x)) = \int_0^\infty d(\delta E)\big(\delta E\cdot\omega_i(z(x);\delta E)\big) \ . \tag{4}$$

The fraction $F_i(z(x))$ of the ions of charge $+ie$ at $z(x)$ is expressed as,

$$F_i(z) = \int_0^\infty f_i(z,E)dE \ , \tag{5}$$

and the mean energy $<E_i(z)>$ and the mean energy loss $\Delta E_i(z)$ of He^{i+} ions at $z(x)$ are derived as,

$$<E_i(z)> = \frac{1}{F_i(z)}\cdot\int_0^\infty E f_i(z,E)dE \ , \tag{6}$$

$$\Delta E_i(z) = E_o - <E_i(z)> \quad , \tag{7}$$

where E_0 is the energy of incident ions. The rate equations for charge state fractions $F_i(z)$ are obtained by integrating Eq. (3) with respect to E as,

$$\frac{dF_i(z)}{dz} = \sum_{j \neq i} \left(Q_{ji}(z) F_j(z) - Q_{ij}(z) F_i(z) \right) \quad , \tag{8}$$

The evolution of the mean energy loss $\Delta E_i(z)$ of He^{i+} ions along $z(x)$ is obtained by multiplying E to Eq. (3) and integrating with respect to E, and using Eqs. (5) to (7) as,

$$\frac{d\left(F_i(z) \Delta E_i(z) \right)}{dz} = F_i(z) S_i(z(x)) \tag{9}$$
$$+ \sum_{j \neq i} \left\{ Q_{ji}(z) F_j(z) \left(\Delta E_j(z) + U_{ji} \right) - Q_{ij}(z) F_i(z) \Delta E_i(z) \right\} \; .$$

Equations (8) and (9) are similar to those derived by Cowern *et al.*[17–20]

7.4.2. Effect of Steps on the Ion Trajectory

Now suppose an ion of energy E impinges on an atomically flat surface of a crystal with a small angle θ_i relative to the surface. If the energy loss of the ion is neglected, the equation of motion of the ion is,

$$M\frac{d^2x}{dt^2} = - \frac{dV(x)}{dx} \quad ,$$
$$M\frac{d^2z}{dt^2} = 0 \quad , \tag{10}$$

where M is the mass of the ion. Since the angle of incidence θ_i is small, the potential V(x) in Eq. (10) is approximated to the continuum planar potential of the surface atomic plane as in the case of planar channeling of ion in crystal.[1,2] With the Molière approximation to the Thomas–Fermi screening function, the potential is expressed as

$$V(x) = E\psi_a^2 \sum_{i=1}^{3} \frac{\alpha_i}{\beta_i} \cdot \exp\left(-\frac{\beta_i x}{a_{TF}} \right) \quad , \tag{11}$$

$$\psi_a = \left(\frac{2\pi Z_1 Z_2 e^2 n_p a_{TF}}{E} \right)^{\frac{1}{2}} \quad , \tag{12}$$

where ψ_a is the characteristic angle for planar channeling, Z_1 and Z_2 are the atomic numbers of ion and target atom respectively, e is the elementary charge, n_p is the atomic density of the surface plane, a_{TF} is the Thomas–Fermi screening distance, and α_i and β_i are the parameters in the Molière approximation to the Thomas–Fermi screening function.[1,2]

The ion is reflected from the surface and scattered at $\theta_s = 2\theta_i$ when the angle of incidence θ_i is less than ψ_a. However, actual

crystal surface is not an ideal mirror for incident MeV ions, and thus the angular distribution of the reflected ions is broadened centered at $\theta_s = 2\theta_i$. The broadening is caused by collisions of ions with thermally vibrating atoms (nuclear scattering), electrons (electronic scattering) and surface irregularities. We have shown from a Monte Carlo simulation of angular distributions of specularly reflected ions from a crystal surface that most of the observed broadening comes from the scattering events at surface steps.[8,9]
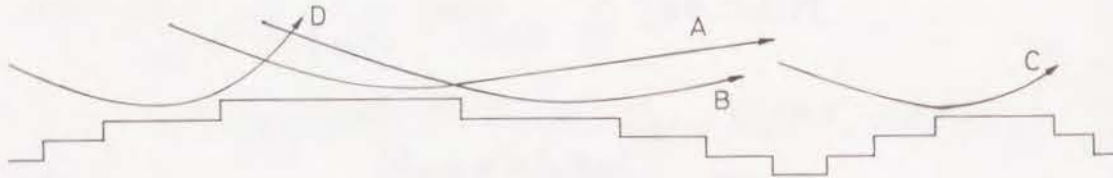
Figure 7.3: The trajectories of scattered ions at the terraced (100) surface of SnTe.

On the other hand, we have shown from atomic force microscopy of the (100) surfaces of epitaxial SnTe crystal that the surface has many small pyramidal hillocks when it is grown at 200 °C at the growth rates larger than about 1 nm/min and that the step

heights are one or two monolayers (3.15 and 6.3 Å).[24] Possible trajectories of the ions at glancing angle incidence on such stepped surface are shown in Fig. 7.3. The ions on the trajectories labeled by A and B which pass over downsteps are scattered at angles smaller than $\theta_s = 2\theta_i$. The ions on the trajectories labeled C and D which pass over upsteps are deflected at angles larger than $2\theta_i$. However, only the trajectories A and C are possible on the present surfaces because of the small pyramidal hillocks.[7,24]

Now consider the trajectories of the type A ions. An ion which has passed over a downstep on its outgoing trajectory is hardly affected by the continuum surface potential as its distance from the surface is larger than the step height (3.15 Å), and thus the trajectory is approximated to a straight line after it passes over the step. Thus we obtain the following relations;

$$x_s = \frac{a_{TF}}{\beta_3} \cdot \ln\left(\frac{\alpha_3}{\beta_3} \cdot \frac{\psi_a^2}{\theta_s \cdot (2\theta_i - \theta_s)} \right), \tag{13}$$

$$z_s = \frac{a_{TF}}{\beta_3 \theta_i} \cdot \ln\left(\frac{\theta_s^2}{\theta_s \cdot (2\theta_i - \theta_s)} \right), \tag{14}$$

where step position z_s, angle of scattering θ_s and the distance x_s of the ion from the surface at the step position are defined in Fig. 7.4. It was assumed in deriving the relations that only the term containing α_3 and β_3 is retained in Eq. (11). The error due to this

approximation is less than 1 % of θ_s for 0.67 MeV He ions at the angle of incidence 7 mrad.

7.4.3. Role of Steps on the Charge State and Energy Loss of Reflected Ions

We have shown in Chapter 4 and Chapter 6 that the position–dependent stopping power $S_i(x)$ and charge exchange probabilities $Q_{ij}(x)$ are rapidly decreasing functions of x.[5-7] Therefore the charge state and energy of the reflected ions having the type A trajectories do not change after they pass over downsteps, since the distances of the ions on the trajectories are more than the step height (3.14 Å) from the surface. Thus the charge state of the ion scattered at an angle θ_s ($< 2\theta_i$) is expressed as,[6]

$$F_i(\theta_i;\theta_s) = F_i(z_s) \quad , \tag{15}$$

where θ_s is related to the position z_s of downstep by Eq. (14). With the use of this relation, we have explained the angular dependence of the charge state distributions of He ions scattered from the (100) surface of SnTe.

It has been shown in Chapter 4 that the energy loss of the ions specularly reflected from the topmost atomic plane on the crystal surface is expressed by integrating the position–dependent stopping power $S(x)$ along its trajectory $z = z(x)$.[5,6] Since the energy of the ion does not change after it passes over a downstep,
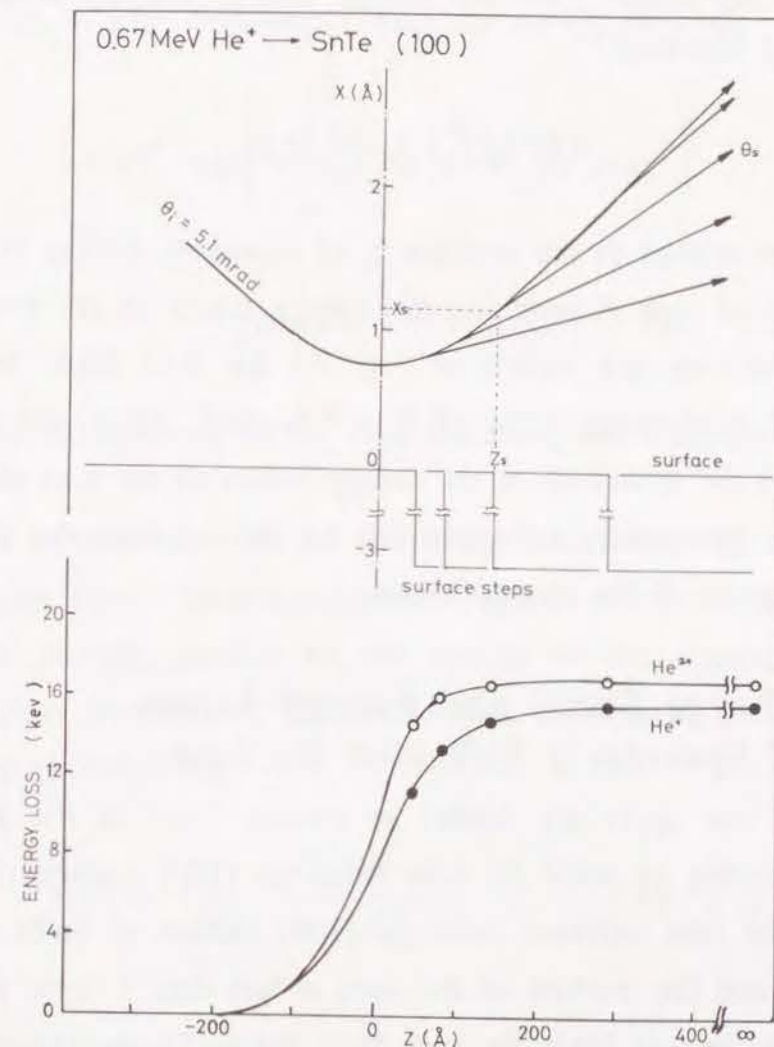
Figure 7.4: The type A trajectories of scattered ions at steps, and the evolution of the energy losses of 0.67 MeV He⁺ and He²⁺ ions on the trajectories. The closest approach of the ions to the surface are at z = 0. This figure is derived with the use of Eqs. (13), (14), (16), and of the experimental energy losses of the ions.

the energy of the ion reflected at an angle θ_s ($< 2\theta_i$) is that of the ion at the downstep. Thus the energy loss of the ion scattered at θ_s ($< 2\theta_i$) becomes,

$$\Delta E_i(\theta_i; \theta_s) = \Delta E_i(z_s) \quad , \qquad (16)$$

where θ_s is related to the position z_s of downstep by Eq. (14). The trajectories of type A ions and the energy losses of the ions along these trajectories are shown in Fig. 7.4 for 0.67 MeV He^+ ions incident at a glancing angle of $\theta_i = 5.1$ mrad. Thus with the use of Eq. (16) the evolution of the energy losses of the ions along the trajectories of specular reflection can be derived from the observed θ_s-dependence of the energy losses.

7.4.4. Charge States and Energy Losses of Specularly Reflected He Ions

Now we apply the model in section 7.4.1 to the glancing angle scattering of MeV He ions from the (100) surface of SnTe. Most of the ions reflected from the (100) surface of SnTe are He^+ and He^{2+}, and the fraction of He^0 ions is less than 1 % at glancing angle scattering of MeV He ions from the (100) surface of SnTe. We therefore consider only the fractions of He^+ and He^{2+}, i.e., $F_1(z)$ and $F_2(z)$. The rate equations for the charge state fractions, Eq. (8), reduce to two simultaneous equations and are solved when the initial fractions are given. When the fraction of He^+ ions in the incident He ions is F_1^{in} at $x = \infty$, $z = -\infty$, and thus $F_2^{in} = 1 - F_1^{in}$, Eq. (8) for $F_1(z)$ is integrated along the trajectory as,

$$F_1(z) = \int_{-\infty}^{z} Q_{21}(x') \cdot \exp\left\{ - \int_{z'}^{z} \left(Q_{12}(x'') + Q_{21}(x'') \right) dz'' \right\} dz'$$
$$+ F_1^{in} \cdot \exp\left\{ - \int_{-\infty}^{z} \left(Q_{12}(x') + Q_{21}(x') \right) dz' \right\} \quad , \qquad (17)$$

and,

$$F_2(z(x)) = 1 - F_1(z(x)) \quad , \qquad (18)$$

where the integrations in Eq. (17) are along the ion trajectory $z(x)$.

For convenience of the following discussion, we define the equilibrium charge state fractions of He ions which are attained for the ions moving parallel to the surface at the distance x. The charge state fractions $F_i^{eq}(x)$ of the ions are related to the charge exchange probabilities;

$$F_i^{eq}(x) = \frac{Q_{ji}(x)}{Q_{12}(x) + Q_{21}(x)} \quad , \qquad (i \neq j) \quad , \qquad (19)$$

where i and j are 1 and 2.

Integrating Eq. (9) along an ion trajectory with the initial condition that $\Delta E_i(-\infty) = 0$, we obtain two relations for the energy losses $\Delta E_1(z)$ and $\Delta E_2(z)$ of He ions at $z(x)$ on the trajectory of specular reflection; the mean value $\Delta E_m(z)$ of the energy losses on the charge states of the He ions as,

$$\Delta E_m(z) = F_1(z)\,\Delta E_1(z) + F_2(z)\,\Delta E_2(z)$$

$$= \int_{-\infty}^{z} \left\{ \left(S_1(x') + Q_{12}(x')U_{12}\right)F_1(z') + \left(S_2(x') + Q_{21}(x')U_{21}\right)F_2(z') \right\} dz' ,$$

$$(20)$$

and the difference $\Delta E_d(z)$ of the energy losses of He^{2+} and He^+ as,

$$\Delta E_d(z) = \Delta E_2(z) - \Delta E_1(z) \qquad (21)$$

$$= \int_{-\infty}^{z} \left\{ \left(S_2(x') + Q_{12}(x')\,U_{12}\,\frac{F_1(z')}{F_2(z')}\right) - \left(S_1(x') + Q_{21}(x')\,U_{21}\,\frac{F_2(z')}{F_1(z')}\right) \right\}$$

$$\cdot \exp\left[-\int_{z'}^{z} \left(Q_{21}(x'')\,\frac{F_2(z'')}{F_1(z'')} + Q_{12}(x'')\,\frac{F_1(z'')}{F_2(z'')} \right) dz'' \right] dz' .$$

From these relations, $\Delta E_1(z)$ is derived:

$$\Delta E_1(z) = \int_{-\infty}^{z} \left[\left(S_1(x')F_1(z') + Q_{21}(x')U_{21}F_2(z')\right) \right. \qquad (22)$$

$$\cdot \left(1 + \frac{F_2(z')}{F_1(z)} \cdot \exp\left\{ -\int_{z'}^{z} \left(Q_{21}(x'') + Q_{12}(x'')\right) dz'' \right\} \right)$$

$$+ \left(S_2(x')F_2(z') + Q_{12}(x')U_{12}F_1(z')\right)$$

$$\left. \cdot \left(1 - \frac{F_1(z')}{F_1(z)} \cdot \exp\left\{ -\int_{z'}^{z} \left(Q_{21}(x'') + Q_{12}(x'')\right) dz'' \right\} \right) \right] dz' .$$

We can obtain similar equation for $\Delta E_2(z)$. Equation (22) is rewritten in a simpler form,

$$\Delta E_i(z) = \frac{1}{F_i(z)} \cdot \int_{-\infty}^{z} \left(M_i(z')P_{ii}(z',z) + M_j(z')P_{ji}(z',z) \right) dz' \quad (i \neq j) \quad (23)$$

$$M_i(z') = S_i(x')F_i(z') + Q_{ji}(x')U_{ji}F_j(z') , \qquad (24)$$

$$P_{ji}(z',z) = \int_{z'}^{z} \left(Q_{ji}(x'') \cdot \exp\left\{ -\int_{z''}^{z} \left(Q_{21}(x''') + Q_{12}(x''')\right) dz''' \right\} \right) dz'' \quad (25)$$

$$P_{ii}(z',z) = 1 - P_{ij}(z',z) . \qquad (26)$$

$M_j(z')dz'$ shows the energy loss of He^{j+} in the interval $(z', z'+dz')$ and is the sum of the energy loss due to the stopping $S_j(x')$ of He^{j+} ions without charge changing and that due to the energy loss U_{ij} in the charge–exchange collision in which He^{i+} ion changes into He^{j+} ion. $P_{ji}(z',z)$ shows the fraction of He ions in the charge state i at the position $z(x)$ which were in the charge state j at the position $z'(x')$. They satisfy the following relations;

$$F_i(z) = P_{1i}(z',z)F_1(z') + P_{2i}(z',z)F_2(z') , \qquad (27)$$

$$P_{i1}(z',z) + P_{i2}(z',z) = 1 , \qquad (28)$$

7.4.5. Derivation of Charge Exchange Probabilities

We write down the position–dependent stopping power for specularly reflected ion with unit charge $+e$ by $S_p(x)$. From the analogy of the stopping power of bulk material, we express the fixed–charge position–dependent stopping power as,

$$S_j(x) = q_j^2 \cdot S_p(x) \ , \tag{29}$$

where $q_j e$ is the effective charge of He^{j+} ion. Substituting Eq. (29) into Eqs. (20) and (21), we obtain the mean value $\Delta E_m(z)$ of the energy losses of He^{2+} and He^+ ions as,

$$\Delta E_m(z) = F_1(z)\,\Delta E_1(z) + F_2(z)\,\Delta E_2(z) \tag{30}$$

$$= \int_{-\infty}^{z} \Big\{ \big(F_1(z')q_1^2 + F_2(z')q_2^2\big) S_p(x')$$

$$+ Q_{12}(x')U_{12}F_1(z') + Q_{21}(x')U_{21}F_2(z') \Big\} dz' \ ,$$

and the difference $\Delta E_d(z)$ of the energy losses of He^{2+} and He^+ as,

$$\Delta E_d(z) = \Delta E_2(z) - \Delta E_1(z) \tag{31}$$

$$= \frac{1}{F_1(z)F_2(z)} \int_{-\infty}^{z} \Bigg[\bigg\{ \big(q_2^2 - q_1^2\big) S_p(x') F_1(z') F_2(z')$$

$$+ Q_{12}(x')\,U_{12} \cdot F_1(z')^2 - Q_{21}(x')\,U_{21} \cdot F_2(z')^2 \bigg\}$$

$$\cdot \exp\bigg\{ -\int_{z'}^{z} \big(Q_{21}(x'') + Q_{12}(x'')\big)\, dz'' \bigg\} \Bigg] dz' \ .$$

From Eqs. (30), (31) and (8), the charge exchange probabilities $Q_{ji}(x)$ are derived as follows;

$$Q_{ji}(x) = \cfrac{\left[\begin{aligned} &F_i(z) \cdot \frac{d\big(q_j^2 \Delta E_i(z) - q_i^2 \Delta E_j(z)\big)}{dz} \\[2mm] &+ \frac{F_i(z)}{F_j(z)} \cdot q_i^2 \big(\Delta E_j(z) - \Delta E_i(z) - U_{ij}\big) \cdot \frac{dF_i(z)}{dz} \end{aligned} \right]}{\left[\begin{aligned} &\big(q_1^2 F_1(z) + q_2^2 F_2(z)\big) \cdot \big(\Delta E_j(z) - \Delta E_i(z)\big) \\[2mm] &+ q_j^2 U_{ji} F_j(z) - q_i^2 U_{ij} F_i(z) \end{aligned} \right]} \tag{32}$$

where $z = z(x)$, and $i \neq j$. This shows that we can determine the position–dependent charge exchange probabilities $Q_{ji}(x)$ from the observed energy losses $\Delta E_i(z)$ and observed charge state fractions $F_i(z)$, if we know the effective charges $q_j e$ and U_{ij}. It is shown in Eq. (32) that the charge exchange probabilities are small when the difference $\Delta E_d(z)$ of the energy losses is large.

Because He^{2+} ion has no electron to surround its nuclear charge, its effective charge is $+2e$, thus $q_2 = 2$, while the effective charge of He^+ ion depends on the He^+ velocity. Now, for convenience in the following analysis, we assume $q_1 = 1$.

From the kinematics of collision process,[25] the energy loss of an ion at electron capture is

$$U_{21} = B_T - B_P \quad , \tag{33}$$

where B_T and B_P are the (positive) binding energies of the captured electron to the target and projectile core, respectively. For the major electron capture channel of $0.67 \sim 1.5$ MeV He^{2+} ions colliding with Sn and Te atoms,[7] B_T is the average of the binding energies of 4s electrons of Sn and Te atoms, which are 133 eV and 162 eV for Sn and Te, respectively[26]. Thus we obtain $U_{21} = 0.09$ keV. For the electron loss process of He^+, we assume that the velocity of the lost electron relative to the ion is small. Thus the ion energy loss on electron loss is expressed as,

$$U_{12} \sim \frac{1}{2} m V^2 \quad , \tag{34}$$

where V is the laboratory–frame velocity of the ion. U_{12} is 0.09 keV and 0.2 keV for 0.67 MeV and 1.5 MeV He ions, respectively.

Now substituting the values of q_1, q_2, U_{12}, and U_{21} into Eq. (32), and using Eqs. (15) and (16) to derive $F_i(z)$ and $\Delta E_i(z)$ from the experimental data and the following relation derived from Eqs. (13) and (14);

$$d\theta_s = \frac{\beta_3}{2 a_{TF}} \cdot \theta_s \cdot (2\theta_i - \theta_s) \cdot dz \quad , \tag{35}$$
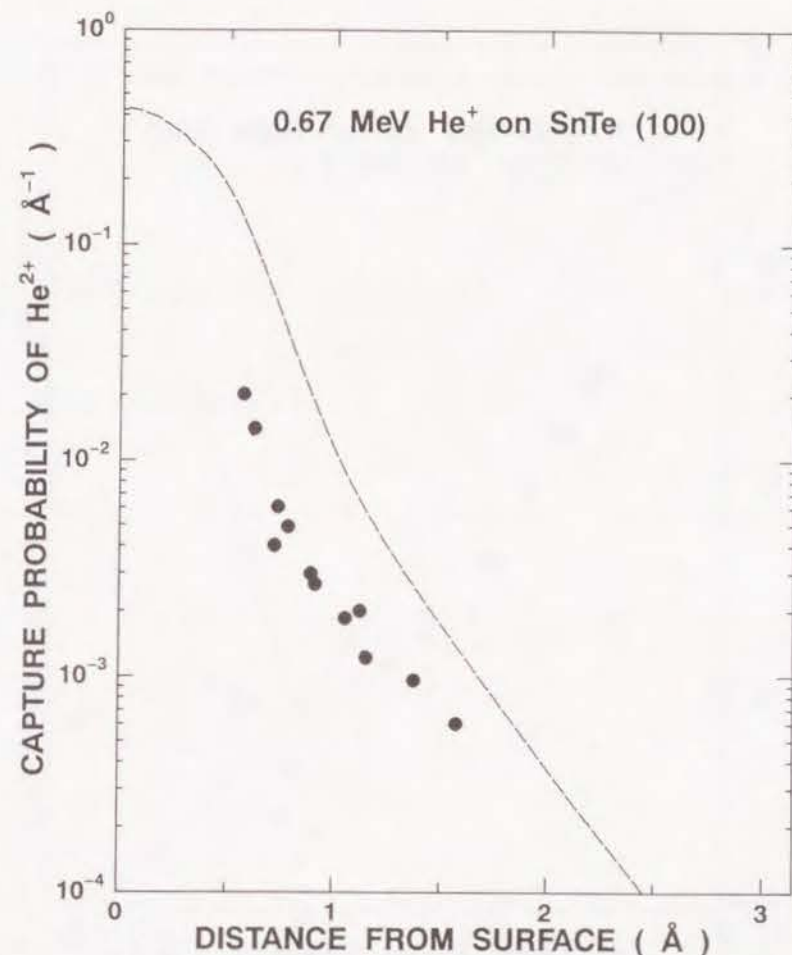
Figure 7.5(a): Experimentally derived position–dependent electron–capture probabilities, $Q_{21}(x)$ for 0.67 MeV He ions at the (100) surface of SnTe. For comparison, the calculated position–dependent charge exchange probabilities are shown by dashed lines, which probabilities are calculated with the use of the Bohr and the Bohr–Lindhard models.
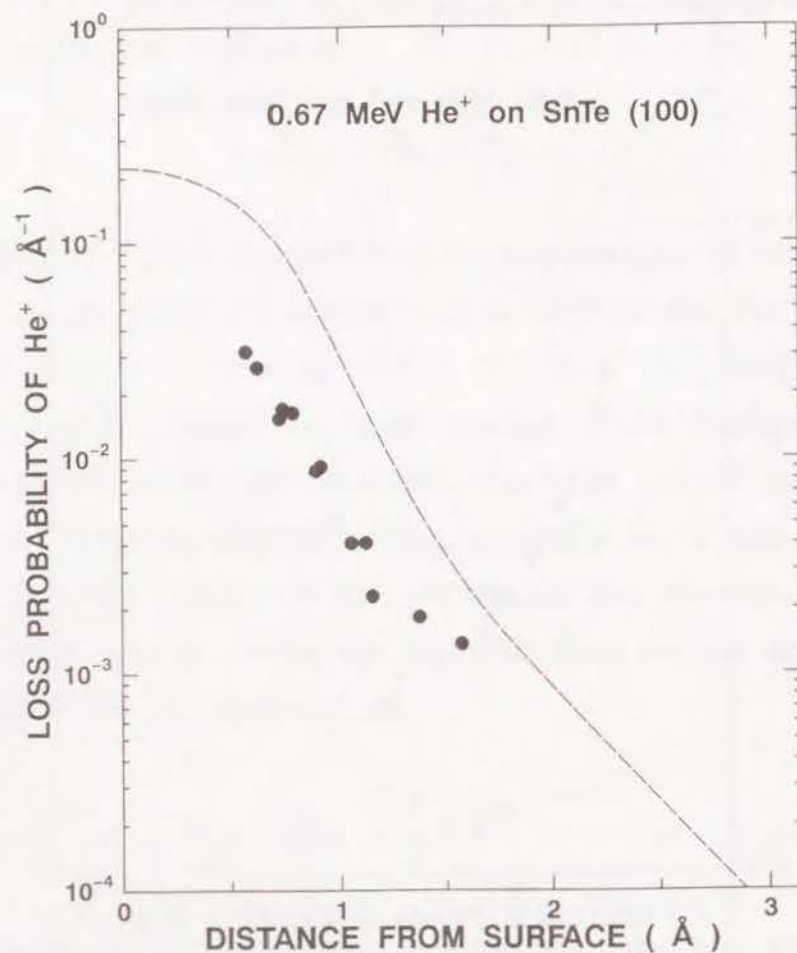
Figure 7.5(b): Experimentally derived position-dependent electron-loss probabilities, $Q_{12}(x)$ for 0.67 MeV He ions at the (100) surface of SnTe. For comparison, the calculated position-dependent charge exchange probabilities are shown by dashed lines, which probabilities are calculated with the use of the Bohr and the Bohr–Lindhard models.
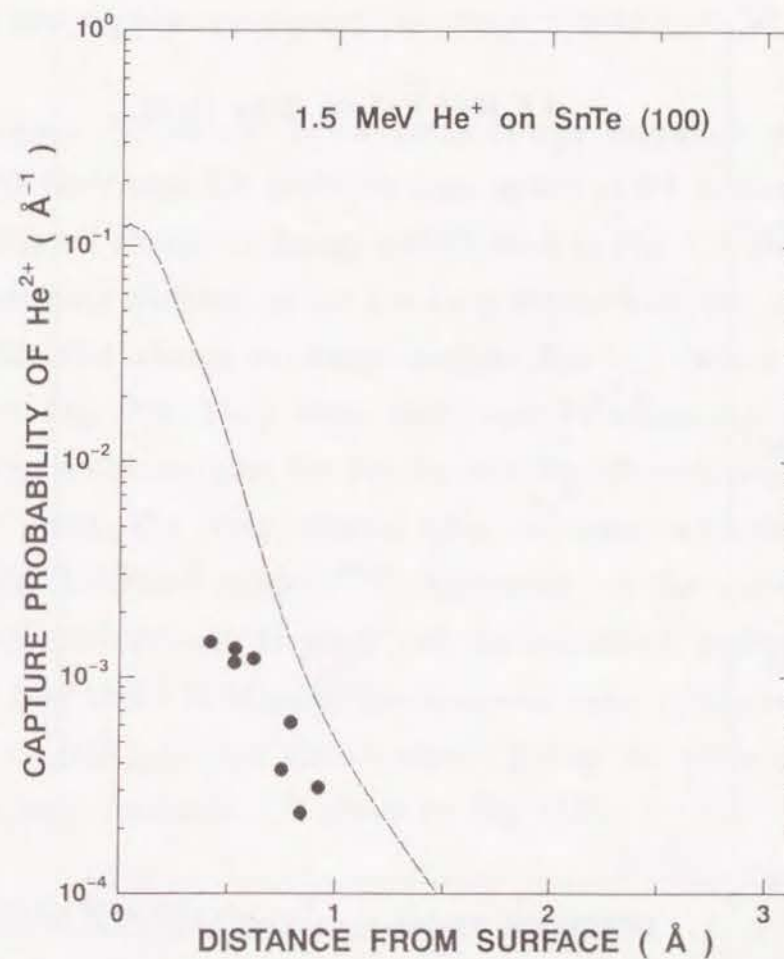
Figure 7.5(c): Experimentally derived position-dependent electron-capture probabilities, $Q_{21}(x)$ for 1.5 MeV He ions at the (100) surface of SnTe. For comparison, the calculated position-dependent charge exchange probabilities are shown by dashed lines, which probabilities are calculated with the use of the Bohr and the Bohr–Lindhard models.

1.5 MeV He$^+$ on SnTe (100)

LOSS PROBABILITY OF He$^+$ (Å^{-1})

DISTANCE FROM SURFACE (Å)
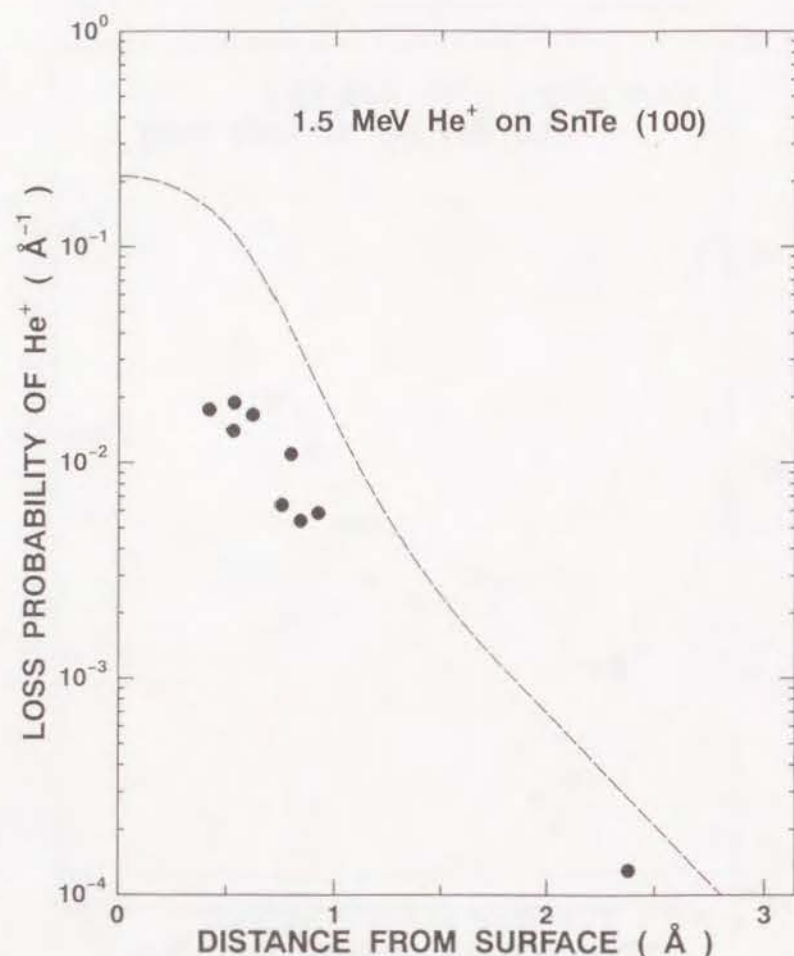
Figure 7.5(d): Experimentally derived position–dependent electron–loss probabilities, $Q_{12}(x)$ for 1.5 MeV He ions at the (100) surface of SnTe. For comparison, the calculated position–dependent charge exchange probabilities are shown by dashed lines, which probabilities are calculated with the use of the Bohr and the Bohr–Lindhard models.

we obtain the position–dependent charge exchange probabilities $Q_{12}(x)$ and $Q_{21}(x)$.

Figure 7.5 shows the obtained charge exchange probabilities for 0.67 MeV and 1.5 MeV He ions at the (100) surface of SnTe. The obtained charge exchange probabilities in Fig. 7.5 decrease with the increasing distance of the ion from the surface. For comparison, the calculated charge exchange probabilities are shown by broken lines in Fig. 7.5. They were calculated by averaging the charge exchange cross sections for He–Sn and He–Te collisions over the surface plane. The cross sections were calculated with the Bohr and the Bohr–Lindhard models.[27,28] Agreement of the calculated and observed probabilities is poor, and the calculated probabilities are almost four times as large as the observed ones. However the ratios of the $Q_{12}(x)/Q_{21}(x)$ are almost equal, giving the same equilibrium charge state fractions, F_i^{eq} given by Eq. (19).

7.5. DISCUSSION

The stochastic model for the probability distribution $f_i(z,E)$ has originally been described by Winterbon[29] and developed by Cowern et al. at foil transmission of fast ions.[17–20] For the better understanding of the physical meaning of Eq. (23) for the energy loss, $\Delta E_i(z)$, we consider two extreme cases. The first is the case where the charge–exchange does not occur during specular reflection. In this case, both $Q_{12}(z)$ and $Q_{21}(z)$ are zero, and $P_{ii}(z',z)$'s defined by Eq. (25) are,

$$P_{ii}(z',z) = 1 \quad,$$
$$P_{ij}(z',z) = 0 \quad, \qquad (i \neq j) \quad. \tag{36}$$

Thus the energy losses are written down simply as

$$\Delta E_i(z(x)) = \int_{-\infty}^{z} q_i^2 \cdot S_p(z'(x')) dz' \quad. \tag{37}$$

The energy loss of He^{+j} ions is proportional to q_j^2.

The second is the case where the charge–exchange occurs too frequently that the ions are in the charge state equilibrium at any point on the trajectory $z(x)$, where the fractions are given by Eq. (19). In this case, it is seen from Eq. (25) that

$$P_{ji}(z',z) = F_i(z(x)) = F_i^{eq}(z(x)) \quad. \tag{38}$$

The energy losses of He^+ and He^{2+} ions are the same and are given as,

$$\Delta E_1(z) = \Delta E_2(z) = \Delta E_m(z) \tag{39}$$

$$= \int_{-\infty}^{z} \left\{ \left(F_1^{eq}(z') q_1^2 + F_2^{eq}(z') q_2^2 \right) \cdot S_p(x') \right.$$

$$\left. + F_1^{eq}(z') F_2^{eq}(z') (U_{12} + U_{21}) \cdot \left(Q_{12}(z') + Q_{21}(z') \right) \right\} dz' \quad.$$

The actual situations are intermediate between the above two extreme cases, and can be solved numerically.

In deriving the charge exchange probabilities from Eq. (32), we assumed that the effective charge $q_1 e$ of He^+ ion is e. This is based on the following consideration: In the cases of foil transmission of fast He^+ ion through foils, the effective charge of He^+ is generally larger than $+e$ except for low velocity He^+ ions where the screening effect by the bound electron in He^+ is rather strong. As the velocity increases, the effective charge becomes larger because the ions are subjected to close collisions with target electrons.[30] On the other hand, at glancing angle scattering of fast ions from a surface, the impact parameter of ion–atom collisions is larger than the Thomas–Fermi screening distance of the collision. Thus the contribution of close collisions to the stopping of the ions is less than that of the ion in solid, and the nuclear charge of He^+ is well screened by the bound electron. Similar situation is realized at channelling ions in crystal. From the observed stopping powers for heavy ions in Au(111) channels, Datz et $al.$ have shown that the screening per electron of the ion, which is defined as $(Z_1 - q_{eff})$ /(number of bound electrons), was about 0.9.[13] This shows that the nuclear charge is well screened by the bound electrons for channeling ions.

The charge exchange probabilities derived in the present Chapter do not agree with the theoretical ones used in the analysis of the charge state distributions of reflected He ions in Chapter 6,
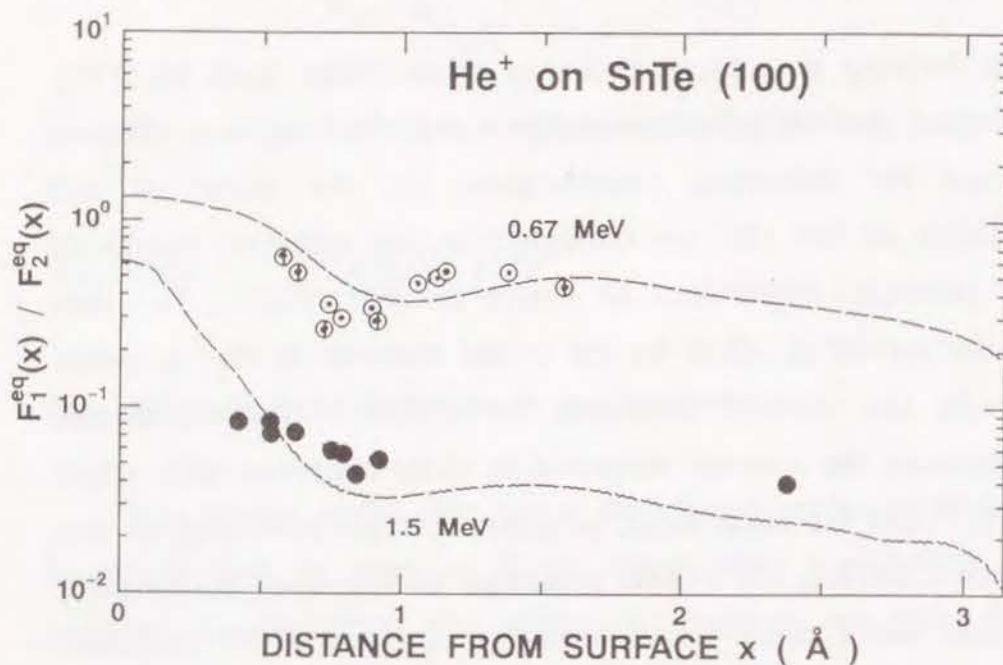
Figure 7.6: Equilibrium charge state fractions $F_i^{eq}(x)$ of 1.5 MeV He ions near the (001) surface of SnTe. Circles are calculated from the charge exchange probabilities derived from the present analysis, while the broken lines are calculated from the theoretical probabilities.

but, the equilibrium charge state factions of He ions calculated with Eq. (19) for these two sets of probabilities agree as shown in Fig. 7.6. Due to this agreement, the observed charge state distributions were explained in terms of the theoretical probabilities in Chapter 6.

7.6. CONCLUSION

We measured charge state fractions and energy losses of He^+ and He^{2+} ions scattered from the (100) surface of a SnTe crystal at glancing angles of incidence for MeV He^+ ions. Based on the model that the deflection of ions from the trajectory of specular reflection occurs at surface step, the observed charge state and energy losses of He ions were related to those of ions just above the step. For the interpretation of the experimental results, a stochastic model was formulated to describe the change in the charge state fraction and energy loss of ions traveling along a surface reflecting trajectory. It was shown from the model that the difference of energy losses of scattered He^+ and He^{2+} ions is useful to derive the position-dependent charge-exchange probabilities of scattered He ions. With the use of the relations of charge state distributions and energy losses of scattered He ions derived from the stochastic model, the charge exchange probabilities of MeV He ions at the (100) surface of SnTe were derived, which depend on the distance from the surface plane.

REFERENCES

1) J. Lindhard, Kgl. Danske Videnskab. Selskab. Mat. Fys. Medd. 34 No.14 (1965).

2) D. S. Gemmell, Rev. Mod. Phys. 46 (1974) 129.

3) K. Kimura, M. Hasegawa, Y. Fujii, M. Suzuki, Y. Susuki and M. Mannami, Nucl. Instrum. and Methods B 33 (1988) 358.

4) M. T. Robinson, Phys. Rev. B 4 (1971) 1461.

5) K. Kimura, M. Hasegawa and M. Mannami, Phys. Rev. B 36 (1987) 7.

6) Y. Fujii, S. Fujiwara, K. Narumi, K. Kimura and M. Mannami, Surf. Sci. 277 (1992) 164.

7) Y. Fujii, S. Fujiwara, K. Kimura and M. Mannami, Nucl. Instrum. and Methods B 58 (1991) 18.

8) M. Mannami, Y. Fujii and K. Kimura, Surf. Sci. 204 (1989) 213.

9) Y. Fujii, K. Kimura, M. Hasegawa, M. Suzuki, Y. Susuki and M. Mannami, Nucl. Instrum. and Methods B 33 (1988) 405.

10) S. K. Allison, J. Cuevas and M. Garcia-Munoz, Phys. Rev. 127 (1962) 792.

11) M. N. Huberman, Phys. Rev. 127 (1962) 799.

12) J. Cuevas, M. Garcia-Munoz, P. Torres and S. K. Allison, Phys. Rev. 135 (1964) A335.

13) S. Datz, J. Gomez del Campo, P. F. Dittner, P. D. Miller and J. A. Biggerstaff, Phys. Rev. Lett. 38 (1977) 1145.

14) J. A. Golovchenko, A. N. Goland, J. S. Rosner, C. E. Thorn, H. E. Wegner, H. Knudsen and C. D. Moak, Phys. Rev. B 23 (1981) 957.

15) J. A. Golovchenko, D. E. Cox and A. N. Goland, Phys. Rev. B 26 (1982) 2335.

16) L. F. Pender and H. J. Hay, Nucl. Instrum. and Methods B 4 (1984) 72.

17) N. E. B. Cowern, P. M. Read, C. J. Sofield, L. B. Bridwell, G. Huxtable, M. Miller and M. W. Lucas, Nucl. Instrum. and Methods B 2 (1984) 112.

18) N. E. B. Cowern, P. M. Read, C. J. Sofield, L. B. Bridwell and M. W. Lucas, Phys. Rev. A 30 (1984) 1682.

19) N. E. B. Cowern, P. M. Read, C. J. Sofield, Nucl. Instrum. and Methods B 12 (1985) 43.

20) L. B. Bridwell, N. E. B. Cowern, P. M. Read and C. J. Sofield, Nucl. Instrum. and Methods B 13 (1986) 123.

21) E. M. Bernstein, Nucl. Instrum. and Methods B 40/41 (1989) 205.

22) H. Ogawa, I. Katayama, H. Ikegami, Y. Haruyama, A. Aoki, M. Tosaki, F. Fukuzawa, K. Yoshida, I. Sugai and T. Kaneko, Phys. Rev. B 43 (1991) 11370.

23) H. Ogawa, I. Katayama, H. Ikegami, Y. Haruyama, A. Aoki, M. Tosaki, F. Fukuzawa, K. Yoshida, I. Sugai, Phys. Lett. A 160 (1991) 77.

24) K. Narumi, Y. Fujii, K. Kimura, M. Mannami and H. Hara to be submitted in Surf. Sci.

25) L. B. Bridwell, H. J. Hay, L. F. Pender, C. J. Sofield and P. B. Treacy, Aust. J. Phys. 40 (1987) 125.

26) H. Herman and S. Skillman, "Atomic Structure Calculations", (Englewood Cliffs, N. J., Prentice–Hall, 1963).

27) N. Bohr, Kgl. Danske Videnskab. Selskab. Mat. Fys. Medd. 18 No.8 (1948).

28) N. Bohr and J. Lindhard, Kgl. Danske Videnskab. Selskab. Mat. Fys. Medd. 28 No.7 (1954).

29) K. B. Winterbon, Nucl. Instrum. and Methods 144 (1977) 311.

30) T. Kaneko, Nucl. Instrum. and Methods B 67 (1992) 73.

Chapter 8

A NEW METHOD
TO DETECT SURFACE STEPS BY
SPECULARLY REFLECTED FAST IONS

ABSTRACT

With the use of a computer program for simulation of a trajectory of a MeV light ion at glancing angle incidence on a crystal surface, scattering phenomena of He ions at the (001) surfaces of SnTe crystals were simulated. It is found that the yield and angular distribution of scattered ions from the surface depend sensitively on the step density on the surface. A new method to detect surface step density by measuring the ion yield at glancing angle incidence of MeV ions on the crystal surface is proposed.

8.1. INTRODUCTION

Most of the conventional experimental methods for surface structure studies are not sensitive to the surface defects except for the reflection high energy electron diffraction (RHEED), in which the intensity oscillation of the RHEED pattern from GaAs surface during its epitaxial growth was interpreted as due to the change in density of surface steps. This intensity oscillation is successfully applied to the monitoring of the process of molecular beam epitaxy of GaAs.[1]

For energetic ions incident on a crystal surface, it has been only the yield of secondary electrons that is known to be affected by the surface atomic steps.[2] In our recent experimental studies of glancing angle scattering of MeV light ions at the (001) surface of SnTe, it has been shown that some of the experimental results cannot be interpreted on the assumption of the scattering of ions at an atomically smooth surface.[3-5] For the better understanding of the experimental results, a computer simulation program for ion scattering at crystal surface has been developed.[6] From comparison of the simulated and the experimental results, it has been concluded that by an introduction of steps at the crystal surface, the energy spectra of scattered ions and the ion yield at surface channelling conditions are well explained.[6,7]

In the present Chapter, the scattering of ions at glancing angle incidence of fast He ions at stepped (001) surfaces of SnTe crystal is studied using the computer simulation. The relation between the yield of scattered ions and the density of steps is studied and a new method utilizing the glancing angle scattering of fast ions is proposed for the purpose of characterization of a crystal surface.

8.2. COMPUTER SIMULATION PROGRAM

A computer program was developed for simulation of ion scattering at glancing angle incidence on a (001) surface of NaCl type crystal. The detail of the program will be explained here.

The basic function of the program is to trace its energy and the trajectory of an ion at a crystal surface. For an ion moving in vacuum nearly parallel to a surface at distances larger than $a_o/2$ from the surface atomic layer, where a_o is the interatomic distance, the interaction is described by a continuum surface planar potential. The potential is defined as

$$U(x) = n_p \int_0^\infty V\left(\sqrt{x^2 + R^2}\right) 2\pi R \, dR , \qquad (1)$$

where x is the distance of the ion from the surface atomic plane, n_p is the density of atoms on the surface atomic plane and $V(r)$ is the ion–atom interaction potential.[8] For ions moving in crystal and in vacuum at distances closer than $a_o/2$ from the surface, the interaction is reduced to a series of isolated binary collisions of the ion and atoms. The correlation of the thermal displacements of atoms from their equilibrium positions is neglected and the displacement of each atom is derived with the use of the isotropic

Gaussian distribution defined by the mean square displacement calculated from the Debye temperature Θ_D, for which 150 K is chosen.

The interaction between the ion and target electrons is approximately expressed by an empirical energy loss function,[5]

$$\frac{dE}{dz} = \frac{A}{\sqrt{E}} \exp\left(-\frac{0.15x}{a_{TF}}\right) \ , \qquad (2)$$

where x is the distance of the ion from atomic layer, A is 2000 MeV$^{3/2}$cm^{-1} and 7700 MeV$^{3/2}$cm^{-1} for H$^+$ and He$^+$ respectively, a_{TF} is the Thomas–Fermi screening distance and E is the ion energy.

For the ion–atom interaction potential V(r), the analytical approximation due to Molière was employed,[10] and the angle of deflection in a binary collision is derived with the use of the impulse approximation. The ion deflection due to electronic scattering is also calculated from the energy loss (derived from Eq. (2)): The energy loss is determined continuously along the ion trajectory for an ion moving in the continuum potential, and between succeeding ion–atom binary collisions for ion moving in crystal. The angular deflection of the ion is obtained from the energy loss with the use of the impulse approximation in ion–electron collision. Thus the calculated ion trajectory is made up of a series of linear hops.

The program can handle ion trajectories at the (001) surface of NaCl type crystal, but it can easily be modified for other types of crystal surface. Surface irregularities, *e.g.*, atomic relaxation, rumpling, reconstruction and steps can also be introduced as shown in the next sub–section.

8.3. EFFECT OF SURFACE STEPS ON ION SCATTERING

To specify the direction of motion of an ion, azimuthal angle ϕ measured from the [100] axis parallel to the surface and glancing angle θ measured from the (001) surface plane are defined. The energy of incident He$^+$ ions was chosen to be 0.7 MeV, and the glancing angles of the ions on the (001) surface of SnTe crystal were chosen to be less than the critical angle θ_c for specular reflection, which is determined for the (001) surface with the use of the (001) continuum surface planar potential

$$E\theta_c^2 = U(a_{TF}) \ ,$$

θ_c is 12.2 mrad for 0.7 MeV He ions. More than 5000 ion trajectories were calculated for a set of initial glancing and azimuthal angles, where the initial ion positions were chosen randomly within an imaginary unit cell at $3a_0$ ($a_0 = 3.14$ Å for SnTe) above the surface. For each incident ion, steps of atomic height, which were parallel to the [010] axis, were introduced on the (001) surface of SnTe crystal. The step separation was random, where only the mean separation, D_s, was given to introduce the

steps. Upward and downward steps viewed from the incident ions were also introduced randomly.



(a)

(b)
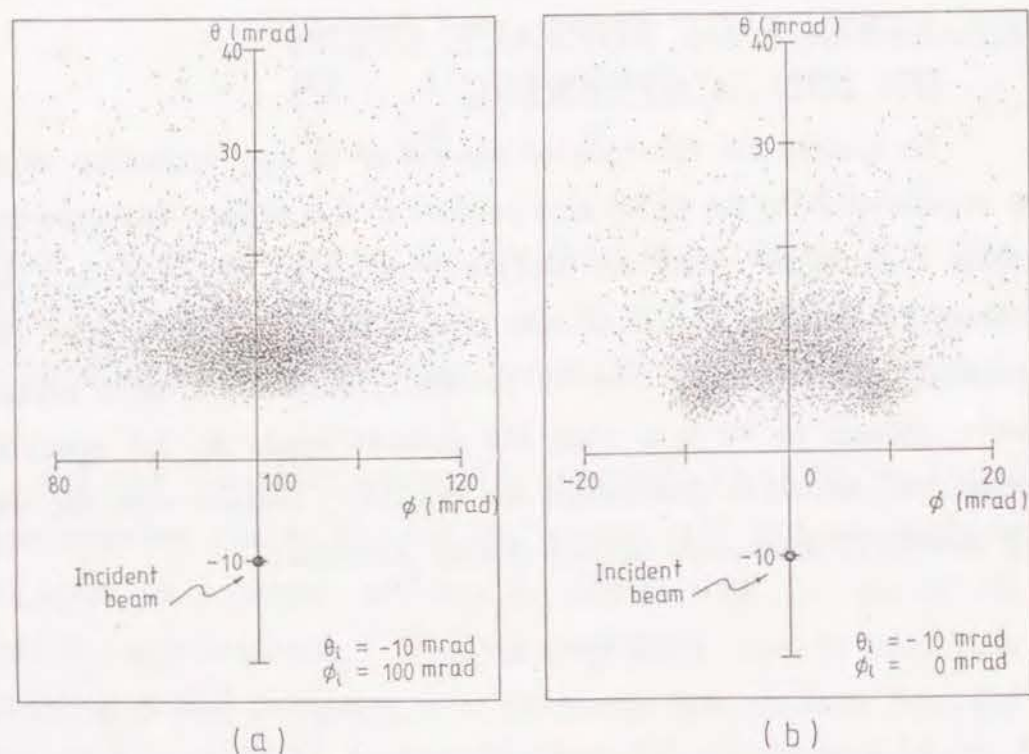
Figure 8.1: Angular distributions of scattered ions at glancing angle incidence of 0.7 MeV He⁺ ions on a flat (001) surface of SnTe. (a) Specular reflection; glancing angle θ_i = 10 mrad, azimuthal angle relative to the [100] axis ϕ_i = 100 mrad. (b) Surface channelling; glancing angle θ_i = 10 mrad, azimuthal angle ϕ_i = 0 mrad.
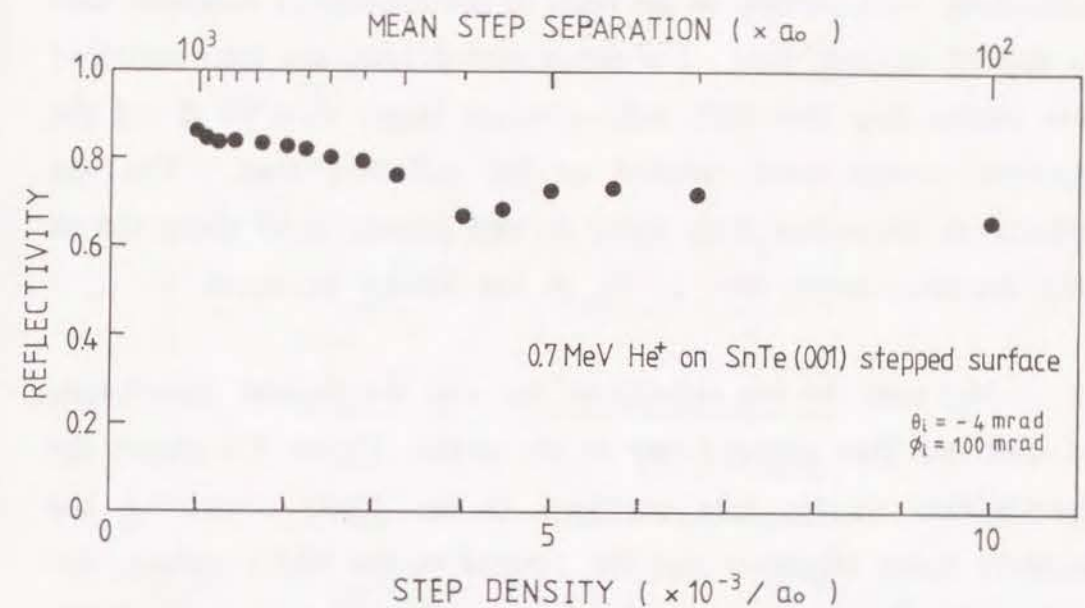
Figure 8.1 shows examples of the calculated angular distributions of He ions scattered from a flat (001) surface of SnTe when the glancing angle θ_i of the incident 0.7 MeV He⁺ ions was 10 mrad. The angular distribution of scattered ions at random incidence is shown in Fig. 8.1(a), where the incident azimuthal angle ϕ_i is 100 mrad. The distribution has a maximum at the direction of specular reflection $\theta = \theta_i$. Due to the multiple nuclear and electronic scattering, the scattered ions are not sharply distributed at the specular reflection angle. In this orientation of the incident He ions, the closest approach of the ions to the surface atomic plane derived from the continuum approximation using Eq. (1) is 1 Å, and thus the incident He⁺ ions can hardly penetrate the surface atomic plane. This is seen in the energy spectrum of scattered ions at the specular reflection angle (Fig. 8.2(a)), where only a peak is seen at the energy slightly less than the energy of incident ions and this is consistent with the fact that no ion penetrates the surface atomic layer.[5] On the other hand, when ϕ_i = 0 mrad, *i.e.* at the [100] surface channelling condition, the scattered ions show an arc pattern due to the reflection of ions by the [100] atomic rows (Fig. 8.1(b)). In this orientation, some of the incident ions can penetrate the surface in between the [100] atomic rows and the yield of reflected ions decreases.

In the following, we will be interested only in the ion scattering at random incidence on the stepped (001) surface of SnTe. At glancing angles less than the critical angle for specular reflection, a fraction of incident ions penetrate the surface at steps,
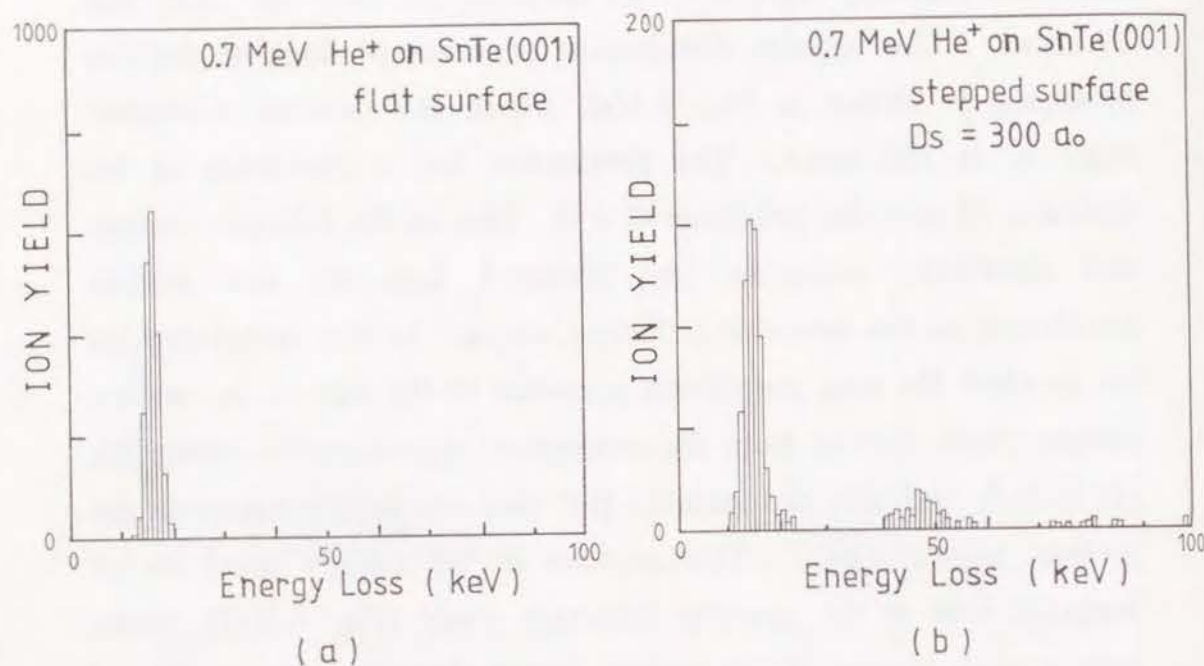
Figure 8.2: Energy spectra of reflected ions in a window 2×2 mrad^2 centered at $\theta = 4$ mrad and $\phi = 100$ mrad, when the glancing and azimuthal angles of incident 0.7 MeV He$^+$ ions are $\theta_i = 4$ mrad and $\phi_i = 100$ mrad respectively (random incidence): (a) On a flat (001) surface. (b) On a stepped surface with mean step separation $D_s = 300a_o$.

Figure 8.3: Dependence of the reflectivity of 0.7 MeV He$^+$ at the (001) surface of SnTe on the step density, where the glancing and azimuthal angles of the incident He$^+$ ions are 4 mrad and 100 mrad respectively. The ions which are trapped in the crystal after travelling in the crystal more than $4000a_o$ are counted as the trapped ions.

because step edges are exposed to the incident ions. Most of the ions which have penetrated into the crystal at the step edges are trapped in between the (001) atomic planes parallel to the surface, *i.e.* the (001) planar channeling occurs. Some of them can emerge

out of the crystal mostly at down steps. Thus the energy spectrum of the ions scattered from the stepped surface has components with larger energy losses as shown in Fig. 8.2(b), since the ions reflected inside the crystal suffer larger energy losses. For the incidence of

0.7 MeV He ions with glancing angle $\theta_i = 4$ mrad, the calculated ion reflectivity is shown in Fig. 8.3. In the calculation the ions reflectivity was defined as the ratio of the number of scattered ions to that of incident ions. For the scattered ions, the ions scattered into angles less than $10\theta_i$ with energies larger than 90 % of the incident energy were counted as the reflected ions. The ion reflectivity decreases from unity at step density 0 to about 0.6 at step densities larger than $10^{-2}/a_o$ as the density increases.

Not only the ion reflectivity but also the angular distribution of scattered ions changes due to the steps. Figure 8.4 shows the distributions of He ions scattered in the plane containing the incident beam direction and the normal to the (001) surface, $i.e.$ along the line connecting the incident beam position and the specular reflection position in Fig. 8.1(a). For each curve, trajectories of 5000 ions were calculated where the glancing angle of incident 0.7 MeV He ions was set at 4 mrad. The distributions have maxima at scattering angle $\theta = 4$ mrad. As the step density, $1/D_s$, increases, the full width at half maxima (FWHM) of the distribution becomes larger and its peak height becomes smaller. From these angular distributions, the step density dependence of the yield at the specular reflection angle was obtained and is shown in Fig. 8.5. In the figure, the yield decreases steadily with the increasing step density and becomes almost independent of the step density at the step densities larger than about a_o/θ_i.
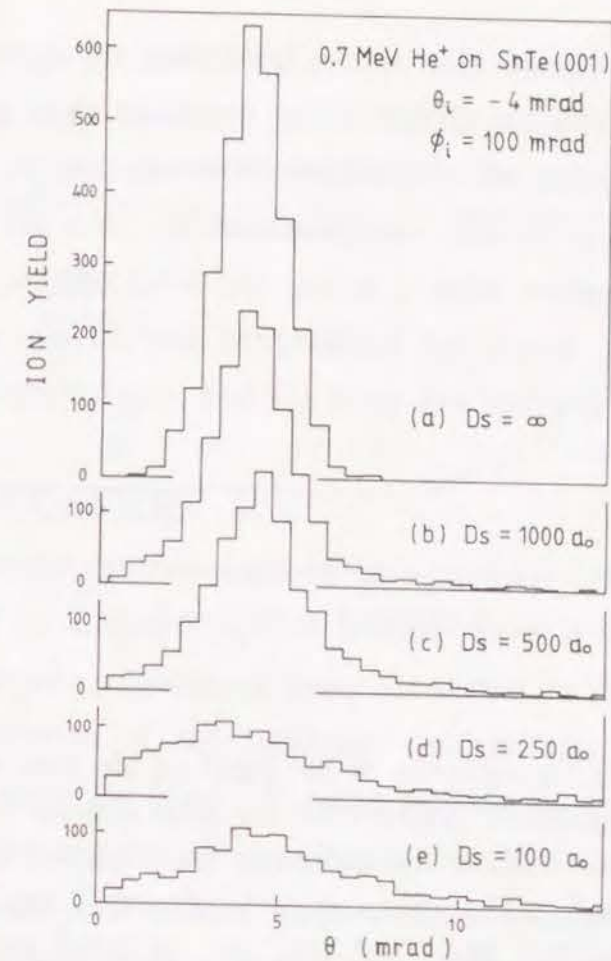
Figure 8.4: Angular distributions of He ions scattered in the plane containing the direction of incident ions and the normal to the (001) surface. The window for accepting the scattered ions has widths, $\Delta\theta = \pm 0.25$ mrad and $\Delta\phi = \pm 1.0$ mrad, and the number of incident He$^+$ ions was 5000. The glancing and azimuthal angles of the incident 0.7 MeV He$^+$ ions are -4 mrad and 100 mrad respectively. The mean step separations D_s are (a) ∞, (b) $1000a_o$, (c) $500a_o$, (d) $250a_o$ and (e) $50a_o$.
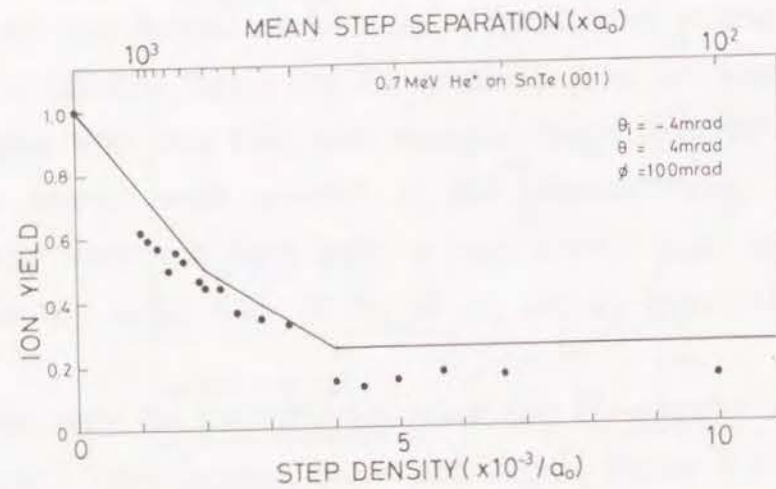
Figure 8.5: Dependence of the yield of He ions at the specular reflection position on the step density $(1/D_s)$. The detector window for accepting the scattered ions is 1×1 mrad^2. The glancing and azimuthal angles of the incident 0.7 MeV He$^+$ ions are -4 mrad and 100 mrad respectively. The solid line shows the calculated yield using Eq. (3).

The energy spectrum of scattered ions, the ion reflectivity, the yield of ions at specular reflection angle and the FWHM of the angular distribution depend on the step density. From the comparison of the calculated results, it is concluded that the yield of ions at specular reflection angle changes most sensitively with the step density.

Although the calculated results only for the 0.7 MeV He ions at glancing angle incidence on SnTe(001) are presented here, similar scattering phenomena were obtained in the calculations for 0.5 to 1.5 MeV He ions. Considering the role of surface steps in the scattering process of a fast ion at a solid surface, we expect that the similar results will be obtained for crystal surface with other crystal structure types and for other ion species.

8.4. DISCUSSION

The yield of ions scattered at a specular reflection angle can be derived by a simple optical model: Four possible geometrical relations of two neighboring steps are shown in Fig. 8.6, which are equally probable if the existence probabilities of upward and downward steps are equal. For ions incident on the stepped surface with glancing angle θ_i, it is assumed that the terrace area which is exposed to the ions reflects the ions at the specular reflection angle and that the ions incident at the step edges penetrate in the crystal. The ion yield at the specular reflection angle $Y(D_s)$ is expressed as

$$
Y(D_s) = \begin{cases} 1 - \dfrac{a_o}{D_s \theta_i} & \left(D_s > \dfrac{2a_o}{\theta_i} \right) , \\[2ex] \dfrac{3}{4} - \dfrac{a_o}{2 D_s \theta_i} & \left(\dfrac{2a_o}{\theta_i} > D_s > \dfrac{a_o}{\theta_i} \right) , \\[2ex] \dfrac{1}{4} & \left(D_s < \dfrac{a_o}{\theta_i} \right) . \end{cases} \tag{3}
$$
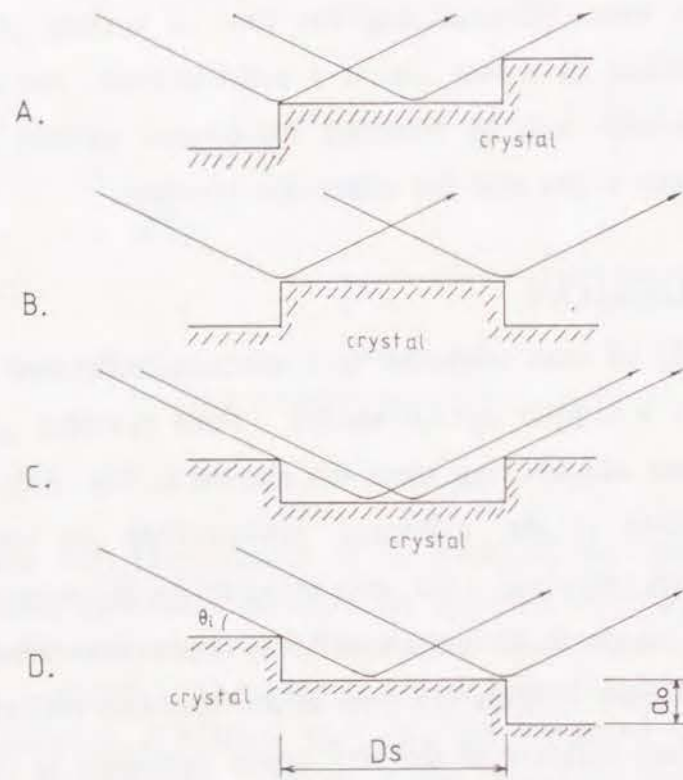
Figure 8.6: Step terrace structures between neighboring steps. Four structural types are equally probable if the densities of upward and downward steps are equal.

The ion yield, Eq. (3), is independent of mean step separation, D_s at step separations smaller than a_o/θ_i, which shows that the incident ions are reflected only at the terrace of type B structure shown in Fig. 8.6 and that the terraces of other types are not exposed to the incident ions. The ion yield given by Eq. (3) is drawn by a solid line in Fig. 8.5. The agreement of the solid line with the simulated results is rather good considering the crude model used in deriving Eq. (3).

The simulated results show that the glancing angle scattering of energetic ions is affected by the existence of steps on the surface. The yield of ions at the specular reflection angle and the ion reflectivity are the quantities which are sensitive to the step density. These quantities are also easily and quickly measured by ion detector. Therefore, it is proposed to use the ion reflectivity or yield of ions at specular reflection angle to detect the density of surface steps. If the layer–by–layer growth occurs by formation of two dimensional nuclei on a surface of a crystal, the step density on the surface will change periodically during the growth. Thus the yield of scattered ions at glancing angle incidence of MeV light ions on the surface will oscillate during the growth of the crystal. Although the probe particles are different, this is a method equivalent to the RHEED intensity measurement, which is currently used to monitor the MBE growth of GaAs or related compound semiconductors.

REFERENCES

1) J. J. Harris and B. A. Joyce, Surf. Sci. Lett., 108 (1981) L441.

2) W. Grazer and C. Varelas, Surf. Sci. 157 (1985) 74.

3) M. Mannami and K. Kimura, Nucl. Instrum. and Methods B27 (1987)442.

4) K. Kimura, A. Nishimura and M. Mannami, Surf. Sci. Lett.183 (1987) L313.

5) K. Kimura, M. Hasegawa and M. Mannami, Phys. Rev. B36 (1987) 7.

6) Y.Fujii, K. Kimura and M. Mannami, Proc. 12th International Conference on Atomic Collisions in Solids

7) K. Kimura, M. Hasegawa, Y. Fujii, M. Suzuki, Y. Susuki and M. mannami, Proc. 12th International Conference on Atomic Collisions in Solids

8) J. Lindhard, Dan. Vidensk. Selsk. Mat.–Fys. Medd. 34 (1965) no. 14.

9) E. R. Cowley, J. K. Darby and G.S. Pawley, J. Phys. C2 (1969) 1916.

10) G. Molière, Zeit. f. Naturfor. 2a 133 (1947).

Chapter 9

PROCESS OF EPITAXIAL GROWTH OF PbSe ON SnTe (001) STUDIED BY GLANCING ANGLE SCATTERING OF MeV He IONS

ABSTRACT

Process of epitaxial growth of PbSe on SnTe (001) under UHV conditions is studied with the use of glancing angle scattering of MeV He ions and transmission electron microscopy. An empirical relationship of the mean separation of misfit dislocations on the PbSe/SnTe interface and the thickness of the layer is derived from TEM observation. Anomalous broadening of the angular distribution of scattered He ions from the surface of PbSe is observed when the thickness of the PbSe layer is between 1 and about 20 nm. From the simulation of ion trajectories at glancing angle scattering from several model surfaces, this anomaly is attributed to the surface wrinkles caused by a square−net of misfit edge dislocations.

9.1. INTRODUCTION

Glancing angle scattering of MeV light ions at a crystal surface was first studied by a group at the University of Sussex,[1] and then by a group at Universität München in relation to the surface channelling of ions.[2] We have studied the glancing angle scattering of MeV H and He ions at SnTe and PbSe (001) surfaces under UHV conditions and have shown that most of the ions are reflected at the topmost atomic layer without penetrating the crystal surface. Thus the closest approach of the reflected ions to the surface atoms can be controlled to be less than 0.1 nm by changing the angle of incidence of the ions to the surface. We can, therefore, study the interactions of the ions which take place outside the solid.[3-8]

In the analyses of the experimental results at specular reflection of MeV ions from clean surfaces,[6,8] we found that the surface steps have considerable effect on the angular distribution, energy loss and charge state distribution of the scattered ions as has been pointed out by Graser and Varelas.[9] From the computer simulation of ion trajectories at glancing angle incidence on a clean (001) surface of SnTe, we showed that the quantity which is most affected by the surface steps is the yield of ions scattered at the angle of specular reflection. We therefore proposed to use the glancing angle scattering of MeV ions for the study of surface steps in Chapter 8.[10] If the layer-by-layer growth takes place, it is expected that the scattering of ions from the growing surface shows periodic changes as the RHEED intensity oscillations from the epitaxial GaAs surface during its MBE growth.[11]

Epitaxial growth of lead chalcogenide crystals and the misfit dislocations formed on the interfaces of the epitaxial bicrystals have been extensively studied by Mathews[12] and Honjo and Yagi[13] with TEM. Our preliminary studies of the PbSe/SnTe system have shown that the misfit dislocations are formed at the interface and that pseudomorphic growth of PbSe takes place when the thickness is less than about 3 monolayers (~1 nm).[14,15] Based on these studies, we report here on our application of the glancing angle scattering of MeV ions to the study of epitaxial growth of PbSe crystal on SnTe(001) under UHV conditions.

9.2. EXPERIMENTAL

The experimental setup is shown in Fig. 9.1. A beam of 0.7 MeV He$^+$ ions from the 4 MV Van de Graaff accelerator of Kyoto University was collimated by a series of apertures to a diameter less than 0.03 mm and to a divergence angle less than 0.06 mrad. The beam was introduced in a UHV scattering chamber (base pressure 3×10^{-10} Torr) via a differential pumping section. A target crystal mounted in a 5-axis precision goniometer was irradiated by the beam at glancing angles less than 10 mrad (~0.6°) to the surface. For the preparation of target crystals we installed two evaporation guns in the scattering chamber. A single crystal of SnTe(001) was grown first on the cleavage surface of 30×30 mm^2 KCl(001) and the PbSe crystal (purity 99.99 %) was
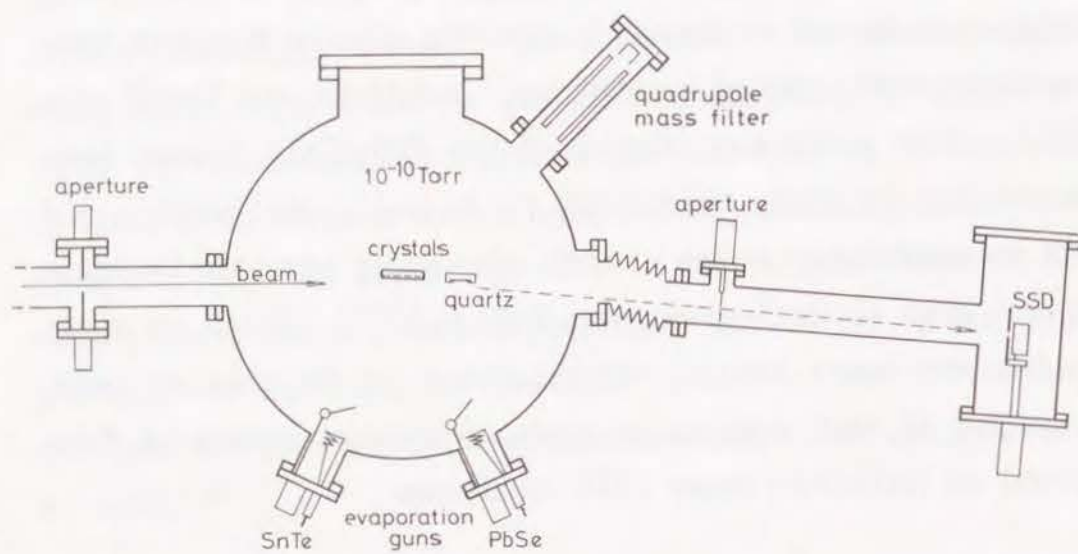
Figure 9.1: Experimental setup for the glancing angle scattering of MeV He ions.

subsequently prepared by epitaxial growth on the SnTe/KCl(001) at a substrate temperature of 200 °C. The growth rate of PbSe was less than 3 monolayers (~1 nm) per hour at the first several monolayers. Thickness of the epitaxial PbSe crystal was monitored with a quartz oscillator microbalance which had been calibrated by RBS. The vacuum was better than 2×10^{-9} Torr during the

growth, and most of the measurements were done at a vacuum in the 10^{-10} Torr range. Glancing angle scattering of He ions was continuously measured during the growth of the PbSe crystal.

For the measurement of the angular distribution of the scattered He ions in the plane containing the normal to the surface and the incident beam, the scattered He ions were selected by an aperture of acceptance half angle 0.33 mrad downstream of the crystals. The direction of incident He^+ beam was carefully adjusted so that surface channelling does not occur. The yield of ions was normalized by the incident ion dose. Energy spectra of the ions were measured with a solid state detector (energy resolution was 15 keV for 0.7 MeV He ions).

In order to study the dependence of the density of misfit dislocations on the thickness of the PbSe layer, TEM observation of the bicrystals was done. For the observation, PbSe/SnTe bicrystals were epitaxially grown on KCl(001) at 200 °C under the conventional vacuum in the 10^{-6} Torr range, since the growth mode of PbSe on SnTe is independent of the vacuum during growth. The thickness of the evaporated PbSe was monitored with a quartz oscillator microbalance. The substrate KCl crystals were dissolved in water and the PbSe/SnTe bicrystals were observed with a transmission electron microscope (HU-11, Hitachi).

9.3. EXPERIMENTAL RESULTS

9.3.1 Misfit Dislocations

Figure 9.2 shows an electron micrograph of PbSe/SnTe bicrystal, where a square–net of dislocations is observed. The thickness of the PbSe layer is 3 nm. The dislocations are edge type and are parallel to the <110> on the (001) interface. The square–net of the dislocations is not regular at thin PbSe layers but becomes regular at thicker PbSe layers. The mean separations of the dislocations were measured at various thicknesses of PbSe crystals. The result is summarized in Fig. 9.3. The mean separation $S(X)$ of the parallel dislocations decreases with the thickness X of the PbSe layer and becomes constant at PbSe thicknesses larger than about 15 nm. The observed mean separations of dislocations are approximately expressed as,

$$S(X) = \frac{a_1 a_2}{\sqrt{2}(a_1 - a_2)} \cdot \frac{X}{X - \frac{3a_2}{2}} \qquad (X > \frac{3a_2}{2})$$

$$= 17.1 + \frac{15.7}{X - 0.92} \ [\ nm\ ] \quad (X > 0.92) \ ,$$

(1)

where a_1 (= 0.630 nm) and a_2 (= 0.614 nm) are the lattice constants of SnTe and PbSe respectively.

Figure 9.2: An electron micrograph of PbSe/SnTe bicrystal, where PbSe is 3 nm thick. Dislocations are parallel to the <110> axes on the (001) interface.
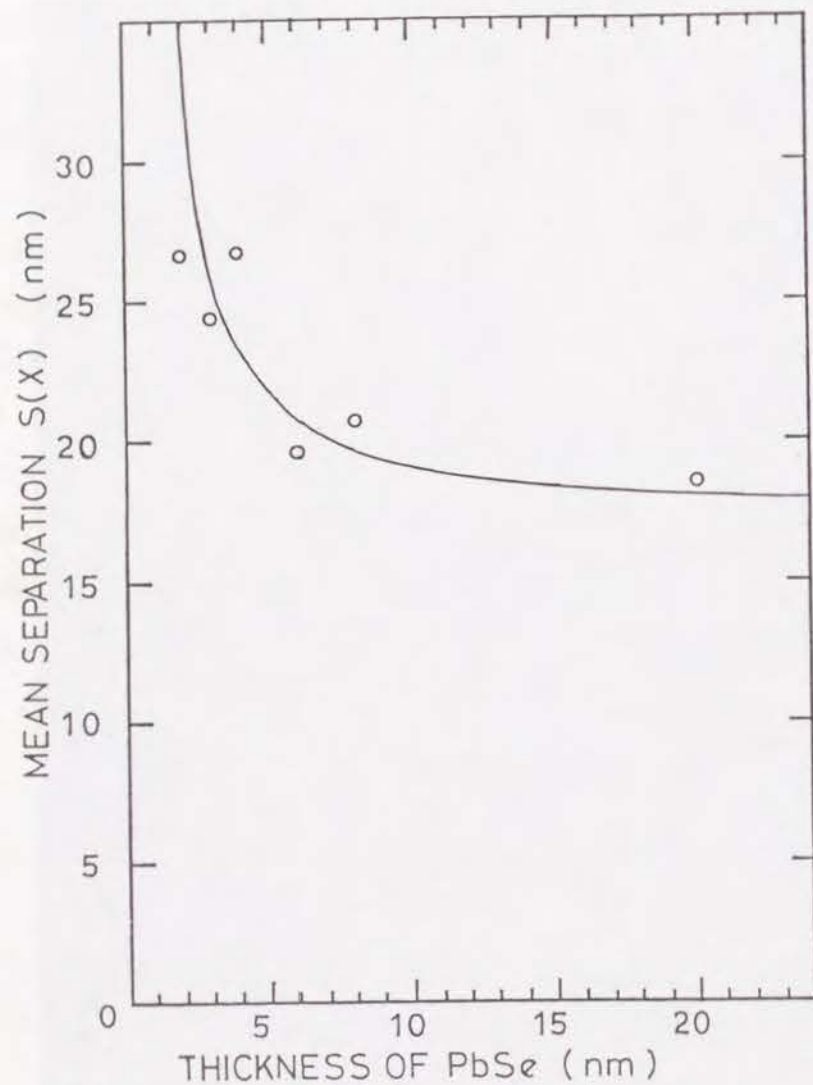
Figure 9.3: Observed dependence of the mean separation S(X) of dislocations on the thickness X of PbSe crystal. The solid line shows the empirical formula.

9.3.2 Angular and Energy Distributions of Reflected Ions

Energy spectra of the specularly reflected He ions from the PbSe/SnTe bicrystals of various thicknesses of PbSe layers are shown in Fig. 9.4. At the incidence of 0.7 MeV He^+ ions on the (001) surface of the substrate SnTe crystal with glancing angle 5 mrad, the spectrum shows the multi–peak structure as shown in Fig. 9.4(a). The highest energy peak (the first peak) is due to the ions reflected at the topmost atomic plane and the other peaks are due to the ions penetrating the crystal surface. The ions penetrate the surface at upward steps and channel through the (001) planar channels parallel to the surface, and then emerge from the surface at downward steps with larger energy losses. These ions form the peaks at lower energies in the energy spectra, which depend on the density and distribution of the steps.[6,8] As the thickness of the PbSe crystal increases to about 3 nm, (Fig. 9.4(d) and (e)) the energy spectrum was blurred and the multi–peak structure disappears. The multi–peak structure appears again when the PbSe layer becomes thicker than about 20 nm as seen in Fig. 9.4(f) and (g).

The angular distribution of scattered ions also changed drastically with the increasing thickness of the PbSe layer. A few examples of the angular distributions of the scattered He ions during the growth of PbSe are shown in Fig. 9.5 at 0.7 MeV He incidence with glancing angle 5 mrad. The distributions have a peak at $\theta_s = 2\theta_i$, where θ_i is the angle of incidence. We defined
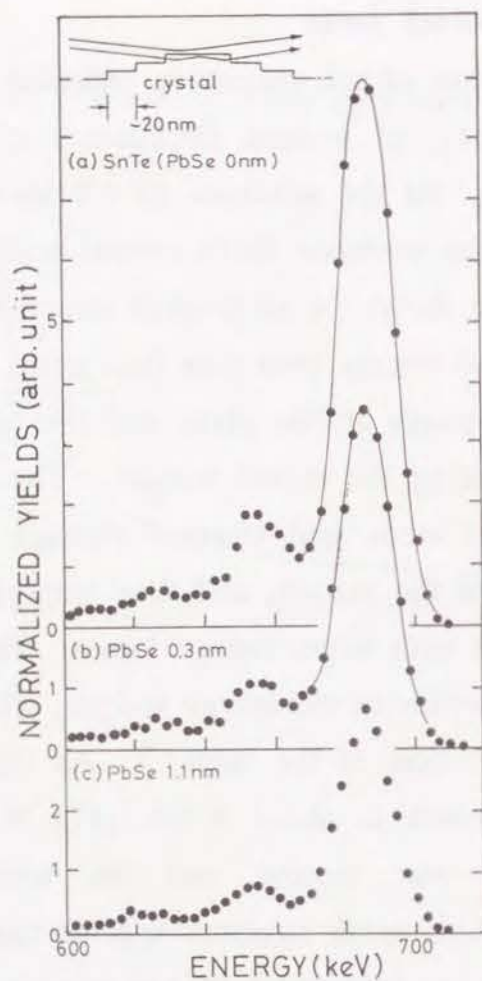
Figure 9.4(a)–(c): Energy spectra of specularly reflected ions at the incidence of 0.7 MeV He$^+$ ions on the PbSe/SnTe during the growth of PbSe. The glancing angle of incident beam was 5 mrad, and the azimuthal angle relative to the [100] on the (001) surface of SnTe was 50 mrad. Thicknesses of PbSe layers are indicated. The inset in (a) shows the terraced surface which gives rise to the energy spectrum showing the clear multi–peak structure.
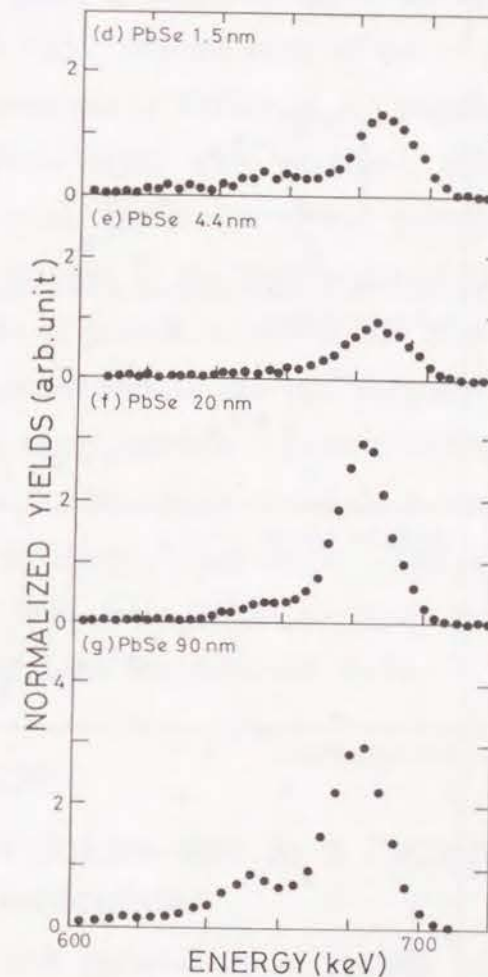
Figure 9.4: Energy spectra of specularly reflected ions at the incidence of 0.7 MeV He$^+$ ions on the PbSe/SnTe during the growth of PbSe. The glancing angle of incident beam was 5 mrad, and the azimuthal angle relative to the [100] on the (001) surface of SnTe was 50 mrad. Thicknesses of PbSe layers are indicated.
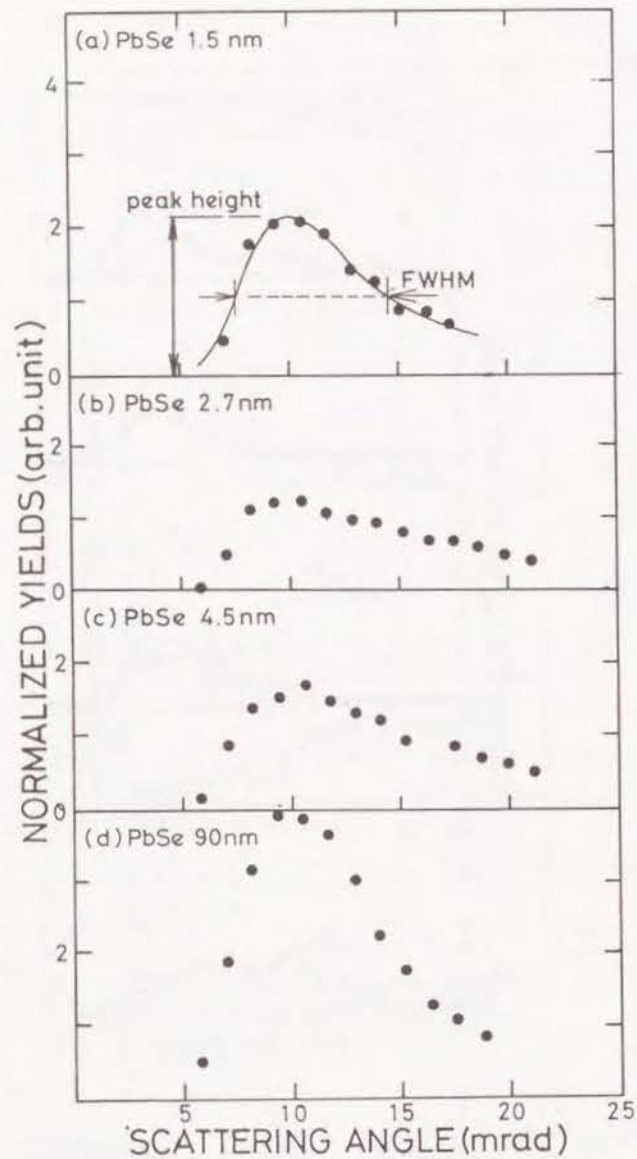
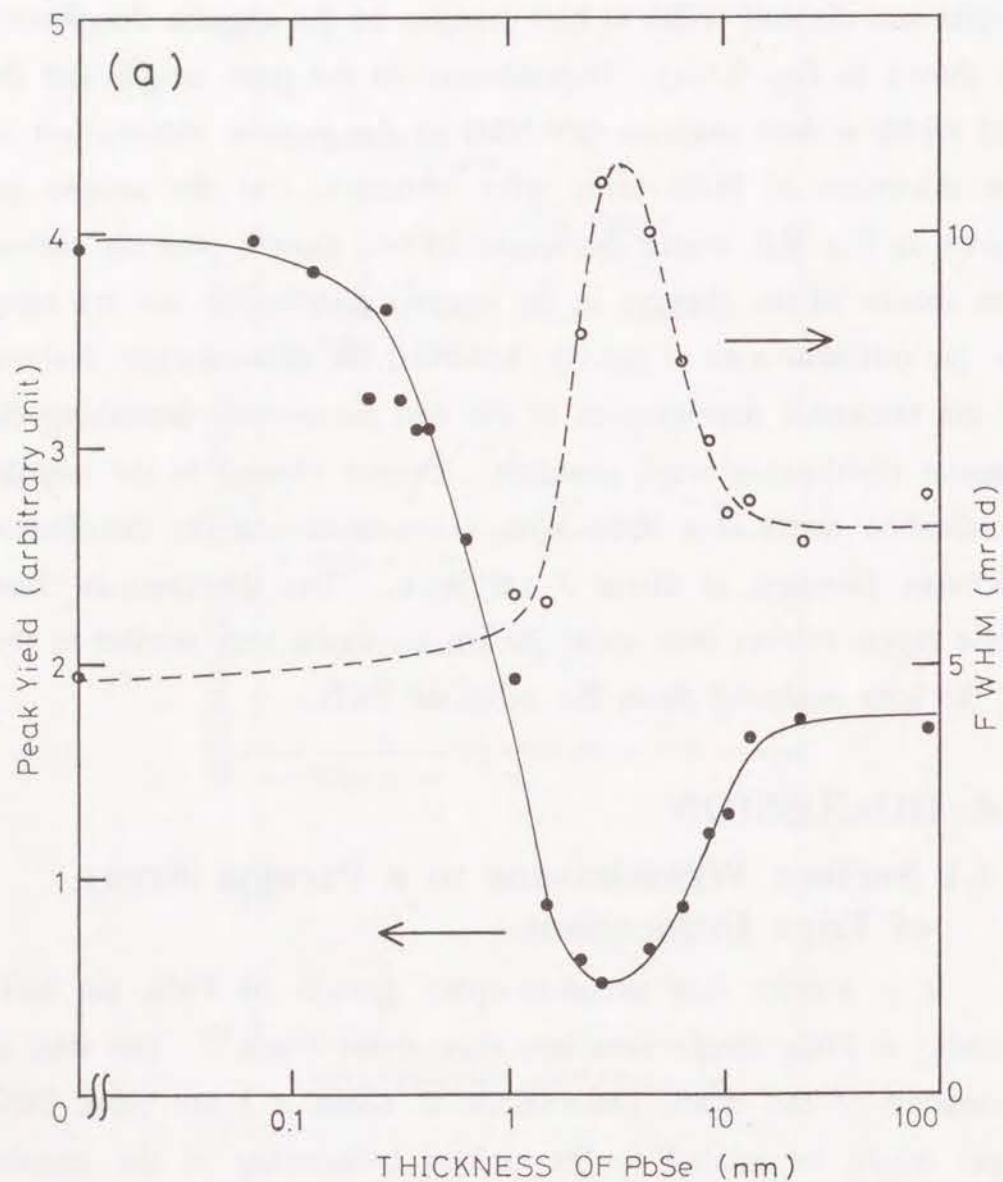**Figure 9.5:** Change in the angular distributions of the scattered He ions at the incidence of 0.7 MeV He$^+$ on the (001) surfaces of PbSe/SnTe during the growth of PbSe. The glancing angle of the beam was 5 mrad. The thicknesses of PbSe layers are indicated.

two parameters to specify the distributions; these are the peak height and the full width at half maxima of the angular distribution as shown in Fig. 9.5(a). Dependences of the peak height and the full width at half maxima (FWHM) of the angular distribution on the thickness of PbSe layer were obtained, and the results are shown in Fig. 9.6, where the results of two growth runs are shown. The details of the changes in the angular distribution are not equal for the different runs of growth, however, the characteristic features of the thickness dependences of the two parameters describing the angular distribution were common. Drastic change in the angular distribution starts at a PbSe layer 1 nm thick and the distribution becomes broadest at about 3 nm thick. The distributions from PbSe layers thicker than about 20 nm are again very similar to that of the ions scattered from the substrate SnTe.

9.4. DISCUSSION

9.4.1 Surface Wrinkles due to a Parallel Array of Edge Dislocations

It is known that pseudomorphic growth of PbSe on SnTe occurs at PbSe thicknesses less than about 1 nm.[15] The start of formation of the misfit dislocations at about a 1 nm thick PbSe layer might be related to the sudden broadening of the angular distribution. It was not easy to relate the changes in both the angular distribution and the energy spectrum that occur at a PbSe layer 3 nm thick and the density of misfit dislocations.

Figure 9.6(a): Dependences of the peak height and FWHM of the angular distribution of scattered He ions on the thickness of PbSe on SnTe (001) at the incidence of 0.7 MeV He$^+$ with glancing angle 5 mrad. Result of one of two growth runs is shown.
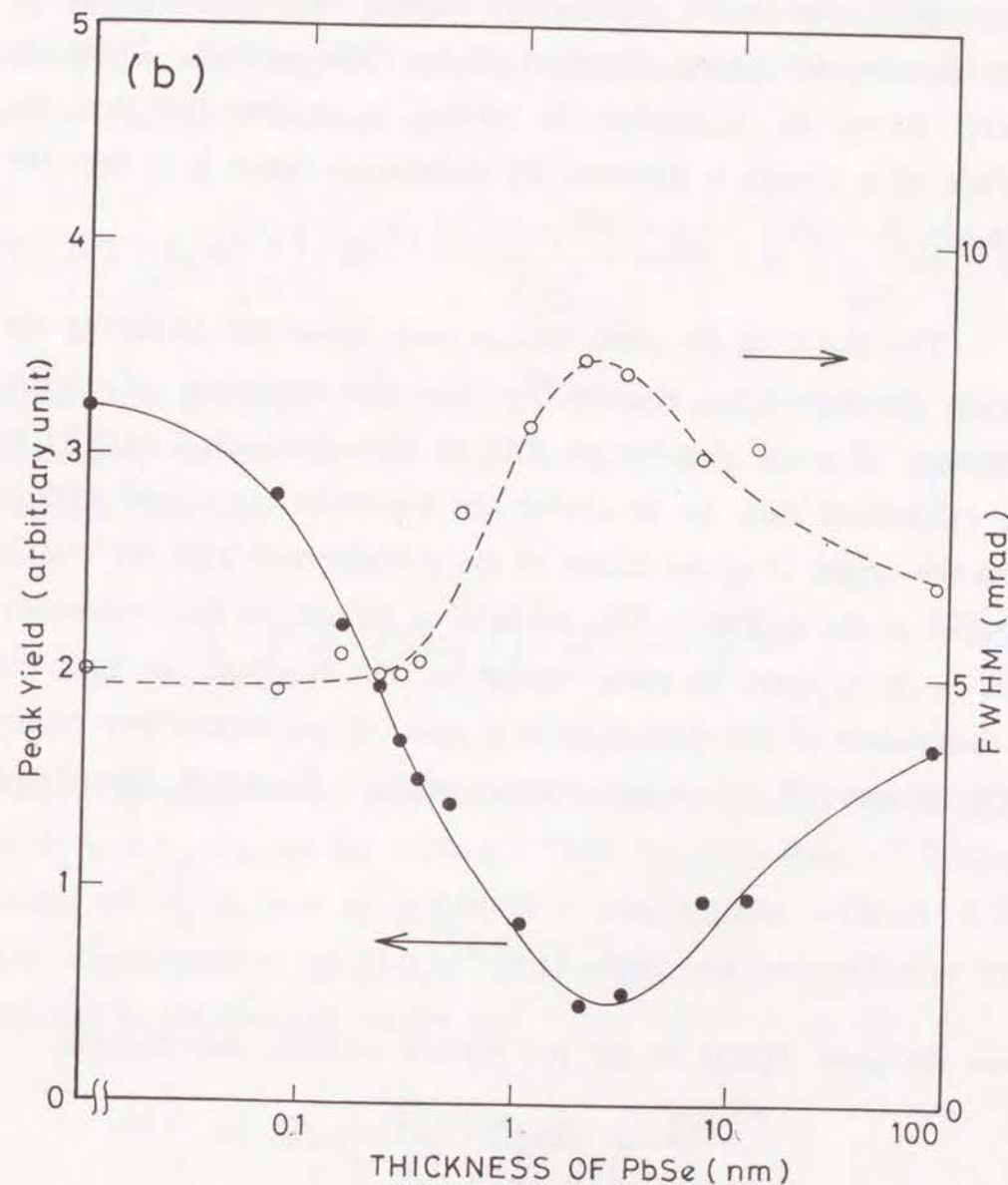
Figure 9.6(b): Dependences of the peak height and FWHM of the angular distribution of scattered He ions on the thickness of PbSe on SnTe (001) at the incidence of 0.7 MeV He$^+$ with glancing angle 5 mrad. Result of one of two growth runs is shown.

In order to relate the formation of dislocations and the observed change in the angular distribution of scattered ions, we first consider the elastic distortion of the PbSe surface. From the elastic theory of dislocation in crystal, it is expected that the surface of a crystal is distorted by dislocation when it is near the surface.

The shape of the solid surface was calculated following the theory developed by Eshelby.[16] For the treatment of elastic distortion of a rod of radius A with an edge dislocation parallel to the cylindrical axis, let us choose the Cartesian coordinate system with the origin O at the center of the cylinder and with the z-axis parallel to the cylinder. The cylinder is infinite in the z-direction and is in a state of plane strain in the xy-plane so that the z-component of the displacement is zero. If we choose two points $P_1(\xi_1,0)$ and $P_2(\xi_2,0)$ on the x-axis, where ξ_1 and ξ_2 are related by

$$\xi_1 \xi_2 = A^2 \ ,$$

then the point P(x,y) on the rod surface satisfies the relations,

$$\frac{r_1}{r_2} = \frac{A}{\xi_1} = \frac{\xi_2}{A} \ ,$$

where $r_1 = \mathbf{r}_1 = PP_1$ and $r_2 = \mathbf{r}_2 = PP_2$.

Suppose that the edge dislocation is eccentric at $(\xi_2,0)$ inside the cylinder and the Burgers vector is $\mathbf{b} = (0,-b)$. Airy stress function χ satisfying the boundary condition that the stress is zero at the surface is derived as,[17]

$$\chi = D(x - \xi_2)\ln\left(\frac{r_2}{r_1}\right) + D\frac{(\xi_1 - \xi_2)(x - X)(x - \xi_1)}{\xi_2 r_1^2} + D\frac{(\xi_1 - \xi_2)r^2}{2A^2}, \quad (2)$$

where $X = (\xi_1+\xi_2)/2$, $D = -\mu b/2\pi(1-\nu)$, and μ and ν are the elastic constants. In the limit of large A, $A-\xi_1 = \xi_2-A = X$, the Airy function becomes

$$\chi = D\cdot(x + X)\cdot\ln\left(\frac{r_2}{r_1}\right) + 2D\cdot\frac{Xx(x - X)}{r_1^2} \ , \quad (3)$$

where the origin of the coordinate is displaced to the middle point of P_1 and P_2, i.e. on the surface. Thus the dislocation of Burgers vector $(0,-b)$ is now at $(-X,0)$ in a semi-infinite solid $(x < 0)$. The displacements u(x,y) and v(x,y) which are perpendicular and parallel to the Burgers vector are

$$u(x,y) = \frac{1-\nu}{2\mu}\int \nabla^2 \chi dx - \frac{1}{2\mu}\frac{d\chi}{dx} \ ,$$

$$v(x,y) = \frac{1-\nu}{2\mu}\int \nabla^2 \chi dy - \frac{1}{2\mu}\frac{d\chi}{dy} \ .$$

Taking account of the boundary conditions, we obtain the components of the displacement at the surface as

$$u(0,y) = \frac{b}{\pi} \frac{X^2}{X^2+y^2} \quad , \tag{4}$$

$$v(0,y) = \frac{b}{\pi}\left[\frac{Xy}{X^2+y^2} - \tan^{-1}\left(\frac{y}{X}\right)\right] \quad . \tag{5}$$

The shape of the surface is determined approximately by u and it has a maximum at y = 0, *i.e.* just above the dislocation. For a regular array of edge dislocations situated at the depth X from the surface, the x-component of the surface displacement (perpendicular to the surface) is expressed by the superposition of that of individual dislocation as

$$U(0,y) = \sum_{n=-\infty}^{n=\infty} u(0,y+nS)$$

$$= \frac{bd}{S} \frac{\sinh(\frac{2\pi X}{S})}{\cosh(\frac{2\pi X}{S}) - \cos(\frac{2\pi y}{S})} \quad , \tag{6}$$
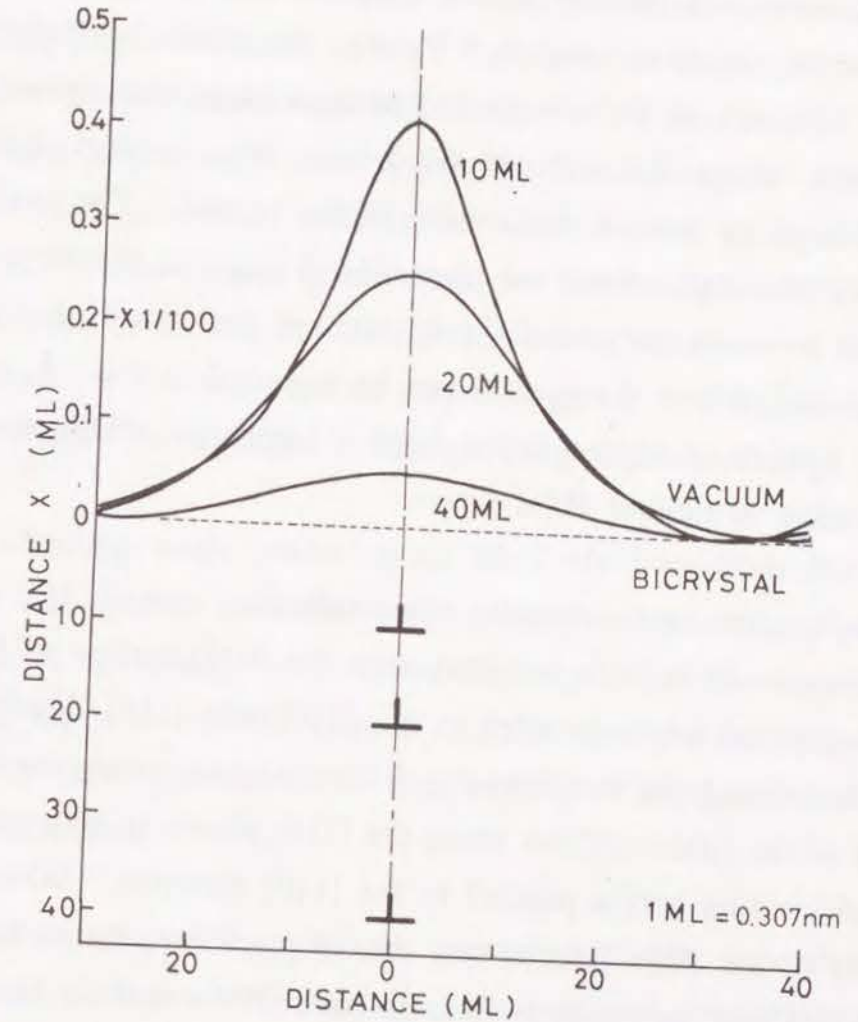
Figure 9.7: Cross sectional views of the wrinkled surfaces of PbSe/SnTe bicrystals. The length in the x-direction in a vacuum is elongated 100 times as large as that parallel to the surface. Thicknesses of the PbSe layers are 10 ML (= 3.1 nm), 20 ML (= 6.1 nm) and 40 ML (= 12.2 nm).

where S is the separation of the edge dislocations. Substituting the empirical relation, Eq. (1), into Eq. (6), the surface shape was calculated, assuming that the elastic properties of PbSe layer and SnTe substrate are equal. Figure 9.7 shows the calculated surfaces, $U(0,y) - U(0,S/2)$, of PbSe/SnTe bicrystals at three thicknesses of PbSe layers, where the scale of the x-axis in a vacuum is 100 times as large as that of the x-axis in the crystal. The surface protrudes at the dislocations; the protrusion is larger at thinner PbSe layers but becomes very small at thicknesses more than about 60 ML ($\sim$20 nm), where the surface can be regarded as flat. It must be noted that the distortion is too large to apply the elastic theory of dislocation at thinner PbSe layers.

There are two mutually perpendicular arrays of edge dislocations in PbSe/SnTe bicrystal, thus the (001) surface of PbSe has two sets of ridges parallel to the [110] and [110] directions. The distorted surfaces shown in Fig. 9.7 are approximately the cross sections of the (001) surfaces along the (110) planes in between the set of dislocation arrays parallel to the [110] direction. When the thickness of the PbSe layer is less than about 5 nm, the surface is so wrinkled that the gradient at some parts of the surface becomes comparable to the angle of incidence of the beam to the surface. The reflection of ions are thus expected to be affected by the wrinkles.

9.4.2 Mode of Epitaxial Growth of PbSe on SnTe (001)

It is known that the angular distribution of scattered ions at glancing angle incidence of MeV light ions on the SnTe surface is affected by the distribution and density of surface steps. Surface with high step density gives rise to the broader angular distribution of reflected ions, thus yielding the smaller peak yield and larger FWHM.[10] The present observation that the details of the observed dependence of the angular distribution on the thickness of PbSe are not equal for different runs of growth suggests that the existence of steps cannot be neglected in the glancing angle scattering.

Glancing angle scattering of MeV He ions from thin PbSe layers was studied in detail, but we could not detect any periodic change in the energy spectra and the angular distributions. This finding suggests that the growth of PbSe does not take place as a layer-by-layer process as in the cases of MBE growth of some semiconductors.

In order to understand the present thickness dependence of scattering from the PbSe surfaces, Monte Carlo simulation of ion trajectories at glancing angle incidence of He ions on the wrinkled surfaces of PbSe/SnTe was performed. The simulation code we used was already developed,[6,10] where the motion of an ion is described by the continuum planar potential at distances more than 0.15 nm away from the surface, and by the binary collisions at the distances closer than 0.15 nm and inside the crystal. For the

energy loss of the ion along its trajectory, the empirical position–dependent stopping power formula was used.[4]

The best agreement of the simulated results with the observation was obtained from the following model of PbSe growth: The initial (001) surface of SnTe has the terraced surface as shown in the inset of Fig. 9.4(a) or with only minor variations.[6] This terraced structure is understood as the remain of the initial island growth of SnTe crystal on KCl(001). At PbSe thicknesses less than 1 nm, the surfaces are poor replicas of the SnTe surface, where the random steps which increase in number with the PbSe thickness are introduced on the terraced surface. The misfit dislocations are introduced at PbSe/SnTe interface when the PbSe layer is about 3 ML and the density of the misfit dislocations is larger at the thicker PbSe layers. Thus the terraced surfaces are wrinkled by the protrusions at the dislocations as shown in Fig. 9.7. The surface wrinkles become smaller when the thickness of PbSe layer is larger than about 20 nm. The surface of PbSe again becomes a poor replica of the initial SnTe surface, where the steps of random distribution are superposed on the terraced surface.

Simulation of ion trajectories at the PbSe surfaces described above has been performed, where more than 10^4 trajectories of He ions are simulated and an angular distribution and an energy spectrum are obtained at an angle of incidence. From the results of simulation, it is shown that not only the surface steps but also the surface wrinkles affect the glancing angle scattering. There are
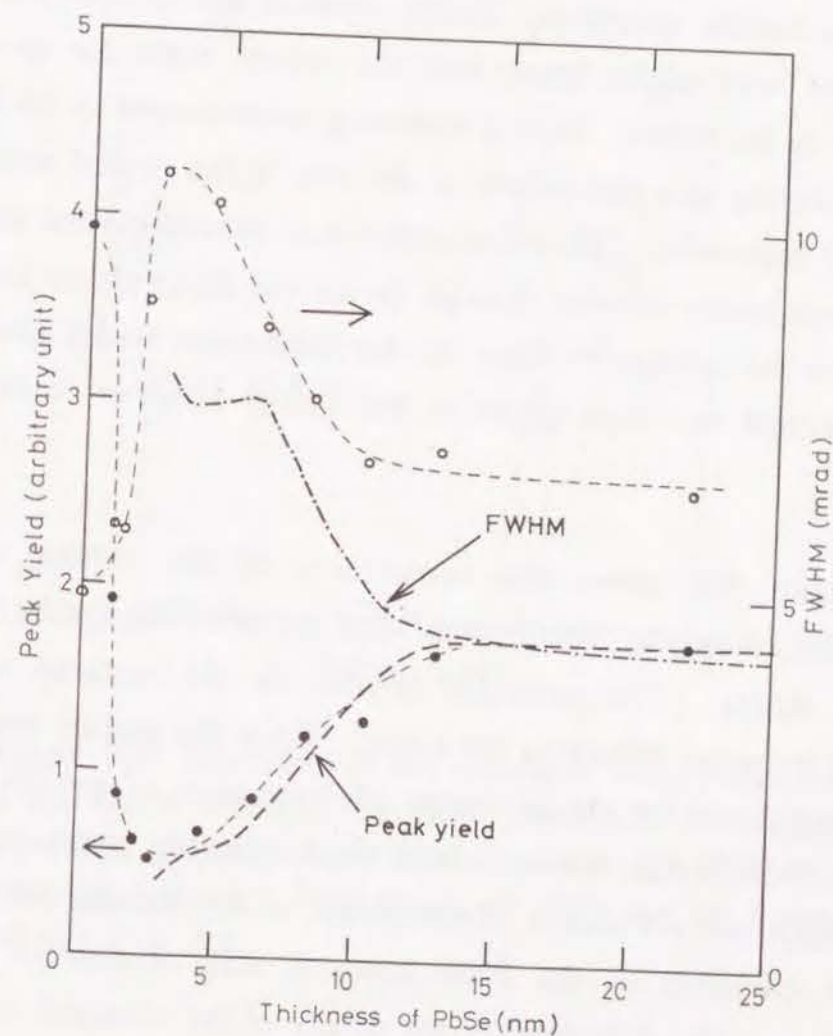
Figure 9.8: Comparison of the simulated and experimental peak height and the full width at half maxima of the angular distribution of the reflected He ions. Effects of terraced surface and the wrinkles due to the square–net of misfit dislocations are considered in the simulation. Energy of incident He⁺ ions was 0.7 MeV. Experimental data are taken from Fig. 9.6(a).

two processes at the wrinkled surface with which the angular distribution of scattered ions becomes broader and the yield at specular reflection decreases: Firstly some of the incident ions hit the surface with angles larger than the critical angle for specular reflection at the ridges. Such a scattering event results in the large angle scattering and penetration of the ions in the crystal which is otherwise impossible. The other is that ions penetrating the surface at the steps hardly channel through the curved (001) planar channel parallel to the surface.[18] Thus the ion trajectories which give rise to the second and third peaks in the energy spectrum cannot be allowed.

Figure 9.8 shows the comparison of the results of the simulation of angular distributions with the observed results shown in Fig. 9.6(a). The simulated results for the surfaces without random steps are shown in the figure. Since the surface distortion calculated from the elastic theory of dislocation is not correct at thinner PbSe layers, the calculated results for the layers less than 3 nm thick are not shown. Dependence of the angular distribution on the thickness of the PbSe layer is well reproduced in the simulation. The difference of the details of the observed thickness dependence at the different runs of growth as shown in Fig. 9.6(a) and (b) can be explained by difference of the density of random steps superposed on the terraced surface, *e.g.* the difference in the FWHM at initial SnTe and thick PbSe is mostly due to the steps.
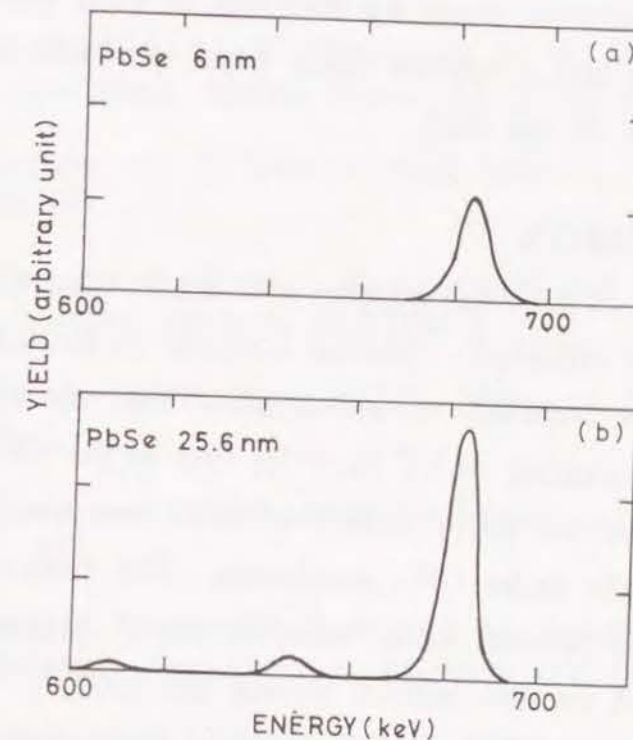
Figure 9.9: Examples of the simulated energy spectra of specularly reflected ions from PbSe/SnTe bicrystals, where the glancing angle of the incident 0.7 MeV He ions was 5 mrad. Thicknesses of PbSe are (a) 6 nm and (b) 25.6 nm.

The observed change in the energy spectrum of specularly reflected ions is also explained with the scattering at the wrinkled surface: Two examples of the simulated energy spectra of the He ions reflected at the angle of specular reflection, $2\theta_i$, are shown in Fig. 9.9 for two typical conditions. The energy resolution of the ion detector was not taken into account in the results. The changes

in the energy spectra during the growth are well reproduced, *i.e.* the peak structure disappears when the thickness of PbSe layer is less than about 15 nm and it appears again when the PbSe layers are thicker than about 20 nm thick.

9.5. CONCLUSION

Dependence of the mean separation of misfit edge dislocations at the interface of PbSe/SnTe epitaxial bicrystal on the thickness of PbSe crystal was obtained by transmission electron microscope. Glancing angle scattering of 0.7 MeV He ions at the (001) surface of PbSe grown on the (001) surface of SnTe was studied during the growth of PbSe under UHV conditions. The epitaxial growth of PbSe does not proceed by a "layer–by–layer" process. Many steps are formed on the surface during the growth, which are perhaps formed by random two dimensional nucleation processes. The anomalous dependence of the angular distribution of reflected He ions on the thickness of PbSe layer was found. Most of the changes in the scattering could be explained by the wrinkles on the surface of PbSe, which are introduced by the strain field of a square–net of misfit edge dislocations near the surface. This is confirmed by the simulation of glancing angle scattering of MeV He ions at the surfaces.

REFERENCES

1) A. D. Marwick, M. W. Thompson, B. W. Farmery and G. S. Harbinson, Radiat. Effects 15 (1972) 195.

2) R. Sizmann and C. Varelas, Nucl. Instrum. Methods 132 (1976) 633.

3) M. Mannami, K. Kimura, K. Nakanishi and A. Nishimura, Nucl. Instrum. Methods B13 (1986) 587.

4) K. Kimura, M. Hasegawa and M. Mannami, Phys. Rev. B36 (1987) 7.

5) K. Kimura and M. Mannami, Nucl. Instrum. Methods B27 (1987) 442.

6) Y. Fujii, K. Kimura, M. Hasegawa, M. Suzuki, Y. Susuki and M. Mannami, Nucl. Instrum. Methods B33 (1988) 405.

7) M. Hasegawa, K. Kimura and M. Mannami, J. Phys. Soc. Japan 57 (1988) 1834.

8) K. Kimura, M. Hasegawa, Y. Fujii. M. Suzuki, Y. Susuki and M. Mannami, Nucl. Instrum. Methods B33 (1988) 358.

9) W. Graser and C. Varelas, Surface Sci. 157 (1985) 74.

10) M. Mannami, Y. Fujii and K. Kimura, Surface Sci. 204 (1988) 213.

11) J.J. Harris and B. A. Joyce, Surface Sci. 108 (1981) L441.

12) J. W. Mathews, Dislocations in Solids, Vol.2, edited by F. R. N. Nabarro, North Holland, Amsterdam 1979, p.461.

13) G. Honjo and K. Yagi, Current Topics in Materials Science, Vol. 6, edited by E. Kaldis, North Holland, Amsterdam 1980, p.195.

14) S. Sawada, K. Kimura and M. Mannami, Jpn. J. Appl. Phys. 22 (1983) 1464.

15) M. Suzuki, H.Kawauchi, K. Kimura and M. Mannami, Surface Sci. 204 (1988) 223.

16) J. D. Eshelby, in "Dislocations in Solids", vol. 1, p.167, ed. F. R. N. Nabarro, North-Holland Pub. Co. (1979)

17) The second term of the right hand side of Eq. (4) is different from the corresponding expression of the Airy function given in reference 15 (Eq. (84)), where ξ_1/ξ_2 is missing.

18) M. Mannami, K. Kimura, Y, Susuki, Y. Fujii, N. Sakamoto, H. Ogawa, I. Katayama, T. Noro and H. Ikegami, Nucl. Instrum. and Methods B33 (1988) 62.

LIST OF PUBLICATIONS

1. "Charge−state Distribution of MeV He Ions Specularly Reflected from a SnTe(001) Surface"
   K. Kimura, Y. Fujii, M. Hasegawa, Y. Susuki and M. Mannami;
   Phys. Rev. B38 (1988) 1052−1057.

2. "Channeling in Bent Crystals: on the Bulk Capture Processes"
   M. Mannami, K. Kimura, Y. Susuki, Y. Fujii, N. Sakamoto, H. Ogawa, T. Noro, I. Katayama and H. Ikegami;
   Nucl. Instr. and Methods. B33 (1988) 62−65.

3. "Secondary Electron Emission due to MeV He Ions at Glancing Incidence Angles on Clean Single Crystal Surfaces"
   M. Hasegawa, K. Kimura, Y. Fujii, M. Suzuki, Y. Susuki and M. Mannami;
   Nucl. Instr. and Methods. B33 (1988) 334−337.

4. "Specular Reflection of Fast Ions at a Single Crystal Surface"
   K. Kimura, M. Hasegawa, Y. Fujii, M. Suzuki, Y. Susuki and M. Mannami;
   Nucl. Instr. and Methods. B33 (1988) 358−364.

5. "Surface Channeling of MeV He$^+$ Ions on a SnTe Single Crystal"
   Y. Fujii, K. Kimura, M. Hasegawa, M. Suzuki, Y. Susuki and M. Mannami;
   Nucl. Instr. and Methods. B33 (1988) 405−408.

6. "A New Method to Detect Surface Steps by Specularly Reflected Fast Ions"
   M. Mannami, Y. Fujii and K. Kimura;
   Surf. Sci. 204 (1988) 213−222.

7. "Glancing Angle Scattering of MeV Light Ions at Clean Solid Surfaces"
M. Mannami, K. Kimura, Y. Susuki, M. Hasegawa and Y. Fujii;
"Ion Beam Interactions with Solids" (Reports of the Special Project Research 1985–1987) 85–93.

8. "Resonant Coherent Excitation of Surface Channeling Ions"
K. Kimura, M. Hasegawa, Y. Fujii, Y. Susuki and M. Mannami;
"Ion Beam Interactions with Solids" (Reports of the Special Project Research 1985–1987) 257–262.

9. "Charge State Distributions of MeV He Ions Channeled through Thin Crystals with Atomically Clean Surfaces"
Y. Fujii, K. Sueoka, K. Kimura and M. Mannami;
J. Phys. Soc. Japan 58 (1989) 2758–2766.

10. "Surface Study with Glancing Angle Scattering of MeV Ions"
Y. Fujii, S. Fujiwara, K. Kimura and M. Mannami;
Proc. of the 2nd International Symposium on Advanced Nuclear Reserch-Evolution by Accelerators, Jan. 24–26, 1990 (Mito Ibaraki, Japan).

11. "Charge State Distribution of MeV He Ions Channeled through Au and SnTe Crystals"
Y. Fujii, K. Sueoka, K. Kimura and M. Mannami;
Nucl. Instr. and Meth. B48 (1990) 121–124.

12. "Position-Dependence of Charge State Distributions of Channeling MeV He Ions in Au Single Crystals"
Y. Fujii, K. Sueoka, K. Kimura and M. Mannami;
Radiat. Eff. 114 (1990) 239–249.

13. "Process of Epitaxial Growth of PbSe on SnTe(001) Studied by Glancing Angle Scattering of MeV He Ions"
Y. Fujii, S. Fujiwara, K. Kimura and M. Mannami;
Radiat. Eff. 116 (1991) 111–123.

14. "Position Dependent Charge Exchange Probability of MeV He Ions"
Y. Fujii, K. Kimura and M. Mannami;
Ann. Rep. Radi. Lab., Kyoto Univ., No.1 (1991) 113–115.

15. "Convoy Electrons Produced at Glancing Angle Scattering of Fast Ions"
K. Kimura, M. Hasegawa, Y. Susuki, Y. Fujii and M. Mannami;
Ann. Rep. Radi. Lab., Kyoto Univ., No.1 (1991) 105–107.

16. "Role of Surface Steps on the Charge State of MeV Ions Specularly Reflected from a Crystal Surface"
Y. Fujii, S. Fujiwara, K. Kimura and M. Mannami;
Nucl. Instr. and Meth. B58 (1991) 18–26.

17. "Epitaxial Growth of Lead Chalcogenides on Tin Telluride (001)"
S. Fujiwara, M. Tsuji, Y. Fujii, Y. Susuki, K. Kimura and M. Mannami;
Bull. Inst. Chem. Res., Kyoto Univ., Vol.69, (1991) 59–66.

18. "Characterization of Surfaces and Epitaxial Foils by Glancing Angle Scattering of Fast Ions"
Y. Fujii, K. Kimura and M. Mannami;
Oyo Busturi, 60 (1991) 1207–1213.

19. "Glowth of Lead Chalcogenides on SnTe (001) studied by Glancing Angle Scattering of Fast Ions"
Y. Fujii, K. Narumi, K. Kimura and M. Mannami;
Proc. 5th Topical Meeting on Crystal Growth Mechanism,
Gero, Gifu Prefec., Jan. 8–10, (1992) 213–216.

20. "Study on Process of Epitaxial Growth of PbSe on SnTe (001) by Glancing Angle Scattering of MeV He Ions"
Y. Fujii, S. Fujiwara, K. Narumi, K. Toba, K. Kimura and M. Mannami;
Ann. Rep. Radi. Lab., Kyoto Univ., No.2 (1992) 104–106.

21. "Position–Dependent Stoping Power of Crystal Surface for MeV He Ions"
K. Kishine, Y. Fujii, K. Narumi, K. Toba, K. Kimura and M. Mannami;
Ann. Rep. Radi. Lab., Kyoto Univ., No.2 (1992) 107–109.

22. "Study of Glowth Proccess of PbSe on SnTe (001) by Ion Scattering"
M. Mannami, Y. Fujii and K. Kimura;
Proc. 3rd Meeting on Crystal Growth Mechanism, Sendai,
Miyagi Prefec., June 3–5, (1992) 182–186.

23. "Energy Loss of Energetic Ions in Surface Blocking"
K. Kimura, H. Ohtsuka, Y. Fujii and M. Mannami;
Phys. Lett. A 163 (1992) 97–100.

24. "Dynamic Response of Surface Electrons to Energetic Ions at Glancing Angle Scattering from Crystal Surfaces"
Y. Fujii, K. Narumi, K. Kishine, K. Kimura and M. Mannami;
Nucl. Instr. and Meth. B67 (1992) 82–86.

25. "Position–Dependent Stopping Powers of the (100) surfaces of Some NaCl– type Crystals for MeV Light Ions"
Y. Fujii, S. Fujiwara, K. Narumi, K. Kimura and M. Mannami;
Surf. Sci. 277 (1992) 164–172.

26. "Energy Loss of 0.7–MeV He Ions due to the Dynamic Response of Surface Electrons"
Y. Fujii, K. Kishine, K. Narumi, K. Kimura and M. Mannami;
Phys. Rev. A 47 (1993) 2047–2054.

27. "Initial Stage of Epitaxial Growth of Lead Chalcogenides on SnTe (100)"
Y. Fujii, K. Toba, K. Narumi, K. Kimura and M. Mannami;
Proc. 6th Topical Meeting on Crystal Growth Mechanism,
Awara, Fukui Prefec., Jan. 20–22, (1993) 267–272.

28. "Real Time Measurement of Crystal Growth by Glancing Angle Scattering of Fast Ions"
Y. Fujii, K. Toba, K. Narumi, K. Kimura and M. Mammami;
Nucl. Instr. and Meth. B79 (1993) 509–512.

29. "Energy Losses of 12–32 keV H^+, He^+ and N^+ Ions at Glancing Angle Scattering from Clean Surfaces of Silicon Crystals"
K. Narumi, Y. Fujii, K. Kishine, S. Fujiwara, K. Kimura and M. Mannami;
J. Phys. Soc. Japan 62 (1993) 1603–1611.

30. "Layer–by–Layer growth studied by Glancing Angle Scattering of Fast Ions"
Y. Fujii, K. Narumi, K. Kimura, M. Mannami, T. Hashimoto, K. Ogawa, F. Ohtani, T. Yoshida and M. Asari;
Appl. Phys. Lett. (1993) (in press).

31. "Interplay of Charge Exchange and Energy Loss of MeV He Ions Specularly Reflected from a Crystal Surface"
Y. Fujii, S. Fujiwara, K. Narumi, K. Kimura and M. Mannami;
Phys. Rev. A (1993) (submitted).

32. "Contribution of Inner Shell Electrons to Position-Dependent Stopping Powers of a Crystal Surface"
K. Narumi, Y. Fujii, K. Kishine, H. Kurakake, K. Kimura and M. Mannami;
Surf. Sci. (1993) (in press).

33. "Observation of Skipping Motion and Subsurface Planar Channeling of 30 keV H^+ Ions on Single Crystal Surfaces"
K. Narumi, Y. Fujii, K. Kimura, M. Mannami and H. Hara;
Surf. Sci. (1993) (submitted).

34. "Study of Layer-by-Layer Glowth by Glancing Angle Scattering of Fast Ions"
Y. Fujii, K. Narumi, K. Kimura, M. Mannami, T. Hashimoto, K. Ogawa, F. Ohtani and T. Yoshida;
Proc. of 5th Meeting on Crystal Growth Mechanism, Sapporo, June 16-18, (1993) 179-184.

35. "Study on Initial Stage of Hetero-Epitaxial Growth by Glancing Angle Scattering of Fast Ions from Surfaces"
Y. Fujii, K. Toba, K. Narumi, K. Kimura and M. Mannami;
Ann. Rep. Radi. Lab., Kyoto Univ., No.3 (1993).

36. "Position-Dependent Charge-Exchange and Energy-Loss Processes of MeV He Ions near a Crystal Surface"
Y. Fujii, S. Fujiwara, K. Narumi, K. Kimura and M. Mannami;
Nucl. Instr. and Meth. B (1993) (submitted).

37. "In-Situ Study of Growing Surface by Glancing Angle Scattering of Fast Ions"
Y. Fujii, T. Hashimoto, K. Ogawa, K. Narumi, M. Fritz, K. Toba, A. Oda, F. Ohtani, T. Yoshida, M. Asari, K. Kimura and M. Mannami;
Proc. of the 3rd IUMRS International Conf. on Advanced Materials, Tokyo, Japan, 31 Aug. - 4 Sept. (1993).

38. "Skipping Motion of 15-30 keV H^+ Ions on Single Crystal Surfaces of KCl and SnTe"
K. Narumi, Y. Fujii, K. Kimura and M. Mannami;
Nucl. Instr. and Meth. B (1993) (submitted).